
From few- to many-body physics in low-dimensional quantum gases

Zur Erlangung des Grades eines Doktors der Naturwissenschaften (Dr. rer. nat.)
Genehmigte Dissertation von Fabian Brauneis
Tag der Einreichung: 07.11.2024, Tag der Prüfung: 09.12.2024

1. Gutachten: Prof. Dr. Hans-Werner Hammer
2. Gutachten: Prof. Artem Volosniev, Ph.D.
Darmstadt, Technische Universität Darmstadt



TECHNISCHE
UNIVERSITÄT
DARMSTADT

Physics Department
Institut für Kernphysik
AG Hammer

From few- to many-body physics in low-dimensional quantum gases

Accepted doctoral thesis by Fabian Brauneis

Date of submission: 07.11.2024

Date of thesis defense: 09.12.2024

Darmstadt, Technische Universität Darmstadt

Bitte zitieren Sie dieses Dokument als:

URN: urn:nbn:de:tuda-tuprints-289464

URL: <http://tuprints.ulb.tu-darmstadt.de/28946>

Jahr der Veröffentlichung auf TUprints: 2024

Dieses Dokument wird bereitgestellt von tuprints,

E-Publishing-Service der TU Darmstadt

<http://tuprints.ulb.tu-darmstadt.de>

tuprints@ulb.tu-darmstadt.de

Die Veröffentlichung steht unter folgender Creative Commons Lizenz:

Namensnennung – Nicht kommerziell – Weitergabe unter gleichen Bedingungen 4.0 International

<https://creativecommons.org/licenses/by-nc-sa/4.0/>

This work is licensed under a Creative Commons License:

Attribution–NonCommercial–ShareAlike 4.0 International

<https://creativecommons.org/licenses/by-nc-sa/4.0/>

Erklärungen laut Promotionsordnung

§ 8 Abs. 1 lit. c PromO

Ich versichere hiermit, dass die elektronische Version meiner Dissertation mit der schriftlichen Version übereinstimmt.

§ 8 Abs. 1 lit. d PromO

Ich versichere hiermit, dass zu einem vorherigen Zeitpunkt noch keine Promotion versucht wurde. In diesem Fall sind nähere Angaben über Zeitpunkt, Hochschule, Dissertationsthema und Ergebnis dieses Versuchs mitzuteilen.

§ 9 Abs. 1 PromO

Ich versichere hiermit, dass die vorliegende Dissertation selbstständig und nur unter Verwendung der angegebenen Quellen verfasst wurde.

§ 9 Abs. 2 PromO

Die Arbeit hat bisher noch nicht zu Prüfungszwecken gedient.

Darmstadt, 07.11.2024

F. Brauneis

Abstract

Macroscopic systems exhibit complex behavior that cannot be understood by studying their few-body components alone. A key challenge in modern physics is to uncover how many-body phenomena emerge from the underlying few-body world. One approach to this problem is to study properties of the system as the particle number increases. Motivated by recent experimental advancements enabling such investigations in ultracold atom systems, this thesis contributes to three goals of the field “few-to-many-body crossover”: 1) Advance numerical investigations of this crossover by improving theoretical tools. 2) Connect many-body concepts with the description of few-to-many systems. 3) Explore basic physics of few-body systems to facilitate new many-body research.

We contribute to the first goal by comparing different renormalization methods for the one-dimensional contact interaction. Although this interaction requires no regularization, renormalized interactions have been shown to significantly improve the convergence of *ab initio* calculations. This expands the accessible parameter space, allowing one to study systems with stronger interactions and larger particle numbers. Our results address a gap in the literature by contrasting commonly used renormalized interactions in cold atom setups, providing valuable guidance for selecting the most suitable renormalization scheme.

Next, we study a one-dimensional system of bosons with a repulsively interacting impurity. Impurities are important for few-to-many studies because they act as probes of the environment. We introduce an experimentally motivated Hamiltonian and connect its energy spectrum to a quasi-particle known as the Bose polaron, thereby achieving the second goal. The connection with this many-body concept offers an intuitive understanding of the system. It enables the exploration of the few-to-many-body crossover in cold-atom polaron problems beyond conventional observables.

In a separate study, we investigate an attractive impurity interacting with bosons in one dimension. The attractive interaction complicates many-body studies of this system as the impurity forms a bound state with the bosons. Therefore, our focus is on characterizing this state. For example, we derive the maximum number of bosons that can be bound to the impurity. This few-body analysis addresses the third goal by providing key insights for many-body research on one-dimensional attractive impurities.

In the final part of this thesis, we examine a two-dimensional system of attractively interacting bosons. Previous research has demonstrated that this system exhibits intriguing universal behavior. Given that most experiments are performed in harmonic traps, we study the influence of such confinement. Specifically, we investigate the transition from a trap-dominated state to an interaction-dominated one. Inspired by the many-body concept of phases, we introduce an observable that can be used as an indicator of the transition in few-to-many systems, contributing to the second goal. Furthermore, we also add to the third goal by studying finite range effects in the few-body sector.

Parts of this thesis have been published in the following articles and preprints:

1. F. Brauneis *et al.*, “Artificial atoms from cold bosons in one dimension”, *New J. Phys.* 24.6 063036 (2022)
2. F. Brauneis *et al.*, “Emergence of a Bose polaron in a small ring threaded by the Aharonov-Bohm flux”, *Communications Physics* 6.1, p. 224 (2023)
3. F. Brauneis *et al.* “Comparison of renormalized interactions using one-dimensional few-body systems as a testbed”, arXiv: 2408.10052 (2024)
4. F. Brauneis, A. Volosniev, H.-W. Hammer “Two-dimensional bosonic droplets in a harmonic trap”, arXiv: 2410.00570 (2024)

Zusammenfassung

Makroskopische Systeme zeigen komplexes Verhalten, das nicht allein durch das Studium ihrer Komponenten verstanden werden kann. Eine zentrale Herausforderung der modernen Physik besteht darin, herauszufinden, wie Vielteilchenphänomene aus der zugrundeliegenden Welt weniger Teilchen hervorgehen. Dazu können Systeme mit zunehmender Teilchenzahl untersucht werden. Motiviert von kürzlichen Fortschritten bei Experimenten mit ultrakalten Atomen, die solche Studien ermöglichen, trägt diese Arbeit zu drei Zielen des Forschungsfeldes „few-to-many-body crossover“ bei: 1) Erweiterung numerischer Untersuchungen durch Verbesserung theoretischer Werkzeuge. 2) Verknüpfung von Vielteilchenkonzepten mit der Beschreibung von few-to-many-Systemen. 3) Untersuchung grundlegender Physik von Wenigteilchensystemen, um zukünftige Vielteilchenforschung zu ermöglichen.

Das erste Ziel wird durch den Vergleich verschiedener Renormierungsmethoden für die eindimensionale Kontaktwechselwirkung erreicht. Obwohl diese Wechselwirkung theoretisch keine Regularisierung erfordert, haben frühere Studien gezeigt, dass renormierte Wechselwirkungen die Konvergenz von *ab initio* Berechnungen erheblich verbessern. Dadurch wird der zugängliche Parameterraum erweitert, einschließlich stärkerer Wechselwirkungen und größerer Teilchenzahlen. Durch diesen Vergleich wird eine Lücke in der Literatur geschlossen, indem gängige renormierte Wechselwirkungen für Systeme kalter Atome gegenübergestellt werden. Somit werden wertvolle Hinweise zur Auswahl des geeignetsten Renormierungsschemas für zukünftige Studien geliefert.

Als nächstes wird ein eindimensionales System von Bosonen mit einer repulsiv-wechselwirkenden Verunreinigung untersucht. Verunreinigungen sind für Studien im Bereich few-to-many wichtig, da sie als Testobjekte der Umgebung fungieren. In diesem Teil der Arbeit wird ein experimentell motivierter Hamiltonoperator eingeführt und dessen Energiespektrum mit einem Quasiteilchen, das als Bose-Polaron bekannt ist, in Verbindung gebracht. Damit wird zum zweiten Ziel beigetragen. Diese Verbindung bietet ein intuitives Verständnis der Physik des Systems und ermöglicht die Untersuchung des few-to-many-body crossovers in Polaron-Problemen bei kalten Atomen über herkömmliche Beobachtungsgrößen hinaus.

In einer separaten Studie wird die Untersuchung auf eine attraktive Verunreinigung

erweitert, die mit Bosonen in einer Dimension wechselwirkt. Die attraktive Wechselwirkung erschwert Vielteilchenuntersuchungen dieses Systems, da die Verunreinigung mit den Bosonen einen Bindungszustand bildet. Daher liegt der Fokus auf der Charakterisierung dieses Zustands. Beispielsweise wird die maximale Anzahl von Bosonen bestimmt, die an die Verunreinigung gebunden werden können. Diese Wenigteilchenanalyse setzt das zweite Ziel um, indem wichtige Erkenntnisse für zukünftige Vielteilchenforschung über eindimensionale attraktive Verunreinigungen geliefert werden.

Im letzten Teil dieser Thesis wird ein zweidimensionales System von attraktiv wechselwirkenden Bosonen untersucht. Frühere Forschungen haben gezeigt, dass dieses System faszinierendes universelles Verhalten aufweist. Da die meisten Experimente in harmonischen Fallen durchgeführt werden, wird deren Effekt untersucht. Genauer gesagt, wird der Übergang von einem fallendominierten zu einem wechselwirkungsdominierten Zustand studiert. Inspiriert von der Vielteilchenbeschreibung von Phasen wird eine Observable eingeführt, welche als Indikator des Übergangs genutzt werden kann. Damit wird zum zweiten Ziel beigetragen. Weiterhin wird das dritte Ziel adressiert, indem endliche Reichweiteneffekte im Wenigteilchensektor untersucht werden.

Teile dieser Thesis wurden bereits in folgenden Artikeln und Preprints veröffentlicht:

1. F. Brauneis *et al.*, „Artificial atoms from cold bosons in one dimension“, *New J. Phys.* 24 063036 (2022)
2. F. Brauneis *et al.*, „Emergence of a Bose polaron in a small ring threaded by the Aharonov-Bohm flux“, *Communications Physics* 6.1, p. 224 (2023)
3. F. Brauneis *et al.* „Comparison of renormalized interactions using one-dimensional few-body systems as a testbed“, arXiv: 2408.10052 (2024)
4. F. Brauneis, A. Volosniev, H.-W. Hammer „Two-dimensional bosonic droplets in a harmonic trap“, arXiv: 2410.00570 (2024)

Contents

1. Introduction	1
1.1. Ultracold atoms	2
1.1.1. Motivation	2
1.1.2. Control and flexibility	3
1.1.3. Few-to-many-body studies	4
1.2. Theoretical approaches	5
1.3. Outline	6
2. Methods	9
2.1. Description of many-body quantum systems	9
2.1.1. Core concepts	10
2.1.2. Formalism of second quantization	11
2.2. Configuration interaction method	13
2.2.1. Practical steps	14
2.3. Flow equation approach	15
2.3.1. Basics	16
2.3.2. Normal ordering and truncation scheme	18
2.3.3. Reference state	20
2.3.4. Error estimation	21
2.3.5. Calculation of observables	21
2.4. Impurity in a one-dimensional ring: transformation to the frame ‘co-moving’ with the impurity	22
2.5. Mean-field approximation for one-dimensional bosonic systems	23
3. Comparison of renormalized interactions using one-dimensional few-body systems as a testbed	27
3.1. Introduction	28
3.2. Formalism	30
3.2.1. Hamiltonian	30
3.2.2. Potentials	30

3.2.3. Configuration interaction method	31
3.2.4. Two-body problem	32
3.3. Renormalized interactions	33
3.3.1. Running coupling constant	34
3.3.2. Effective interactions	37
3.4. Results	40
3.4.1. Energy	41
3.4.2. Density	43
3.4.3. Transformation of operators	45
3.4.4. Transition matrix elements	48
3.5. Conclusions	51
3.5.1. Summary	51
3.5.2. Outlook	52
4. Emergence of a Bose polaron in a small ring threaded by the Aharonov-Bohm flux	55
4.1. Introduction	56
4.2. System	58
4.2.1. Co-moving frame	60
4.3. Methods	60
4.3.1. Mean-field approximation	60
4.3.2. Flow equation approach	62
4.3.3. Validity of mean-field approximation	64
4.4. Results and discussion	64
4.4.1. Energy spectrum	64
4.4.2. Effective mass	66
4.4.3. Currents	68
4.4.4. Role of defects	71
4.5. Conclusions	74
4.5.1. Summary	74
4.5.2. Outlook	75
5. Artificial atoms from cold bosons in one dimension	79
5.1. Introduction	80
5.2. Formulation	82
5.2.1. Hamiltonian	82
5.2.2. Physical picture	83

5.3. Mean-field approximation for the heavy impurity problem	85
5.3.1. Mean-field solutions	85
5.3.2. Point of Transition	87
5.4. Mean-field results in the zero-density limit	89
5.4.1. Many-body bound state	90
5.4.2. Point of transition	91
5.4.3. Scattering state	91
5.5. Flow equation results: approach to the zero-density limit	92
5.5.1. Energies	93
5.5.2. Densities and phase fluctuations	95
5.6. Mobile impurity	97
5.6.1. Mean-field analysis	98
5.6.2. Flow equation results	98
5.7. Conclusions	99
5.7.1. Summary	99
5.7.2. Outlook	99
6. Two-dimensional bosonic droplets in a harmonic trap	105
6.1. Introduction	106
6.2. Formulation and Methods	108
6.2.1. System	108
6.2.2. Methods	111
6.3. Results	113
6.3.1. Minimization of variational ansatz	113
6.3.2. Transition indicator: static response	116
6.3.3. Influence of finite range effects	118
6.4. Conclusions	120
6.4.1. Summary	120
6.4.2. Outlook	121
7. Summary and Outlook	123
A. Renormalized interactions in one dimension: Derivations, fitting analysis, larger particle number, technical details and alternative convergence plots	145
A.1. Energy convergence for the bare contact interaction	145
A.2. Analysis of convergence	148
A.2.1. Energy	149
A.2.2. Density	151

A.2.3. One-body Hamiltonian	151
A.2.4. Transition matrix elements	153
A.3. Two-dimensional harmonic oscillator	156
A.4. Convergence of energy for larger particle number	159
A.4.1. Calculation in relative coordinates	160
A.4.2. Energy convergence $1 + N$ system	162
A.4.3. Energy convergence $2 + N$ system	163
A.5. Implementation of effective interactions	163
A.5.1. Implementation of $V_{\text{eff}}^{\text{rel}}$	163
A.5.2. Implementation of $V_{\text{eff}}^{\text{rel}+\text{cm}}$	165
A.6. Transformation of operators	166
A.6.1. Two-body system	166
A.6.2. Many-body system	167
A.6.3. Implementation for $V_{\text{eff}}^{\text{rel}}$	169
A.6.4. Implementation for $V_{\text{eff}}^{\text{rel}+\text{cm}}$	169
A.7. Derivation of the running coupling constant $g_{\text{unconf.}}(\lambda)$ in free space	170
A.8. Connecting quantum numbers to momenta	171
A.9. Additional convergence plots	172
A.9.1. Convergence plots as a function of $1/n$	172
A.9.2. Double logarithmic plots	172
B. Aharonov-Bohm Bose polaron: Generalization, definitions and analysis convergence towards thermodynamic limit	183
B.1. Coupling flux to bosons and impurity	183
B.2. Mass imbalance	185
B.3. Definition of effective mass	187
B.4. Convergence towards thermodynamic limit	188
B.4.1. Self-energy of the impurity	188
B.4.2. Effective mass	189
C. Bosonic artificial atom in one dimension: Benchmarks, mean-field derivations and additional data for few-body limit	191
C.1. Comparison between the ML-MCTDHX and IM-SRG	191
C.2. Mean-field solution for hard-wall boundary conditions	194
C.3. Zero-Density Limit within Mean-field Approximation	194
C.3.1. Many-body bound state	195
C.3.2. Point of transition	196
C.4. Smallest artificial atom	197

D. Two-dimensional bosonic droplets: Variational ansatz	199
D.1. Details on variational ansatz	199
D.2. Alternative variational ansatz	201

1. Introduction

The subjects of many scientific fields are large composite systems whose properties are determined by their microscopic constituents. In sociology, for example, one goal is to understand how a large community made up of many individuals – each with their own views and properties – behaves collectively. A biological example is a cell, which is composed of molecules, which in turn consist of atoms. This complex composition enables a wide variety of biological mechanisms such as communication within the cell. In physics, we describe large systems (large typically means in the thermodynamic limit, i.e., an infinite number of particles) by their macroscopic properties, such as energy, pressure, or their phase. These macroscopic properties must ultimately be determined by the underlying microscopic Hamiltonian.

However, it is naive to assume that solving the few-body problem will directly reveal the many-body properties. As Anderson put it: “More is different” [1]. For example, when many particles interact via two-body interactions, solving the two-body problem alone is insufficient to describe the entire system. Consider an electron moving through an ion crystal: even though this system can be modelled using only two-body interactions, a faithful description requires solving the many-body Schrödinger equation. This is a highly non-trivial task and one must resort to approximations, which is typical for large systems. For our example, Landau and Pekar showed that by introducing a quasi-particle called “polaron” the description can be simplified considerably [2]. Instead of considering the electron and all its interactions, the polaron concept is introduced: A quasi-particle which behaves similar to the electron but has modified single-particle parameters such as self-energy and effective mass which depend on the interactions¹.

Interesting questions that arise in this context are: How do many-body phenomena emerge from their underlying few-body physics? How many particles are needed to show “many-body” effects such as quasi-particles, superfluidity² and phase transitions? Experiments with Helium have shown that superfluidity can emerge with as few as 60

¹For example, stronger interactions result in a polaron with an increased effective mass, meaning it moves slower than the bare particle.

²A state certain systems acquire when cooled to very low temperatures, where an object can move through it without friction.

Helium atoms [3], a surprisingly small number. Atomic nuclei offer another example of systems with a finite number of particles where phenomena typically associated with the thermodynamic limit, such as the emergence of collective modes or signatures of superfluidity, have been observed [4, 5]. Additionally, an interesting question is whether there is new physics in the parameter region between the few- and the many-body domain, known as the mesoscopic or few-to-many region. Do we gain insight into the many-body world by studying this domain?

Such questions are studied by considering the “few-to-many-body crossover” which is an active field of research (see, e.g., Refs. [6–14] and references therein). This thesis contributes to three goals of this field:

1. Advance numerical investigations of this crossover by improving theoretical tools.
2. Connect many-body concepts with the description of few-to-many systems.
3. Explore basic physics of few-body systems to facilitate new many-body research.

Studying the few-to-many-body crossover in “standard” physical systems, such as those in nuclear or solid-state physics, is often challenging due to complex interactions and limited tunability. Therefore, we focus on systems of ultracold atoms, which have simple interactions and are highly tunable. For example, the dimension of a system can be reduced (see below), which allows us to focus on low-dimensional setups.

1.1. Ultracold atoms

1.1.1. Motivation

One of the guiding principles in physics is to simplify the description of physical phenomena by focusing only on the relevant degrees of freedom. A historical example is the use of the Ising model to understand ferromagnetism and phase transitions. While it is a significant simplification compared to more realistic models like the Heisenberg model, its simplicity made it solvable and provided important insights [15]. For a theoretician, implementing a simpler system can be “easily” achieved by neglecting certain parts of a Hamiltonian or simplifying interactions. With the advent of ultracold atom systems, this approach also became experimentally viable.

Simulation of complex many-body phenomena became possible with the first realization of a Bose-Einstein condensate (a state where the majority of particles occupy the same quantum state) in ultracold atom systems [16, 17]. Since then, the field of cold atom physics expanded significantly, providing a versatile platform for fundamental tests of

quantum mechanical properties, for building and testing descriptive models [18–21]. Ultracold atoms are also considered as a potential platform for quantum computing [22]. These experimental advances motivate further theoretical studies, as the high tunability of experiments allows one to use ultracold atoms as a “physicist’s playground” [9]. The insights gained from ultracold atoms can, in turn, help to better understand more complex systems.

1.1.2. Control and flexibility

The versatility of ultracold atoms stems from high control over many different parameters. For example, different types of atoms can be selected, enabling the study of fermionic, bosonic, or even mixed systems [18]. Additionally, the type of interaction can be modified. Typically, atoms interact via the van der Waals potential, which can be treated as a contact interaction for ultracold atoms [18, 23]. However, long-range interactions can also be studied, e.g., by choosing atoms that showcase dipolar interaction [24–26]. Using Feshbach resonances, one can tune the strength of atom-atom interactions by applying an external magnetic field [27]. This flexibility even allows one to tune the interaction from strongly repulsive to strongly attractive, which is used to study phenomena such as the BCS-BEC crossover (for reviews, see Refs. [28, 29]).

Furthermore, the trapping confinement of the atoms can be manipulated. This allows one to effectively change the system’s dimensionality by freezing out spatial degrees of freedom (see Refs. [6, 18]). Imagine a cigar-shaped trap modelled by the generic potential

$$W = \frac{m}{2} (\omega_x^2 x^2 + \omega_y^2 y^2 + \omega_z^2 z^2), \quad (1.1)$$

that becomes increasingly more elongated, $\omega_z \ll \omega_x, \omega_y$. The translational excitations along the length of the trap ($\hbar\omega_z$) require less energy, while the vertical excitation energy ($\hbar\omega_x, \hbar\omega_y$) increases. If temperatures are low enough, vertical excitations are no longer accessible, and the system becomes effectively one-dimensional (1D). Today, 1D and 2D setups of ultracold quantum gases are commonly prepared [6, 18].

Studying low-dimensional systems is particularly interesting for several reasons. Firstly, reducing the system’s dimensionality can help reduce its complexity. For instance, in 2D and in 1D the aforementioned Ising model is analytically solvable [30, 31]. Another class of analytical solvable systems in 1D are equal mass particles interacting via contact interaction confined to a ring, i.e., periodic boundary conditions; for fermions this system is known under the name of Gaudin-Yang model while for bosons it is called the Lieb-Liniger model. Their solution can be obtained using the Bethe Ansatz [32–36]. Such analytical solutions can offer valuable insights. Secondly, low-dimensional systems can exhibit vastly

different physical properties compared to their 3D counterparts, making their physics fascinating on their own. For example, the so-called Tonks-Girardeau gas describes a 1D system of impenetrable bosons that can be mapped onto non-interacting fermions [37]. This prediction was successfully tested in cold atom experiments [38]. In 2D, intriguing effects also emerge. For example, Hammer and Son showed that a system of bosons with attractive contact interaction exhibits a universal many-body bound state [39]. For a large number of particles, its binding energy is fully determined by the two-body ground state energy; increasing the particle number simply results in an exponential increase of the binding energy by a constant scaling factor, $E_{N+1}/E_N = 8.567$. This means that although the system is not in the thermodynamic limit, it can still be considered a many-body system because the addition of a particle only leads to an absolute change of the properties of the system while relative quantities remain unchanged.

1.1.3. Few-to-many-body studies

In recent years, systematic bottom-up studies of many-body effects starting from few-body systems have become possible in ultracold atom systems (see, e.g., Ref. [6] and references therein). These experiments began with the breakthrough of preparing a 1D system in a harmonic trap where the particle number could be tuned between 1 and 10 fermions by “spilling” the remaining ones [40]. After that, the “Formation of a Fermi Sea One Atom at a Time” was studied (see below for more details) [41]. The experiments were then extended to two dimensions, where a precursor of a quantum phase transition was observed [42]. In the same setup, the pair correlation function of fermions was directly measured, which enabled studies of the emergence of Cooper pairs from the few-body limit [43]. Another work explored the emergence of hydrodynamics [44].

A key element of Ref. [41] was the introduction of a particle with a different spin (a so-called impurity) into the system, where it acted as a probe for the environment. The interaction energy, i.e., the energy difference for the system with and without the impurity, was measured for an increasing fermion number. This allowed the authors to determine how many fermions are needed to screen the impurity and thus, to form a Fermi sea around the impurity. Surprisingly, only a handful of fermions were sufficient.

The idea of using an impurity as a probe for few-to-many-body studies dates back to earlier experiments. In the above-discussed experiment from Ref. [3], a similar approach was used to determine how many helium-4 atoms are required for superfluidity. An impurity in the form of a single molecule was inserted into superfluid helium-4 and non-superfluid helium-3 droplets consisting of about 10^4 atoms. Then, the infrared spectrum of the impurity was measured. The spectra showed qualitatively different behavior which was attributed to the superfluid nature of helium-4. To test how many helium-4 atoms

are needed to show superfluidity, helium-4 atoms were added to the helium-3 droplet, effectively screening the impurity. For approximately 60 atoms, the spectrum of helium-4 was recovered. The authors interpreted this system as the minimum required to form superfluidity in helium around an impurity.

In general, studying the effects of impurities is fascinating, as their introduction – a seemingly small change in the system – can have tremendous effects on the system’s overall properties.

1.2. Theoretical approaches

For most Hamiltonians, obtaining an analytical solution is not possible. Therefore, approximations, such as the mean-field ansatz, are often applied to gain physical insight into the system’s properties. While these techniques can be powerful, one must be cautious and verify the validity of the approximations. This can be done either through physical arguments or, alternatively, by performing *ab initio* calculations, i.e., numerically solving the many-body Schrödinger equation³. This is often the only viable option if approximations do not describe the relevant physics faithfully.

One of the simplest numerical methods is the exact diagonalization, also known as the configuration interaction (CI) method [45–54], which we employ in this thesis. While theoretically exact, meaning no approximations are required beyond a finite Hilbert space, this method suffers from exponentially growing Hilbert spaces with increasing particle numbers, making calculations with more than a handful of particles impractical. To overcome this issue, various numerical methods have been developed, such as the multi-layer multi-configuration time-dependent Hartree method for atomic mixtures [55–57], coupled cluster methods [58–60], flow equation approaches [61–63], extensions to the CI method like the importance-truncated CI [64, 65], and Monte Carlo methods (see, e.g., Refs. [66, 67] and references therein). All of these techniques introduce an approximation to the Schrödinger equation, resulting in a controllable error. For different systems, different methods are better suited than others and, in order to ensure that the error is small, a comparison to other methods or an estimate of this error is necessary.

In this thesis, we employ the CI method and the flow equation method for bosons. The latter is motivated by its use in condensed matter [68] and nuclear physics [69, 70], where it has been applied to nuclei with more than 50 nucleons (in this context, it is often called in-medium similarity renormalization group, which we will also use in this thesis). The bosonic flow equation approach has recently been applied in the context of

³The challenges associated with this are very similar to those faced in nuclear structure and quantum chemistry.

ultracold quantum gases to study the properties of one-dimensional systems with and without impurities (see Refs. [61, 71, 72] for previous works and Refs. [62, 63] for works that are discussed in Chaps. 4 and 5 of this thesis. Additionally, we use the mean-field approximation for bosonic systems to gain analytical and physical insight.

1.3. Outline

In this thesis, different systems of low-dimensional ultracold atoms are studied to contribute to the field of the few-to-many-body crossover. We begin with two method-oriented chapters. In Chap. 2, we introduce the methods used throughout the thesis, including a short introduction into the description of many-body systems and an explanation of the two *ab initio* methods employed. We also show how to simplify the study of a one-dimensional system with an impurity and briefly discuss how such systems can be investigated using the mean-field approximation.

The first goal, “Advance numerical investigations of this crossover by improving theoretical tools”, is met in Chap. 3, where different renormalized interactions are compared. The results of this chapter can help future *ab initio* studies to expand the parameter regime and thereby aid the study of the few-to-many-body crossover.

The following chapters focus on physical results. In Chap. 4 and Chap. 5, we study one-dimensional systems of bosons with an impurity. As discussed above, impurities can probe the environment in the few-to-many-body transition. In Chap. 4, we introduce an experimentally motivated Hamiltonian and connect its description with the many-body concept of a polaron. This allows for a few-to-many study of the effective mass of a one-dimensional Bose polaron. To the best of our knowledge, such an investigation has not been conducted previously. This chapter addresses the second goal: “Connect many-body concepts with the description of few-to-many systems”.

While in Chap. 4, we focus on a repulsively interacting impurity, in Chap. 5 the effects of an attractively interacting impurity are studied. The attractive interaction leads to bosons bound to the impurity which complicates theoretical studies, as only few bosons are bound while the remaining ones occupy scattering states. To alleviate this issue and facilitate many-body investigations, we study the bound state in detail. Among other things, we derive the maximum number of bound particles. These results pave the way for future many-body studies of attractive impurities, e.g., they might be used to construct effective models that allow for an easier description of the many-body system. Therefore, this chapter contributes to the third goal: “Explore basic physics of few-body systems to facilitate new many-body research.”

Finally, in Chap. 6, we extend our study to two-dimensional systems, specifically focusing

on a system of attractively interacting bosons in 2D (see above). It exhibits intriguing universal behavior such as an exponentially increasing binding energy with the addition of another particle, see Ref. [39]. This exponential increase makes experimental tests of universal properties challenging, requiring a few-to-many approach where the particle number is increased one by one. Since most experiments are conducted in harmonic confinements, we analyze how this influences the results of Ref. [39]. In particular, we explore the transition from a trap-dominated regime to an interaction-dominated one. Motivated by the description of phase transitions, we introduce an observable that can be used to identify analogs of such transitions in few-to-many systems (see the second goal: “Connect many-body concepts with the description of few-to-many systems”). Additionally, we investigate the effects of finite-range interaction for a few particles, contributing to the third goal: “Explore basic physics of few-body systems to facilitate new many-body research.”.

We summarize our findings in Chap. 7 and provide an outlook on future research topics. Appendices provide technical details and additional information to support our findings and conclusions.

2. Methods

As mentioned in Chap. 1, only few physical systems can be solved analytically. Typically, one has to resort either to approximations such as the mean-field ansatz or to numerical methods to study the few-to-many-body crossover. The purpose of this chapter is to introduce the relevant methods used in this thesis.

We start by briefly explaining how many-body physics can be described. In particular, we will introduce the formalism of second quantization. This formalism builds the basis of the *ab initio* methods used in this thesis: The configuration interaction method and the flow equation approach. We will provide a short introduction to both methods and summarize their advantages and disadvantages. Afterwards, we will demonstrate how the analysis of an impurity embedded in a sea of particles can be simplified for one-dimensional models with periodic boundary conditions (i.e., confined on a ring). The study of impurity systems provides valuable insight into the few-to-many-body crossover, as impurities embedded in a particle sea serve as probes for the environment (see Chap. 1). Lastly, we will shortly discuss the mean-field approximation for bosonic problems, focusing specifically on the key concepts relevant to this thesis. The mean-field approximation greatly simplifies their description; for certain systems even allowing for a semi-analytical treatment of the many-body Schrödinger equation. It is a powerful and versatile tool for the description of weakly interacting bosons [73, 74].

2.1. Description of many-body quantum systems

Before we explain the *ab initio* methods used in this thesis, we need to establish the necessary theoretical foundation to describe many-body quantum systems. In particular, we introduce the formalism of second quantization which will be the basis for our numerical methods. This discussion follows Ref. [75].

2.1.1. Core concepts

In the following, we describe a system consisting of N particles. The N -body Hilbert space

$$\mathcal{H}^{(N)} = \mathcal{H}_1 \otimes \mathcal{H}_2 \otimes \dots \otimes \mathcal{H}_N, \quad (2.1)$$

is given by a tensor product of the single particle Hilbert spaces \mathcal{H}_i . To describe a specific state of the N -body system, we first write the many-body basis as a direct product of the one-body basis states

$$|\phi_N\rangle = |i_1\rangle |i_2\rangle \dots |i_N\rangle \equiv |i_1 i_2 \dots i_N\rangle, \quad (2.2)$$

where $|i_j\rangle$ is the i -state of the j -th particle. With this many-body basis, it is possible to represent any many-body state, Ψ_N .

In this thesis, we describe quantum systems consisting of indistinguishable particles¹, i.e. observables shall remain unchanged under the exchange of particles. This leads to the following constraint on the many-body state:

$$\mathcal{P}_{\alpha\beta} |\Psi(1, \dots, \alpha, \dots, \beta, \dots, N)\rangle = \pm |\Psi(1, \dots, \beta, \dots, \alpha, \dots, N)\rangle \quad (2.3)$$

with $\mathcal{P}_{\alpha\beta}$ the permutation operator, which exchanges α -th particle with the β -th. The plus sign corresponds to a symmetric exchange of two particles, which are called bosons, while the minus sign corresponds to the antisymmetric exchange, so-called fermions.

Because symmetric or antisymmetric states can only be expanded in symmetric or antisymmetric many-body basis states, we define the symmetrization operator

$$S_{\pm} |i_1 i_2 \dots i_N\rangle = \frac{1}{\sqrt{N!}} \sum_{\mathcal{P} \in S_N} (\pm 1)^{\mathcal{P}} \mathcal{P} |i_1 i_2 \dots i_N\rangle, \quad (2.4)$$

where S_N is the permutation group of all N particles, to construct symmetrized basis states. The short-hand notation $(-1)^{\mathcal{P}}$ implies that a minus sign is used if the permutation is odd and a plus sign if the permutation is even.

Now, we have a formal definition of many-body states obeying either fermionic or bosonic exchange symmetry. However, this description is quite cumbersome because the symmetrization operation grows combinatorically with the number of particles.

¹In Chaps. 4, 5 we also consider an impurity embedded into a sea of indistinguishable particles. However, we exclude the impurity particle by performing a transformation to relative coordinates, see below Sec. 2.4 for more details.

2.1.2. Formalism of second quantization

Symmetric or antisymmetric states are fully characterized by their occupation numbers. We can utilize this to define so-called occupation number states. For example, for bosons such a state is defined as

$$|n_1, n_2, \dots\rangle = S_+ |i_1 i_2 \dots i_N\rangle \frac{1}{\sqrt{n_1! n_2! \dots}} \quad (2.5)$$

with n_i the number of particles occupying the i -th state. These states build an orthonormal basis of \mathcal{H} and span the so-called Fock space, which is the direct sum of the Hilbert spaces containing a specific number of particles

$$\mathcal{H} = \mathcal{H}^{(0)} \oplus \mathcal{H}^{(1)} \oplus \mathcal{H}^{(2)} \oplus \dots \quad (2.6)$$

We can now define operators that allow for a transition between the Hilbert space with N particles to the space with $N \pm 1$. For bosons they are defined via:

$$a_i |n_0, \dots, n_i, \dots\rangle = \sqrt{n_i} |n_0, \dots, n_i - 1, \dots\rangle, \quad (2.7)$$

$$a_i^\dagger |n_0, \dots, n_i, \dots\rangle = \sqrt{n_i + 1} |n_0, \dots, n_i + 1, \dots\rangle \quad (2.8)$$

while for fermions

$$b_i |n_0, \dots, n_i, \dots\rangle = n_i (-1)^{\sum_{j<i} n_j} |n_0, \dots, n_i - 1, \dots\rangle, \quad (2.9)$$

$$b_i^\dagger |n_0, \dots, n_i, \dots\rangle = (1 - n_i) (-1)^{\sum_{j<i} n_j} |n_0, \dots, n_i + 1, \dots\rangle. \quad (2.10)$$

These operators are called annihilation and creation operators. A many-body basis state can now be written as:

$$|\phi\rangle_{\text{bosons}} = \prod_i \frac{1}{\sqrt{n_i}} (a_0^\dagger)^{n_0} (a_1^\dagger)^{n_1} \dots |0\rangle \quad (2.11)$$

$$|\phi\rangle_{\text{fermions}} = (b_0^\dagger)^{n_0} (b_1^\dagger)^{n_1} \dots |0\rangle. \quad (2.12)$$

The symmetric exchange symmetry for bosons imposes the following permutation relations:

$$[a_i, a_j] = [a_i^\dagger, a_j^\dagger] = 0, \quad [a_i, a_j^\dagger] = \delta_{ij} \quad (2.13)$$

with $[a, b] = ab - ba$ the commutator. For fermions, we get a similar expression

$$\{b_i, b_j\} = \{b_i^\dagger, b_j^\dagger\} = 0, \quad \{b_i, b_j^\dagger\} = \delta_{ij} \quad (2.14)$$

with $\{a, b\} = ab + ba$ the anticommutator.

In the following we simplify the notation by using a_i and a_i^\dagger for both, fermions and bosons; the type of particles will always be clearly stated.

One can use these creation and annihilation operators to express any operator. For example, a typical Hamiltonian with kinetic energy, an external trapping potential (W) and a two-body interaction (V) can be written as

$$\begin{aligned} H &= -\frac{\hbar^2}{2m} \sum_{i=1}^N \nabla_i^2 + \sum_{i=1}^N W(\vec{x}_i) + \frac{1}{2} \sum_{\alpha \neq \beta} V(x_\alpha, x_\beta) \\ &= \sum_{ij} A_{ij} a_i^\dagger a_j + \sum_{ijkl} B_{ijkl} a_i^\dagger a_j^\dagger a_k a_l, \end{aligned} \quad (2.15)$$

where $A_{ij} = \langle i|A|j\rangle$ and $B_{ijkl} = \langle ij|B|kl\rangle$. To calculate these matrix elements one can project onto coordinate space and calculate:

$$A_{ij} = -\frac{\hbar^2}{2m} \int d^d x \phi_i^*(\vec{x}) \nabla^2 \phi_j(\vec{x}) + \int d^d x \phi_i^*(\vec{x}) W(\vec{x}) \phi_j(\vec{x}) \quad (2.16)$$

$$B_{ijkl} = \int d^d x_1 \int d^d x_2 \phi_i^*(\vec{x}_1) \phi_j^*(\vec{x}_2) V(\vec{x}_1, \vec{x}_2) \phi_k(\vec{x}_1) \phi_l(\vec{x}_2) \quad (2.17)$$

with d denoting the dimension.

Using the creation and annihilation operators we can also define so-called “field operators”

$$\Psi(\vec{x}) = \sum_i \phi_i(\vec{x}) a_i, \quad \Psi^\dagger(\vec{x}) = \sum_i \phi_i^*(\vec{x}) a_i^\dagger, \quad (2.18)$$

which fulfill the following commutation relation

$$[\Psi(\vec{x}), \Psi(\vec{x}')] = [\Psi^\dagger(\vec{x}), \Psi^\dagger(\vec{x}')] = 0, \quad [\Psi(\vec{x}), \Psi^\dagger(\vec{x}')] = \delta^{(d)}(\vec{x} - \vec{x}'). \quad (2.19)$$

Above commutation relation holds for bosons. For fermionic systems, the field operators can be defined analogously with the respective anti-commutators.

The interpretation of the field operators is that they create/annihilate a particle at position \vec{x} . Using these operators, we can write the Hamiltonian with kinetic energy, external trapping potential and two-body interaction as

$$\begin{aligned} H &= \int d^d x \left(\frac{\hbar^2}{2m} \nabla \Psi^\dagger(\vec{x}) \nabla \Psi(\vec{x}) + \Psi^\dagger(\vec{x}) W(\vec{x}) \Psi(\vec{x}) \right. \\ &\quad \left. + \frac{1}{2} \int d^d x' \Psi^\dagger(\vec{x}) \Psi^\dagger(\vec{x}') V(\vec{x}, \vec{x}') \Psi(\vec{x}') \Psi(\vec{x}) \right). \end{aligned} \quad (2.20)$$

The described formalism is called “second quantization”. It is often advantageous in the description of many-body quantum systems as it allows for an easy and systematic representation of many-body basis states. We will utilize this formalism (more specifically the occupation number representation) in the next two sections where we explain our *ab initio* methods.

2.2. Configuration interaction method

In this section, we give a short introduction to the configuration interaction (CI) method (also known as exact diagonalization method). A more detailed explanation of the method can be found, e.g. in Refs. [8, 50]. The code used in this thesis was developed by the Lund cold atom group [8, 9]. For applications of this method in this thesis see Chap. 3 and Chap. 6.

To study the few-to-many-body crossover theoretically, we solve the many-body Schrödinger equation. An analytical solution exists only for a few systems and typically one has to resort to numerical methods to find the eigenenergies and eigenstates of the Hamiltonian. One of the most straightforward numerical approaches for this is the so-called CI method. This method has been used in many different fields, see, e.g., Ref. [54] for applications in the context of nuclear physics, Ref. [76] for quantum chemistry or Ref. [6] cold quantum gases.

The basic idea is to expand the Hamiltonian matrix in a (many-body) basis. This matrix is then diagonalized giving access not only to the eigenenergies of the system but also to the corresponding eigenvectors. These can then be used to calculate any observable of the system, e.g., density, pair correlation functions, etc.. Furthermore, the properties of the ground state as well as excited states can be calculated. This makes this method one of the most versatile *ab initio* methods.

This flexibility, however, comes with a price: In practical calculations, we have to restrict the Hilbert space to be finite. Thus, such calculations are only meaningful if the used basis is sufficiently large. This condition is fulfilled when increasing the Hilbert space does not lead to a change in the calculated observables. However, as we show below, the size of the Hilbert space grows rapidly with the number of particles. Therefore, calculations for systems with more than a handful of particles are virtually impossible. Furthermore, if the eigenstates of the system have only little overlap with the basis states, i.e., if the basis is made of the non-interacting eigenstates but the system has strong interactions, a large number of basis states can be needed to adequately describe the system. Therefore, the accessible parameter space of the CI method is limited by the number of particles and the strength of the interactions. We will discuss this shortcoming and possible improvements

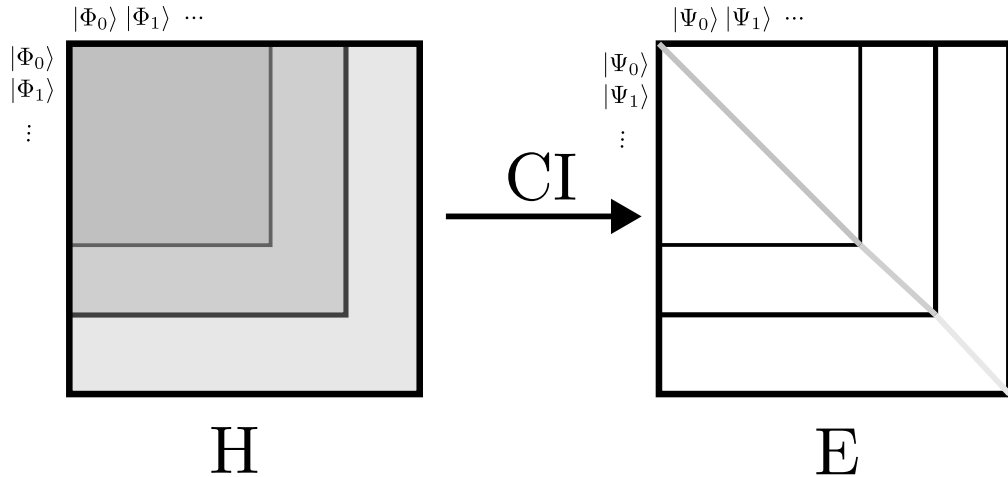


Figure 2.1.: **Illustration of the CI method.**

The basis states $|\Phi_i\rangle$ are used to construct the Hamiltonian matrix H . This matrix is then diagonalized. After the diagonalization, the matrix E is diagonal with the eigenstates $|\Psi_i\rangle$. The different sizes of the squares shall illustrate the truncation and subsequent increase of the cutoff.

in Chap. 3.

2.2.1. Practical steps

Let us briefly summarize the necessary steps for a CI calculation. For a schematic depiction of the method see Fig. 2.1.

1. **Many-body basis.** The first step is to find a suitable many-body basis, $\{|\Phi_0\rangle, |\Phi_i\rangle, \dots\}$. In this thesis, we always solve the one-body part of the Hamiltonian to get access to a set of one-body basis states $|i\rangle$. For example, if we study a system on a ring, we can use a plain wave or sin/cos basis. After determining the single-particle states, we can construct our set of many-body basis states within the formalism of second quantization (see Eqs. (2.11), (2.12)).
2. **Truncation.** There are several ways to restrict the Hilbert space to a finite size. One can restrict the set of one-body basis states to only include the n lowest one-body basis states [50, 77] or fix a maximal many-body energy as in Refs. [52, 78]. Other possible choices use selection rules imposed by symmetries [45, 52] or employ

importance truncation as in Refs. [64, 65, 79] – an iterative scheme which selects the most important many-body basis states.

- 3. Building the Hamiltonian matrix.** Here, the formalism of second quantization allows for an easy setup. One calculates the matrix elements A_{ij} and B_{ijkl} , Eq. (2.15), once. Afterwards, the creation and annihilation operators simply act on the many-body basis states written in occupation number representation. At this point, the above-mentioned limitations of the CI-method enter. Assume we have N fermions and we choose to truncate the one-body basis to include the first n elements. In this case, the dimension of the Hilbert space is

$$\dim(\mathcal{H}) = \binom{n}{N}. \quad (2.21)$$

Therefore, the size of the Hilbert space grows rapidly and can become too large to be handled. This can be the case if either many basis states are required to represent the true eigenstates of the Hamiltonian (e.g. for strong interactions) or if a system with many particles is studied.

- 4. Diagonalizing the Hamiltonian matrix.** Often, the Hamiltonian matrix contains many zero elements, making the matrix sparse. In this case, an optimized diagonalization algorithm like the Arnoldi/Lanczos method [80] can be used. The resulting eigenvalues are the eigenenergies of the system and the eigenvectors are the eigenstates. The eigenvectors can be used to calculate the expectation value of any operator, as soon as this operator is written in the second quantization formalism.
- 5. Checking convergence.** The final step is to ensure that the chosen truncation is large enough for the eigenvectors to properly approximate the true eigenstates. To verify this, one calculates the expectation value of the operator of interest for different truncations, such as different numbers of one-body basis states, and checks if the change in the expectation value becomes sufficiently small. Alternatively, one can extrapolate the results from a finite cutoff to an infinite cutoff, as discussed in Refs. [50, 59].

2.3. Flow equation approach

As we have discussed in the previous section, the CI method can only be used for a handful of particles. However, for the study of the few-to-many-body crossover, simulations with more particles are necessary. There exists a plethora of different numerical methods that

try to circumvent this problem by imposing different approximations to the many-body Schrödinger equation. Some examples are the multi-layer multi-configuration time-dependent Hartree method for atomic mixtures [55–57] or coupled cluster methods [58–60]. Another class of methods to solve the many-body Schrödinger equation are Monte-Carlo methods, see, e.g. Refs. [66, 67].

In this thesis, we use the flow equation approach (also called in-medium similarity renormalization group method, short IM-SRG)². This method has been used with great success in nuclear physics to study nuclei with more than 50 nucleons (see, e.g., Refs. [69, 70])³. It is also used in condensed matter systems, see, e.g. Ref. [68]. For one-dimensional bosonic systems, the method was developed in the group of Hans-Werner Hammer [61, 71, 72] and we further applied this method [62, 63], see also Chap. 4 and Chap. 5. The core idea of this method is to start with a reference state which should approximate the true state of the system⁴. Then, this reference state is transformed via a (unitary) transformation to the true eigenstate of the system. If one performs the full unitary transformation, the numerical cost of this method is comparable to the CI method. To be able to calculate properties of systems with larger particle numbers, one therefore truncates parts of the transformation as we discuss below. This also introduces a truncation error (or even renders the calculation completely impossible) if the overlap between the reference state and the true ground state of the system is too small. However, as long as the reference state is a good approximation of the true eigenstate, the method is a viable alternative to the CI approach for larger particle numbers [68, 70, 71].

In this thesis, we focus on the flow equation approach for bosons. More details on the method can be found in Ref. [71] and Ref. [61]. For a detailed review about the flow equation approach for fermions in the context of nuclear physics, we refer to Ref. [70].

2.3.1. Basics

The flow equation approach was developed independently by Wegner [82] and Glazek and Wilson [83]. The idea is to perform a continuous unitary transformation of the Hamiltonian

$$H(s) = U(s)H(s=0)U^\dagger(s), \quad (2.22)$$

where s plays formally the role of an imaginary time. As s approaches infinity, the Hamiltonian matrix becomes block-diagonal. This means that the matrix element previously

²Throughout the thesis we will use both expressions interchangeably.

³It is also used in nuclear physics to soften the interaction between the nucleons such that other *ab initio* methods converge faster. If it is used in this context, it is called similarity renormalization group [81].

⁴For example, for a system of weakly interacting bosons, one can use a product state ansatz for the reference state.

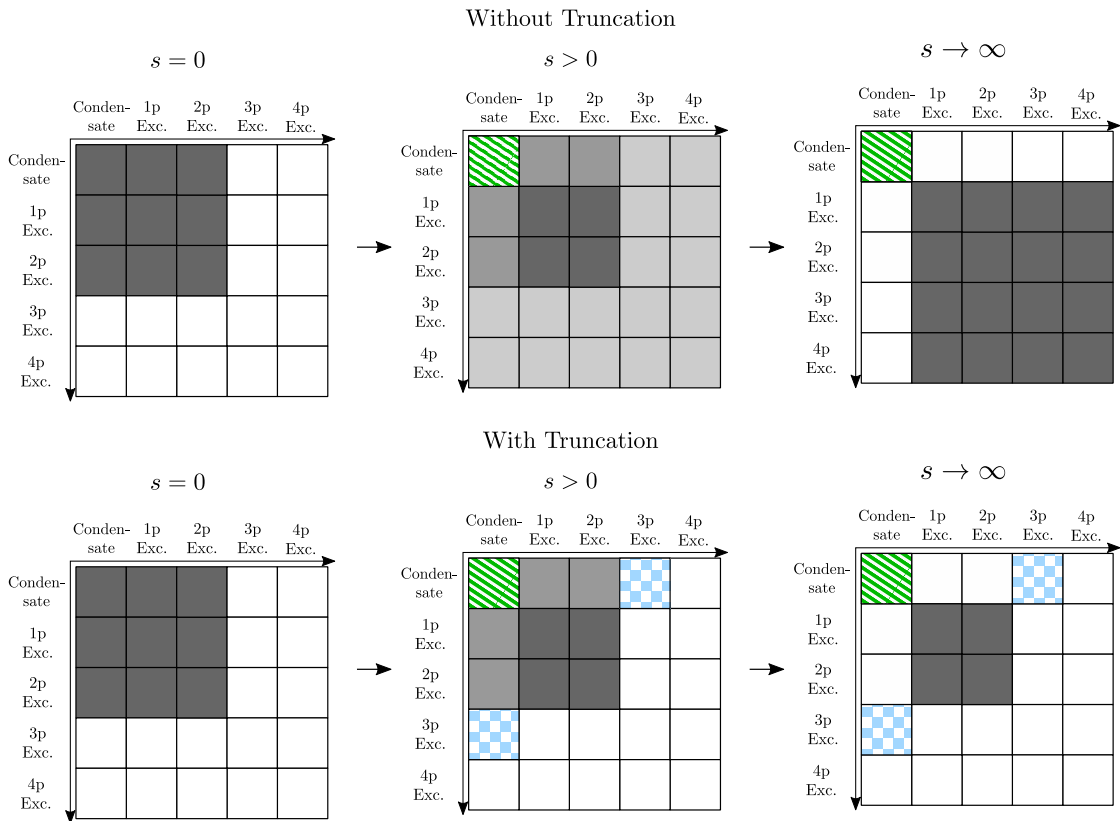


Figure 2.2.: Illustration of the flow equation approach.

The upper row depicts the unitary transformation of the Hamiltonian matrix to a block-diagonal form. This effectively decouples the reference state matrix element (depicted with hatched green) from all excitations. The bottom row illustrates our truncation scheme of induced many-body elements: We approximately include three-body terms (represented with checkered blue) which couple to the reference state. All other induced matrix elements are truncated. After the flow equation converges, these elements are used to estimate the truncation's accuracy. Figure taken from Ref. [61].

associated with the reference state becomes “decoupled” from excitations, meaning that it now describes the ground state of the system. Finding the unitary matrix U directly is difficult and instead, we solve the equivalent flow equation [68]

$$\frac{dH}{ds} = [\eta, H] \quad (2.23)$$

with $\eta(s) = \frac{dU}{ds}U^\dagger$ the so-called generator. This representation allows us to choose the antihermitian generator η for each step of the flow equation so that we can steer the flow in the desired direction.

However, solving the full flow equation for a many-body system leads to similar problems as faced by the CI method: The commutator between the generator and the Hamiltonian induces many-body terms. Taking into account all of these terms and then solving the flow equations amounts to a numerical effort similar to the CI method. Instead, we have to truncate the many-body terms in a meaningful way and ensure that their truncation has only a small influence on the resulting ground state. We show a schematic illustration of the method in Fig. 2.2.

2.3.2. Normal ordering and truncation scheme

To establish a meaningful truncation scheme, we first normal order the Hamiltonian with respect to a reference state, $|\Psi_{\text{ref}}\rangle$ (in our case a condensate, see Eq. (2.36) below). We define the following contractions, following Ref. [71]:

$$: a_i^\dagger a_j : = a_i^\dagger a_j - IC_{ij}, \quad (2.24)$$

$$: a_i^\dagger a_j^\dagger a_k a_l : = a_i^\dagger a_j^\dagger a_k a_l - IC_{ijkl} - \frac{N-1}{2N}(1 + P_{ij})(1 + P_{kl})C_{jk} : a_i^\dagger a_l :, \quad (2.25)$$

where a_i^\dagger is a creation operator, $C_{ij} = \langle \Psi_{\text{ref}} | a_i^\dagger a_j | \Psi_{\text{ref}} \rangle$ and $C_{ijkl} = \langle \Psi_{\text{ref}} | a_i^\dagger a_j^\dagger a_k a_l | \Psi_{\text{ref}} \rangle$. The number of bosons is given by N ; \mathbf{I} denotes the identity operator; the operator P_{ij} exchanges the indices i and j .

With this, we can rewrite a Hamiltonian with one- and two-body operators:

$$H = \sum_{i,j} A_{ij} a_i^\dagger a_j + \frac{1}{2} \sum_{i,j,k,l} B_{ijkl} a_i^\dagger a_j^\dagger a_k a_l, \quad (2.26)$$

to its normal ordered form:

$$H = \epsilon N \mathbf{I} + \sum_{i,j} f_{ij} : a_i^\dagger a_j : + \frac{1}{2} \sum_{i,j,k,l} \Gamma_{ijkl} : a_i^\dagger a_j^\dagger a_k a_l :, \quad (2.27)$$

with

$$\epsilon N = \sum_{m,n} A_{mn} C_{mn} + \frac{1}{2} \sum_{m,n,o,p} B_{mnop} C_{mnop}, \quad (2.28)$$

$$f_{ij} = A_{ij} + \frac{N-1}{N} \sum_{m,n} B_{imnj} C_{mn}, \quad (2.29)$$

$$\Gamma_{ijkl} = B_{ijkl}. \quad (2.30)$$

$\epsilon N = E$ is the ground state energy while f_{ij} (Γ_{ijkl}) describes one-particle (two-particle) excitations. Since we have a system of bosons, we impose the bosonic symmetry $B_{ijkl} = B_{jikl} = B_{ijlk}$.

Our truncation scheme for the flow equation is now as follows: We truncate all operators with rank higher than two, keeping only three-body operators that couple to the condensate, i.e. contain at least one $a_0^\dagger a_0$ operator. For these operators, we assume that the occupation in the ground state is macroscopic, so that we can treat them as a number, i.e. we replace $a_0^\dagger a_0$ by N (see Ref. [71] for details).

This results in a closed system of differential equations, which we solve numerically:

$$\frac{d\epsilon}{ds} = S_{00} + (N-1) \left(\frac{1}{2} \sum_m S_{00mm00} - S_{000000} \right), \quad (2.31)$$

$$\begin{aligned} \frac{df_{ij}(s)}{ds} = & -(N-1)^2 (S_{0i00j0} + S_{0ij000} + S_{000ij0}) + (N-1) \sum_m S_{i0mm0j} \\ & + (N-1) S_{0ij0} + \frac{(N-1)(N-2)}{2} (S_{00ji00} + S_{0i00j0} D_j D_i) \\ & + \frac{(N-1)(N-2)}{2} (S_{0ij000} D_i + S_{000ij0} D_j) + S_{ij}, \end{aligned} \quad (2.32)$$

$$\begin{aligned} \frac{d\Gamma_{ijkl}(s)}{ds} = & \frac{(1+P_{ij})(1+P_{kl})}{2} \left(S_{ijkl} \right. \\ & - (N-1) (S_{ijk00l} + S_{i00jkl}) + \frac{1}{2} \sum_m S_{ijmmkl} \\ & + (N-2) D_i D_l S_{0ikjl0} + (N-2) I_{ij} D_l S_{ijk00l} \\ & \left. + (N-2) D_i I_{kl} S_{i00jkl} + (N-2) I_{ij} I_{kl} S_{ij00kl} \right), \end{aligned} \quad (2.33)$$

with $D_i = 2 - \delta_{i0}$, $I_{ij} = 1 + \delta_{i0}\delta_{j0} - 2\delta_{j0}$, and

$$\begin{aligned}
S_{ij}^{(1)} &= \sum_m (\eta_{im} f_{mj} - f_{im} \eta_{mj}) , \\
S_{ijkl}^{(2)} &= \sum_m (\eta_{im} \Gamma_{mjkl} - \Gamma_{ijkm} \eta_{ml} + \eta_{ijkm} f_{ml} - f_{im} \eta_{mjkl}) , \\
S_{ijklmn} &= \sum_o (\eta_{ijko} \Gamma_{olmn} - \Gamma_{ijk o} \eta_{olmn}) .
\end{aligned} \tag{2.34}$$

For the generator we choose to use the matrix elements which couple the condensate to the excitations:

$$\eta = \sum_i f_{i0} : a_i^\dagger a_0 : + \frac{1}{2} \sum_{i,j} \Gamma_{ij00} : a_i^\dagger a_j^\dagger a_0 a_0 : - \text{H.c.} . \tag{2.35}$$

This choice can be justified *a posteriori* if indeed the reference state becomes decoupled from all excitations, i.e. when the matrix elements f_{i0} and Γ_{ij00} vanish. For other possible choices of the generator see Ref. [71].

2.3.3. Reference state

The transformation of the Hamiltonian via the flow equation can be seen as a transformation of the reference state to the true ground state of the system. To ensure that the truncated many-body operators have only a small impact on the flow equation, the reference state must provide a good representation of the true ground state of the system. As we are interested in the ground state of a system of bosons, a natural choice for the reference state is a condensate ansatz:

$$\Psi_{\text{ref}}(x_1, x_2, \dots, x_N) = \prod_{\alpha=1}^N f(x_\alpha), \tag{2.36}$$

where $f(x)$ describes a single particle orbital. There are different possible choices for f . For example, one can use the lowest state of the one-body basis. Another option would be to first solve the Gross-Pitaevskii equation (i.e. to find the f which minimizes the energy functional, see below). We found that the most robust choice for the reference state stems from an iterative calculation. Starting with the lowest state of the one-body basis as f , we calculate the density of the system with the flow equation approach (see below for an explanation how observables are calculated with this method). Then we use this density to define a new f . These steps are repeated until the results from the flow equations no longer vary (see Ref. [61] for details).

2.3.4. Error estimation

There are two sources of inaccuracies in the flow equation method:

- 1) The finite number of basis states used for the construction of the Hamiltonian matrix,
- 2) The truncation of many-body operators.

For the first one, we can follow a similar pattern as for the CI-method. We increase the number of basis states and calculate for each cutoff the observables of interest. Afterwards, we check if they are already converged or we interpolate to the infinite cutoff limit. The error from this interpolation contributes to an error of the flow equation approach, see Ref. [61].

For the second contribution, we estimate the truncation error of the ground-state energy using second-order perturbation theory (for further details we refer to [71])

$$\delta\epsilon \simeq \frac{1}{N} \sum_p \frac{(\langle \Psi_p | \int_0^\infty W(s) ds | \Psi_{\text{ref}} \rangle)^2}{\langle \Psi_p | H | \Psi_p \rangle - \langle \Psi_{\text{ref}} | H | \Psi_{\text{ref}} \rangle}, \quad (2.37)$$

where $W(s)$ are all truncated three-body operators. Ψ_p describes a state that contains three-body excitations. We estimate the expectation value $\langle \Psi_p | H | \Psi_p \rangle$ in the denominator by three one-body excitations, i.e. the matrix elements f_{ii} .

2.3.5. Calculation of observables

To calculate observables other than the energy, we need to transform the corresponding operator alongside the Hamiltonian. This means that additionally to solving Eq. (2.23), we compute

$$\frac{dO}{ds} = [\eta, O] \quad (2.38)$$

simultaneously. Induced higher-order terms are truncated according to the same truncation scheme as for the Hamiltonian.

To estimate the truncation error for O , we cannot use Eq. (2.37). Because we truncate induced many-body operators, the flow equation does not represent a unitary transformation. Therefore, in general, $H(s)$ and $O(s)$ do not commute, i.e. they do not have the same eigenstates. Instead, we define a ‘‘relative truncation error’’ (see Ref. [61] for more details)

$$\Delta = \frac{\delta\epsilon}{\epsilon}, \quad (2.39)$$

with $\delta\epsilon$ being the error estimate from Eq. (2.37) and ϵ the resulting ground state energy per particle. Now, we estimate the truncation error of the operator to be

$$\delta O = \Delta \langle O \rangle. \quad (2.40)$$

We want to stress that this is only an estimate of the truncation error for observables which has been shown to be a useful phenomenological estimate, see Ref. [61] and Refs. [62, 63] which are also discussed in this thesis in Chaps. 5, 4.

2.4. Impurity in a one-dimensional ring: transformation to the frame ‘co-moving’ with the impurity

As discussed in Chap. 1, studying impurity systems provides valuable insights into the few-to-many-body crossover, as the impurity can serve as a probe of the environment. To facilitate studies of such systems, in this section we demonstrate how the description of a one-dimensional system with an impurity atom can be simplified when the system is confined to a ring, i.e., if the system has periodic boundary conditions and if the interactions are translationally invariant⁵. Note that such conditions can be prepared experimentally, see e.g. Refs. [89, 90]. This approach is used in Chap. 4 and Chap. 5 where we discuss a system of bosons with an impurity in one dimension.

The Hamiltonian of interest reads

$$H = -\frac{\hbar^2}{2m} \frac{\partial^2}{\partial y^2} - \frac{\hbar^2}{2M} \sum_{i=1}^N \frac{\partial^2}{\partial x_i^2} + c \sum_{i=1}^N \delta(x_i - y) + g \sum_{i<j} \delta(x_i - x_j), \quad (2.41)$$

y (x_i) is the position of the impurity (i th bath particles), m refers to the mass of the impurity atom, and M denotes the mass of a bath particles. We impose periodic boundary conditions, i.e. $\Psi(y+L, \{x_i\}) = \Psi(y, \{x_i\})$ and $\Psi(y, \{x_0, \dots, x_i+L, \dots, x_N\}) = \Psi(y, \{x_i\})$, where $\Psi(y, \{x_i\})$ describes the wave function of the system. Therefore, it is sufficient to restrict the coordinates to $y \in [0, L]$, $x_i \in [0, L]$. We model the atom-atom interactions by contact interactions [91]. The parameters c and g determine the impurity-particle and particle-particle interaction strength.

Since the interactions depend only on the relative distance between two particles and because we employ periodic boundary conditions, the Hamiltonian is translationally invariant. Therefore, the total (quantized) momentum of the system, $P = 2\pi n/L$, $n \in \mathbb{Z}$, is conserved. We can exploit this to simplify the description of the system. We eliminate the impurity coordinate from the Schrödinger equation by writing the wavefunction as [92]

$$\Psi(y, \{x_i\}) = \tilde{\Psi}(\{z_i\}) e^{iPy}, \quad (2.42)$$

⁵We want to note that this transformation can also be applied in higher dimensions, see e.g. Refs. [84–88]. However, in this thesis, we apply this approach only for one-dimensional systems. Also, note that a similar transformation can be performed for a harmonic trapping potential [49].

where $z_i = L\theta(y - x_i) + x_i - y$ with $\theta(x)$ being the Heaviside step function. In other words: Instead of solving the Schrödinger equation for $N + 1$ particles, we solve the Schrödinger equation for N particles. The corresponding Hamiltonian for the wavefunction $\tilde{\Psi}$ reads

$$\mathcal{H}_P = -\frac{\hbar^2}{2M} \sum_{i=1}^N \frac{\partial^2}{\partial z_i^2} - \frac{\hbar^2}{2m} \left(\sum_{i=1}^N \frac{\partial}{\partial z_i} \right)^2 + \frac{i\hbar P}{m} \sum_{i=1}^N \frac{\partial}{\partial z_i} + g \sum_{i<j} \delta(z_i - z_j) + c \sum_{i=1}^N \delta(z_i). \quad (2.43)$$

The transformation $\{y, x_i\} \rightarrow \{z_i\}$ can be interpreted as a coordinate-space analog of the Lee-Low-Pines transformation [93].

This form of the Hamiltonian, Eq. (2.43), has a few advantages over the original form, Eq. (2.41):

1. Instead of working with $N + 1$ particles, we only work with N particles.
2. The impurity-particle interaction can be implemented as a boundary condition for the CI-method, Sec. 2.2, or the flow equation approach, Sec. 2.3. Therefore, only the particle-particle interaction together with the mixed derivative can lead to off-diagonal elements in the Hamiltonian matrix. This allows us to study strongly interacting impurities while keeping the size of the Hilbert space sufficiently small.
3. In Chap. 4 we will show that this representation also allows for a connection between an external artificial gauge flux and the total momentum which will greatly simplify the analysis of this system.
4. We can use this representation to get semi-analytical insight into the system by using the mean-field approximation (see below) even for strong impurity-particle interaction. This has been used e.g. in Refs. [62, 63, 72, 94–98].

2.5. Mean-field approximation for one-dimensional bosonic systems

As described above, few many-body systems can be solved analytically. However, for a weakly interacting Bose gas, we can exploit the fact that it can exhibit Bose-Einstein condensation (BEC) [16, 17]. In a BEC the ground state is macroscopically occupied, and the system exhibits off-diagonal long-range order. This allows for an approximate (semi-analytical) description of the wavefunction using a product state ansatz (also called

a condensate ansatz):

$$\Phi(\vec{x}_1, \dots, \vec{x}_N) = \prod_{i=1}^N f(\vec{x}_i). \quad (2.44)$$

The idea of the mean-field approximation is to find the single particle orbital f that minimizes the ground-state energy. Once f is determined, any observable of the system can be calculated within this approximation.

However, care must be taken when using the mean-field description as it only works well when the system exhibits off-diagonal long-range order. In particular, in 1D and 2D systems density fluctuations can be suppressed while phase fluctuations (also known as phase correlations) destroy the off-diagonal long-range order [99, 100]. This issue can be mitigated if the system is trapped. In this case, the phase fluctuations can be small on the order of the trapped system such that the mean-field approximation can still be valid [101]⁶. Still, strong interactions can enhance phase fluctuations and reduce the applicability of the mean-field ansatz. The use of the mean-field approximation can be motivated by physical arguments, i.e. when we focus on local properties of the system, or validated through *ab initio* calculations.

The mean-field approximation is a powerful and versatile tool that has been used extensively for describing bosonic systems. In this section, we focus on a one-dimensional system with an impurity, where the single-particle orbital f can be found semi-analytically. This will enable us in Chaps. 4, 5 to a) simplify the analysis of the system, b) extend our research to particle numbers outside the range of *ab initio* calculations and c) gain analytical insights. We also apply a product state ansatz in Chap. 6 for a two-dimensional system of attractive bosons, where we will detail our approach to finding f . Since a more in-depth explanation of the mean-field approximation is beyond the scope of this thesis, we refer interested readers to Refs. [73, 74].

We use the Hamiltonian of N bosons, which are interacting via contact interaction, and a single impurity, which also interacts via a contact interaction with the bosons, in a system with periodic boundary conditions, i.e. on a ring. We simplify the description by going to the frame ‘co-moving’ with the impurity, see Sec. 2.4. To find the optimal f , we insert the product state ansatz into the Schrödinger equation ‘co-moving’ with the impurity, Eq. (2.43), and minimize the ground-state energy of the system under the condition that the total particle number is conserved⁷. With this, we derive the following

⁶Note that this is also consistent with the fact that in 1D and 2D systems BEC can only occur for trapped systems, not in free space.

⁷This condition leads to the constraint that the orbital f has to be normalized to one $\int_0^L f^*(z)f(z)dz = 1$.

non-linear differential equation for f

$$-\frac{\hbar^2}{2\kappa} \frac{d^2 f}{dz^2} + \frac{i\hbar P}{m} \frac{df}{dz} + g(N-1)f(z)^3 + c\delta(z)f(z) = \mu f(z), \quad (2.45)$$

where $\kappa = mM/(m+M)$ is the reduced mass and μ is the chemical potential. This equation is known as the Gross-Pitaevskii equation (GPE) [73, 74]. To obtain a semi-analytical solution to the GPE, we use the fact that the equation is integrable for $c=0$, with Jacobi elliptic functions as the solution [102]. For non-zero values of c , the impurity-boson δ -interaction is implemented as the boundary condition,

$$\left. \frac{\partial f}{\partial z} \right|_{z=L^-}^{z=0^+} = 2c\kappa f(0), \quad (2.46)$$

which, together with the normalization condition, determines the solution of the GPE. We can use this solution to calculate any observable of the system. For example, the energy of the system is given by

$$\frac{E}{N} = \mu - \frac{g(N-1)}{2} \int_0^L |f(x)|^4 dx. \quad (2.47)$$

In Chaps. 4 and 5, we benchmark the outcome of the mean-field approach against *ab initio* calculations to justify its use. Furthermore, we directly estimate the strength of beyond-mean-field effects, by using the one-body density matrix prescription from Refs. [73, 101, 103]

$$\rho(x, x') \equiv \langle \Phi | \sum_{i,j} \phi_i^*(x) \phi_j(x') a_i^\dagger a_j | \Phi \rangle = \sqrt{\rho(x)\rho(x')} \exp \left\{ -\frac{\delta\Phi_{xx'}}{2} \right\} \quad (2.48)$$

with $\rho(x)$ the density and $\delta\Phi_{xx'}$ phase fluctuations. The quantity $\delta\Phi_{xx'}$ is a measure of the off-diagonal long-range order. Its calculation allows us to further test the validity of the mean-field approach. If $\delta\Phi_{xx'}$ vanishes, the system is in a coherent state, i.e. it is well described by the condensate wave function. As soon as the system becomes more correlated, e.g. because of stronger interactions, phase fluctuations grow which means that the mean-field approach is less justified. Note that $\delta\Phi_{xx'}$ is not only useful for theoretical analysis of beyond-mean-field effects. It can also be measured in experimental settings through methods like Bragg spectroscopy and interferometry [104].

3. Comparison of renormalized interactions using one-dimensional few-body systems as a testbed

As stated in the introduction, Chap. 1, one goal of this thesis is “Advance numerical investigations of the few-to-many crossover by improving theoretical tools”. In this chapter, we contribute to this goal by comparing different renormalization methods for the one-dimensional contact interaction. Although this interaction requires in principle no regularization, previous studies have shown that the use of renormalized interactions improves the convergence of numerical *ab initio* calculations considerably [77, 105–111]. This enables studies in an increased parameter space, i.e. stronger interactions and larger particle numbers which is important for studies of few-to-many systems. We hope that renormalized interactions will eventually become a standard approach in *ab initio* studies within the cold atom community and that the discussion in this Chapter will assist readers in selecting the most appropriate method for their problem.

We compare three different renormalization methods: a ‘running coupling constant’, where we use the two-body ground state energy as renormalization condition as well as two effective interaction approaches which further include information about excited states. We use the configuration interaction method to calculate the energy and density of a few-fermion system in a harmonic oscillator. A comparison with the bare contact interaction shows that the running coupling constant approach improves the convergence significantly. An effective interaction that is constructed from the relative part of the energy spectrum shows a similar improvement. We achieve even better convergence with an effective interaction which additionally includes center-of-mass excitations. Furthermore, we also discuss a transformation of operators alongside the renormalization for effective interactions. Therefore, we calculate the expectation value of the one-body Hamiltonian and transition matrix elements. Our results demonstrate that this transformation can significantly improve the accuracy.

Parts of this chapter have been published in this or similar form in our manuscript “Comparison of renormalized interactions using one-dimensional few-body systems as a

testbed” [112]. Note that the implementation of the configuration-interaction method used in this chapter was provided by the Lund cold atom group, see e.g. Refs. [8, 9].

3.1. Introduction

As discussed in Chap. 1, recent experimental advances in cold-atom physics have enabled the creation and study of (quasi) one-dimensional (1D) systems consisting of a few (up to 10) particles in a highly controllable setting [12, 40, 41]. Since the particle number can be controlled, few-to-many body studies, such as the convergence of the self-energy of an impurity in a one-dimensional Fermi gas, are possible. These advancements also motivated theoretical studies on such systems [6, 113]. There exists a plethora of numerical methods such as the multi-layer multi-configuration time-dependent Hartree method for atomic mixtures [55–57], coupled cluster methods [58–60], flow equation approaches [61–63], or exact diagonalization methods, also known as the configuration interaction method (CI) [45–53] and its extension, the importance truncated CI [64, 65]¹. Although these methods are very powerful, they often face problems when a large Hilbert space is needed, e.g. because of strong interactions or because of large particle numbers, since computational resources are limited (see also Chaps. 1, 2).

Similar problems are also faced in the nuclear structure community. There, renormalization methods (such as so-called “Lee-Suzuki” transformations [114] or renormalization group ideas [81, 115]) have been developed to transform the nuclear potential. Their aim is to decrease the size of the needed Hilbert space which enabled considerable progress in nuclear structure calculations over the last twenty years [116]. Recently, similar “effective interaction” methods have also been used for cold-atom setups [77, 105–107], see also Refs. [108–111] for other related approaches.

For a one-dimensional contact interaction, in principle, no regularization is needed (unlike in 2D or 3D). However, Refs. [77, 105–111] have demonstrated that the usage of renormalized interactions significantly reduces the Hilbert space needed for converged results. This enables calculations with stronger interactions and larger particle numbers. To the best of our knowledge, there is so far no direct comparison of the different renormalization schemes: all were only benchmarked against the bare contact interaction. The goal of this chapter is to fill this gap and to compare different renormalization schemes used for 1D cold atom systems. Furthermore, we will also discuss the unitary transformation of operators alongside the renormalization of the interaction. Although this procedure is well-known in nuclear physics [116], it has yet not been applied to one-dimensional

¹In this thesis, we only use the CI and flow equation method, see Chap. 2.

few-body problems. Our results will show that this transformation can be necessary to achieve converged results for observables other than the energy.

In this chapter, we provide a short introduction to renormalized interactions and a detailed comparison of their convergence patterns. We hope that a reader can decide afterward on the most suitable method for their problem. Out of the three renormalized interactions we use, the simplest method to implement is the running coupling constant approach. It fixes the two-body ground-state energy in a truncated Hilbert space and might be used for preliminary qualitative calculations. The most precise results are obtained with an effective interaction that reproduces the full low-energy spectrum of the two-body problem. To the best of our knowledge, this interaction has not been used before in few-body calculations of cold atom systems. We will showcase that it outperforms previously used effective interactions which only consider the relative part of the energy spectrum.

Note that while we focus in this chapter on one-dimensional setups, our results can also be extended to studies of 2D systems, which have also been realized experimentally [42, 43, 117]. In the outlook, we will show a preliminary comparison of two different renormalization schemes, see also Refs. [51–53, 79] for studies on 2D systems. For 3D systems, most studies using renormalized interactions were performed for nuclear systems, see e.g. Ref. [116] and references therein, but some works also studied cold atom systems [105].

For our comparative study, we use a system of fermions that interact via zero-range interaction and are trapped by a harmonic oscillator potential. This is a well-studied system for which many properties are already known (see, e.g., [45–47, 59, 118, 119]). At the same time, convergence in a harmonic oscillator is slow [59] which makes this system an ideal testbed for a comparison study of renormalized interactions. Additionally, the two-body solution is known analytically [120, 121] which will help us in the construction of effective interactions.

We use the CI method for the simulation of this system (for an explanation of the CI method see Sec. 2.2). This method is “exact” in the sense that no additional approximations besides a finite Hilbert space are performed. This has the benefit that no approximations on the many-body Schrödinger equation disguise the usefulness of the renormalized interactions. The CI method can be used to study excited states as well as dynamical observables like the transition rate between different states, which is not possible with most other numerical methods. The price one has to pay for this is that calculations with more than a handful of particles become nearly impossible. Still, the main characteristics of renormalized interactions can be studied using small systems.

This chapter is structured as follows: We start by introducing the system in Sec. 3.2. There, we will also introduce our basis and cutoff scheme of the CI method. After that, in Sec. 3.3 we briefly showcase the basic ideas behind a running coupling constant approach by showing results in momentum space. Then, we explain the different renormalization

schemes used in this Chapter: A running coupling constant approach that fixes the two-body ground-state energy in a truncated Hilbert space, an effective interaction that reproduces the relative energy spectrum and an effective interaction that reproduces the full energy spectrum (relative and center-of-mass excitations). In Sec. 3.4 we compare these different interactions in terms of their convergence for the energy and density. Furthermore, we discuss a transformation of operators alongside the renormalization for one-body operators (the one-body part of the Hamiltonian: kinetic energy and harmonic confinement) and for a two-body observable (transition matrix elements from the ground state to an excited state induced by a periodic modulation of the interaction). Lastly, in Sec. 3.5 we will summarize our findings and give a short outlook into future research opportunities. In particular, we will showcase some preliminary results for 2D systems. In App. A we provide additional details.

3.2. Formalism

3.2.1. Hamiltonian

Our system consists of spin-1/2 fermions confined by a 1D harmonic oscillator potential (see Fig. 3.1). Its Hamiltonian reads

$$H = T + W + \sum_{i < j} V(x_i, x_j), \quad (3.1)$$

where x_i is the coordinate of particle i in the laboratory frame and $V(x_i, x_j)$ describes the interaction potential. The one-body parts of the Hamiltonian are the kinetic energy T and the harmonic trapping potential W :

$$T = - \sum_{i=1}^N \frac{\hbar^2}{2m} \frac{\partial^2}{\partial x_i^2} \quad W = \sum_{i=1}^N \frac{m\omega^2}{2} x_i^2, \quad (3.2)$$

where $N = N_\uparrow + N_\downarrow$ is the number of fermions. The interaction conserves the spin of the particles such that N_\uparrow and N_\downarrow are fixed. Since we have a system of ultra-cold fermions, we assume zero-range contact interaction [18, 23]. Due to the Pauli exclusion principle, only fermions with different spin can interact. In what follows, we will use a system of units such that $\hbar = m = \omega = 1$.

3.2.2. Potentials

As sketched in Fig. 3.1, we use four different interaction potentials in this chapter. We employ the ‘bare contact interaction’, $V(x_1, x_2) = g\delta(x_1 - x_2)$, as a baseline for the

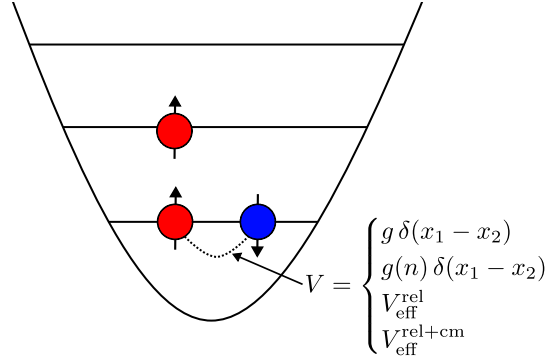


Figure 3.1.: **Sketch of the system.**

Depicted is a system with spin-up and spin-down fermions in a harmonic trap. We use four different two-body interactions: a bare contact interaction, $g\delta(x_1 - x_2)$; a contact interaction with a running coupling constant, $g(n)\delta(x_1 - x_2)$, where n is the one-body cutoff in our calculations; an effective interaction defined in relative coordinates, $V_{\text{eff}}^{\text{rel}}$; an effective interaction that includes relative and center-of-mass excitations, $V_{\text{eff}}^{\text{rel+cm}}$ (see the text for more details). Figure taken from Ref. [112].

renormalized interactions and we work with three different renormalized interactions: (i) A contact interaction with a running coupling constant $V(x_1, x_2) = g(n)\delta(x_1 - x_2)$, where n is the cutoff on the basis states included in our calculations (see Sec. 3.3.1); (ii) an effective interaction, $V_{\text{eff}}^{\text{rel}}$, which is defined in relative coordinates using the exact two-body solution (see Sec. 3.3.2) and (iii) $V_{\text{eff}}^{\text{rel+cm}}$, an effective interaction where the full two-body spectrum is used for its construction (see Sec. 3.3.2).

3.2.3. Configuration interaction method

We use the CI method to solve the Schrödinger equation of our system. For an explanation of the method we refer to Sec. 2.2. To expand the Hamiltonian matrix, we use the one-body eigenstates of the non-interacting system, i.e. the eigenfunctions of the 1D harmonic oscillator:

$$\Phi_l(z) = \frac{1}{\sqrt{2^l l!}} \left(\frac{1}{\pi}\right)^{\frac{1}{4}} e^{-\frac{1}{2}z^2} H_l(z), \quad (3.3)$$

where H_l is the l -th Hermite polynomial. For the truncation, we use the n lowest one-body basis states². Although more sophisticated truncation schemes exist, such as fixing the energy of the many-body basis states [52, 78], selection rules imposed by symmetries [45] or importance truncation as in Refs. [64, 65, 79], we focus here on the most general truncation as our focus is on comparing different renormalized interactions. Therefore, we do not optimize the truncation scheme.

As a reminder: For a system with N_\uparrow spin-up and N_\downarrow spin-down fermions the Hilbert space for the CI method grows as

$$\dim \mathcal{H} = \binom{n}{N_\uparrow} \binom{n}{N_\downarrow}, \quad (3.4)$$

where $\binom{n}{k} = n! / (k!(n-k)!)$ is the binomial coefficient. This means that we can only study systems where the size of the one-body basis needed for convergence is sufficiently small. As we will show below, the usage of renormalized interactions can help to decrease the size of the Hilbert space needed for convergence.

3.2.4. Two-body problem

Note that for $N_\uparrow = N_\downarrow = 1$ there exists an analytical solution. We will use this exact solution later for the construction of the renormalized interaction. The solution reads [120, 121]

$$\Psi_i(x, X) = \Phi_{n_i}(X) \psi_{\nu_i}(x) \quad (3.5)$$

with $x = (x_1 - x_2)/\sqrt{2}$ and $X = (x_1 + x_2)/\sqrt{2}$ being the relative and center-of-mass coordinates respectively. Because the contact interaction acts only on the relative part of the wavefunction, the center-of-mass solution $\Phi_{n_i}(X)$ is simply the harmonic oscillator eigenfunction with eigenenergy $E_{n_i} = n_i + 1/2$. Furthermore, odd relative states are not influenced by the interaction and their solutions are therefore also the ones from the non-interacting harmonic oscillator. The even states are

$$\psi_{\nu_i}(x) = \mathcal{N}_{\nu_i} e^{-x^2} U(-\nu_i, 1/2, x^2), \quad (3.6)$$

where U is the Tricomi function [102]. The parameter $\mathcal{N}_{\nu_i} = \sqrt{\frac{\Gamma(-\nu_i+1/2)\Gamma(-\nu_i)}{\pi(\psi(-\nu_i+1/2)-\psi(-\nu_i))}}$, with Γ the gamma function and ψ the digamma function, is the normalization coefficient. The eigenenergy of these states is given by $\epsilon_{\nu_i} = 2\nu_i + 1/2$ with ν_i determined from

$$2\sqrt{2}\Gamma(-\nu_i + 1/2) = -g\Gamma(-\nu_i). \quad (3.7)$$

²For our system, the number of one-body basis states corresponds to an energy cutoff $n + 1/2$.

3.3. Renormalized interactions

In this section, we want to introduce commonly used renormalized interactions in one-dimensional systems, see e.g. Refs. [50, 106, 108, 110, 111].

Let us first motivate the use of renormalized interactions. If we have ‘strong’ interactions, we need a ‘large’ Hilbert space, i.e. ‘many’ one-body basis states, to achieve accurate results, see Sec. 3.4. Therefore, calculations for few-body systems with strong interactions or for a medium number of particles with moderate interactions are very hard if not impossible. This is where renormalized interactions come into play: The numerical value of ‘many’ is drastically decreased by using them. This allows one to increase the available parameter space, i.e. stronger interactions and/or larger particle numbers. The idea of a renormalized interaction is to fix physical parameters (e.g. the ground-state energy of two particles or the phase shift, i.e. the scattering length) in a finite Hilbert space. One can interpret the truncation of the Hilbert space as effectively changing properties of the interaction, such as the two-body ground-state energy. A renormalization of the interaction reverses this process and leads to a description of the actual physical quantities.

In this chapter, we use three different renormalization schemes for the contact interaction, i)-iii) mentioned above in Sec. 3.2 (see also Fig. 3.1). Below, we will benchmark their convergence against the bare contact interaction, which serves as a baseline, and compare their performance with each other. Before we explain these different methods, we review the relevant literature. A similar approach to the running coupling constant was used in Ref. [111]. In this work, the authors found an analytical expression for a running coupling constant based on truncating the exact solution of two particles interacting in a harmonic oscillator. Note that our approach is more general as we explicitly fine-tune the interaction strength for each cutoff to reproduce the two-body ground state energy (for details see Subsec. 3.3.1). Therefore, it can be easily extended also to other geometries or interactions even if no analytical two-body solution is available. Ref. [108] introduces another modification of a running coupling constant. There, the energy of strongly repulsive bosons was used as a renormalization condition. This renormalized interaction can be used for one-dimensional geometries where the energy of infinitely strongly repulsive bosons can be calculated exactly because they can be described as non-interacting fermions [37, 122].

Applications of the effective potential $V_{\text{eff}}^{\text{rel}}$ are discussed, e.g., in Refs. [50, 77, 105, 106]. In Ref. [115] the connection between effective interaction and renormalization group ideas is studied in the context of nuclear physics. The interaction $V_{\text{eff}}^{\text{rel+cm}}$ is based on the same idea as $V_{\text{eff}}^{\text{rel}}$ but instead of using only the relative part of the exact two-body energy spectrum, it takes into account the full one. To the best of our knowledge, it has not been explored previously in the context of low-dimensional ultracold gases.

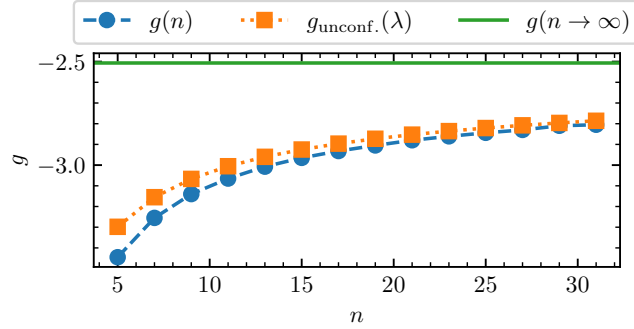


Figure 3.2.: **Comparison of running coupling constants.**

Running coupling constant for the unconfined system as well as for the 1D harmonic oscillator for $g(n \rightarrow \infty) = -2.5607$ (corresponding to $E_{1+1} = -1$, the two-body energy in the trapped system). Dots show $g(n)$, the running coupling constant used for harmonic confinement, which is calculated by explicitly fixing the two-body ground state energy of two interacting particles in a harmonic trap for each single-body cutoff n . Squares show $g_{\text{unconf.}}$, the running coupling constant in free space, given by Eq. (3.10). To relate the momentum space cutoff λ with the one-body cutoff n we used Eq. (3.14). Figure taken from Ref. [112].

Setting up these effective potentials is slightly more complicated than the running coupling constant approach (see below). However, as we will demonstrate in Sec. 3.4, the boost in convergence can be larger than for $g(n)\delta$. In particular, effective interactions allow for a transformation of operators alongside the renormalization which can be necessary to improve the convergence of certain observables.

3.3.1. Running coupling constant

To introduce the concept of a running coupling constant, we first showcase how the contact interaction can be renormalized in an unconfined system. This way, we can introduce a momentum space cutoff and illustrate the basic ideas of the running coupling concept. Our calculations adapt the approach presented for 2D systems in Ref. [123]. Afterwards, we will make the connection to our truncation in the CI method for a trapped system.

Unconfined system

To renormalize the two-body contact interaction, we consider the Schrödinger equation in free space. It is sufficient to focus on the problem in relative coordinates, $x = (x_1 - x_2)/\sqrt{2}$,

$$\left(-\frac{1}{2}\frac{\partial^2}{\partial x^2} + \frac{g}{\sqrt{2}}\delta(x)\right)\Psi(x) = E_{1+1}^{\text{unconf.}}\Psi(x), \quad (3.8)$$

where $E_{1+1}^{\text{unconf.}}$ is the two-body energy in the unconfined system. Here, we only consider $g < 0$ because we want to use the two-body binding energy ($E_{1+1}^{\text{unconf.}} < 0^3$) as the renormalization condition. For $g > 0$, we would need to use a different renormalization condition such as the phase shift of two scattered particles.

Solving Eq. (3.8) leads to the following equation for the two-body ground state energy (see App. A.7 for details):

$$-\frac{1}{g} = \frac{1}{\sqrt{2}\pi} \int_{-\infty}^{\infty} \frac{dk}{k^2 - 2E_{1+1}^{\text{unconf.}}}. \quad (3.9)$$

Because we are in 1D, the integral on the right side converges⁴. To restrict the Hilbert space (as mandatory for numerical calculations), we introduce a momentum space cutoff λ . Note that λ is a continuous parameter while the energy cutoff n described above for the CI-method is discrete. Below, we connect these two cutoffs for ‘large’ values with the semi-classical approximation⁵.

Let us now introduce the running coupling constant $g_{\text{unconf.}}(\lambda)$. To this end, we fix the two-body ground state energy $E_{1+1}^{\text{unconf.}}$ independent of λ and tune $g_{\text{unconf.}}(\lambda)$ such that Eq. (3.9) with $k \in [-\lambda, \lambda]$

$$-\frac{1}{g_{\text{unconf.}}(\lambda)} = \frac{1}{\pi\sqrt{|E_{1+1}^{\text{unconf.}}|}} \arctan \left[\frac{\lambda}{\sqrt{|2E_{1+1}^{\text{unconf.}}|}} \right] \quad (3.10)$$

holds. This equation is the central equation for the running coupling constant in free space. It renormalizes the interaction strength such that for each momentum space cutoff λ the two-body ground state energy, $E_{1+1}^{\text{unconf.}}$, remains the same. This means that instead of the

³Note that for 1D systems, there is always a bound state if $g < 0$ [124].

⁴For 2D it diverges logarithmically and for 3D linearly, i.e. one has to regularize the zero-range potential, see e.g. Refs. [23, 51, 123] for possible regularization schemes.

⁵The semi-classical approximation can only be used if the energy of an excited state is so large, that excitations to states with higher energy can be neglected. For the harmonic oscillator, one can define this region also by the asymptotic approximation of Hermite polynomials [125].

bare value of g , $E_{1+1}^{\text{unconf.}}$ is now the measure of the interaction strength and determines the physical properties of the system.

For large values of λ this leads to

$$-\frac{1}{g_{\text{unconf.}}(\lambda)} \simeq \frac{1}{2\sqrt{|E_{1+1}^{\text{unconf.}}|}} - \frac{\sqrt{2}}{\pi\lambda}. \quad (3.11)$$

This equation gives us the well-known solution for the Schrödinger equation in full space $g_{\text{unconf.}}(\lambda \rightarrow \infty) = -2\sqrt{|E_{1+1}^{\text{unconf.}}|}$ [124]. This term also allows us to estimate the convergence of the energy $E_{1+1}^{\text{unconf.}}(\lambda)$ as a function of the momentum space cutoff λ if the bare contact interaction is used. We treat the second term on the right-hand-side of Eq. (3.11) as a perturbation (for details see App. A.1):

$$E_{1+1}^{\text{unconf.}}(\lambda) \simeq E_{1+1}^{\text{unconf.}}(\lambda \rightarrow \infty) + \frac{\sqrt{2}C}{\pi\lambda}, \quad (3.12)$$

where $C = g^2 \langle \Psi | \delta(x) | \Psi \rangle$ is the contact parameter [126]. The functional behavior of the convergence in free space is in agreement with Refs. [71, 110]. Below, we will show that the convergence behavior is dependent on the trapping potential.

1D Harmonic oscillator

As written above, the cutoff in our CI-calculations is not a finite momentum space cutoff λ but instead the number of one-body basis states used, n . For the running coupling constant

$$V = g(n)\delta(x_1 - x_2) \quad (3.13)$$

we explicitly tune $g(n)$ for each cutoff such that the two-body ground state energy remains fixed. In a trapped system, this approach can be used for attractive as well as for repulsive interactions.

Let us now $g(n)$ with the running coupling constant in the unconfined system, $g_{\text{unconf.}}(\lambda)$. We start by finding a relation between the momentum space cutoff λ and n . We use the Wilson–Sommerfeld quantization condition $\oint_{H(p,x)=E} p dx = 2\pi n$ which results in

$$\lambda = 2\sqrt{n}. \quad (3.14)$$

We show the details of this connection together with an extension for general polynomial potentials in App. A.8. One can see that the convergence for a harmonic oscillator is slow (see also Ref. [59]) which makes the use of renormalized interactions particularly useful.

We show a comparison plot of the two running coupling constants, $g(n)$ and $g_{\text{unconf.}}(2\sqrt{n})$ in Fig. 3.2. Using $E_{1+1}^{\text{unconf.}} = -g(n \rightarrow \infty)^2/4$ and Eq. (3.10) allows us to calculate $g_{\text{unconf.}}$. For $g(n)$ we calculate the exact two-body ground state energy (see Eq. (3.7)) and tune $g(n)$ for each cutoff such that this energy remains fixed. We can see that both running coupling constants show qualitatively the same behavior and for large cutoffs, they even agree quantitatively (less than 1% disagreement for $n \geq 21$). The small discrepancies for small cutoffs are due to the semi-classical approximation that we used to derive Eq. (3.14). It only holds in the limit of large quantum numbers.

3.3.2. Effective interactions

One can include (additionally to the ground state) also information about excited states to renormalize a potential. In nuclear physics, this approach is known under the name of “Lee-Suzuki” transformation [114, 116] and in the cold atom community these interactions are often called effective interactions, see e.g. [50, 53, 105, 106]. In this renormalization procedure, the two-body potential is constructed such that in a truncated Hilbert space the exact two-body eigenspectrum is reproduced. To make this chapter self-contained, we explain the idea below (note that this follows closely Refs. [50, 105, 127]). Although setting up these effective interactions can be more complicated than using a running coupling constant, they have additional advantages. For example, they allow for a transformation of operators alongside the renormalization of the potential, which can lead to improved convergence as we show below.

General framework

We start by writing the Hamiltonian of a two-body system as

$$H^{(2)} = U^\dagger \tilde{H}^{(2)} U. \quad (3.15)$$

The tilde denotes that $\tilde{H}^{(2)} = E^{(2)}$ is a diagonal matrix with the eigenenergies on the diagonal; the matrix U is a unitary matrix which has the eigenvectors as columns $U_{ij} = \langle i | \Psi_j \rangle$, where $|i\rangle$ is a two-body basis state and $|\Psi_j\rangle$ an eigenstate of the interacting two-body system: $H^{(2)} |\Psi_j\rangle = E_j |\Psi_j\rangle$. Formally, we can write the truncation of the Hilbert space via so-called projection operators $P_{\mathcal{M}}$ with \mathcal{M} the Hilbert space in which we perform our CI calculation. With this, we can define the matrices $U_{\mathcal{M}\mathcal{M}} = P_{\mathcal{M}} U P_{\mathcal{M}}$, $E_{\mathcal{M}\mathcal{M}} = P_{\mathcal{M}} E^{(2)} P_{\mathcal{M}}$. It is important to note that for a finite Hilbert space \mathcal{M} , $U_{\mathcal{M}\mathcal{M}}$ is not unitary. Even though $U_{\mathcal{M}\mathcal{M}} U_{\mathcal{M}\mathcal{M}}^\dagger$ is diagonal, the diagonal matrix elements are smaller

than one. However, we can define a unitary matrix $Q_{\mathcal{M}\mathcal{M}} = U_{\mathcal{M}\mathcal{M}} \left(\sqrt{U_{\mathcal{M}\mathcal{M}}^\dagger U_{\mathcal{M}\mathcal{M}}} \right)^{-1}$ ⁶. With these definitions, we are now able to define an effective Hamiltonian in a truncated Hilbert space:

$$H_{\mathcal{M}\mathcal{M}}^{\text{eff}} = Q_{\mathcal{M}\mathcal{M}}^\dagger E_{\mathcal{M}\mathcal{M}} Q_{\mathcal{M}\mathcal{M}}. \quad (3.16)$$

Next, we extract the effective interaction by subtracting the kinetic energy:

$$V_{\mathcal{M}\mathcal{M}}^{\text{eff}} = H_{\mathcal{M}\mathcal{M}}^{\text{eff}} - P_{\mathcal{M}} T P_{\mathcal{M}}, \quad (3.17)$$

where T describes the kinetic energy matrix. One important feature of this effective interaction is that its construction can be interpreted as a unitary transformation of the Hamiltonian [116, 127], see also App. A.6.

This allows us to also transform operators alongside the renormalization of the interaction. For a one-body operator

$$O^{(1)} = \sum_{\alpha=1}^N O_{\alpha}, \quad (3.18)$$

where O_{α} is an operator written in first quantization (in second quantization it reads $O^{(1)} = \sum_{ij} a_{ij} a_i^\dagger a_j$), many-body operators are induced by the unitary transformation, i.e. by the renormalization. Since we built the effective interaction using the two-body solution, we include induced two-body operators and neglect higher-order ones (see also Ref. [127]). This leads to

$$O_{\text{eff}}^{(1,2)} = \sum_{\alpha=1}^N O_{\alpha} + Q_{\mathcal{M}\mathcal{M}}^\dagger \tilde{O}_{\mathcal{M}\mathcal{M}}^{(2)} Q_{\mathcal{M}\mathcal{M}} - O_{\mathcal{M}\mathcal{M}}^{(2)}, \quad (3.19)$$

where

$$O_{\mathcal{M}\mathcal{M}}^{(2)} = P_{\mathcal{M}} \sum_{\alpha>\beta=1}^N (O_{\alpha} + O_{\beta}) P_{\mathcal{M}}. \quad (3.20)$$

Remember that the tilde, $\tilde{O}_{\mathcal{M}\mathcal{M}}^{(2)}$, means that the operator is expanded in the eigenstates of the interacting two-body system $|\Psi_i\rangle$, while $O_{\mathcal{M}\mathcal{M}}^{(2)}$ is written in the two-body basis states $|i\rangle$. A two-body operator

$$O^{(2)} = \sum_{\alpha,\beta=1}^N O_{\alpha\beta}, \quad (3.21)$$

⁶Note that for increasing Hilbert spaces, the normalization of this operator, $\left(\sqrt{U_{\mathcal{M}\mathcal{M}}^\dagger U_{\mathcal{M}\mathcal{M}}} \right)^{-1}$, converges towards unity.

with $O_{\alpha\beta}$ an operator in first quantization (in second quantization it reads $O^{(2)} = \sum_{ijkl} b_{ijkl} a_i^\dagger a_j^\dagger a_k a_l$) is transformed as

$$O_{\text{eff}}^{(2)} = Q_{\mathcal{M}\mathcal{M}}^\dagger \tilde{O}_{\mathcal{M}\mathcal{M}}^{(2)} Q_{\mathcal{M}\mathcal{M}}. \quad (3.22)$$

For a derivation of the transformation of operators alongside the renormalization see App. A.6.

We build the effective interaction using the exact solution presented in Eqs. (3.5), (3.7). This solution is written in terms of relative and center-of-mass coordinates. Therefore, the transformation of operators is straightforward, if an operator factorizes in these coordinates. If it does not, more involved calculations are needed. For details on how the transformation of operators can be implemented for our two effective interactions see App. A.6.3, A.6.4. Note that also other renormalization methods exist which allow for a transformation of operators alongside the renormalization such as the similarity renormalization group method used in nuclear physics [81]⁷.

Effective interaction from the energy spectrum in relative coordinates: $V_{\text{eff}}^{\text{rel}}$

We employ two different effective interactions following the general framework presented above, using the exact two-body solution Eq. (3.5). Our first approach is to build the effective interaction matrix in relative coordinates, i.e. using only ψ_{ν_i} from above. Then, this interaction matrix is transformed to the laboratory frame (the frame defined in Eq. (3.1)), in which the CI calculations are performed. Note that this approach is only possible because the exact two-body solution factorizes in center-of-mass and relative part where only the latter is affected by the interaction. This approach is the one used in previous studies on effective interactions in systems of cold atoms, see e.g. Refs. [50, 105, 106]. For completeness, we present the relevant set of equations to set up this interaction in App. A.5.1, see also Ref. [50].

Note that with this interaction, the full two-body spectrum is not immediately converged for a finite cutoff. The reason is that relative and center-of-mass coordinates are coupled in a truncated Hilbert space. Therefore, building the effective interaction matrix in relative coordinates and then transforming to the laboratory frame leads only to an approximate two-body spectrum. However, typically for the low-energy part of the spectrum the coupling between relative and center-of-mass coordinates is weak and with increasing cutoff this coupling vanishes.

⁷In Ref. [116] this method is compared against a running coupling constant approach in the context of nuclear physics.

Effective interaction from the full two-body energy spectrum: $V_{\text{eff}}^{\text{rel+cm}}$

The second effective interaction is based on the full two-body solution, i.e. including center-of-mass excitations and relative ones. This approach leads to the exact two-body spectrum for any one-body cutoff because it accounts for the coupling of relative and center-of-mass coordinates in a finite Hilbert space. This comes at the price that construction of the interaction matrices for $V_{\text{eff}}^{\text{rel+cm}}$ is more complicated to construct than for $V_{\text{eff}}^{\text{rel}}$. The reason for this is that the overlap between the laboratory frame and the exact two-body solution has to be known. As we will show below, $V_{\text{eff}}^{\text{rel+cm}}$ leads to an improved performance. Also, note that this interaction is the only option if one has trapping geometry or bare interaction for which the exact two-body solution does not factorize in relative and center-of-mass coordinates⁸. We show the relevant set of equations for the construction of this interaction in App. A.5.2.

3.4. Results

Now, we will benchmark the convergence of the four different interactions – bare contact interaction⁹ $g\delta$, running coupling constant $g(n)\delta$ (see Sec. 3.3.1), $V_{\text{eff}}^{\text{rel}}$ (see Sec. 3.3.2) and $V_{\text{eff}}^{\text{rel+cm}}$ (see Sec. 3.3.2) – against each other. To this end, we will discuss the convergence for the energy and density. Furthermore, we discuss additionally the effect of the transformation of operators alongside the renormalization presented in Eqs. (3.19) and (3.22) for the expectation value of the kinetic energy and the trapping confinement as well as for transition matrix elements.

We will use two different sets of particle numbers: $1 + 1$ and $1 + 3$ fermions. As we show in App. A.4 our conclusions also hold for larger particle numbers, which is particularly important for future few-to-many-body studies. Although the $1 + 1$ system is used for the renormalization of our interactions, not all observables, like the density, are fixed by the renormalization schemes. This means that for such observables a large number of basis states might be needed for converged results. Because of its simplicity, the $1 + 1$ system will provide us with valuable insight into the convergence properties. Furthermore, because of the existence of an exact solution, we have an accurate benchmark for large cutoffs. From a practical point of view, the the results for the $1 + 3$ system are more relevant for

⁸Note however, that for non-harmonic traps one can still employ a harmonic oscillator basis and use the effective interactions discussed in this Chapter. This in turn will result in an off-diagonal one-body Hamiltonian matrix A_{ij} .

⁹Only for a one-dimensional system the bare coupling constant leads to a well-defined system, i.e. for higher dimensional ones, there is no benchmarking against the bare coupling constant possible.

future few-to-many calculations as no exact solution exists and *ab initio* calculations are necessary to gain insight into the few-to-many-body crossover.

We showcase results for two representative interaction strengths: One for a repulsive and one for an attractive interaction. We verified that our conclusions also hold for other interaction strengths. We use one-body cutoffs from $n = 11$ up to $n = 31$ which means that for our particle numbers, the calculations can be performed on a normal computer. As we will demonstrate, the renormalized interactions allow one to achieve converged results with these cutoffs.

3.4.1. Energy

We start our comparison by studying the interaction energy, $E(g) - E(g = 0)$. We show the results for the different interactions in Figure 3.3 as a function of the one-body cutoff parameter, n . To judge the convergence, we use the harmonic oscillator energy unit, $\hbar\omega = 1$, as the relevant scale. Because we use the two-body ground state as the renormalization condition for the running coupling constant, we show results for the second excited state for the $1+1$ system (the first excited state is a center-of-mass excitation and therefore not useful). For the $1+3$ system, we present results for the ground state.

Because there exists an exact solution for the $1+1$ system, Eq. (3.7), we can compare the numerical results against it. As expected, the renormalized interactions converge faster to the limit $n \rightarrow \infty$ than the bare interaction. For example, the running coupling constant, $g(n)\delta(x)$, with a cutoff of $n = 31$ deviates from the exact result by $E(n = 31) - E(n = \infty) \approx 0.035$ while for the bare contact interaction, $g\delta(x)$, $E(n = 31) - E(n = \infty) \approx 0.33$. For $V_{\text{eff}}^{\text{rel}}$ we observe a similar convergence pattern as for the running coupling constant. For $V_{\text{eff}}^{\text{rel+cm}}$ the $1+1$ spectrum is converged for all cutoffs by construction.

For the $1+3$ system we can see that $V_{\text{eff}}^{\text{rel+cm}}$ leads to the best convergence. Already for $n \simeq 21$ the change in the energy with increasing cutoff is smaller than 1% on the harmonic oscillator energy unit, e.g. $E(n = 21) - E(n = 31) \lesssim 0.004$. Therefore, we use the value with the highest cutoff of this interaction as a benchmark for the other interactions, i.e. $E(n \rightarrow \infty) \approx E(n = 31)$. As for the $1+1$ system, we can see that $g(n)\delta(x)$ and $V_{\text{eff}}^{\text{rel}}$ perform similarly, e.g. for the largest cutoff we have $E(n = 31) - E(n \rightarrow \infty) \approx 0.05$. Also similar to the $1+1$ system is the performance of the bare contact interaction. There, we have a significant deviation from the converged result: $E(n = 31) - E(n \rightarrow \infty) \approx 0.7$.

As stated above, this slow convergence of the bare contact interaction is expected. We can estimate the convergence of the energy for large cutoffs ($n \rightarrow \infty$) by using Eqs. (3.11) and (3.14) (for details and a comparison to the data see App. A.1):

$$E_{g\delta}(n) \simeq E_{g(n)\delta}(n) + \frac{C}{\pi\sqrt{2n}}, \quad (3.23)$$

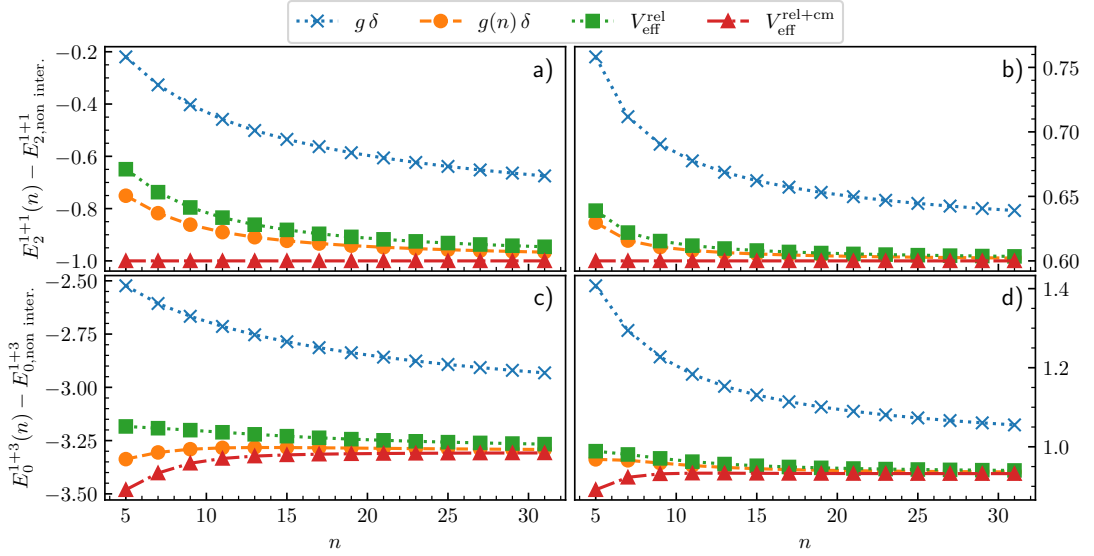


Figure 3.3.: **Interaction energy of the system for different particle numbers and interactions as a function of the cutoff parameter n .**

Panels a) and b) show the interaction energy ($E(g) - E(g = 0)$) of the second excited state for $1 + 1$ particles; panels c) and d) are for the ground state of $1 + 3$. Panels a) and c) are for attractive interaction with $g = -2.5067$ (which corresponds to $E_{1+1} = -1$); b) and d) show results for repulsive interactions, $g = 3$ (which corresponds to $E_{1+1} = 1.6$). Numerical data are shown with markers of different shapes; lines are added to guide the eye. The interested reader can see these data plotted as a function of $1/n$ and as double logarithmic plots for the $1 + 1$ system in App. A.9.1, A.9.2. Figure modified from Ref. [112].

where $E_V(n)$ describes the energy calculated with the potential V in the Hilbert space with cutoff n ; $C = g^2 \langle \Psi | \sum_{i < j} \delta(x_i - x_j) | \Psi \rangle$ is the contact parameter [126]. As shown above, the running coupling constant leads to fast convergence which means that we can assume $E_{g(n)}(n)$ to be constant for sufficiently large cutoffs. Therefore, we can estimate the convergence rate of the bare contact interaction, to be $1/\sqrt{n}$ for any number of particles, in agreement with the numerical analysis of Ref. [59].

To further analyze the convergence behavior, we performed a fitting analysis of the data

motivated by Eq. (3.23)

$$E_V(n) = E_V(n \rightarrow \infty) + \frac{A_V}{n^{\sigma_N}}. \quad (3.24)$$

Note that in general, the parameters $E_V(n \rightarrow \infty)$, A_V and σ_N depend on the used interaction potential V . To increase readability, in the following we will explicitly state the used potential and omit the subscript V . We show the results of the fits and a detailed discussion of these data in App. A.2. This analysis further solidifies our statements above: The renormalized interactions lead to a faster convergence rate, signaled by a larger value σ , than the bare interaction, in agreement with previous studies [50, 108, 111]. Furthermore, they show that $V_{\text{eff}}^{\text{rel}}$ leads to a similar improvement as the running coupling constant approach while $V_{\text{eff}}^{\text{rel+cm}}$ has the fastest convergence.

Finally, we want to mention a typical feature of renormalized interactions: For the $1+3$ system, some energies converge from below when increasing the Hilbert space (see also the non-monotonic behavior of renormalized interactions for the other observables discussed below). This may seem contradictory to the variational behavior of CI calculations with non-renormalized interactions but can be easily understood using the running coupling constant, see e.g. Fig. 3.2: Upon larger cutoffs, the attractive interaction effectively weakens, see Eq. (3.10), which means that the energy increases. Therefore, there is a competition between a decreasing energy because of the larger cutoff and an increase because of a weaker interaction¹⁰. Note that this feature is not necessarily a disadvantage; we can utilize it to approximate the error due to the finite cutoff. If one interaction converges from above and one from below, we can use the deviations between these two to estimate the value in infinite Hilbert space and to judge the convergence.

3.4.2. Density

Here, we study the density of the ground state for an attractive interaction, which is defined as

$$\rho(z) = \sum_{i=1}^N \delta(z - x_i) = \sum_{i,j} \phi_i(z) \phi_j(z) a_i^\dagger a_j. \quad (3.25)$$

We show our results in Fig. 3.4. In the left panels, we display the density calculated with the bare contact interaction and the running coupling constant approach. In the right ones, we showcase the density in the center of the trap calculated with all interactions as a function of the cutoff parameter n .

¹⁰Note that while we did not observe any oscillatory behavior, we cannot rule it out. However, for large cutoffs, we also expect that any potential oscillations are suppressed.

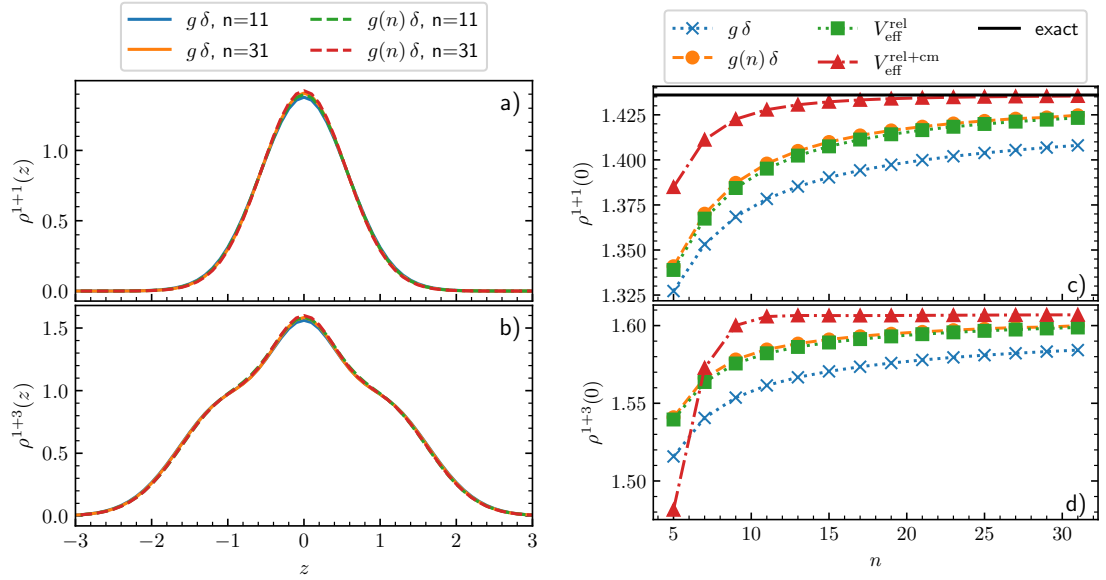


Figure 3.4.: **Density of the ground state for different particle numbers and interactions as a function of the cutoff parameter n .**

Panels a) and b): Density of the ground state calculated with the potentials $g\delta(x)$ and $g(n)\delta(x)$ and two cutoff parameters. Panels c) and d): Density of the ground state in the center of the trap as a function of the cutoff parameter n for the four potentials considered in this chapter. Panels a) and c) show results for the $1 + 1$ system; panels b) and d) are for $1 + 3$. All panels are for attractive interactions $g = -2.5067$, which corresponds to $E_{1+1} = -1$. Numerical data in panels c) and d) are shown with markers of different shapes. Lines are added to guide the eye. In Apps. A.9.1, A.9.2, we also present these data as a function of $1/n$ and as double logarithmic plots for the $1 + 1$ system. Figure modified from Ref. [112].

The induced two-body operator, see Eq. (A.47),

$$\rho^{(2)}(z_\alpha, z_\beta) = \rho(z_\alpha) + \rho(z_\beta) \quad (3.26)$$

does not factorize in relative $z_{\alpha,\beta} = \frac{1}{\sqrt{2}}(z_\alpha - z_\beta)$ and center-of-mass $Z_{\alpha,\beta} = \frac{1}{\sqrt{2}}(z_\alpha + z_\beta)$ coordinates. Hence, the computation of the transformed operator is not straightforward (for details see App. A.6). Because the density converges fast with $V_{\text{eff}}^{\text{rel+cm}}$ even without

a transformation of the operator alongside the interaction (see Subsec. 3.3.2), we leave a study of the transformation of the density operator to future works.

As we can see in the left panel, the overall shape of the density is reproduced well with both interactions even for small cutoffs. However, large cutoffs are needed to get accurate values for the density, in particular in the center of the trap, $\rho(z = 0)$ ¹¹. Similar to the energy, $V_{\text{eff}}^{\text{rel+cm}}$ performs best. A comparison to the exact two-body solution shows that the exact value is reached fast. For the 1 + 3 system this interaction also shows the fastest convergence while $g(n)\delta(x)$ and $V_{\text{eff}}^{\text{rel}}$ perform similarly. The bare contact interaction showcases the slowest convergence.

These conclusions are further supported by a fitting analysis with the function

$$O(n) = O(n \rightarrow \infty) + \frac{A}{n^\sigma}. \quad (3.27)$$

For a detailed description and the results of this fitting procedure, we refer to App. A.1. The discussion in this subsection showcases that although the renormalized interactions are constructed to improve the convergence for the energy, they also lead to a faster convergence for the density, in agreement with previous studies [50, 108, 111].

3.4.3. Transformation of operators

In this section, we discuss the transformation of operators alongside the renormalization of interactions, which, to the best of our knowledge, has not been explored previously in the context of cold atoms. To this end, we calculate the expectation value of the one-body parts of the Hamiltonian, i.e. the kinetic energy operator T ¹² and the trapping potential W , see Eq. (3.2), whose expectation value is the mean-square radius for our system. As discussed above, the effective interactions ($V_{\text{eff}}^{\text{rel}}$ and $V_{\text{eff}}^{\text{rel+cm}}$) are constructed via unitary transformations which can also be used to transform operators (for details see App. A.6). Since the running coupling constant approach is not related to a unitary transformation, we cannot transform operators for this interaction. As for the energy, we use the harmonic oscillator energy unit, $\hbar\omega = 1$, as relevant scale for the convergence.

¹¹We have checked that even if one considers the relative density, $(\rho_{n=11}(z) - \rho_{n=31}(z))/\rho_{n=31}(z)$, the dependence on the cutoff at the trap center is of the same order of magnitude as at the edges of the system.

¹²Note that strictly speaking the kinetic energy is not an observable quantity. Although its expectation value is well-defined in one dimension, for higher dimensional systems it diverges, see e.g. Ref. [128] where this is shown with Tan's contact parameter [129]. We still calculate the expectation value of T because it is one of the simplest operators which factorizes in center-of-mass and relative coordinates and which is sensitive to local changes of the wave function.

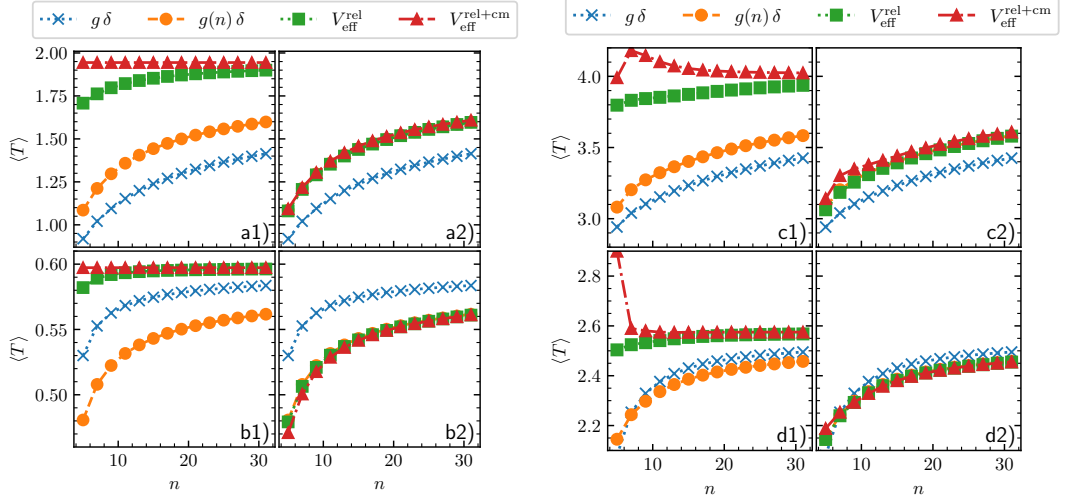


Figure 3.5.: **Expectation value of the kinetic energy operator, $\langle T \rangle$, for different particle numbers and interactions as a function of the cutoff parameter n .**

Panels *1) show results where the operator T has been transformed together with $V_{\text{eff}}^{\text{rel}}$ and $V_{\text{eff}}^{\text{rel+cm}}$, while panels *2) show results where only the potential is renormalized but the operator T remains unchanged. Panels a) and b) are for the 1+1 system, while panels c) and d) are for 1+3 particles. Panels a) and c) show results for an attractive interaction with $g = -2.5067$ (corresponds to $E_{1+1} = -1$) while panels b) and d) are for repulsive interaction with $g = 3$ (corresponds to $E_{1+1} = 1.6$). Data is shown with markers; lines are added to guide the eye. We show these data also as a function of $1/n$ and double logarithmic plots for the 1 + 1 system in Apps. A.9.1, A.9.2. Figure modified from Ref. [112].

When transforming the operators T and W alongside the effective interactions, Eq. (3.19), two-body operators are induced, see Eq. (3.20)

$$T^{(2)} = \sum_{ijkl} t_{ijkl} a_i^\dagger a_j^\dagger a_k a_l, \quad W^{(2)} = \sum_{ijkl} w_{ijkl} a_i^\dagger a_j^\dagger a_k a_l, \quad (3.28)$$

where $t_{ijkl} = \delta_{j,l} t_{ik} + \delta_{i,k} t_{jl}$, and $w_{ijkl} = \delta_{j,l} w_{ik} + \delta_{i,k} w_{jl}$ with $t_{ik} = -\int dx \Phi_i(x) \Phi_k''(x)/2$ and $w_{ik} = \int dx \Phi_i(x) x^2 \Phi_k(x_1)/2$. Because these two-body operators factorize in center-of-mass and relative coordinates, it is straightforward to calculate $\tilde{T}^{(2)}$ and $\tilde{W}^{(2)}$, the expectation values with respect to the analytical two-body solution.

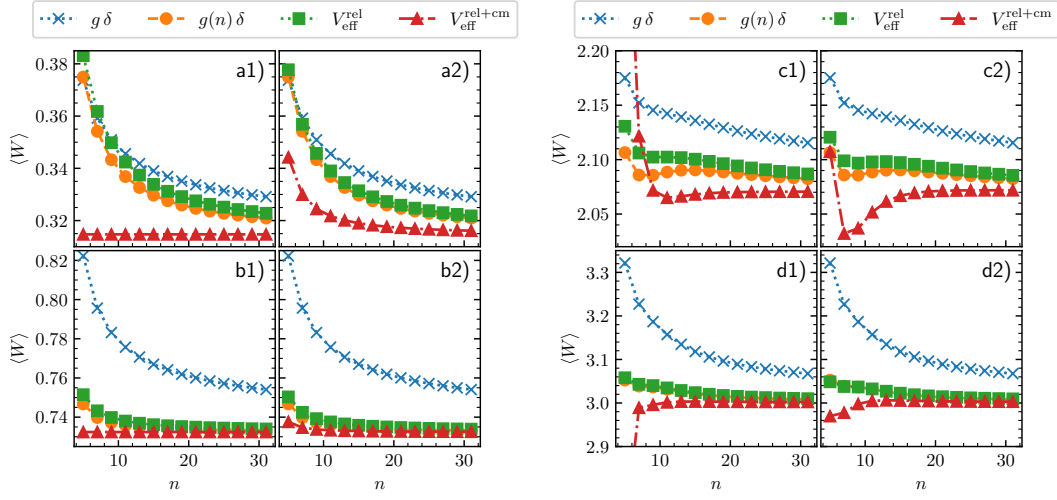


Figure 3.6.: **Expectation value of the trap operator, W , for different particle numbers and interactions as a function of the cutoff parameter n .**

Panels *1) show results for $\langle W \rangle$ when the operator W has been transformed together with $V_{\text{eff}}^{\text{rel}}$ and $V_{\text{eff}}^{\text{rel+cm}}$, while panels *2) correspond to only renormalizing the interaction while keeping W unchanged. Panels a) and b) are for the 1 + 1 system, while panels c) and d) are for 1 + 3 particles. Panels a) and c) show results for attractive interaction $g = -2.5067$ (corresponds to $E_{1+1} = -1$); panels b) and d) depict the convergence for repulsive interaction $g = 3$ (corresponds to $E_{1+1} = 1.6$). Data is shown with markers; lines are added to guide the eye. We show these data also as a function of $1/n$ and double logarithmic plots for the 1 + 1 system in App. A.9.1, A.9.2. Figure modified from Ref. [112].

We show in Fig. 3.5 the results for the expectation value of the kinetic energy. In panels *1) we show $\langle T \rangle$ when T is transformed alongside the renormalization while in panels *2) we show results when only the interaction but not the operator has been transformed. We provide a quantitative analysis of our data with the same fitting procedure as above, Eq. (3.24), in App. A.2.

We see that a transformation of the operator can be necessary to improve the convergence: For attractive interaction, the convergence of $\langle T \rangle$ is improved only slightly compared to the bare contact interaction if a non-transformed operator is used. For the repulsive interaction, the data converges even slower. We can understand this behavior

using the running coupling constant approach. If we have repulsive interactions, the renormalization leads to a weaker interaction ($g(n)$ is smaller than g). This results in a smaller expectation value of the kinetic energy. At the same time, increasing the cutoff results in an increased value, i.e., the renormalization works against the convergence in this case. For attractive interaction, it is exactly the opposite: The renormalization leads to a stronger interaction, i.e. a larger value of the observable just as an increasing cutoff also increases the value of the kinetic energy. However, if the kinetic energy operator is transformed, the convergence properties of the effective interactions are improved significantly. Similar to the energy and the density, $V_{\text{eff}}^{\text{rel+cm}}$ leads to the fastest convergence. For the $1 + 1$ system, the results are converged for any cutoff (this is by construction) but also for the $1 + 3$ system $V_{\text{eff}}^{\text{rel+cm}}$ leads to converged results within our truncation range.

For the trapping potential, shown in Fig. 3.6, the transformation of the operator is not as important – there is barely any difference visible between the panels *1) and *2). The potentials $V_{\text{eff}}^{\text{rel}}$ and $g(n)\delta$ result in similar convergence patterns that are faster than the bare contact interaction while $V_{\text{eff}}^{\text{rel+cm}}$ leads to virtually converged results already for $n \simeq 25$ (relative difference is $\simeq 0.01$). Again, we provide a detailed analysis with a fitting procedure in App. A.2.

The results in this subsection can be summarized as follows: For observables that are sensitive to local changes of the wavefunction (such as the kinetic energy), the transformation of operators alongside the renormalization is more important than for observables that are sensitive to global properties (such as the trapping potential, i.e. the mean-square radius). However, further research is needed to prove this statement.

3.4.4. Transition matrix elements

As a last observable we study the transition rate between the ground state and an excited state upon a small periodic modulation of the interaction. To the best of our knowledge, for this observable the improved convergence of renormalized interactions has not been demonstrated before. It is interesting to calculate this observable for two reasons: 1) the corresponding two-body operator is sensitive to two-body correlations between the fermions. This means that it is sensitive to local changes in the wavefunction and should therefore further showcase the importance of transforming the operator alongside the interaction. 2) this operator is a useful probe in cold atom systems. It has been used to study the few-body precursor of a phase transition in a two-dimensional system of a two-component Fermi gas, theoretically [52] as well as experimentally [42]. It has been further explored in few-body bosonic droplets [65].

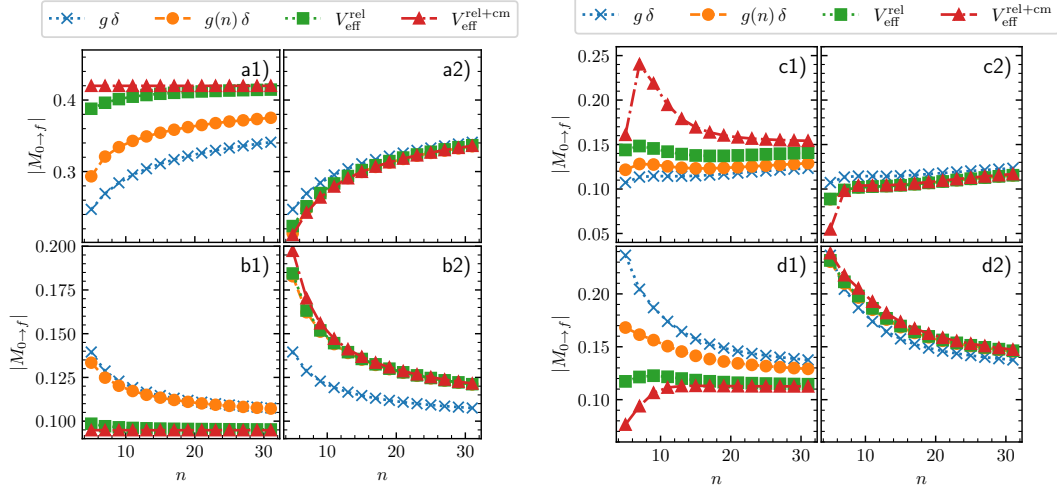


Figure 3.7.: **Transition matrix elements from the ground state to the lowest-energy state that can be excited by a periodic modulation of the interaction, $M_{0 \rightarrow f}$, for different particle numbers and interactions as a function of the cutoff parameter n .**

Panels *1) show $M_{0 \rightarrow f}$ if the operator has been transformed together with the potential while panels *2) show results when only the potential has been renormalized but the operator remains unchanged. Panels a) and b) are for the 1 + 1 system while panels c) and d) are for 1 + 3 particles. Panels a) and c) show results for attractive interaction with $g = -2.5067$ (corresponds to $E_{1+1} = -1$); panels b) and d) depict repulsive interaction with $g = 3$ (corresponds to $E_{1+1} = 1.6$). Our data are shown with markers; lines are added to guide the eye. We show these data also as a function of $1/n$ and double logarithmic plots for the 1 + 1 system in App. A.9.1, A.9.2. Figure modified from Ref. [112].

We consider a periodic modulation of the interaction strength

$$g(t) = g(0) + \eta \sin(\omega t), \quad (3.29)$$

where we assume that $|\eta| \ll |g(0)|$. Using Fermi's golden rule, the transition rate from the ground state $|0\rangle$ to an excited state $|f\rangle$ as $R_{0 \rightarrow f} \propto \eta^2 |M_{0 \rightarrow f}|^2 \delta(E_f - E_0 - \omega)$ can be

estimated. Therefore, we have to calculate the transition matrix element

$$M_{0 \rightarrow f} = \langle \Psi_f | \sum_{i < j} \delta(x_i - x_j) | \Psi_0 \rangle. \quad (3.30)$$

Since this matrix element is only dependent on the relative coordinates, it is straightforward to calculate the transformation of the corresponding operator for the renormalization using the effective interactions, Eq. (3.22). Additionally, we can even introduce a heuristic transformation for the running coupling constant approach. We interpret this regularization scheme as a transformation of the delta-function potential, which implies the ‘natural’ transformation of the transition matrix element:

$$\delta(x_i - x_j) \rightarrow \frac{g(n)}{g} \delta(x_i - x_j). \quad (3.31)$$

We show our results for $|M_{0 \rightarrow f}|$ from the ground state to the first excited state accessible through a modulation of the contact interaction¹³ in Fig. 3.7. As we can see, the transformation of the observable is necessary to achieve accurate results. If we do not transform the observable, the results based upon the bare contact interaction are in fact more accurate than the ones using the renormalized interactions. The explanation is the same as in the previous subsection: The renormalization works against the convergence. Therefore, only by transforming the operator, i.e. by using Eq. (3.30) and Eq. (3.22), can we achieve a boost in convergence. We provide a detailed quantitative analysis of the data with the fitting procedure in App. A.2.

Comparing the different interactions, we see again that the highest accuracy is achieved using the $V_{\text{eff}}^{\text{rel+cm}}$ interaction. This is particularly noticeable for the 1 + 3 system and attractive interaction. There, the fitting routine with Eq. (3.24) gives meaningful results only for $V_{\text{eff}}^{\text{rel+cm}}$ and a transformed observable. In particular, the fit does not produce an accurate parameter c (remember, the extrapolated value of the observable in infinite Hilbert space) for the data calculated with the bare contact interaction, at least for the considered truncated Hilbert spaces. Another interesting feature of these parameters is that the data defy the naive expectation that the convergence patterns for systems with more than two particles should be comparable to those for the 1 + 1 system. This idea is based upon the fact that the transition matrix elements are a two-body operator, and hence their convergence can be studied with the 1 + 1 system. Instead, we can clearly see that even though the data for the 1 + 1 system with attractive interaction can be fitted by Eq. (3.24), for the 1 + 3 system only data obtained with $V_{\text{eff}}^{\text{rel+cm}}$ and a transformed

¹³The periodic modulation of the interaction can only couple states which have the same center-of-mass quantum number.

observable are useful in our fitting procedure, i.e. for an extrapolation to infinite Hilbert space (see App. A.2 for a quantitative discussion).

A comparison between the effective interactions and the running coupling constant approach shows that the use of $V_{\text{eff}}^{\text{rel+cm}}$ and $V_{\text{eff}}^{\text{rel}}$ is advantageous over the use of $g(n)\delta$ in computations of $M_{0 \rightarrow f}$. This is expected as the transformation of the operator for the running coupling constant, Eq. (3.31), is only a heuristic transformation while for $V_{\text{eff}}^{\text{rel}}$ and $V_{\text{eff}}^{\text{rel+cm}}$ the transformation is based upon a unitary transformation (see App. A.6). Nevertheless, the running coupling constant approach with the heuristically transformed operator improves the convergence for all considered cases except for $1 + 1$ and repulsive interaction, where $g(n)\delta$ and $g\delta$ lead to similar results. To give some numbers: For the $1 + 3$ system and repulsive interactions, $M_{0 \rightarrow f}$ changes by 3% when increasing the cutoff parameter from $n = 25$ to $n = 31$ for $g\delta$ while for $g(n)\delta$ this change is 2%. The largest improvements in the accuracy of results are seen for the effective interactions: For $V_{\text{eff}}^{\text{rel}}$ the corresponding difference is 0.6% and for $V_{\text{eff}}^{\text{rel+cm}}$ it is only 0.05%.

This subsection emphasizes the importance of renormalizing the interaction and also of transforming operators, like transition matrix elements, in numerical studies of few-fermion models. In particular, we can achieve precise numerical results for attractive $1 + 3$ systems with only $n \simeq 30$, resulting in matrices that can be diagonalized on a standard PC.

3.5. Conclusions

3.5.1. Summary

In this chapter, we compared different renormalization schemes for the one-dimensional contact interaction. In agreement with previous studies [50, 105, 108, 111], the accuracy of numerical many-body calculations can be improved considerably by renormalizing the interaction, i.e. by explicitly including information about converged two-body energies in the many-body calculations with a truncated Hilbert space. Therefore, the usage of renormalized interactions improves *ab initio* studies of the few-to-many-body crossover.

We found that the simple running coupling constant approach (used e.g. in Refs. [108, 111]) is a good starting point for approximate calculations of the energy spectrum. It is easy to set up and provides a similar boost in performance as the effective interaction approach, which uses the relative energy spectrum for the renormalization, $V_{\text{eff}}^{\text{rel}}$, used in Refs. [50, 77, 105]. Furthermore, because of its simplicity, $g(n)\delta$ is transparent and can be helpful in understanding the concepts of renormalized interactions. The largest boost in convergence was obtained with the effective interaction which includes the full two-body

spectrum, i.e. relative and center-of-mass excitations, $V_{\text{eff}}^{\text{rel+cm}}$. This potential has not been used before in the context of cold atom systems (to the best of our knowledge). We hope that our results will motivate its use in future studies.

For observables other than the energy, we discussed the unitary transformation of operators alongside the renormalization of the interaction – something which is possible with the effective interactions, $V_{\text{eff}}^{\text{rel+cm}}$ and $V_{\text{eff}}^{\text{rel}}$, as they are generated by a unitary transformation. We observed that this transformation (in particular for the kinetic energy and the transition matrix elements) can be necessary to improve the convergence over the bare contact interaction. In particular, for $V_{\text{eff}}^{\text{rel+cm}}$ this allowed us to obtain numerically exact results for relatively small sizes of the Hilbert space. The difference between $V_{\text{eff}}^{\text{rel}}$ and $V_{\text{eff}}^{\text{rel+cm}}$ can be understood from the harmonic trapping confinement which breaks the translational invariance of the system. Only for an infinite basis, the relative and center-of-mass motion decouple in a harmonic oscillator. The effective interaction $V_{\text{eff}}^{\text{rel+cm}}$ corrects for this finite basis artifact and, therefore, converges more quickly. Note that for large basis sizes, relative and center-of-mass motions are effectively decoupled and $V_{\text{eff}}^{\text{rel}}$ gives similar results as $V_{\text{eff}}^{\text{rel+cm}}$.

3.5.2. Outlook

Even though we demonstrated a necessity for the transformation of operators for the kinetic energy and transition matrix elements, our results for the expectation value of the trapping potential showed almost no influence on the transformation of the corresponding operator. Furthermore, for the density we also showed that renormalized interactions without a transformation of the operator leads to large improvements. Currently, our understanding is that observables that are influenced by “global” properties of the wave function are less susceptible to this transformation than “local” observables. The reasoning behind this is that the latter class is sensitive to changes of the wave function at short length scales which are determined mainly by particle-particle interactions. However, a more systematic study of the effect of the transformation of operators is needed. This is in particular important for the use of the running coupling constant approach, $g^{(n)}\delta$, as this renormalization scheme does not allow for a transformation of operators alongside the renormalization.

We want to emphasize that, as already described in the introduction of this chapter, the use of renormalized interactions is not limited to calculations based upon the CI method. Indeed, the interactions discussed in this chapter can be easily implemented into other *ab initio* methods (e.g. the flow equation method introduced in Sec. 2.3). Provided the method also uses a one-body basis cutoff scheme, the interactions can be implemented in exactly the same way. This combination will allow for calculations of an

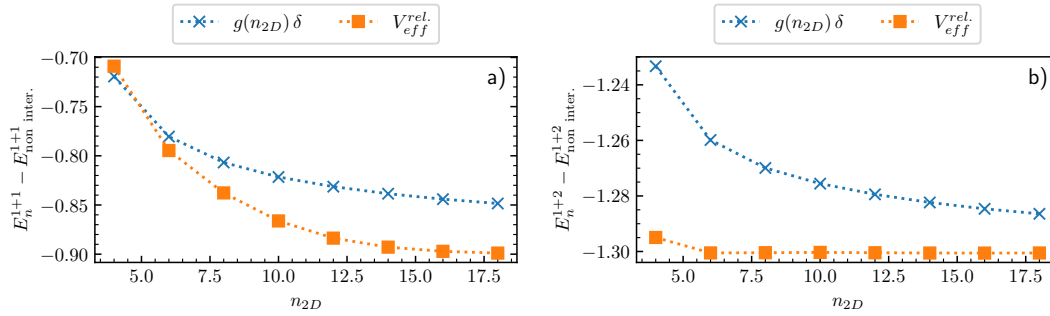


Figure 3.8.: **Interaction energies of a two-dimensional harmonic oscillator for particles interacting via $g(n_{2D})\delta$ or V_{eff}^{rel} as a function of the cutoff n_{2D} .**

Panel a) shows the first excited state of the $1 + 1$ system with a vanishing total angular momentum. Panel b) shows the energy of the ground state for $1 + 2$ particles. The parameters are chosen such that the ground state energy of two fermions is $E_{1+1} = 1.1$. Our data are shown with markers; lines are added to guide the eye. Figure modified from Ref. [112].

increased parameter space, i.e. larger particle numbers and stronger interactions, which is important for works on the few-to-many-body transition. In an upcoming study, we will combine renormalized interactions and an extension of the CI method, the importance truncated CI (see e.g. Refs [64, 65, 79]) to calculate systems with larger particle numbers (mainly enabled by the importance truncation) and stronger interactions (mainly enabled by renormalized interactions) than possible without these improvements. We discuss parts of this study in the outlook of Chap. 5.

Also, note that our results are not limited to contact interactions or to one dimension. For example, studies using cold dipoles such as Refs. [24–26] might benefit from the use of renormalized interactions. Furthermore, odd-channel interactions, which need to be regularized, might be another interesting application of our interactions [6, 130, 131]. Our study also motivates the extension of our comparative study to regularization methods used for two-dimensional systems [51–53]. In particular as two dimensions are less explored in this context than one or three spatial dimensions. We showcase a preliminary comparison between the running coupling constant approach and the V_{eff}^{rel} interaction for a two-dimensional harmonic oscillator confinement in Fig. 3.8, see App. A.3 for the details of our calculation such as the Hamiltonian and basis functions. The cutoff is given by the maximum one-body energy, n_{2D} , used to construct the Hamiltonian. For this system, the bare contact interaction diverges and we follow the prescription of Ref. [51]

to regularize it: We fix the two-body ground state energy for each cutoff, i.e. we use a running coupling constant approach. We show results for the first excited state of $1 + 1$ particles with the total angular momentum of zero and the ground-state energy for the $1 + 2$ system¹⁴. Note that although it appears as if the energy for the $1 + 2$ system calculated with the effective interaction is already converged for $n_{2D} = 8$, there is still a slight increase in the energy, and a more rigorous study similar to Sec. 3.4 is needed for two-dimensional systems. We also expect that the use of effective interactions together with a transformation of operators will boost calculations of observables other than the energy.

¹⁴We have observed similar convergence patterns also for other particle numbers such as $3 + 3$ fermions.

4. Emergence of a Bose polaron in a small ring threaded by the Aharonov-Bohm flux

Studying impurities embedded in a medium is crucial for understanding the few-to-many-body crossover, e.g., they can serve as probes for their environment. As introduced in Chap. 1, the description of many-body systems with impurities can be simplified by introducing quasi-particles, such as a polaron – an impurity dressed by its interactions with the surrounding environment. A polaron behaves similarly to an impurity in free space but has modified one-body parameters, such as the effective mass. Until now, it has been unclear how to investigate the emergence of the effective mass starting from a few particles. In this chapter, we introduce a few-to-many system that enables such a study by connecting its description with the many-body concept of a polaron, thereby contributing to the second goal outlined in Chap. 1.

We consider an impurity in a one-dimensional sea of bosons under the influence of an Aharonov-Bohm flux. The Aharonov-Bohm flux is typically studied in the context of a single particle, where it provides fundamental insights into the coupling between gauge potentials and matter. Here, we extend this model to incorporate interactions with other particles. We demonstrate that the ground state of our system can be described using the many-body concept of a polaron. This enables us to intuitively explain the energy spectrum by introducing the effective mass. To the best of our knowledge, this is the first time that the effective mass has been defined for a finite number of particles, extending the conventional study of the few-to-many-body crossover in impurity systems beyond the usual self-energy analysis [12]. Furthermore, we demonstrate how currents in the system can be tuned by modifying impurity-boson interactions, and we discuss the influence of defects in our setup. Our findings propose the Aharonov-Bohm ring as a novel platform for the few-to-many-body crossover of quasi-particles that arise from impurities immersed in a medium.

Parts of this chapter have been published in this or similar form in our manuscript “Emergence of a Bose polaron in a small ring threaded by the Aharonov-Bohm flux” [63].

4.1. Introduction

In the idealized model of a ring threaded by the Aharonov-Bohm (AB) flux, a particle moves in a region without any magnetic field. However, the presence of magnetic flux still manifests itself in a minimal substitution $-i\partial/\partial x \rightarrow -i\partial/\partial x + \Phi$, where the position-independent parameter Φ determines the strength of the flux. This model provides insight into many fundamental physical phenomena. For example, it showcases the significance of potentials in quantum mechanics [132], geometric phases [133], the Josephson effect and persistent currents [134, 135]. AB physics is most often based upon a single-particle picture [136, 137], which already has the power to explain some experiments qualitatively such as spectroscopy in semiconductor rings [138]. However, one-body studies neglect interactions of a charge carrier with other particles, in particular, with the environment. Therefore, they should be extended for realistic systems. In this chapter, we discuss such an extension assuming a one-dimensional bosonic environment.

We investigate one of the simplest two-component many-body models – a particle (impurity) coupled to the AB flux that interacts with a weakly interacting Bose gas. Besides AB physics, this setup is motivated by recent cold-atom experiments on Bose polarons [139–145]. As described in Chap. 1, impurities have been used in previous studies to explore the few-to-many-body crossover because they act as a probe for the environment. For example, in Ref. [12], the self-energy of an impurity was measured for an increasing number of sea particles, which allowed one to test how many fermions are needed to build a Fermi sea.

Theoretical and experimental advances in realizing ring-shaped trapping potentials and artificial gauge fields with neutral cold atoms (see e.g. Refs. [89, 90, 146]) are another motivation to study our system. So far, ring-shaped condensates with effective gauge potentials have not been engineered in impurity systems. We will show below that this combination leads to rich physics. Note that systems with polaritons might also be another setup to test our results because of recent advances in engineering ring-shaped potentials [147–149] and tunable gauge fields [150].

Let us first briefly review known few-body physics in the AB ring. For identical particles, there is no interplay between particle-particle interactions and the AB flux. Hence, the flux couples only to the total angular momentum of the system, shifting the global energy minimum but leaving the internal dynamics unperturbed [137, 151–153]. This also applies to distinguishable particles with identical masses and fluxes, though, for such systems, the AB flux can change the ground state symmetry, see, e.g., Ref [154]. For particles with different masses or charges (e.g., electrons and holes [155, 156]), the AB flux and the internal structure are coupled. For two particles, this can modify the threshold for binding (which may preclude the formation of excitons for weakly attractive

potentials in one dimension [157]) or lead to the formation of dark excitonic states [158]. As far as we are aware, systems with more than two particles have not been explored extensively.

In this chapter, we focus on dressing the impurity, a typical many-body phenomenon that affects system properties such as transport and magnetization. Therefore, our results complement earlier studies on small systems which used few-body approaches. Our key finding is that an impurity threaded by an AB flux and interacting with bosons, which are both confined to a one-dimensional ring, can be described in terms of the one-dimensional Bose polaron. Consequently, the concepts and ideas developed for such systems [72, 94, 159–166] can be applied here. This connection allows us to draw a number of useful conclusions:

1. Prior studies of the Bose polaron provide insights into the properties of our system and offer an intuitive interpretation of our results. This insight can also be beneficial for the interpretation of numerical lattice simulations that consider electron-phonon interactions, see, e.g., Ref. [167].
2. The AB ring serves as a conceptual model for defining the effective mass in a finite-size system, enhancing the understanding of the crossover from few- to many-body systems. In particular, our work opens the door for studying this crossover beyond the self-energy of an impurity [12].
3. Persistent currents be used to examine the phase coherence of the polaron across the AB ring providing information about the validity of the Bose-polaron concept in one dimension.

This chapter is structured as follows: First, we introduce our system and showcase the connection between the AB flux and the total momentum of the system by transforming the Hamiltonian to the frame “co-moving” with the impurity (see Sec. 2.4). This connection is one of the key methodological findings of this chapter. Afterwards, we will shortly discuss the methods used in this chapter. We use the mean-field approximation [MFA] (see Sec. 2.3 for details) and we present the solution to the Gross-Pitaevskii equation of this system. We further employ the *ab initio* method of the flow equation approach (see Sec. 2.5) for which we discuss our choice for the reference state and explain the used one-body basis. We use this method to discuss the validity of the MFA. Then, we present our main results: We start by discussing the energy spectrum, which we interpret in terms of the Bose polaron. We use this connection to define and calculate the effective mass in a finite setting. This allows us to discuss the convergence of the effective mass towards the thermodynamic limit. Furthermore, we set limits for the applicability of the polaron

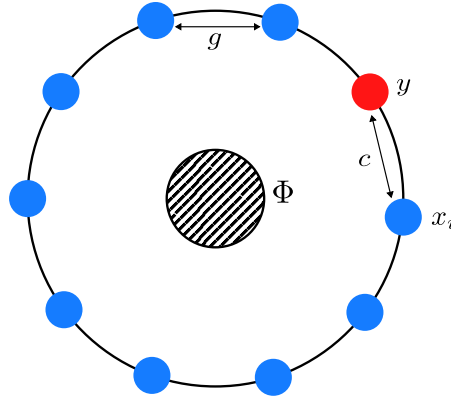


Figure 4.1.: **Sketch of the system.**

Blue balls show bosons at positions x_i ; the impurity is a red ball at position y . The AB flux is depicted via the hatched circle and its value is presented by Φ . The strength of the boson-boson (impurity-boson) interaction is given by g (c). Figure modified from Ref. [63].

approximation. Then, we calculate currents in our system and demonstrate how we can tune the current of the impurity and bosons via the interactions. As a last result, we shortly discuss the influence of defects in our system. We conclude this chapter with a summary of our findings and discuss future research enabled by our setup. In particular, we explain why further few-to-many-body studies on the critical velocity in a one-dimensional Bose gas are interesting. We provide additional information in App. B.

4.2. System

We study a one-dimensional system of N bosons and a single impurity atom, as illustrated in Fig. 4.1. We impose periodic boundary conditions, i.e. the system is contained on a ring of length L . The position of the impurity (i -th boson) is given by Ly (Lx_i); the mass of the impurity (a boson) is m (M). We assume that the impurity is coupled to the AB flux Φ/L ¹. Note that we have neutral particles and therefore Φ is not generated by a magnetic flux threading the ring. Instead, alternative mechanisms are implied [146, 168], such as stirring with a weak external potential at speed v , in which case $\Phi = mvL/\hbar$.

¹It is worth noting that the more general case, where the AB flux is coupled to both particle species, can be easily incorporated into our model, see App. B.1.

The Hamiltonian reads

$$\mathcal{H} = \frac{\hbar^2}{2mL^2} \left(-i \frac{\partial}{\partial y} + \Phi \right)^2 - \frac{\hbar^2}{2ML^2} \sum_i \frac{\partial^2}{\partial x_i^2} + V_{ib} + V_{bb}. \quad (4.1)$$

For the impurity-boson, V_{ib} , and boson-boson, V_{bb} , interactions we use delta-function potentials

$$V_{ib} = \frac{c}{L} \sum_{i=1}^N \delta(x_i - y), \quad V_{bb} = \frac{g}{L} \sum_{i,j} \delta(x_i - x_j), \quad (4.2)$$

where c and g define the strength of the interactions.

For simplicity, we shall use a system of units in which $\hbar = M = 1$. In this chapter, we assume that the bosons and the impurity have identical masses, $m = 1$. Note however that a mass imbalance does not change the main conclusions, see App. B.2. The dimensionless parameters c/g and $\gamma = gL/N$ determine all physical properties as long as the particle number N remains fixed. Here, we focus on $c > 0$ to avoid bound states [62, 169, 170] that are beyond the polaron physics. We discuss the implications of an attractive impurity in Chap. 5. We consider a weakly-interacting Bose gas for which the MFA (see Sec. 2.5) can be employed, i.e. we use $\gamma = 0.2$. Note that the case with $\gamma = 0.2$ and $N = 19$ for $\Phi = 0$ was considered in Ref. [171] providing us with a reference point to benchmark our numerical calculations.

In the following analysis, we will use the Hamiltonian from Eq. (4.1). However, it is important to note that the parameter Φ can in principle be excluded from this Hamiltonian via a gauge transformation $\Psi \rightarrow e^{i\Phi y} \Psi$, where Ψ is the wave function. The flux effect is then incorporated into a "twisted" boundary condition, i.e. the wave function has to acquire a phase $e^{i2\pi\Phi}$ after a complete turn [172, 173]. This condition implies that the energy spectrum must be a periodic function with period $\Phi/(2\pi)$ (see Fig. 4.3 for a schematic sketch of the energy spectrum). For general multi-component systems, such as strongly interacting Bose-Fermi mixtures, a smaller period of the ground-state energy is possible [153, 154]. However, as we demonstrate below, this does not occur for an impurity in a weakly-interacting Bose gas, whose low-energy spectrum resembles that of a single particle.

Without flux, $\Phi = 0$, our system is one of the most studied one-dimensional models [6, 113, 174, 175]. This allows us to use already known methods to solve the system with $\Phi \neq 0$. In particular, we work in the frame co-moving with the impurity (see Sec. 2.4), where the MFA (see Sec. 2.5) and flow equation approach, also called in-medium similarity renormalization group method [IM-SRG] (see Sec. 2.3), provide powerful theoretical tools. These methods enable us to explore the impact of the AB flux on the properties

of the one-dimensional polaron problem beyond previous studies [176, 177], which examined relevant molecular-crystal models. Specifically, we can define and analyze flux-independent properties of the Bose polaron, such as the effective mass, in a finite system.

4.2.1. Co-moving frame

We use the transformation of the Hamiltonian to the frame co-moving with the impurity, which is introduced in Sec. 2.4, to simplify the description of our system². The Schrödinger equation in the co-moving frame reads

$$\left[-\frac{1}{2} \left(\sum_i \frac{\partial}{\partial z_i} \right)^2 - \frac{1}{2} \sum_i \frac{\partial^2}{\partial z_i^2} + \frac{(P + \Phi)^2}{2} + L^2 V_{ib} + L^2 V_{bb} + i(P + \Phi) \sum_i \frac{\partial}{\partial z_i} \right] \tilde{\Psi} = E \tilde{\Psi}, \quad (4.3)$$

where E is the dimensionless energy of the system. The total momentum of the system, P , is quantized to fulfill the periodic boundary conditions: $P = 2\pi n$, where n is an integer. The AB flux Φ , however, is a continuous parameter. The transformation to the frame co-moving with the impurity reveals an important connection: Φ and P enter this equation together as a sum $\mathcal{P} = P + \Phi$. Therefore, we interpret \mathcal{P} as a “continuous effective total momentum” that determines the total current in the system. This interpretation is crucial for understanding the system’s properties in terms of an effective one-body picture. We will use this below to intuitively explain our results for the energy spectrum and currents and to define the effective mass in a finite system. Note that $\tilde{\Psi}_P^*$ solves the Schrödinger Eq. (4.3) with $-\mathcal{P}$, which is a manifestation of time-reversal symmetry.

4.3. Methods

4.3.1. Mean-field approximation

To gain semi-analytical insight into the system, we apply the MFA, see Sec. 2.5. The Gross-Pitaevskii equation for our system reads

$$-\frac{1}{2\kappa} \frac{\partial^2 f}{\partial z^2} + i \frac{\mathcal{P}}{m} \frac{\partial f}{\partial z} - i(N-1) \frac{P_{\text{bos}}}{m} \frac{\partial f}{\partial z} + g(N-1)|f|^2 f = \mu f, \quad (4.4)$$

²Note that the transformation to the co-moving frame has been used to study the few-to-many-body transition of the self-energy of the Bose-polaron with $\Phi = P = 0$ [72]. Here, we study this transition for non-vanishing P , where the continuous parameter Φ provides a bridge between the discrete values of P .

where μ is the chemical potential, $\mathcal{P} = P + \Phi$ is the “total” momentum, $\kappa = m/(m + 1)$ is the reduced mass, and

$$P_{\text{bos}} = -i \int f^* \frac{\partial f}{\partial z} dz \quad (4.5)$$

is the momentum of one boson. We implement the impurity-boson interaction as a boundary condition

$$f'(0^+) - f'(0^-) = 2c\kappa f(0). \quad (4.6)$$

This Gross-Pitaevskii equation has been discussed before, see, e.g., Ref. [63, 178]. For convenience of the reader, we summarize its solution. We simplify the notation by introducing the momentum of the impurity as

$$P_{\text{imp}} = \mathcal{P} - (N - 1)P_{\text{bos}}. \quad (4.7)$$

Then, we rewrite f

$$f(z) = h(z)e^{i\theta(z)}, \quad (4.8)$$

which leads to the two coupled differential equations:

$$-h'' + (\theta')^2 h - 2P_{\text{imp}}\theta' h \frac{\kappa}{m} + 2\kappa g(N - 1)h^3 - 2h\kappa\mu = 0, \quad (4.9)$$

$$-\theta'' h - 2\theta' h' + 2P_{\text{imp}}h' \frac{\kappa}{m} = 0. \quad (4.10)$$

Their solutions read

$$h(z) = \sqrt{(s_2 - s_1) \text{sn}(A|p)^2 + s_1}, \quad (4.11)$$

$$\theta(z) = \frac{\text{dn}(A|p) \sqrt{\kappa g(N - 1) s_1 s_2 s_3} \Pi\left(1 - \frac{s_2}{s_1}; \text{am}(A|p)|p\right)}{2s_1(K(p) - \alpha) \sqrt{1 - p \text{sn}(A|p)^2}} + zP_{\text{imp}} \frac{\kappa}{m}. \quad (4.12)$$

with $p = \frac{s_2 - s_1}{s_3 - s_1}$, $\alpha = F\left(\sin^{-1}\left(\sqrt{\frac{s_{\text{min}} - s_1}{s_2 - s_1}}\right) \middle| p\right)$, $\beta = E\left(\sin^{-1}\left(\sqrt{\frac{s_{\text{min}} - s_1}{s_2 - s_1}}\right) \middle| p\right)$ and $A = \alpha + 2z(K(p) - \alpha)$. sn and dn are Jacobi elliptic functions, $F(K)$ is the (complete) elliptic integral of first kind, E the elliptic integral of second kind, Π the elliptic integral of third kind and am is the Jacobi amplitude [102].

The parameters s_1, s_2, s_3 characterize the solution and are eventually determined from the particle number and interaction strengths. The impurity boundary condition³ gives

³Note that there exist three different solutions to this condition, i.e., three different values of s_{min} . We take the solution that reproduces the physical behavior of the Bose polaron in the limit $\mathcal{P} \rightarrow 0$ discussed in Ref. [72].

s_{min} as a function of s_1, s_2, s_3 . To determine s_1, s_2, s_3 we solve a set of equations: One which demands that $f(z)$ solves the Gross-Pitaevskii equation, one for the normalization of f , and one for the periodicity of f :

$$4p(K(p) - \alpha)^2 - \kappa g(N - 1)(s_2 - s_1) = 0, \quad (4.13)$$

$$-\frac{(s_1 - s_3)(\alpha - \beta - K(p) + E(p))}{\alpha - K(p)} + s_1 = 1, \quad (4.14)$$

$$\theta(0) = \theta(L). \quad (4.15)$$

These equations are solved numerically under the condition that $s_1 \leq s_2 \leq s_3$.

The chemical potential is given by

$$\mu = \frac{1}{2}g(s_1 + s_2 + s_3). \quad (4.16)$$

The solution, Eqs. (4.11), (4.12), allows us to calculate all observables of the system, such as energy or currents, within the MFA.

4.3.2. Flow equation approach

Even though we consider a weakly interacting Bose gas, as described in Sec. 2.5 care must be taken when the MFA is employed in one-dimensional systems. To ensure the applicability of the MFA, we use the beyond mean-field flow equation approach as benchmark. For details on this method, we refer to Sec. 2.3. In this section, we only briefly discuss the reference state and one-body basis used in this chapter.

For the one-body basis, we solve the one-body Hamiltonian in the frame co-moving with the impurity for $\Phi = P = 0$, i.e. we use sin/cos functions which include the impurity-boson interaction. Because the odd states are zero at the position of the impurity, they are not affected by the strength of the interaction while for even states, we solve

$$\left. \frac{\partial \phi_i}{\partial z_i} \right|_{0+}^{0-} = 2c\kappa \phi_i(0). \quad (4.17)$$

The basis states also fulfill periodic boundary conditions, $\phi_i(0) = \phi_i(L)$. In our calculations, we use a finite number of basis states with $n \in [11, 13, 15, 17, 19, 21]$ and extrapolate to infinite Hilbert space according to the description in Sec. 2.3.

As described in Sec. 2.3, we construct the reference state iteratively, beginning with the ground state of the one-body basis. Using the flow equation approach, we calculate the density and phase for $\mathcal{P} = 0$ and use the results as a new reference state. This process is

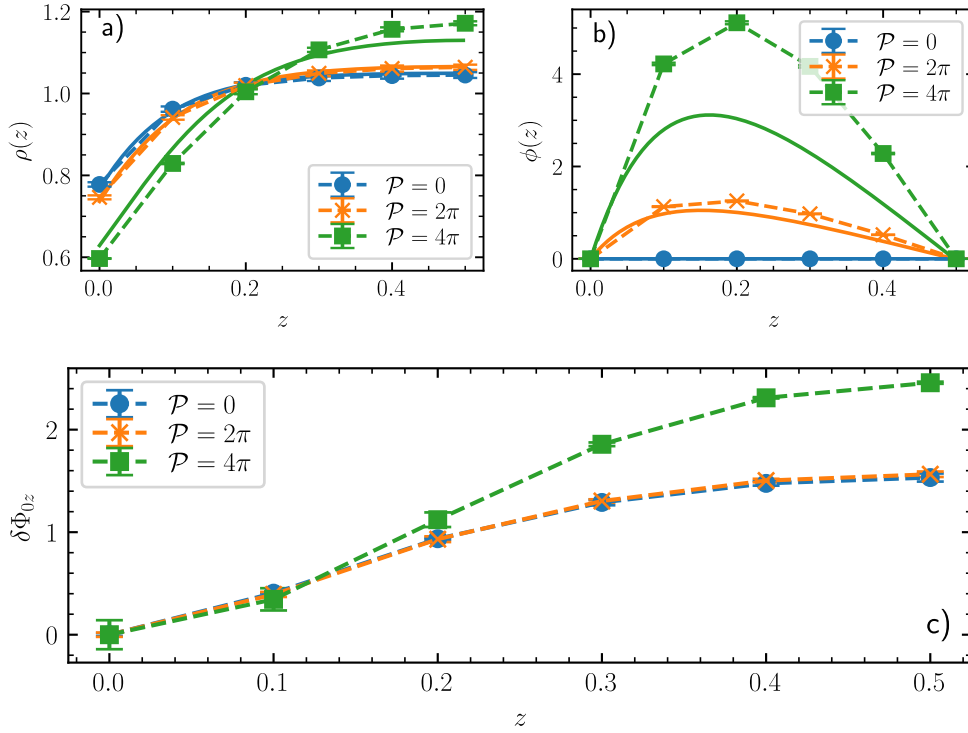


Figure 4.2.: **Mean-field validation: Density, phase and phase fluctuations.**

Density [a)], phase [b)] and phase fluctuations [c)] for $N = 19$, $M = m = 1$, $\gamma = 0.2$, $c/g = 1$ and different total momenta \mathcal{P} (given in the legend). Solid lines show the results from the MFA; the symbols demonstrate the IM-SRG results. Dashed lines between these symbols are added to guide the eye. Figure taken from Ref. [63].

repeated until both, phase and density, remain unchanged upon an additional iteration. Next, we increment \mathcal{P} slightly and repeat the iterative calculation. This continues until the desired value of \mathcal{P} is achieved or the flow equations diverge. While other choices for the reference state, such as the mean-field solution, are possible, we found that this procedure allows us to compute system properties over a wider range of \mathcal{P} .

4.3.3. Validity of mean-field approximation

To test the validity of the MFA, we calculate the density

$$\rho(z) = \sum_{i,j} \phi_i(z) \phi_j(z) a_i^\dagger a_j \quad (4.18)$$

and the phase

$$\theta(z) = \text{Im} \left[\log \left(\sum_{i,j} \phi_i^*(0) \phi_j(z) a_i^\dagger a_j \right) \right] \quad (4.19)$$

for $\mathcal{P} = 0, 2\pi, 4\pi$ with MFA and the flow equation method, see Fig. 4.2. For $\mathcal{P} = 0$ and $\mathcal{P} = 2\pi$, we find good agreement between the two methods. However, for the largest considered effective total momentum, $\mathcal{P} = 4\pi$, noticeable differences are seen. In particular, the phase predicted from the MFA appears to be too small.

Additionally, we estimate directly the off-diagonal long-range order by calculating phase fluctuations, see Sec. 4.3.1, Eq. (2.48). The results are also shown in Fig. 4.2. In agreement with the results for density and phase, for $\mathcal{P} = 0$ and $\mathcal{P} = 2\pi$ phase fluctuations are nearly identical and small while for $\mathcal{P} = 4\pi$ there is a considerable increase. We conclude that care must be taken when systems with $\mathcal{P} > 2\pi$ are studied. In the remainder of this chapter, we show IM-SRG results for certain values of \mathcal{P} to further justify the use of the MFA. In the outlook, Sec. 4.5.2 we discuss excitations of the Bose gas due to the flux/momentum which is directly connected to the limitations of the MFA.

4.4. Results and discussion

4.4.1. Energy spectrum

In Fig. 4.3, we present a sketch of the ground state energy as a function of the flux Φ for different quantized momenta P , which shows that the energy is periodic in Φ . The Schrödinger equation in the co-moving frame, Eq.(4.3), offers a simple explanation for why different momenta correspond to different periods of Φ : P and Φ always appear as the sum $\mathcal{P} = P + \Phi$. Additionally, the energy spectrum is symmetric under the transformation $\Phi \rightarrow -\Phi$ due to time-reversal symmetry. In what follows we calculate the lowest-energy states for fixed values of P , so-called Yrast states (cf. [137]), and currents for $0 \leq \Phi \leq \pi$. These values of the flux determine the experimentally relevant parameters.

We show the energy spectrum for the first and second Yrast state in Fig. 4.4. In agreement with our discussion on the validity of the MFA, we find good agreement also

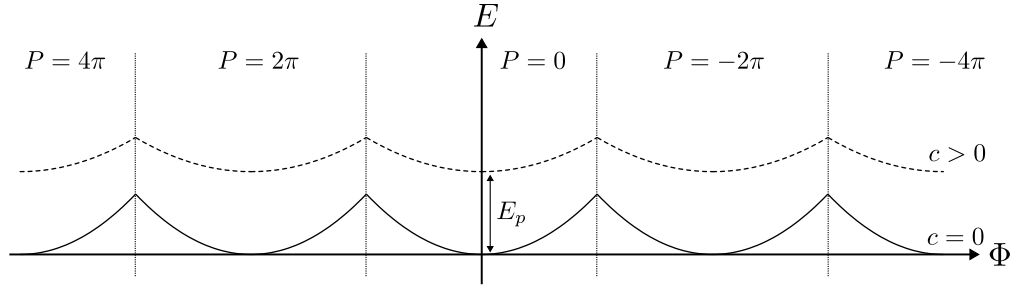


Figure 4.3.: **Sketch of the ground state energy.**

Schematic depiction of the ground-state energy as a function of the flux with ($c > 0$) and without ($c = 0$) impurity-boson interaction. The interaction leads to an energy shift E_p at $\Phi = 0$ and a different curvature for finite values of Φ . The quantized momentum of the system is P/L . The shift of the energy spectrum, E_p , and the change of the curvature can be parameterized by effective one-body parameters, see text for details. Figure modified from Ref. [63].

for the energy for⁴ $|\mathcal{P}| \leq 2\pi$. Furthermore, we see that for $\Phi = \pm\pi$ there is a level crossing between the two Yrast states with $P = 0$ and $|P| = 2\pi$. This is a consequence of the rotational symmetry of the problem in the co-moving frame, see Eq. (4.3). We can destroy this rotational symmetry by introducing a defect into the system which will result in an avoided level crossing. We discuss this below in Subsec. 4.4.4.

We also show the ground-state energy of a non-interacting impurity ($c = 0$) which is simply given by $E(P, \Phi) - E(P = 0, \Phi = 0) = (P + \Phi)^2/2$. We see that the impurity-boson interaction leads to a smaller curvature of the energy, i.e., the solid curves representing the energy of the interacting impurity are always below the dotted line corresponding to the non-interacting one. This is also depicted in Fig. 4.3, however, in this sketch, the self-energy of the impurity, E_p is not yet subtracted. The stronger the impurity-boson interaction, the more pronounced this effect (compare the left and right panels of Fig. 4.4). This feature can be easily understood using the concept of a polaron and its effective mass which we will discuss in the next subsection.

⁴We will discuss the reason for worse agreement of the MFA for high values of P in the outlook, see Sec. 4.5.2.

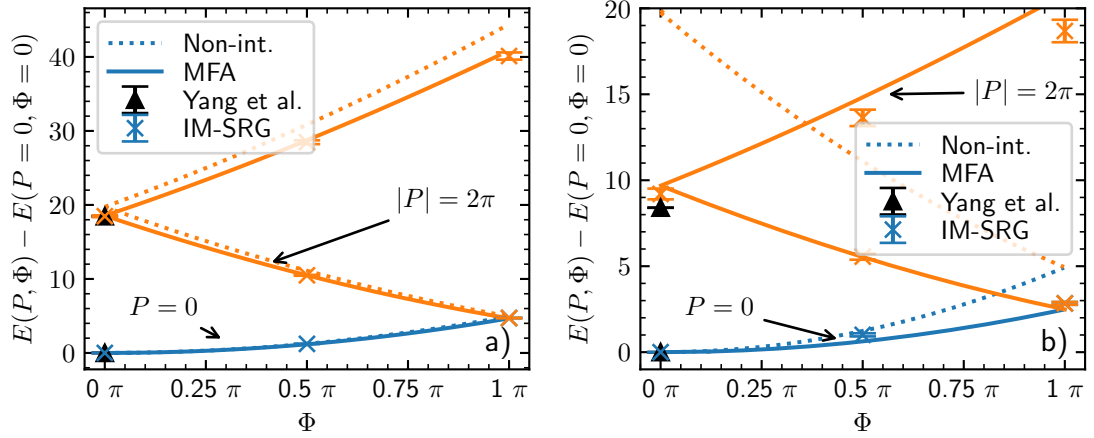


Figure 4.4.: **The energy spectrum as a function of the AB flux, Φ .**

Different colors correspond to different values of the momentum: Blue $P = 0$ and orange $|P| = 2\pi$. The parameters of the system are $N = 19$, $\gamma = 0.2$, and $c/g = 1$ [a)], $c/g = 5$ [b)]. The data are obtained using the MFA (solid curves) and the IM-SRG (crosses with error bars), black triangles show results from Yang et al. [171] for $\Phi = 0$. The dotted curves show the energy of the non-interacting system. Figure modified from Ref. [63].

4.4.2. Effective mass

Let us start by introducing the concept of the effective mass in the thermodynamic limit for an impurity embedded into a sea of particles⁵: The low-energy spectrum of the system shows a quadratic increase with the effective total momentum (see, e.g., [94, 96] for a discussion of one-dimensional Bose polarons)

$$\lim_{P \rightarrow 0} [E(P, \Phi = 0) - E(P = 0, \Phi = 0)] = \frac{P^2}{2m_{\text{eff}}^{\text{TD}}}, \quad (4.20)$$

with $m_{\text{eff}}^{\text{TD}}$ the effective mass in the thermodynamic limit⁶. This equation is one of the core concepts of the polaron approximation and of effective one-body descriptions of mobile impurities. However, this definition is not useful for finite-size systems because P is discrete.

⁵We consider the case of $\Phi = 0$ for this introduction.

⁶For different definitions of the effective mass see App. B.3.

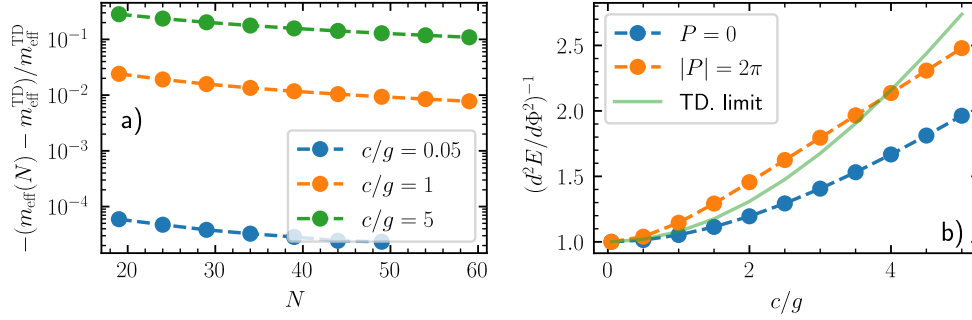


Figure 4.5.: **Effective mass for a finite-size system.**

a): Convergence of the effective mass to its thermodynamic limit for $\gamma = 0.2$ and different values of c/g . b): Inverse of $\frac{d^2 E}{d\Phi^2}$ for $\Phi \rightarrow 0$ with $P = 0$ and $|P| = 2\pi$. The parameters of the system are $N = 19, \gamma = 0.2$. The green curve shows the known result for $P \rightarrow 0$ in the thermodynamic limit (TD. limit) [94, 96]. The data in both panels are obtained using the MFA. Figure taken from Ref. [63].

To introduce a definition of the effective mass in a finite system, we employ the connection between the flux Φ and the quantized total momentum P via $\mathcal{P} = P + \Phi$. Φ is an external parameter, which means that it is continuous. Time-reversal symmetry suggests that $E(\Phi, P = 0)$ is proportional to Φ^2 for small values of Φ . The mean-field calculation also shows this behavior. Therefore, we define – in analogy to the Bose-polaron problem in the thermodynamic limit – the effective mass of an impurity in a small AB ring by

$$\lim_{P, \Phi \rightarrow 0} [E(P = 0, \Phi) - E(P = 0, \Phi = 0)] = \frac{\Phi^2}{2m_{\text{eff}}}. \quad (4.21)$$

This expression links our system to the established polaron problems, enabling predictions about an impurity's behavior in the AB ring. For example, it easily explains why the curvature of the energy spectrum decreases with increasing impurity-boson interaction: The effective mass increases with c . This also means that we reduce the current associated with the impurity when c is increased, as discussed below.

Because we are now able to define an effective mass in a few-to-many setting, we can use the AB ring as a physical testbed for studying the few-to-many-body crossover of one-dimensional Bose-polaron problems. We illustrate this crossover for the effective mass in Fig. 4.5. We see that for weak impurity-boson interactions ($c/g = 0.05$) the effective mass converges quickly to the thermodynamic limit. However, for strong interactions

($c/g = 5$) the convergence is slow, i.e. many bosons are needed to screen the impurity for large values of c/g . In App. B.4 we compare the convergence of the effective mass with the self-energy of the impurity. This analysis indicates that the effective mass converges to the thermodynamic limit more slowly than the self-energy. In particular, the convergence rate of the effective mass strongly depends on the impurity-boson interaction – opposite to the self-energy, which appears to converge nearly independently of the interaction.

For both one-body parameters, the underlying process for the convergence is the same: The high compressibility of a weakly-interacting Bose gas requires a large number of bosons to screen a strongly interacting impurity. The number of bosons required for effective screening depends significantly on the parameter γ . This can be seen most clearly for $\gamma \rightarrow \infty$: In this case, the bosons behave like non-interacting spin-polarized fermions and only a handful of particles are needed to screen the impurity, cf. [12, 179, 180]. Hence, the crossover from few-to-many-body should be analyzed separately for fermions and weakly-interacting bosons.

Finally, we note that the polaron approximation with an effective mass computed with Eq. (4.21), describes only the Yrast curve with $P = 0$ well. We show this in Fig. 4.5 by plotting the second derivative of the energy in the limit $\Phi \rightarrow 0$ for $P = 0$ and $|P| = 2\pi$ using the mean-field results. If we consider a non-interacting impurity, this derivative is given by $1/m$ for all values of P . This is not the case for an interacting one: Instead, for $P = 0$ the result is the effective mass in the finite-sized setting $1/m_{\text{eff}}$. Figs. 4.4, 4.5 show that the effective mass increases for stronger impurity-boson repulsion in agreement with our expectations. Furthermore, we can also see that for the $|P| = 2\pi$ state additional effects come into play and change the second derivative. The underlying physics will become more clear below when we discuss currents. The difference between “effective masses” defined for $P = 0$ and $|P| = 2\pi$ showcases limitations of the use of the quasiparticle picture for a small AB ring. Nonetheless, the polaron model describes the qualitative aspects of the spectrum even for $P \neq 0$.

4.4.3. Currents

The AB flux induces impurity and bosonic currents. We define them via the continuity equations for the impurity and bosons in the laboratory frame:

$$\frac{\partial \rho_I}{\partial t} = -\frac{\partial j_I}{\partial y}; \quad \frac{\partial \rho_B}{\partial t} = -\frac{\partial j_B}{\partial x}, \quad (4.22)$$

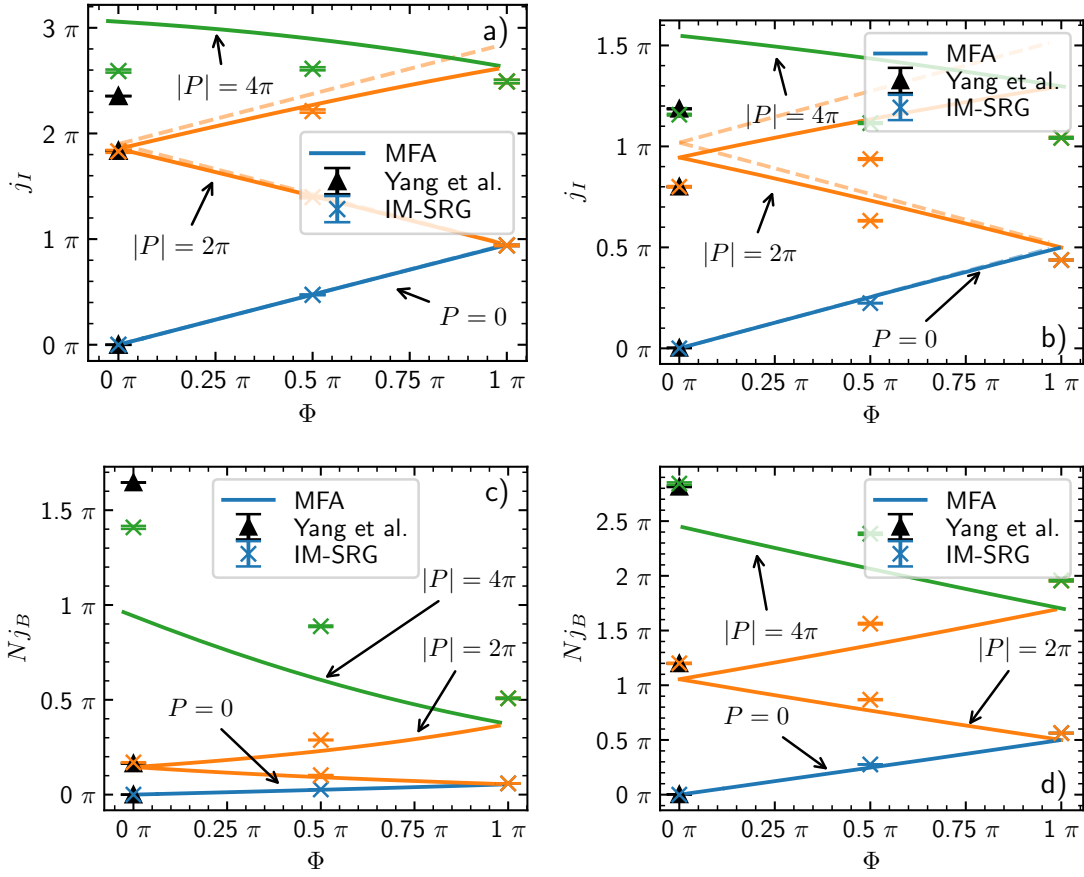


Figure 4.6.: **Currents in the system.**

Panels a) and b) present the impurity current while c) and d) show the bosonic one. Blue, orange, and green colors are for $P = 0$, $|P| = 2\pi$, and $|P| = 4\pi$, correspondingly. The parameters of the system are $N = 19$ and $\gamma = 0.2$. Panels a) and c) show results for $c/g = 1$, whereas b) and d) are for $c/g = 5$. The data were obtained with the MFA (solid lines) and the IM-SRG (crosses). Black triangles are the results of Yang et al. [171] for $\Phi = 0$. Dashed lines in a) and c) show the impurity current in the polaron approximation $j_I = \mathcal{P}/m_{\text{eff}}$. Here, m_{eff} is calculated within the MFA using Eq. (4.21). Figure modified from Ref. [63].

where tL^2 is the time and ρ_I (ρ_B) is the probability density of the impurity (bosonic) cloud. The (local) probability currents are given as

$$j_I = -\frac{i}{2} \int dx_1 \dots dx_N \left(\Psi^* \frac{\partial \Psi}{\partial y} - \Psi \frac{\partial \Psi^*}{\partial y} \right) + \Phi \rho_I, \quad (4.23)$$

$$j_B = -\frac{i}{2} \int dy dx_2 \dots dx_N \left(\Psi^* \frac{\partial \Psi}{\partial x_1} - \Psi \frac{\partial \Psi^*}{\partial x_1} \right). \quad (4.24)$$

Due to rotational symmetry, j_I , j_B , ρ_I and ρ_B are position-independent. This allows us to work with the more convenient integral quantities, e.g., $\rho_I = \int \rho_I dy / (2\pi)$. Using these quantities, it is straightforward to show that $j_I + N j_B = \mathcal{P}$. Hence, the current of the total density, $\rho_I + N \rho_B$, (also called the total current) is given by $\mathcal{P} = P + \Phi$. It is important to note that although the AB flux is coupled only to the impurity, boson-impurity interactions also generate a bosonic current. We show results for the currents for $c/g = 1$ and $c/g = 5$ in Fig. 4.6 (with other parameters being $N = 19$, $\gamma = 0.2$). We can see that a stronger impurity-boson interaction leads to increased bosonic currents.

This observation can be easily explained with the Bose-polaron picture. We can relate the impurity current and the energy using the Hellmann–Feynman theorem

$$j_I = \frac{\partial E}{\partial \Phi}. \quad (4.25)$$

This is also the standard definition of the current in a one-body problem, see Ref. [137]⁷. Combining this with the polaron picture for $P = 0$ leads to $j_I = \Phi / m_{\text{eff}}$ which connects the current (and transport properties) of the impurity to the effective mass of the polaron. Due to the conservation of the total current, the bosonic current in the same approximation is $N j_B = (1 - 1/m_{\text{eff}})\Phi$. The bosonic current generated by the AB flux follows the impurity, resulting in the renormalization of the impurity’s mass. This simple calculation shows that in the polaron picture, the currents depend linearly on Φ , with the slope fully determined by the properties of the polaron: its effective mass.

The range of validity of the polaron approximation is determined by \mathcal{P} and the impurity-boson interaction strength. To showcase this, we display in Fig. 4.6 the linear behavior of the impurity current by dashed lines. For the weaker impurity-boson interaction, $c/g = 1$, we can see that the polaron approximation is accurate for $|\mathcal{P}| \lesssim 2\pi$. However, for stronger interactions, $c/g = 5$, we start to see deviations from the linear increase already for $|\mathcal{P}| \lesssim \pi$. In the limit of $c \rightarrow \infty$, the polaron approximation is only accurate for $\mathcal{P} \rightarrow 0$. Our interpretation is that coherent propagation of the impurity becomes infeasible

⁷Note that this expression provides an indirect way for measuring currents by studying the energy landscape of the problem with RF spectroscopy (cf. Scazza et al. [181]).

for strong boson-impurity interactions and finite fluxes. As $c \rightarrow \infty$, an impurity can coherently exchange positions with a boson only on timescales of $1/c$. Therefore, strong (fast) impurity currents excite bosons, leading to a nonlinear increase in the currents with Φ , see also Ref. [171]. In the outlook of this chapter, Sec. 4.5.2, we shortly discuss excitations of the Bose-gas⁸. One can quantify these non-linear effects, by considering the above-discussed second derivative of the energy, see Fig. 4.5⁹. As discussed before (see also Figs. 4.5), for $|P|=2\pi$ the second derivative is larger than expected from the polaron approximation and this difference increases with stronger impurity-boson interaction.

Fig. 4.6 also shows another interesting feature: For $|P|=4\pi$, the current of the impurity seems to remain nearly constant as a function of Φ . We call this current critical because increasing the value of the flux only generates a stronger current in the bosons. We can see that the value of this critical current, j_I^{cr} , decreases when increasing c . This is in agreement with previous mean-field studies [95, 182]. However, we can see that the MFA predicts a critical current which is larger than the flow equation results.

This current can be compared to the critical velocity observed when an object moves through a superfluid (cf. Landau critical velocity). Interestingly, the MFA predicts unphysical values of the critical velocity, larger than the speed of sound, for weak interactions (small c/g) [95]. Unfortunately, we are not able to determine the critical velocity using the flow equation approach, as this method becomes unstable for high values of \mathcal{P} . In the outlook of this chapter, Sec. 4.5.2, we discuss possible future research perspectives about the critical velocity in one dimension in more detail.

4.4.4. Role of defects

The system's rotational symmetry results in a double degeneracy in the Yrast energy spectrum, as shown in Fig. 4.4 at $\Phi = \pm\pi$. However, in a realistic setup, this symmetry is broken due to defects, causing avoided crossings in the energy spectrum as illustrated in Fig. 4.7. The avoided crossings lead to vanishing one-body currents in the system, impacting transport properties of the system [136].

Note that one of the simplest experimental realizations of an AB flux in cold-atom systems is implementing a rotating weak link [183]. This utilizes the equivalence between the Coriolis force in a non-inertial frame and the Lorentz force acting on a charged particle in a uniform magnetic field. The introduction of a rotating link serves as a “defect” potential in the system. Its effects are explored in this subsection.

⁸These excitations are also the reason for the breakdown of the MFA for large values of the effective total momentum, see below.

⁹Note that one can arrive at the same conclusions by considering the bosonic current as it is related to the impurity current via $Nj_B = P + \Phi - j_I$.

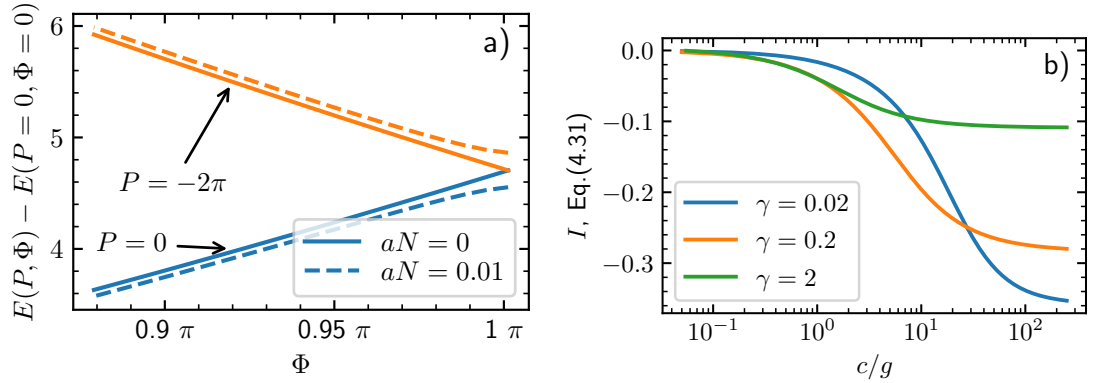


Figure 4.7.: **Effect of a defect on the energy crossing.**

Panel a) shows the energy for $P = 0$ and $P = -2\pi$ as a function of the flux with and without a defect. The solid lines show results for the unperturbed system while the dashed lines correspond to a perturbation strength of $aN = 0.01$. The other parameters of the system are $N = 19$, $\gamma = 0.2$ and $c/g = 1$. Panel b) depicts the result of Eq. (4.28) in the thermodynamic limit as a function of the impurity-boson interaction strength c/g for different boson-boson interactions γ . All data are obtained with the MFA. Figure taken from Ref. [63].

Let us consider a small perturbation to the Hamiltonian:

$$\mathcal{H}_W = \mathcal{H} + W, \quad (4.26)$$

where \mathcal{H} is the original Hamiltonian from Eq. (4.1) and

$$W = \frac{a}{L} \sum_i \delta(x_i). \quad (4.27)$$

This additional term describes a short-range potential coupled exclusively to the Bose gas. The current of the impurity is sensitive to W only via the impurity-boson interaction, and therefore the avoided crossing should contain information about the impurity-boson correlation function. This approach is similar to the concept of impurities acting as probes for their environment (see Chap. 1): introducing an impurity (or defect) modifies the system's properties, allowing insights into the medium. For example, in Ref. [12], the self-energy of the impurity was measured to determine how many fermions are needed

to build a Fermi sea around an impurity. Here, the size of the avoided energy crossing depends on the impurity-boson interaction. Therefore, measuring this crossing reveals information about interactions within the system.

If the perturbation is small, $a \rightarrow 0$, we can consider the defect to have a negligible impact on our system, except near the degeneracy points at $\Phi = \pm\pi$. In the vicinity of these points, we use degenerate state perturbation theory to calculate the energy:

$$\mathcal{H}_W \simeq \begin{pmatrix} E_0 + L^2 \langle \Psi_0 | W | \Psi_0 \rangle & L^2 \langle \Psi_0 | W | \Psi_1 \rangle \\ L^2 \langle \Psi_1 | W | \Psi_0 \rangle & E_1 + L^2 \langle \Psi_1 | W | \Psi_1 \rangle \end{pmatrix},$$

where $E_0 \simeq \Phi^2/(2m_{\text{eff}})$ ($E_1 \simeq \Phi^2/(2m_{\text{eff}})$) is the energy of the Yrast state with $P = 0$ ($|P| = 2\pi$); Ψ_0 (Ψ_1) is the corresponding eigenstate. We can use the MFA to get an expression for these matrix elements

$$\langle \Psi_i | W | \Psi_j \rangle = \frac{a}{L} N \alpha^{N-1} \int e^{i(P_j - P_i)y} f_i^*(y) f_j(y) dy,$$

where $\alpha = \int f_i^*(z) f_j(z) dz$, and subscripts determine the Yrast state, e.g., $i = 0$ corresponds to $P = 0$.

We are mostly interested in the influence of the perturbation on the avoided crossing. For $\Phi = \pm\pi$, $f_1 = f_0$ and the matrix element $\langle \Psi_i | W | \Psi_j \rangle$ is solely determined by the density in the co-moving frame¹⁰. Because the density is sensitive to the impurity-boson interaction, the splitting of the energy levels is dependent on the value of c . For example, if we consider a non-interacting impurity, $c = 0$, the defect destroys only the rotational invariance of the Bose gas. In this case, $|f|^2$ is constant and $\langle \Psi_i | W | \Psi_j \rangle = 0$, i.e. there is no avoided energy level crossing.

We show in panel a) of Fig. 4.7 the energy difference $E(P, \Phi) - E(P = 0, \Phi = 0)$ for a small value of a . The key observation is, that in the presence of W the energies of the first and second Yrast state no longer cross.

The difference between the energies, $\Delta E = 2aLNI$, is determined by the integral

$$I = \int e^{i2\pi y} |f_0(y)|^2 dy. \quad (4.28)$$

We estimate it by using the density in the thermodynamic limit at $\Phi = 0$ [72]:

$$|f_0(y)|^2 \simeq \frac{L\mu}{g(N-1)} \tanh^2 \left(\sqrt{\mu\kappa} L \delta \left[\frac{(z - L/2)}{\delta L} + \frac{1}{2} \right] \right),$$

¹⁰Or equivalently by the impurity-boson correlation function in the laboratory frame.

where

$$\delta \simeq 1 + \frac{2d}{\sqrt{\gamma\kappa N}}, \quad d = \frac{1}{2} \operatorname{asinh} \left(\frac{2\rho}{c} \sqrt{\frac{\gamma}{\kappa}} \right), \quad (4.29)$$

$$\mu \simeq \gamma\rho^2 \frac{N-1}{N} \left(1 - 2 \frac{\tanh(d) - 1}{\sqrt{\gamma\kappa N}} \right). \quad (4.30)$$

In panel b) of Fig. 4.7 we show the energy splitting for increasing values of c . Because we have zero-range interactions, the value of I converges to a constant value for $c \rightarrow \infty$. This constant value is determined from the boson-boson interaction strength, γ . It is noteworthy that for small values of γ , the impurity can substantially modify the density of the bosons, resulting in increased values of I .

Finally, we mention an interference effect that appears if we place a second small perturbation into the system:

$$W = \frac{a}{L} \sum_i (\delta(x_i) + \delta(x_i + d)). \quad (4.31)$$

Analog to our previous calculation, we define

$$I = \left(1 + e^{i2\pi d} \right) \int e^{i2\pi y} |f_0(y)|^2 dy. \quad (4.32)$$

For $d = 1/2$, this matrix element becomes zero, leading to a crossing of the energy levels again (within the lowest order of perturbation theory). We can understand this from the effective restoration of the rotational symmetry when the two perturbations are placed opposite to each other¹¹.

4.5. Conclusions

4.5.1. Summary

Let us summarize this chapter: We investigated an impurity coupled to the AB flux in a bosonic medium, starting by connecting the AB flux to the system's quantized total momentum via a transformation to the frame co-moving with the impurity. This enabled us to simplify the description of the system (with a finite number of particles) using many-body techniques developed for the Bose polaron. We argued that our setup serves

¹¹This phenomenon also occurs with more than two perturbations, as long as they are symmetrically positioned on the ring, e.g. three defects arranged in an equilateral triangle.

as a testbed for studying the crossover from few-to-many-body behavior in cold-atom polaron problems. For example, observing persistent currents in the AB ring with an impurity could reveal valuable insights into the coherence properties of the Bose polaron.

To study the system, we applied the MFA and the flow equation approach. In particular, we used the latter to check the validity of the MFA. We calculated the energy spectrum and currents. The connection of our system with the Bose polaron allowed for an intuitive and simple interpretation of our results. Furthermore, we defined the effective mass of the polaron for a finite number of bosons in an experimentally feasible way which – to the best of our knowledge – was not proposed before. We explored its convergence towards the thermodynamic limit and found that a large number of bosons ($N > 50$) is required for this convergence even for moderate impurity-boson interaction strength. Comparing with the self-energy of the impurity, we found that the effective mass approaches the thermodynamic limit more slowly. Furthermore, the convergence rate of the self-energy is independent on the impurity-boson interaction strength while the effective mass exhibits a strong dependence. We also tested the validity of the polaron approximation, observing that it holds for smaller values of the AB flux as the impurity-boson interaction increases. In the limit of $c \rightarrow \infty$, the approximation only holds as $\mathcal{P} \rightarrow 0$. Nevertheless, even for impurity-boson interactions five times larger than the boson-boson interaction, the polaron approximation remains valid up to $\Phi \approx \pi$. Lastly, we examined the role of defects in the system and showed that they lead to avoided energy level crossings between different Yrast states. We argued that the size of this level splitting is sensitive to the interactions of the system.

4.5.2. Outlook

As already discussed in the main text, for “large” values of \mathcal{P} the AB ring features a critical current j_I^{cr} which no longer depends on Φ . As we can relate the energy of the system to the bosonic current via the Hellmann-Feynman theorem $E = E^{cr} + j_I^{cr} \Phi$, this can be interpreted in terms of few-body precursor of collective excitations in a Bose gas. In other words, the AB ring provides a platform for studying a few-body analogue of the critical velocity in a Bose-polaron problem.

The value of the critical velocity in a one-dimensional Bose gas is unknown, and further studies are needed to clarify the mechanisms that determine it. Understanding those is essential for current research on non-equilibrium dynamics, addressing questions such as: “How does the impurity behave when it is injected into the Bose gas?” or “What happens to the one-dimensional polaron if the impurity acquires a velocity larger than the critical velocity?”, see for example Refs. [95, 98, 182, 184–187]. Future bottom-up studies offer an exciting opportunity to identify the effects that set the critical velocity. In

the following subsection, we explore some of the challenges associated with the critical velocity in one-dimensional Bose gases.

Critical velocity of an impurity in a one-dimensional Bose gas

In Ref. [182] the critical velocity with which a Bose gas can flow around an object was defined using the MFA. This setup is similar to the one discussed in this chapter, an impurity embedded into a sea of bosons. Therefore, naively one can apply the same definition for the critical velocity as in Ref. [182]. As explained in Sec. 4.3.1, there exist three different solutions to the Gross-Pitaevskii equation. One solution is unphysical because it contains an imaginary part; another solution corresponds to the polaron solution of Ref. [72] for $\mathcal{P} \rightarrow 0$ (this is the one we used in the main part of the work) and the third one corresponds to a soliton, see Ref. [95]. The critical velocity was defined in Ref. [182] as the value of $v_{\text{imp}}^{\text{crit.}} = P_{\text{imp}}^{\text{crit.}}/m$ for which the three solutions are equal.

However, this definition faces a problem for our system: For weak impurity-boson interactions, it predicts a critical velocity larger than the speed of sound, $v_s = \sqrt{gN/LM}$, see Ref. [95]. We illustrate this in Fig. 4.8 where we show the impurity velocity as a function of \mathcal{P} for different impurity-boson interactions. We can clearly see that the MFA overestimates the critical velocity and, in particular for very weak impurity-boson interaction [see panel a)], predicts a velocity larger than the speed of sound, which is unphysical. Therefore, further studies using *ab initio* methods are important to a) calculate the critical velocity and b) to understand the beyond-mean-field effects that determine it. Unfortunately, the IM-SRG method is not able to predict the correct value of the critical current for weak impurity-boson interactions and/or large particle numbers: It starts to diverge for too large values of \mathcal{P} . While the method used in Ref. [171] allows for larger values of P , in this work the authors did not consider the AB flux and therefore there exist results only for discrete values of \mathcal{P} . This does not allow for a precise determination of the critical velocity. In future studies, one should check if the system studied in this chapter can be investigated using the method of Ref. [171].

One can understand why the MFA predicts wrong results for the critical velocity by considering the case of vanishing impurity-boson interaction, $c \rightarrow 0$. In this case, we approximate the system to be the well-known Lieb-Liniger gas which is exactly solvable [32, 33]. For the Lieb-Liniger gas, we include bosonic currents via two types of excitations: type-I and type-II excitations. While the former corresponds to phononic excitations, the latter has been shown to be connected with highly correlated states [188]. Interestingly, in one-dimensional systems, the latter excitation is energetically more favorable [33].

We show a plot of the energy for $c \rightarrow 0$ as a function of \mathcal{P} in Fig. 4.8, panel d). We consider two cases: The solid blue line is the energy of the system when all bosons are in

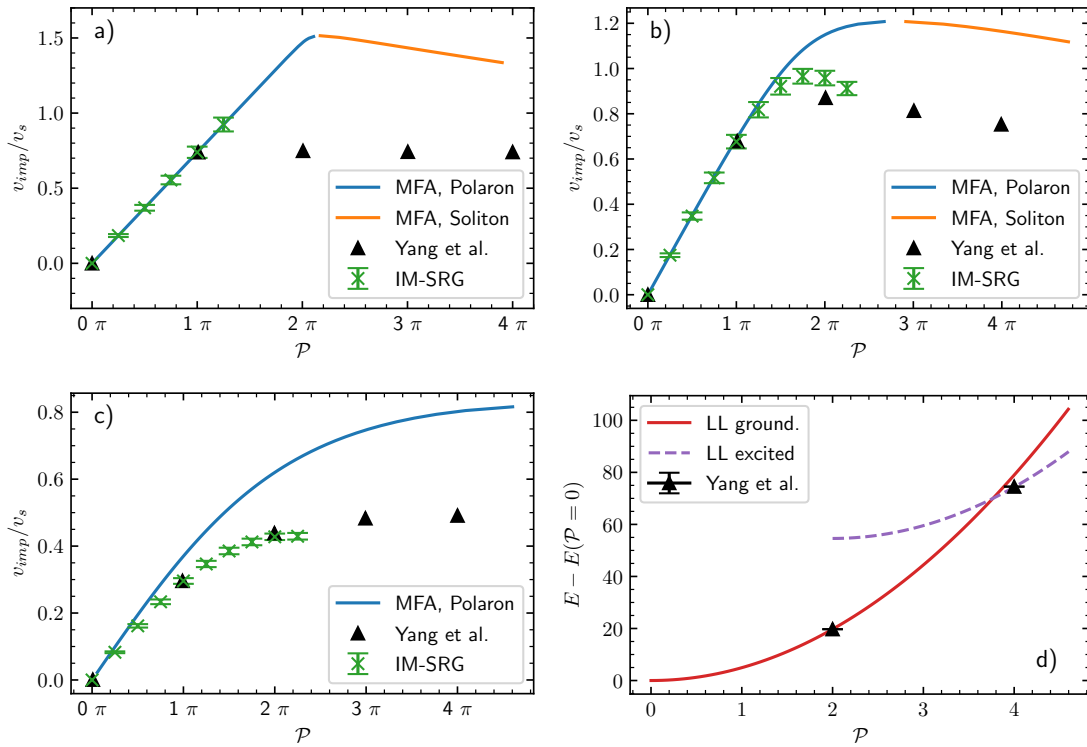


Figure 4.8.: **Impurity velocity for different impurity-boson interaction strengths and energy for a non-interacting impurity ($c \rightarrow 0$).**

Panels a), b), c) show the impurity velocity as a function of P calculated with IM-SRG (crosses) and mean-field (solid lines). Additionally shown are results from Ref. [171] (triangles). Panels a) and b) show polaron and the soliton mean-field solutions while for panel c) only the polaron solution was obtained. Different panels correspond to different impurity-boson interaction strengths: Panel a) $c/g = 0.05$, b) $c/g = 1$, c) $c/g = 5$.

Panel d) depicts the energy for $c \rightarrow 0$, i.e., when the Bose gas can be described by the Lieb-Liniger model. The energy is shown for the Bose-gas ground or first excited state (see text for details). The parameters of the system are $N = 19$ and $\gamma = 0.2$. The triangles show the results from Ref. [171]. Panel d) modified from Ref. [63].

the ground state and the impurity carries the effective total momentum:

$$E(\mathcal{P}) - E(\mathcal{P} = 0) = \frac{\mathcal{P}^2}{2}. \quad (4.33)$$

The dashed orange line corresponds to the case where the Bose gas carries a momentum of $|P|= 2\pi$, i.e. it is in an excited state, while the remaining momentum is distributed to the impurity¹²:

$$E(\mathcal{P}) - E(\mathcal{P} = 0) = E_{\text{bosons}} + \frac{(\mathcal{P} - 2\pi/L)^2}{2}. \quad (4.34)$$

Additionally, we also show the results from Ref. [171] for $\mathcal{P} = 2\pi, 4\pi$ to determine which case corresponds to the ground state of the system.

For small values of \mathcal{P} it is energetically more favorable to include all \mathcal{P} in the impurity. However, for $\mathcal{P} < 4\pi$ there is a crossing of the curves and it is favorable to have the Bose gas excited. Note that because the type-II excitation is energetically more favorable, this state is highly correlated and therefore out of reach for the MFA. The flow equation approach shares the same problem as it uses a condensate as a reference state, i.e. if a condensate is not a good approximation the flow equations diverge, see Sec. 2.3. We see this for example for $c/g = 0.05$ close to the point where it is energetically more favorable to excite the Bose-gas [e.g., $\mathcal{P} \simeq 3.8\pi$ in Fig. 4.8, panel d)]. Interestingly, for stronger interactions, the flow equation method converges for larger values of \mathcal{P} , e.g. for $c/g = 5$ it is in good agreement with Ref. [171] even for $\mathcal{P} = 4\pi$. This suggests that impurity interactions modify bosonic excitations, so that a condensate approximation, the reference state of the IM-SRG method, has a larger overlap with the true ground state of the system. Since these excitations ultimately determine the critical velocity in one-dimensional Bose gases, this raises the question of how impurity interactions alter bosonic excitations and, consequently, which physical phenomena determine the critical velocity of the one-dimensional Bose gas. We leave these questions to future studies.

¹²We retrieve E_{bosons} from Ref. [171]

5. Artificial atoms from cold bosons in one dimension

This chapter “explores basic physics of few-body systems to facilitate new many-body research”, one of the goals introduced in Chap. 1. As discussed earlier, in Chaps. 1, Chap. 4, studying systems with impurities can provide important information on the few-to-many-body crossover. In the previous chapter, we discussed a repulsively interacting impurity in a weakly repulsive one-dimensional Bose gas; now we extend our investigation to an attractive impurity.

Due to the attraction, bosons can be bound to the impurity. This complicates many-body studies of such systems, as we show in the outlook of this chapter, Subsec. 5.7.2. Therefore, our focus is on characterizing the bound state of the impurity and the bosons to pave the way for future few-to-many studies with attractive impurities.

First, we analyze our setup using the mean-field approximation in a finite ring. We find two different solutions, which correspond in the low-density limit, i.e. an infinite line, to the asymptotic cases:

1. All bosons are bound to the impurity.
2. All bosons occupy scattering states.

We derive the critical condition under which either the first or the second case occurs. In the low-density limit, we demonstrate that this condition sets the maximum number of bosons that bind to the impurity, forming a so-called ‘artificial atom’. Furthermore, we validate the mean-field approximation through comparison with beyond mean-field *ab initio* calculations. Despite beyond-mean-field effects destroying long-range order in the Bose gas, we find that the mean-field prediction for the maximum number of bound bosons still holds.

Our few-body findings are important for understanding artificial atoms in low-density Bose gases with both static and mobile impurities, as well as to advance few-to-many studies of polarons with attractive impurity-boson interactions. Furthermore, the existence of different states offers an exciting opportunity to explore the transition between them from a few-to-many perspective, see Subsec. 5.7.2.

Parts of this chapter have been published in this or similar form in our manuscript “Artificial atoms from cold bosons in one dimension” [62]. Note that the results presented in Sec. 5.4 were calculated in part by Timothy Backert [189]. The data shown in Fig. 5.7 were provided by Lila Chergui [190].

5.1. Introduction

If the probability of finding parts of a system infinitely far from each other vanishes, such a state is called “bound state”. Determining conditions under which bound states occur is one of the basic problems in quantum mechanics. While these issues often arise in few-body systems, their relevance extends to many-body physics as well. For example, a low-energy model of a dilute many-body system may include bound states as effective components. Moreover, the transition from an unbound to a bound state can offer insight into the precursors of quantum phase transitions (see Ref. [65]).

In only a few special cases are there results that provide conditions for binding. For example, in one (1D) and two (2D) spatial dimensions, any attractive potential supports a two-body bound state. However, in three dimensions (3D), only sufficiently “deep” potentials can lead to bound states [191, 192]. For systems with more than two particles, there are no general conditions for binding known, and (until now) there is no universal theoretical approach to determine such. Furthermore, most systems are not analytically solvable – except for a few cases, sometimes within certain approximation. Often, one has to employ numerical methods to solve the problem. In this chapter, we will discuss a system for which we can find an analytical mean-field solution: bound states formed by weakly repulsive bosons bound to an attractive short-range potential [170, 193–195]. Due to the similarity of such a system with an atom (the role of the attractive nucleus is played by the impurity potential while the repulsive nature of the electrons is captured by the repulsive interaction between the bosons), we refer to this system as ‘artificial atom from bosons’.

Artificial atoms have been primarily studied in either one or three spatial dimensions. In 3D, different studies utilizing different theoretical models show disagreement on the number of bosons that can be bound to an impurity [170, 193–195]. A similar puzzle arises in 1D. While studies based on the mean-field approximation (MFA) predict a finite number, which depends on the interactions in the system (see Refs. [169, 170]), phenomenological arguments of Ref. [194] claim that only a single boson can be bound. This argument suggests that a dilute Bose gas can always be mapped onto a system of non-interacting fermions. Due to the Pauli exclusion principle, this implies that only a single boson can be bound. These different results highlight the need for further investigation on the ‘artificial

atom’.

Since these problems involve an impurity embedded into a medium, they not only provide insight into conditions for binding, they further contribute to the understanding of the physics of Bose polarons (see, e.g., [140–142]), in particular onto the polaron-to-molecule transition region. As discussed in Chap. 1 and shown in Chap. 4, understanding such systems sheds light on the crossover from few-body to many-body physics. This chapter extends our analysis to attractively interacting impurities, laying foundations for future investigations into the few-to-many-body crossover. Here, we will focus on the 1D artificial bosonic atom.

To study the artificial atom, we derive a mean-field solution in a finite ring. This solution rigorously demonstrates that an impurity can support a many-boson bound state. Extending the solution to an infinite line reveals three distinct scenarios based on the number of bosons and interactions: i) *Many-body bound state*: Below a critical particle number, all bosons are bound to the impurity, leading to an exponentially decaying density, consistent with previous studies [169, 170]. ii) *Critical state*: At the critical particle number, all bosons remain bound, but the density decays as $1/x^2$. iii) *Scattering state*: Beyond the critical number, some bosons occupy scattering states, indicating a non-vanishing probability of finding bosons far from the impurity.

We validate these mean-field results using the flow equation method, also called in-medium similarity renormalization group method [IM-SRG] (see Sec. 2.3)¹. The *ab initio* calculations reveal phase coherence in the vicinity of the impurity, see Fig. 5.4. We conclude that the MFA works well when all bosons are bound to the impurity. However, as soon as bosons occupy the whole space, phase fluctuations increase. This indicates that the argument of Ref. [194] (that bosons fermionize in artificial atoms in 1D) occurs only for bosons in scattering states.

This chapter is structured as follows: In Section 5.2 we introduce the system under consideration and provide a short intuitive description of the relevant physics. After that, we present in Section 5.3 our mean-field solution which we expand to the zero-density limit in Sec. 5.4. Then, we benchmark our mean-field solution against the flow equation method in Sec. 5.5. We further extend our results to mobile impurities in Sec. 5.6. In Section 5.7 we summarize our results and provide an outlook in which we discuss how our results may be useful for future few-to-many-body studies. We provide additional information in App. C.

¹Furthermore, we also benchmark the flow equation method against the well-established multi-layer multi-configuration time-dependent Hartree method for atomic mixtures (ML-MCTDHX) [56] in App. C.1.

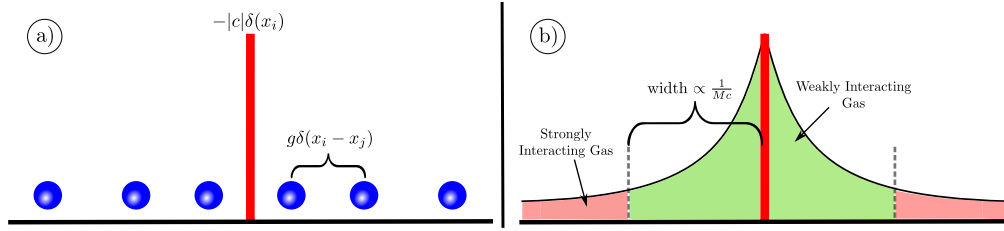


Figure 5.1.: **Illustration of the system and sketch of the Bose gas density in the zero-density limit.**

Panel a) illustrates our system. Similar to Fig. 4.1, blue balls show the N bosons. However, in this chapter we focus on an impurity potential and therefore we depict it here with the red line.

Panel b) depicts a sketch of the density of the Bose gas for a finite value of N , and large system size (i.e., zero-density limit) assuming that $g/|c| \ll 1$. In the vicinity of the impurity (at distances $\sim 1/(Mc)$) the impurity-boson attraction leads to a high Bose-gas density. This results in a weak effective boson-boson interaction because we have a 1D system. For larger distances from the impurity, the Bose-gas density becomes low, which strongly increases the effective boson-boson interaction, see text for details. Figure taken from Ref. [62].

5.2. Formulation

5.2.1. Hamiltonian

We study a similar system as in the previous chapter: N bosons with an impurity in one-dimension with periodic boundary condition, i.e. on a ring². A sketch of our system can be found in Fig. 5.1. In contrast to the previous chapter, now we focus on an attractive impurity instead of a repulsive one.

The standard Hamiltonian which describes such systems in cold-atom physics (see, e.g., [6, 113] and references therein) is similar to the one used in the previous chapter, Chap. 4,

$$H = -\frac{1}{2m} \frac{\partial^2}{\partial y^2} - \frac{1}{2M} \sum_{i=1}^N \frac{\partial^2}{\partial x_i^2} + c \sum_{i=1}^N \delta(x_i - y) + g \sum_{i,j} \delta(x_i - x_j), \quad (5.1)$$

²For completeness, we also present results for a box trap in C.1 and C.2. Such boundary conditions can also be realized in experiments [196, 197].

where we have used a system of units in which $\hbar = 1$. The position of the impurity (i th boson) is described by the coordinates $y(x_i)$, m parameterizes the mass of the impurity while M is the boson mass. Because s -wave scattering is dominant in the ultracold regime, we model the atom-atom interactions by delta-function potentials [91]. The parameter c determines the impurity-boson interaction strength while g describes the boson-boson interaction. Due to Feshbach resonances, these interactions can be tuned in an experiment via external fields to virtually any value [27]. We consider attractive impurity-boson interaction, $c < 0$, and repulsive boson-boson interaction, $g > 0$.

Our model is characterized by three parameters that define the length scales: $1/(Mg)$, $1/(M|c|)$ and L . One of these parameters can be used to define the system of units. In this chapter, we use $1/(M|c|)$ as the unit-defining length scale because it is the only relevant length scale for the impurity-boson bound state if $N = 1$ or $g = 0$ (see Eq. (5.2)). The corresponding two dimensionless parameters are the relative interaction strength $\alpha = c/g$ and the dimensionless length $LM|c|$. Note that it is sometimes useful to express the latter as $LM|c|/N$ or equivalently as $M|c|/\rho$, where $\rho = N/L$ is the density of the Bose gas without the impurity. This parameterization will be especially convenient when we consider the zero-density limit ($L \rightarrow \infty$ and N is finite) in Sec. 5.5.

In the main part of this chapter, we will focus on a heavy impurity $m/M \rightarrow \infty$. However, we will show in Sec. 5.6 that our results also apply to a mobile one. Without loss of generality, we fix the impurity position at $y = 0$. Note that a heavy impurity can be realized experimentally by using atom species with different masses, e.g., ${}^7\text{Li}$ (bosons) and ${}^{174}\text{Yb}$ (impurity) [198]. In this case, one can neglect the kinetic energy of the impurity. Alternative realizations of an impurity potential include a localized external field (light blade) to trap the impurity atom [140] or to directly produce a delta-function potential³ [199].

5.2.2. Physical picture

Before we analyze the Hamiltonian, we provide some intuition into the physics of the system, which is driven by the interplay between attractive impurity-boson and repulsive boson-boson interactions. For a non-interacting Bose-gas ($g = 0$) an arbitrary number of bosons can be bound to the impurity because the delta-function potential supports a single bound state (see, e.g., [124]). In the opposite limit, if the bosons are impenetrable ($1/g = 0$), they can be described by spin-polarized fermions (an effect called “fermion-

³Note that different experimental realizations might lead to different finite range effects whose investigation we leave to future studies.

ization”) [37], and only a single boson can be trapped by the impurity⁴. For a finite boson-boson repulsion, this implies that the interplay between the attraction from the impurity and the repulsion between the bosons should lead to a critical number of bosons, N_{cr} , that can be bound to the impurity.

We estimate this critical number in this chapter using the MFA (Sec. 4.3.1), see also Refs. [169, 170]) which we benchmark with the flow equation method below. However, let us provide some physical arguments as to why the MFA leads to an accurate estimate of the critical number N_{cr} (see Fig. 5.1 for an illustration of our arguments):

Consider the zero-density limit, i.e. $L \rightarrow \infty$ and N fixed and assume strong attractive interaction $g/|c| \ll 1$. To parameterize the effective boson-boson interaction strength, we use the natural parameterization $Mg/\rho(x)$, where $\rho(x)$ is the density of the Bose gas, see, e.g., Ref. [73]. Because the impurity is attracting the bosons, the Bose-gas density is largest in the vicinity of the impurity, and, hence the boson-boson repulsion is the weakest. Towards the edges, the density decays which results in stronger interaction. Note that this is a particularity of 1D systems: A lower density corresponds to stronger interactions (in 3D this relation is reversed: High densities correspond to strong interactions)⁵. For a non-interacting Bose-gas ($g = 0$), we can write the Bose-gas density as $\rho(x) = N|c|Me^{-2M|cx|}$ [124]. If we assume that this density approximately also describes the density for a weakly interacting Bose-gas $g/|c| \ll 1$, we can conclude that:

$$\frac{g}{\rho(x)} \simeq \frac{g}{NM|c|} e^{2M|cx|}. \quad (5.2)$$

This result implies that the MFA describes the Bose gas well in the vicinity of the impurity. We can characterize the width of the ‘mean-field’ region by $1/(M|c|)$. If all bosons are bound, the probability of finding a boson far away from the impurity vanishes. Therefore, in this case, the MFA describes the system well. However, if bosons occupy scattering states, this probability becomes non-zero, making the bosons strongly repellent. In that case, the MFA no longer applies. We validate this line of argument using *ab initio* calculations in Sec. 5.4.

⁴Note that when we consider a mobile impurity, also more fermions can become bound if the mass of the impurity is lighter than the one of the fermions [200].

⁵This can be explained in the following way: To determine if interactions are strong or weak one should compare the scale of the potential energy with one given from the kinetic energy. The potential energy scales in every dimension linearly with the density ρ , $E_{\text{pot}} \propto \rho$. The kinetic energy, however, scales like $E_{\text{kin}} \propto 1/r_{\text{ipd}}^2$ with r_{ipd} the inter-particle distance. In 3D, it is given by $r_{\text{ipd}} \propto 1/\rho^{1/3}$ but in 1D it is $r_{\text{ipd}} \propto 1/\rho$. Therefore, in 1D the kinetic energy scales like $E_{\text{kin}} \propto \rho^2$ but in 3D it scales like $E_{\text{kin}} \propto \rho^{2/3}$. This means that in 1D a high density leads to a dominating kinetic energy, i.e. weak interactions, while in 3D potential energy dominates, i.e. strong interactions.

5.3. Mean-field approximation for the heavy impurity problem

Because of our physical picture, see above, it is reasonable to assume that the majority of the bosons are weakly interacting. This motivates the use of the MFA, i.e. we use a product state ansatz for the ground state wave function: $\Phi = \prod_i f(x_i)$, where $f(x)$ describes the single-particle function that minimizes the energy of the system. The Gross-Pitaevskii equation (GPE) for our system reads (for details see Sec. 2.5):

$$-\frac{1}{2M} \frac{d^2 f}{dx^2} + g(N-1)f(x)^3 + c\delta(x)f(x) = \mu f(x), \quad (5.3)$$

where μ describes the chemical potential⁶. Because we consider the system to be on a ring, f has to fulfill periodic boundary conditions, $f(-L/2) = f(L/2)$ (we briefly discuss a system with a box trap in App. C.2). As discussed in Sec. 2.5, phase fluctuations can be large for one-dimensional systems [73, 100, 202, 203] and we therefore also check the validity of the MFA, at least for the bosons in the vicinity of the impurity, with *ab initio* calculations in Sec. 5.5.

To find a solution to Eq. (5.3), we follow the prescription given in Sec. 2.5: We use the known solutions for $c = 0$ and implement the impurity-boson interaction as a boundary condition at $x = 0$. We find two solutions, which we present below. By expanding the ring size $L \rightarrow \infty$, we can adiabatically connect the two solutions to two different physical states: (i) all bosons are bound to the impurity⁷, (ii) no boson is bound, see Sec. 5.4. Both solutions are equivalent at the threshold for binding, which we call ‘‘point of transition’’ (PoT). This chapter’s focus is on systems with a finite ring size L . This allows us to directly benchmark the mean-field solution against the *ab initio* calculations. Furthermore, finite-sized systems are experimentally relevant. Finally, a finite value of L allows us to study the case of $N > N_{\text{cr}}$. This case is relevant for understanding the transition of this system to the thermodynamic limit which we leave to further studies.

5.3.1. Mean-field solutions

One solution to Eq. (5.3) reads

$$f_{\text{mhb}}(x) = \sqrt{\frac{4K(p_{\text{mhb}})^2}{MgL^2\delta^2(N-1)}} \text{ds} \left(2K(p_{\text{mhb}}) \left[\frac{|x|}{\delta L} + \frac{1}{2} - \frac{1}{2\delta} \right], p_{\text{mhb}} \right), \quad (5.4)$$

⁶Note that, this equation was also derived and studied in a system different from ours: A heavy atom in a strong magnetic field, see parameter regime 5 (‘region 5’) of Ref. [201].

⁷Note that the bound-state solution has already been discussed in Refs. [169, 170] for $L \rightarrow \infty$.

with the Jacobi elliptic function ds [102]. The solution fulfills periodic boundary conditions and further it is parity symmetric $f_{\text{mbb}}(-x) = f_{\text{mbb}}(x)$. The chemical potential is

$$\mu_{\text{mbb}} = \frac{2K(p_{\text{mbb}})^2(1 - 2p_{\text{mbb}})}{M\delta^2L^2},$$

where K is the complete elliptic integral of the first kind.

The second solution to Eq. (5.3) is given by the Jacobi elliptic function ns :

$$f_{\text{scatt}}(x) = \sqrt{\frac{4K(p_{\text{scatt}})^2}{MgL^2\delta^2(N-1)}} \text{ns} \left(2K(p_{\text{scatt}}) \left[\frac{x}{\delta L} + \frac{1}{2} - \frac{1}{2\delta} \right], p_{\text{scatt}} \right). \quad (5.5)$$

The corresponding chemical potential is

$$\mu_{\text{scatt}} = \frac{2K(p_{\text{scatt}})^2(p_{\text{scatt}} + 1)}{M\delta^2L^2}.$$

To determine the parameters $p_{\text{scatt}} \in [0, 1)$, $p_{\text{mbb}} \in [0, 1)$ and⁸ δ we solve two additional equations given from the normalization condition and the boundary condition given by the impurity-boson potential

$$\int_{-L/2}^{L/2} |f(x)|^2 dx = 1, \quad \left. \frac{df}{dx} \right|_{x \rightarrow 0^+} = Mcf(0).$$

We can rewrite these conditions in a more explicit form, e.g. for f_{mbb} the normalization condition reads

$$\mathcal{E} \left(K - \frac{K}{\delta}, p \right) + (1-p)\text{nd} \left(\frac{K}{\delta}, p \right) \text{sc} \left(\frac{K}{\delta}, p \right) - \epsilon(p) + \frac{1-p}{\delta}K = \frac{MgL\delta(N-1)}{4K}, \quad (5.6)$$

where $K = K(p)$, and $p = p_{\text{mbb}}$ (\mathcal{E} , ϵ , sc and nd are standard Jacobi functions [102]). The boundary condition due to the impurity-boson interaction is written as

$$2K(p_{\text{mbb}}) \frac{\text{sc} \left(\frac{K(p_{\text{mbb}})}{\delta}, p_{\text{mbb}} \right)}{\text{nc} \left(\frac{K(p_{\text{mbb}})}{\delta}, p_{\text{mbb}} \right)} = \frac{M|c|\delta L}{\text{dc} \left(\frac{K(p_{\text{mbb}})}{\delta}, p_{\text{mbb}} \right)}. \quad (5.7)$$

⁸If one allows for negative values of p , the two solutions can be transformed into one another via $p_{\text{mbb}} = -\frac{p_{\text{scatt}}}{1-p_{\text{scatt}}}$. The parameter δ remains unchanged in this transformation.

Note that these two equations, Eq. (5.6) and Eq. (5.7), can only be fulfilled for $N \leq N_{\text{cr}}$, i.e., f_{mbb} describes only systems with particle numbers less or equal to the critical one. The solution f_{scatt} on the other hand describes systems with $N \geq N_{\text{cr}}$. The value of N_{cr} is presented in the next section, see Eq. (5.10).

We call the first solution many-body bound state ('mbb') and the second scattering state ('scatt') because for a large system ($L \rightarrow \infty$) N_{cr} determines the maximum number of bosons that can be bound to the impurity, see Ref. [169, 170] and the discussion in the next section. One can see this, e.g., from the fact that for large system sizes the chemical potential is negative (positive) for the first (second) solution because $p_{\text{mbb}} \rightarrow 1$ and $p_{\text{scatt}} \rightarrow 1$ for $L \rightarrow \infty$. This showcases that the first solution describes a many-body bound state where the energy decreases if more particles are added while the second is applicable if the bosons occupy scattering states and increase the energy upon adding additional ones.

To illustrate the mean-field solutions, we show plots of them in Fig. 5.2 for different values of N and L . The attractive impurity-boson interaction leads to bunching of the bosons at the position of the impurity. We further show in this figure the energy per particle. Increasing the particle number leads to a decrease in the binding energy per particle (i.e. it increases the energy per particle) which is due to the repulsive boson-boson interaction. This also leads to a flatter profile of the density. We also show the parameters p and δ in the figure insets as a function of the particle number. We can see that increasing the particle number forces to $\delta \rightarrow 1$. For the parameter p , we can see that it first drops to 0 at $N = N_{\text{cr}}$ and that it then rises again to $p \rightarrow 1$ (note that we omitted the subscripts: p corresponds to p_{mbb} for $N \leq N_{\text{cr}}$ and p_{scatt} for $N \geq N_{\text{cr}}$). If we increase the ring size, p also increases. We find empirically that for $L \rightarrow \infty$, $p \rightarrow 1$ except in the vicinity of N_{cr} . For the chemical potential, as shortly mentioned above, we find that for the largest ring size and $N \lesssim N_{\text{cr}}$ it becomes negative, see Fig. 5.2 c).

5.3.2. Point of Transition

As already mentioned for certain parameters in the system, both solutions are equal. In this case $p_{\text{mbb}} = p_{\text{scatt}} = 0$ (cf. the insets in Figs. 5.2 a) and b)). We can simplify the mean-field solution at the PoT to:

$$f_{\text{PoT}}(x) = \sqrt{\frac{\pi^2}{MgL^2\delta^2(N-1)}} \frac{1}{\cos\left(\frac{\pi(x-L/2)}{\delta L}\right)} \quad (5.8)$$

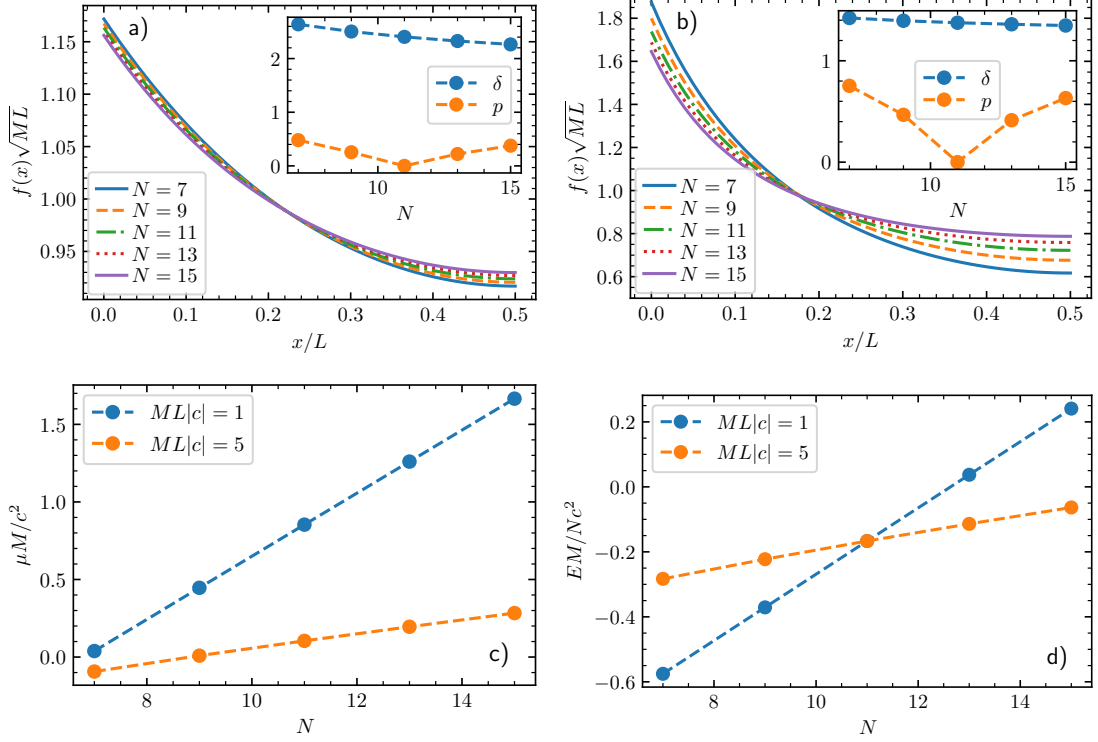


Figure 5.2.: **Mean-field wave function, chemical potential and energy for different system sizes.**

The upper panels show the mean-field solutions for different numbers of particles. Panel a) showcases the solutions for $LM|c|=1$ while panel b) is for $LM|c|=5$. The relative interaction strength is fixed to $\alpha = -5$. Therefore, the maximal particle number in a bound state is $N_{\text{cr}} = 11$, see Eq. (5.10). In the insets, we show the parameters p and δ as a function of the particle number. The lower panels depict the corresponding chemical potential [c]) and the energy per particle [d]) for different system sizes (see legend). Figure taken from Ref. [62].

with the corresponding chemical potential

$$\mu_{\text{PoT}} = \frac{\pi^2}{2M\delta^2 L^2}.$$

Note that the chemical potential at the PoT vanishes for large system sizes, $L \rightarrow \infty$.

Because at the PoT the parameter p is already determined, the normalization and impurity-boson boundary condition lead to only one equation for the parameter δ

$$\pi \tan\left(\frac{\pi}{2\delta}\right) = M|c|L\delta, \quad (5.9)$$

and determine the critical number of bosons to be

$$N_{\text{cr}} = \frac{2|c|}{g} + 1. \quad (5.10)$$

Note that for a non-interacting Bose gas, $g \rightarrow 0$, $N_{\text{cr}} \rightarrow \infty$ and $N_{\text{cr}} = 1$ when $g \rightarrow \infty$, in agreement with our discussion in Sec. 5.2.2.

Interestingly, Eq. (5.9), which determines δ , depends only on the dimensionless parameter $M|c|L$, while the critical boson number N_{cr} depends only on the ratio $|c|/g$. This suggests an unexpected decoupling of δ and N_{cr} which implies, for example, a scale invariance of the problem at the point of transition, and leads to a number of surprising consequences. For example, if $N = N_{\text{cr}}$ the state becomes a zero pressure state: it costs no energy to adiabatically change the radius of the ring, i.e. the energy of the system does not depend on L :

$$E = -\frac{N_{\text{cr}}c^2M}{6}. \quad (5.11)$$

We will use this unique signature later to identify the PoT from the numerical calculations. Further, Eq. (5.11) gives an upper bound on the exact value of the energy because the mean-field calculation is a variational minimization of the energy. This rigorously shows that it is energetically more favorable to bind many bosons to the impurity than simply binding a single one. For the latter, the ground state energy is $-Mc^2/2$. Already for $N_{\text{cr}} \geq 3$ Eq. (5.11) leads to an even lower energy.

5.4. Mean-field results in the zero-density limit

Here, we discuss the mean-field solution for an expanding ring size, $L \rightarrow \infty$, while keeping the number of particles fixed, i.e. the limit of vanishing density, $\rho \rightarrow 0$ (for a discussion of the many-body bound state solution in this limit see Refs. [169, 170] and for details of our calculation App. C.3). This limit will support our characterization of the mean-field solution in the previous section and give valuable insight into the related physics.

5.4.1. Many-body bound state

We start by considering Eq. (5.4). For a vanishing density, $\rho \rightarrow 0$, $p_{\text{mbb}} \rightarrow 1$ (cf. Fig. 5.2) and we can write Eq. (5.4) as

$$f_{\text{mbb}}(x > 0) = \sqrt{\frac{2\zeta(2\zeta + 1)}{x_{\text{mbb}}}} \frac{1}{(2\zeta + 1)e^{x/x_{\text{mbb}}} - e^{-x/x_{\text{mbb}}}}, \quad (5.12)$$

where

$$\zeta = \frac{N_{\text{cr}} - N}{N - 1}, \quad x_{\text{mbb}} = \frac{1}{M|c|} \frac{N_{\text{cr}} - 1}{N_{\text{cr}} - N} \left(= \frac{1}{M|c|} \frac{\zeta + 1}{\zeta} \right).$$

We define the quantity x_{mbb} as the characteristic width of the state⁹. By definition, the quantity ζ is zero for $N > N_{\text{cr}}$ and we can interpret ζ as an ‘order’ parameter of our system. ζ is positive for a many-body bound state and vanishes if we approach the point of transition.

The corresponding chemical potential is

$$\mu_{\text{mbb}} = -\frac{1}{2Mx_{\text{mbb}}^2}. \quad (5.13)$$

Note that it is negative which implies that adding additional bosons will lower the total energy – a typical signature of a many-body bound state. Further, we write the energy of this state as

$$E_{\text{mbb}} = -\frac{N}{Mx_{\text{mbb}}^2\zeta^2} \left(\frac{\zeta(\zeta + 1)}{2} + \frac{1}{6} \right). \quad (5.14)$$

We can further investigate the mean-field wave function in this limit, Eq. (5.12), by expanding it for large values $|x|$. This results in

$$f_{\text{mbb}}(|x| \gg x_{\text{mbb}}) \simeq \sqrt{\frac{2\zeta}{(2\zeta + 1)x_{\text{mbb}}}} e^{-\frac{|x|}{x_{\text{mbb}}}}. \quad (5.15)$$

The exponential decaying tail with characteristic width of x_{mbb} is yet another typical characteristic of a bound state (see, e.g., Ref. [191]). Note that this equation only holds for $N < N_{\text{cr}}$. At the critical particle number $N = N_{\text{cr}}$, $\zeta \rightarrow 0$, $x_{\text{mbb}} \rightarrow \infty$. We describe this limit below.

⁹The characteristic width of the many-body bound state x_{mbb} is proportional to the characteristic size of a one-body bound state $1/M|c|$. However, it can be considerably larger because x_{mbb} depends also on N .

5.4.2. Point of transition

At the PoT, $\zeta = 0$, i.e. $N = N_{\text{cr}}$, we can write the mean-field solution as

$$f_{\text{PoT}}(x) = \sqrt{\frac{|c|M}{2}} \frac{1}{M|cx|+1}. \quad (5.16)$$

Now, there is still a finite probability to find a boson in the vicinity of the impurity potential although we are at the threshold of binding. This shows that the many-body problem is fundamentally different from the one-body system [see Eq. (5.2)] in which case this probability would vanish in the limit $L \rightarrow \infty$.

The length x_{mbb} diverges in this limit, so we shall define another quantity to characterize the size of this state. Because the tail of the wave function decays like $1/x$, the root-mean-square radius cannot be taken. Instead, we define the size of the state as

$$x_{\text{PoT}} = \frac{1}{|c|M}.$$

The physical meaning of this quantity is that it defines the spatial region which contains half of the probability density:

$$\int_{-x_{\text{PoT}}}^{x_{\text{PoT}}} f_{\text{PoT}}^2(x) dx = 1/2.$$

Interestingly, this definition results in x_{PoT} to be the size of a one-particle bound state [Eq. (5.2)], which supports the physical picture we have given in Sec. 5.2.2.

Because the chemical potential is zero, no energy is gained if additional bosons are added to the system, hence, we interpret these particles to occupy scattering states in a free space. This also means that for low densities $\rho \rightarrow 0$ Eq. (5.11) gives the energy of the system for all $N \geq N_{\text{cr}}$. Note that since the state in Subsec. 5.3.2 is of zero pressure, its energy is the same as for a system with a finite ring length, Eq. (5.11).

5.4.3. Scattering state

Lastly, we discuss the expansion of the scattering state, Eq. (5.5), which reads for $\rho \rightarrow 0$ as

$$f_{\text{scatt}}(x) \simeq \sqrt{\frac{1}{MgL^2\delta^2(N-1)}} \ln\left(\frac{16}{1-p_{\text{scatt}}}\right) \coth\left(\ln\left(\frac{16}{1-p_{\text{scatt}}}\right) \left[\frac{x}{\delta L} + \frac{\delta-1}{2\delta}\right]\right).$$

Interestingly, for this function, it is impossible to fulfill normalization and delta-potential boundary conditions at the same time. If we want to fulfill the latter condition, we get a

non-normalizable wave function for $L \rightarrow \infty$. On the other hand, if we start by normalizing this function, we get a constant function in space and we cannot include any impurity-boson boundary condition. To explain this contradiction, remember that the mean-field solution assumes all particles to occupy the same orbital. As soon as $N > N_{\text{cr}}$, all particles must therefore occupy scattering states which means that they distribute over the whole system. For $\rho \rightarrow 0$ this means that they will not be affected by the impurity potential. It is important to note that this state cannot be the physical ground state: The energy of a state with N_{cr} bound bosons and the additional ones in scattering states is lower. Therefore, we conclude that the MFA cannot be used to describe the state of the system in this case.

To improve the MFA, we would have to use a variational ansatz which for large (but finite) L includes two parts: One which describes the many-body bound state and another which contains the bosons occupying scattering states. The latter might be described by a Tonks-Girardeau gas in the low-density limit. We leave an investigation of this ansatz to future studies.

5.5. Flow equation results: approach to the zero-density limit

So far, our discussion was solely based on the MFA. Even though we have argued in Subsec. 5.2.2 why it can be applied, we further test its validity by employing beyond-mean-field *ab initio* calculations. For this purpose, we use the flow equation approach¹⁰, see Sec. 2.3. Here, we only explain the used reference state and one-body basis. For the latter, the solution of the one-body Hamiltonian in the co-moving frame is used, i.e. we have sin/cos solutions which incorporate the impurity-boson interaction. We use a basis with $n \in \{11, 13, 15, 17, 19, 21\}$ basis states. To construct the reference state, we use an iterative scheme. We start by using the lowest state of the one-body basis and calculate the density of the system. The density is then used as a new reference. This procedure is repeated until there is no change upon an additional iteration.

Our focus in this section is on the validity of the MFA for an increasing ring size. We will compare the mean-field predictions for the energy and density of the system and, furthermore, we will estimate off-diagonal phase fluctuations which are beyond-mean-field corrections. These fluctuations can become important far from the impurity potential as described in Subsec. 5.2.2, see also Fig. 5.1 b).

¹⁰We further benchmarked flow equation results against results obtained with the well-established ML-MCTDHX (see e.g. Ref. [56, 57] in App. C.1).

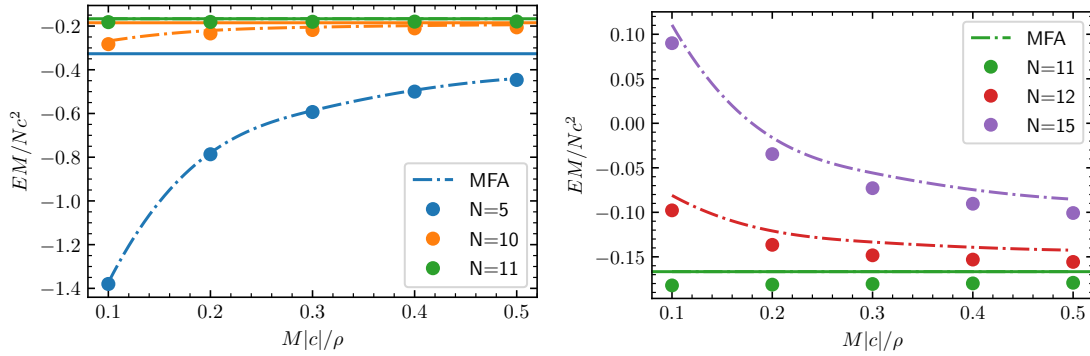


Figure 5.3.: **Mean-field vs IM-SRG: Energy as a function of density.**

Energy per particle for different particle numbers as a function of the inverse density $M|c|/\rho$. Circles show results obtained with the IM-SRG while the dashed-dotted curves represent mean-field results. Solid (horizontal) lines correspond to the mean-field prediction for the zero-density limit, see Eq. (5.14). In the left panel, we show data for $N \leq N_{\text{cr}}$ and in the right one for $N \geq N_{\text{cr}}$. We use a relative interaction strength of $\alpha = -5$ so that $N_{\text{cr}} = 11$. Note that the numerical error bars of the IM-SRG data are smaller than the sizes of the markers. Figure modified from Ref. [62].

5.5.1. Energies

Let us start by comparing the energy per particle as a function of the inverse density ($1/\rho$) for different values of N , see Fig. 5.3. We choose interaction strengths such that the maximum number of bound bosons is $N_{\text{cr}} = 11$.

The IM-SRG results agree with the mean-field predictions. Small deviations are only visible for $N \gtrsim N_{\text{cr}}$. These deviations are due to beyond-mean-field effects which are included in the IM-SRG method. Furthermore, we can see that the energy per particle, for particle numbers larger than the critical one, decreases. We expect that in the limit $\rho \rightarrow 0$ all energies for $N > N_{\text{cr}}$ to approach the energy of N_{cr} bound bosons, Eq. (5.11). Unfortunately, the IM-SRG method starts to become inaccurate for densities lower than $M|c|/\rho \geq 1$, which means that we cannot follow this convergence. For the largest considered particle numbers, the flow equations even diverge for larger values of L . We interpret this as a sign that the reference state, a condensate is no longer an approximation of the ground state, i.e. the system becomes more correlated. Therefore, the MFA is also no longer a good approximation, see Sec. 2.3.

We can further see that for $N < N_{\text{cr}}$ the energy increases with decreasing density (with increasing ring sizes). This is a typical signature of bound states for $L \rightarrow \infty$: The potential energy dominates over the kinetic energy which means that increasing the ring size leads to a lower binding energy as the probability of staying close to the impurity decreases. This can be illustrated by considering a single boson bound to the impurity. In this case, the binding energy is given by

$$\frac{\sqrt{2M|E|}}{M|c|} \tanh(\sqrt{2|E|}ML) = 1,$$

which results in $E = -\frac{Mc^2}{2} - 2Mc^2 e^{-2M|c|L}$ for $M|c|L \gg 1$.

For $N = N_{\text{cr}}$ we can see that the IM-SRG results also display a nearly constant energy as predicted by the zero-pressure mean-field state, Eq. (5.11). The weak dependence on the density hints at small beyond-mean-field effects.

If the particle number is larger than the critical one, $N > N_{\text{cr}}$, we can see that the energy decreases with a lower density. This is also a typical sign of N_{cr} bound bosons with additional ones occupying scattering states. For a scattering state, the kinetic energy dominates over the potential one. This means that increasing the system size lowers the total energy. The kinetic energy of the bosons in scattering states decreases approximately like $\sim 1/L^2$ which leads to an approximate behavior for $L \rightarrow \infty$

$$E \simeq -\frac{MN_{\text{cr}}c^2}{6} + \frac{2\pi^2\mathcal{N}(\mathcal{N}+1)(2\mathcal{N}+1)}{3ML^2}, \quad (5.17)$$

where $\mathcal{N} = (N - N_{\text{cr}} - 1)/2$ for odd values of $N - N_{\text{cr}}$ and

$$E \simeq -\frac{MN_{\text{cr}}c^2}{6} + \frac{2\pi^2\mathcal{N}(\mathcal{N}+1)(2\mathcal{N}+1)}{3ML^2} - 2\frac{\mathcal{N}^2\pi^2}{ML^2}, \quad (5.18)$$

with $\mathcal{N} = (N - N_{\text{cr}})/2$ for even values of $N - N_{\text{cr}}$.

These expressions describe a sum of N_{cr} bound bosons while the remaining $N - N_{\text{cr}}$ occupy scattering states which are described in the low-density limit by a Tonks-Girardeau gas. For this expression, we have assumed that there is no interaction between the many-body bound state and the bosons occupying scattering states¹¹.

¹¹In Eqs (5.17) and (5.18) we assumed that the ring size is sufficiently large, i.e. $1/k_F \gg 1/|c|M$ with k_F the Fermi wavelength corresponding to the Tonks-Girardeau gas and $1/|c|M$ the characteristic width of the many-body bound state. If we assume that $k_F = \pi\rho$, we derive the condition $M|c|/\rho \gg \pi$. From this condition, it follows that the ring sizes we used in Fig. 5.3 are too small to numerically confirm Eqs. (5.17) and (5.18).

To summarize our discussion of the IM-SRG data for the energy: The data does support the existence of two different physical states. A many-body bound state with a critical number and another state where additional bosons occupy scattering states. The IM-SRG results also confirm the zero pressure characteristic of the critical state.

5.5.2. Densities and phase fluctuations

Next, we compare the predictions of the MFA and the IM-SRG method for the Bose-gas density

$$\rho(x) = \langle \Phi_{gr} | \sum_{i=1}^N \delta(x - x_i) | \Phi_{gr} \rangle, \quad (5.19)$$

with $|\Phi_{gr}\rangle$ being the ground state. Furthermore, we estimate beyond-mean-field effects by calculating phase fluctuations (also known as phase correlations), $\delta\Phi_{xx'}$, see Eq. (2.48). As written in Sec. 2.5, this quantity can be interpreted as a measure of the off-diagonal long-range order, which vanishes for a condensate.

We show results for these two observables in Fig. 5.4, for $L = 0.1N/M|c|$ and $L = 0.5N/M|c|$. We see that for all considered parameters, the IM-SRG results for the density are in good agreement with the MFA. Because of the attractive impurity-boson interaction, the density is highest in the vicinity of the impurity potential.

At the same time, the calculation of phase fluctuations reveals that beyond-mean-field effects are becoming more important for increasing ring lengths. We notice considerable increasing phase fluctuations for the largest ring size and $N \geq N_{cr}$, in particular in the region with low densities. This observation supports the physical picture given in Subsec. 5.2.2: low densities lead to strong interactions and a correlated state. We characterize the local interaction strength by $Mg/\rho(x)$. Surprisingly, even in regions where the MFA is not expected to work well, e.g. if $Mg/\rho(x)$ is at the order of one, the mean-field and IM-SRG results are in good agreement for the density. Note that the MFA is also valid for the smallest non-trivial many-body bound system, a two-boson artificial atom, see App. C.4.

Further, phase fluctuations, and therefore beyond-mean-field corrections, are strongest for the largest N . Our understanding is the following: If we have $N = 15$ bosons but $N_{cr} = 11$, four bosons are not bound to the impurity. Therefore, these bosons are distributed more evenly over the whole ring which means that there is a higher probability of strong boson-boson interaction in the low-density region. This leads to large correlations. In the opposite case of small particle numbers, e.g. $N = 5$, phase fluctuations can still be small in regions where the density is low because the probability of finding two bosons which interact far away from the impurity is exponentially suppressed.

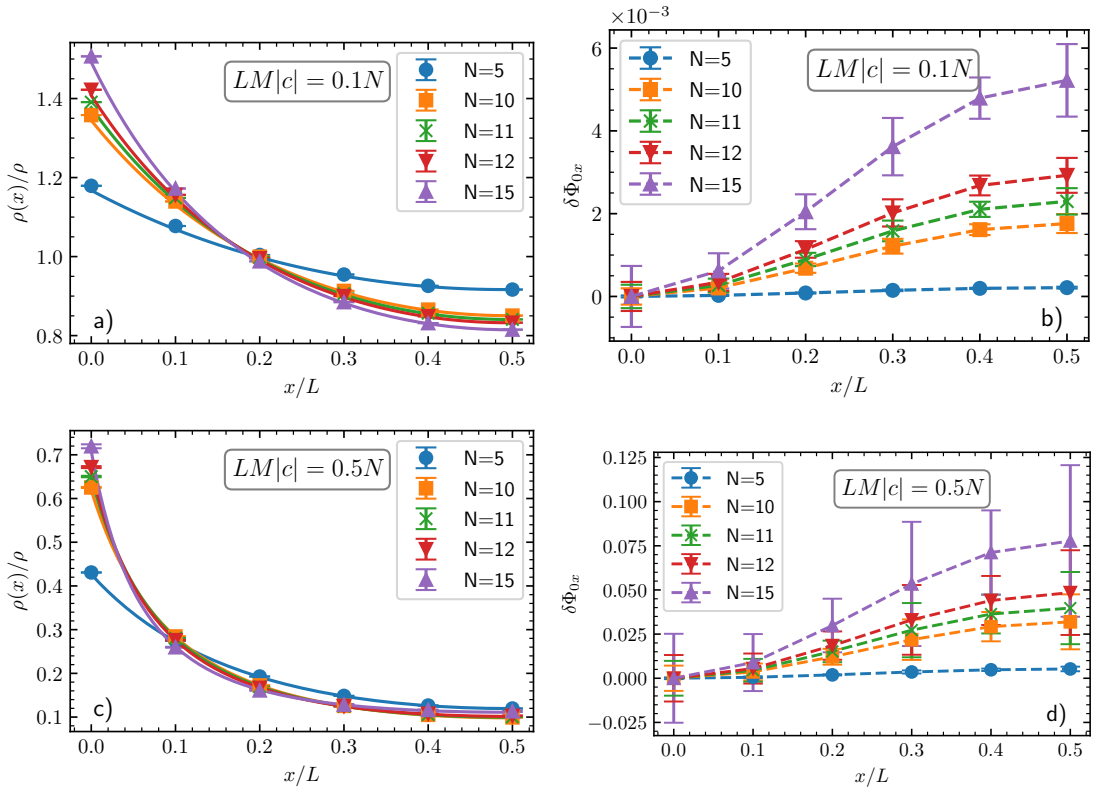


Figure 5.4.: **Mean-field vs IM-SRG: Density and phase fluctuations.**

Panel a) and c) show the Bose-gas density, where circles are results obtained with the IM-SRG and solid curves correspond to mean-field results (Eqs. (5.4), (5.8)). In panels b) and d) we show phase fluctuations whose non-zero values correspond to beyond-mean-field correlations. The dashed curves are plotted to guide the eye. The numerical error bars are calculated according to the prescription given in Sec. 2.3. The data we show correspond to many-body bound, critical and scattering states. We fix $\alpha = -5$, thus, the critical number of bosons supported by the bound state is $N_{\text{cr}} = 11$. In panels a) and b) we show results for $LM|c| = 0.1N$ ($M|c|/\rho = 0.1$) while in c) and d) we have $LM|c| = 0.5N$ ($M|c|/\rho = 0.5$). Figure taken from Ref. [62].

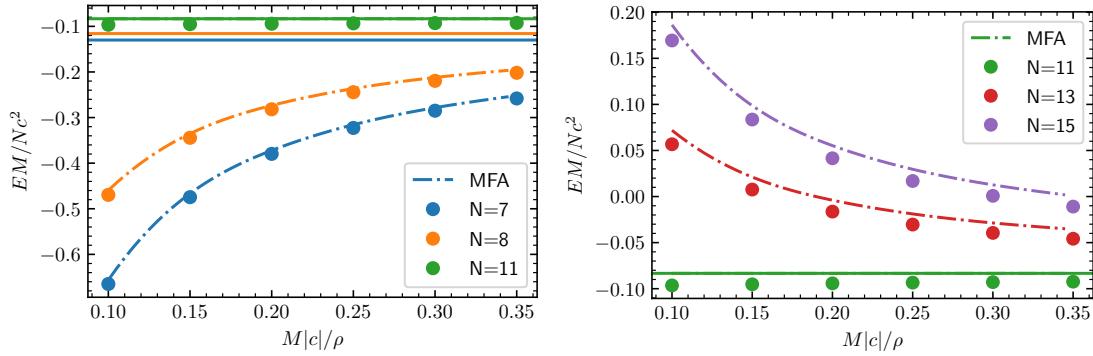


Figure 5.5.: **Mobile impurity: energy as function of the density.**

Energy per particle for a mobile impurity ($m = M$) as a function of the inverse density $1/\rho$ for different values of N . Circles are data obtained with the IM-SRG while dashed-dotted curves represent the mean-field results. Solid (horizontal) lines correspond to the mean-field prediction for the zero-density limit, see Eq. (5.14). The left (right) panel shows the energy for $N \leq N_{\text{cr}}$ ($N \geq N_{\text{cr}}$). We use a relative interaction strength of $\alpha = -5$ which leads to $N_{\text{cr}} = 11$. Note that the numerical error bars calculated within IM-SRG according to Sec. 2.3 are smaller than the sizes of the markers. Figure modified from Ref. [62].

5.6. Mobile impurity

So far, we have only considered a heavy impurity in this chapter, i.e. an impurity potential. However, as described in the introduction, Chap. 1, a single mobile impurity atom in a weakly interacting Bose gas is an experimentally relevant system [140, 204], which motivated theoretical studies of a ‘Bose-polaron’, see, for example, Chap. 4 and also Refs. [72, 94, 97, 162, 163, 166, 205]. In this section, we also consider a mobile impurity and complement above studies by considering the many-body bound state that follows from our results in the previous sections.

5.6.1. Mean-field analysis

As shown in Sec. 2.4, we can transform the Hamiltonian of our system, Eq. (5.1), to the co-moving frame because the total momentum of the system is conserved. This leads to

$$\mathcal{H}_P = -\frac{1}{2M} \sum_i^N \frac{\partial^2}{\partial z_i^2} - \frac{1}{2m} \left(\sum_i^N \frac{\partial}{\partial z_i} \right)^2 + \frac{iP}{m} \sum_i^N \frac{\partial}{\partial z_i} + g \sum_{i<j} \delta(z_i - z_j) + c \sum_{i=1}^N \delta(z_i), \quad (5.20)$$

where P is a quantum number – the total (angular) momentum of the system. We are only interested in the ground state of the system and hence consider $P = 0$.

With this, we can also write the GPE in the co-moving frame (see also Sec. 2.5):

$$-\frac{1}{2\kappa} \frac{d^2 f}{dz^2} + g(N-1)f(z)^3 + c\delta(z)f(z) = \mu f(z), \quad (5.21)$$

where $\kappa = mM/(m+M)$ is the reduced mass. A comparison with Eq. (5.3) shows that the two equations are equivalent up to a change of the boson mass M which is replaced by κ . Therefore, all of our mean-field results from Secs. 5.3 and 5.4 can also be applied to a mobile impurity¹².

5.6.2. Flow equation results

To validate our MFA with the IM-SRG method, we focus on the equal mass case with $m = M$. We show in Fig. 5.5, the ground-state energy as a function of the inverse density $1/\rho$ - equivalent to Fig. 5.3. We see that the MFA results agree well with the IM-SRG calculation. We can also see that we have the same behavior when decreasing the density (increasing the ring size): For $N < N_{\text{cr}}$ the energy increases, for $N = N_{\text{cr}}$ it remains nearly constant and for $N > N_{\text{cr}}$ it decreases. Interestingly, Eq. (5.10) suggests that the critical number of bosons that can be bound to the impurity does not depend on the mass of the impurity. Our numerical calculations also support this claim. Note that this is exactly opposite to the behavior for fermions, see Ref. [200]: There, the mass ratio between impurity and fermions determines the maximum number of bound fermions.

A comparison for density and phase fluctuations is similar to the one in Fig. 5.4 and we therefore refrain from discussing it further.

¹²Because we kept the boson mass M in all equations, one simply needs to swap M with κ .

5.7. Conclusions

5.7.1. Summary

Let us summarize this chapter: We studied an attractive impurity in a one-dimensional sea of repulsive bosons. We discussed that there exists a many-body bound state which we call a one-dimensional artificial atom made of bosons. We started by analyzing the system with the MFA for a finite ring length L . We found two solutions which, by expanding the ring size to $L \rightarrow \infty$, could be identified with two different physical scenarios where the bosons are either bound to the impurity or occupy scattering states. We also found an analytic condition for the critical line that separates these states which depends only on the ratio between the impurity-boson interaction strength and the boson-boson repulsion¹³. We showed that at this critical particle number, the state is a zero-pressure state, i.e. its energy is independent of the ring size.

Furthermore, we used the *ab initio* beyond-mean-field flow equation method to benchmark the validity of the MFA¹⁴. We found that the MFA is well justified to describe artificial atoms in one dimension. Our numerical calculations also confirmed the existence of bound, critical and scattering states. They also revealed quantum fluctuations beyond the MFA in the tail of the wave functions. Our conclusion is that only bosons in the vicinity of the impurity can be well described with the MFA, while bosons far away from the impurity can interact strongly. We argued that their influence can be neglected if all particles are bound to the impurity because then the probability of finding bosons in the strongly interacting region vanishes¹⁵. The main focus of this chapter was on heavy impurities; however, we also showed that our results can be easily extended to mobile ones.

5.7.2. Outlook

Our few-body results facilitate studies of many-body physics which use artificial atoms as elementary building blocks. For example, tuning the interactions to induce a transition from a many-body bound state to a scattering state could enable the emergence of different phases, such as a Mott insulator or superfluid, in a lattice of heavy impurities immersed in a Bose gas. To better understand such systems, further studies on the effective interaction between two artificial atoms are needed.

¹³This means that the maximum number of bosons that can be bound to an impurity within our set of approximations is independent of the mass ratio of the particles, exactly opposite to the result for fermions [200].

¹⁴We further benchmarked this method against the well-established ML-MCTDHX method, see App. C.1.

¹⁵Note that we showed this even for the two-boson system where we considered boson-boson repulsion as strong as the impurity-boson attraction, see App. C.4

The transition towards the thermodynamic limit is interesting to study. This requires a good understanding of the case $N > N_{\text{cr}}$. As explained in the main part of this chapter, the MFA cannot properly describe a state where N_{cr} bosons are bound while the remaining ones occupy scattering states. Therefore, we have to better understand the transition between the many-body bound state and the scattering state. This can be done, e.g. in few-to-many-body studies to understand beyond-mean-field effects. This transition might also be interesting to study in the context of precursors of quantum phase transitions in few-body systems, see e.g. Refs. [9, 42, 52, 65, 206–208]. Our results allow for important insight into the bound state and will be helpful for such studies. We want to expand upon these ideas below.

Transition between many-body bound state and scattering state

We want to start by showing that for large values of $L|c|$ the state with $N > N_{\text{cr}}$ exhibits large phase fluctuations. These beyond-mean-field effects complicate many-body investigations of our system. In Fig. 5.6, we show the Bose-gas density, Eq. (5.19), and phase fluctuations, Eq. (2.48), for $c/g = -10$ ($N_{\text{cr}} = 21$) and for $\alpha = 13$ ($N_{\text{cr}} = 27$) for the three cases of all bosons bound, the critical state and additional bosons occupying scattering states. As can be seen, for weaker impurity-boson interaction, the results of the MFA agree with the IM-SRG calculation. Phase fluctuations, although increasing with larger particle numbers, are small for all considered cases. However, for stronger attraction, we see that the density from the MFA only agrees with the IM-SRG results for bound and critical state. For the scattering state, the density – in particular at the position of the impurity – deviates strongly from the IM-SRG calculation. Furthermore, we can also see that while the phase fluctuations for the bound and critical states are small, for the scattering state they are important. This shows, that the the MFA can no longer describe this state. For even stronger impurity-boson interactions, the IM-SRG diverged for particle numbers larger than the critical one, making a study of polaron properties in the thermodynamic limit impossible with our methods.

To better understand why the MFA starts to deviate, we show phase fluctuations for the scattering state with respect to the position of the impurity but also with respect to $x' = L/2$, the point farthest away from the impurity. For both cases, phase fluctuations increase only slightly for points near the reference point. Roughly at $x = L/4$ they start to increase more rapidly. The crucial insight from this chapter – that only $N = N_{\text{cr}}$ bosons are bound – suggests that a two-condensate ansatz might be necessary to describe this system accurately. Specifically, there are bound bosons forming a condensate near the impurity potential, leading to low phase fluctuations in the vicinity of the impurity. However, far from the impurity potential, bosons primarily occupy scattering states, forming a separate

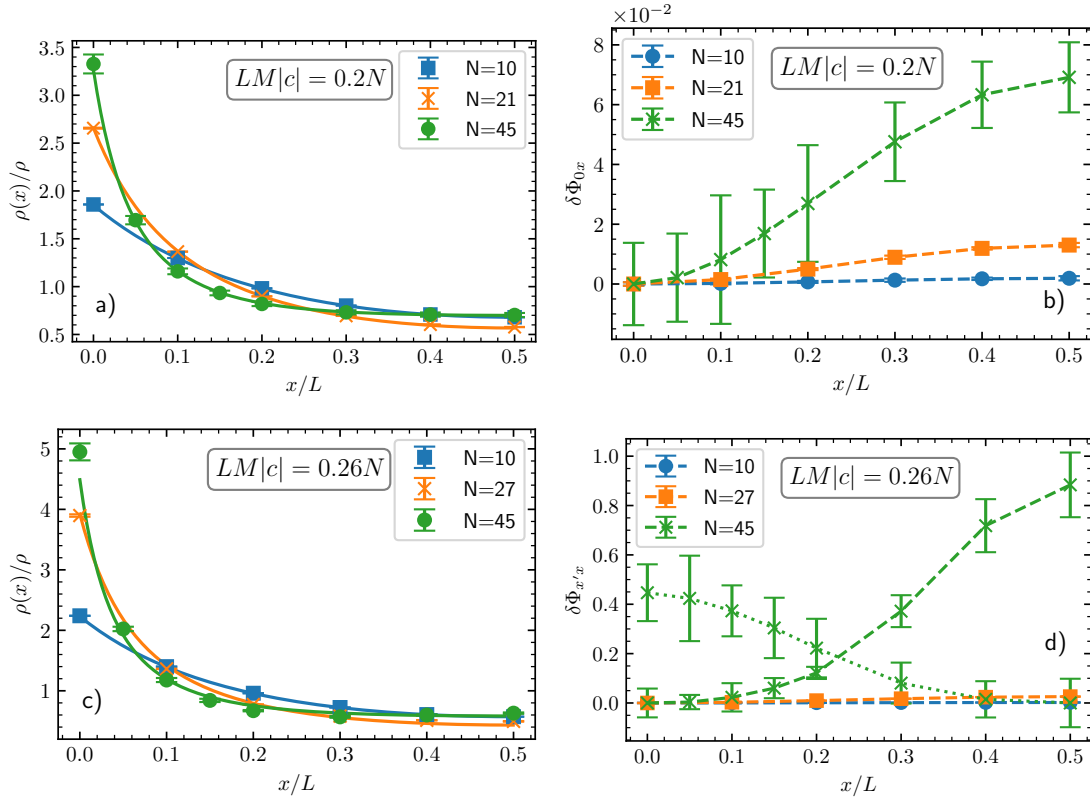


Figure 5.6.: **Breakdown of mean-field approximation.**

We show density and phase fluctuations for particle numbers corresponding to many-body bound, critical and scattering states (see legend) for stronger interactions and larger particle numbers than considered in the main text. In panels a) and b) we use $\alpha = 10$ ($N_{\text{cr}} = 21$) while in c) and d) we show results for $\alpha = 13$ ($N_{\text{cr}} = 27$). We show the Bose-gas density in panels a) and c), where symbols are results obtained with the IM-SRG and solid curves correspond to mean-field results (Eqs. (5.4), (5.8)). In panels b) and d) we show phase fluctuations. In panel b) all phase fluctuations are calculated with respect to $x' = 0$. In panel d), the curves connected with dashed lines also correspond to $x' = 0$ while the ones connected with dotted lines have $x' = L/2$ (see legend). The dashed/dotted curves are plotted to guide the eye. The numerical error bars are calculated according to the prescription given in 2.3.

condensate. At the point where these two states mix, a significant increase in phase fluctuations is observed¹⁶. We want to stress that the co-existence of two condensates is a hypothesis and a systematic study with increasing impurity-boson interaction (i.e. increasing N_{cr}) is needed to understand the corresponding beyond-mean-field effects from the bottom-up and to justify the two condensate ansatz. Nevertheless, using this ansatz might allow for a better understanding of the few-to-many-body crossover for systems with attractive impurities.

To better understand the transition from the many-body bound state to the scattering state, one can study the excitation spectrum. This is motivated by a recent paper, Ref. [65], where a very similar system was studied: A balanced Bose-gas mixture with interspecies attraction and intraspecies repulsion. There, the focus was on the transition from a homogeneous to a self-bound droplet state. It was studied by increasing particle numbers from $2 + 2$ up to $6 + 6$ particles. The authors of Ref. [65] argued that the transition can be interpreted in terms of a few-body spontaneous phase transition. Signs of this transition were visible, e.g., in the excitation spectrum. Our system is strongly connected with the system studied in Ref. [65]. The main difference is that instead of a balanced Bose-gas mixture, there is a strong asymmetry in the particle numbers: We have only one attractive particle of species “a” (the impurity) and N particles of species “b” (our bosons). However, the basic mechanism behind the localization from a homogeneous state to a droplet state is the same: Bosons are bound to the attractive species. Consequently, advancing the study of our impurity system with the numerical methods of Ref. [65] will allow us to use our insights into the binding properties of the impurity to shed more light on the few-to-many-body crossover of this transition.

We show in Fig. 5.7 a plot of the excitation spectrum for a mobile impurity of mass $m = M$ for different total momenta P . These data have been calculated by Lila Chergui using an importance truncated CI calculation together with a running coupling constant approach (see Chap. 3) [190]. We observe the same signature of a spontaneous phase transition as in Ref. [65]: There is an excitation whose energy first decreases as a function of the impurity-boson interaction strength and then increases again¹⁷. At the same time, we can see that there also exist states, whose excitation energy becomes small for strong interactions and remains nearly constant. This behavior is a typical sign of a spontaneous phase transition

¹⁶If we have weaker impurity-boson interactions, a smaller number of bosons is bound. Additionally, the spatial extension of the bound state is larger, see Eq. (5.4.2), which means that there is an overall lower probability of finding bound bosons. Therefore, the incorrect approximation that they also occupy scattering states might not have an important influence on the validity of the MFA.

¹⁷Note that the flow equation method becomes unstable in the region where this excitation has its minimum: For the flow equation method to work, there has to be a gap in the excitation energy spectrum, see e.g. Refs. [68, 70].

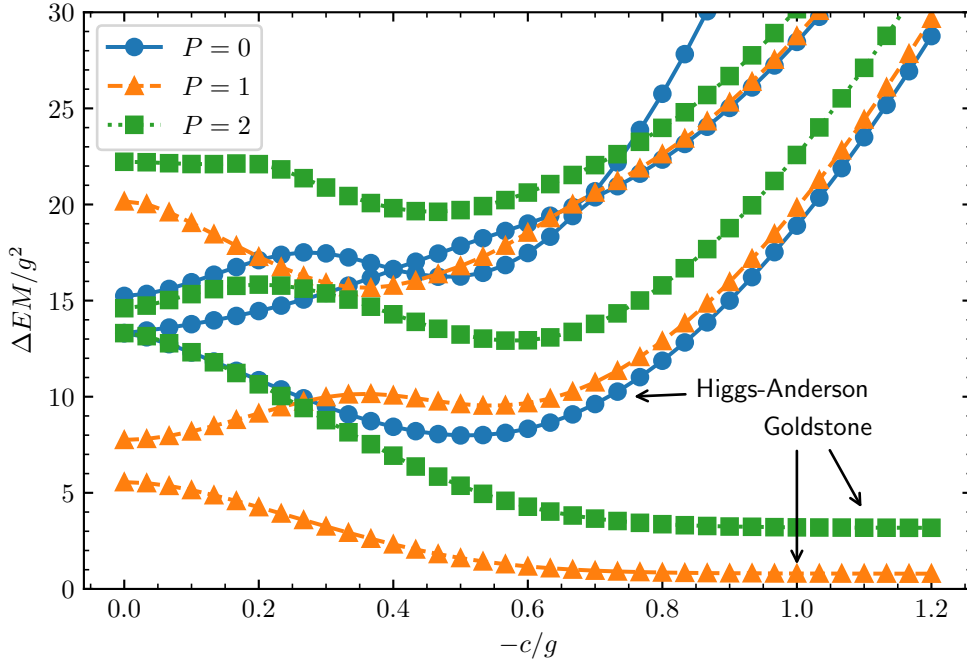


Figure 5.7.: **Excitation spectrum for a mobile impurity.**

We show the excitation energy spectrum, $\Delta E = E_i - E_0$, as a function of the relative interaction strength α for $N = 6$ bosons with equal impurity and boson mass $m = M$. In this plot, we use the boson-boson repulsion to set the units, the remaining length scale is $LMg = 0.6\pi$. Different symbols/line styles correspond to different values of the total momentum (see legend). We also denote which excitations we characterize as Higgs-Anderson and Goldstone modes. The data are obtained using an importance truncated configuration interaction method calculation with a plane wave basis and 60 one-body basis states. To improve convergence, a running coupling constant approach was used, see Chap. 3. The data shown in this plot was calculated by Lila Chergui [190].

where the former excitation can be related to a Higgs-Anderson mode while the latter corresponds to Goldstone modes [9, 42, 52, 206–208]¹⁸. The interpretation of these

¹⁸Because we have a finite number of particles, the Higgs-Anderson mode minimum is non-zero and also the Goldstone modes in the strongly attractive limit still showcase a non-zero energy.

modes is that we have a spontaneous transition from a homogeneous superfluid to a localized bosonic droplet, which breaks the translational symmetry of the system¹⁹.

This discussion shows that the system studied in this chapter provides important foundations for future few-to-many-body studies of phase transitions, see Refs [9, 42, 52, 65, 206–208] for related works in the context of cold atoms. The results from this chapter allow for a deeper physical insight into binding of bosons to the impurity. For example, one can estimate the position of the Higgs-mode minimum via the critical binding condition.

¹⁹Note that this transition only occurs for a mobile impurity. For an impurity potential, the translational symmetry is explicitly broken.

6. Two-dimensional bosonic droplets in a harmonic trap

In this thesis, the focus was so far on one-dimensional systems. Motivated by recent experimental advances in few-to-many-body studies of two-dimensional (2D) fermions [42–44, 117], we now extend our study to 2D systems. Specifically, we investigate a system of attractively interacting bosons. Hammer and Son showed that the ground state of this system exhibits universal behavior when the interaction is of zero range: for a large particle number, $N \gg 1$, it forms a droplet state whose binding energy depends solely on the two-body ground-state energy and increases exponentially with each added particle [39]. Further, the shape of the ground state of the system is not changed when the particle number is increased; there is only a change in its radius by a given factor.

As explained in the introduction, Chap. 1, typically one defines a “many-body system” as a one in the thermodynamic limit (i.e., infinitely many particles), where the addition of particles does not change the system’s properties. However, this definition does not hold for two-dimensional attractive bosons, as increasing the particle number always decreases the ground state energy. Instead, we define the system as many-body once the particle number is large enough to show universal behavior. Further increasing the particle number leaves relative properties of the system, such as the energy ratio, E_{N+1}/E_N , unchanged. In Ref. [209] it is shown numerically that for more than twenty particles the universal relations of Ref. [39] hold.

In this chapter, we investigate the influence of a harmonic trap on the results of Ref. [39]. More specifically, we focus on the transition between a trap-dominated state and an interaction-dominated droplet state. Using a variational approach, we show that this transition occurs abruptly at a critical interaction strength, whose value becomes universal (when properly scaled with particle number) as the particle number increases. This chapter addresses the second goal of the thesis “Connect many-body concepts with the description of few-to-many systems” by using concepts from the classical description of phase transitions to further characterize the transition. Therefore, we analyze the static response of the Bose gas, which is related to the isothermal compressibility. Furthermore, we add to the third goal, “Explore basic physics of few-body systems to facilitate new

many-body research”, by performing *ab initio* calculations for a small number of particles to examine the influence of finite-range effects on this transition. We find that such interactions wash out the point of transition.

Our results pave the way for future few-to-many tests on the emergence of universality in 2D. This applies not only to experimental realizations of this system but also to future *ab initio* investigations of the transition starting from just a few particles. Such theoretical studies will lead to a deeper understanding, for example, by further exploring the influence of small finite-range effects or by examining precursors of quantum phase transitions, similar to studies on 2D fermions [42, 52].

Parts of this chapter have been published in this or similar form in our manuscript “Two-dimensional bosonic droplets in a harmonic trap” [210]. Note that the implementation of the configuration-interaction method used in Subsec. 6.3.3 of this chapter was provided by the Lund cold atom group, see, e.g., Refs. [8, 9].

6.1. Introduction

In their study on attractively interacting bosons in 2D, Hammer and Son utilized the scale invariance of the 2D contact interaction to introduce a renormalization group (RG) improved coupling constant [39]. This allowed them to describe the system employing a mean-field ansatz, with which they showed that the system exhibits universal properties. For a sufficiently large number of particles, the ground state of the system is completely characterized by the two-body binding energy. Adding an additional boson to the system simply leads to a change in the characteristic size of this state, $R_{N+1}/R_N = 0.3417$, while the (negative) energy decreases by a factor of $E_{N+1}/E_N = 8.567$. These findings were later confirmed by *ab initio* calculations [209, 211, 212], which showed that indeed the predicted energy ratio is approached with increasing particle number.

So far, there has been no experimental verification of these results. Due to the exponentially shrinking size, testing these predictions experimentally is challenging. Techniques developed for few-to-many studies must be employed, such as increasing the particle number one by one. As discussed in Chap. 1, cold atomic gases offer a promising platform for realizing such investigations. Two-dimensional bosonic systems have already been prepared, as demonstrated in Ref. [213], and recent few-to-many-body experiments in 2D have shown sufficient control over the particle number, though primarily in fermionic setups [42–44, 117].

A key difference between standard cold-atom experiments and the system described in Ref. [39] is the presence of harmonic confinement, which introduces an additional length scale. As a result, the findings of Ref. [39] apply only when interactions are strong enough

for the trapping potential to be negligible, i.e., when R_N is considerably smaller than the length scale set by the trap. In the opposite limit of weak interactions, properties of the system must be primarily driven by the trapping potential. This chapter aims to provide insight into the transition between these two regimes. Specifically, we show that this transition occurs at a critical interaction strength in the many-body limit. The value of this interaction strength becomes universal if properly scaled, revealing information about universality in 2D. This might allow for future experimental few-to-many-body studies on its emergence. Additionally, our results motivate further *ab initio* studies on attractively interacting bosons in 2D trapped systems, see Sec. 6.4.

In this chapter, we lay the groundwork for such studies by presenting an intuitive physical picture based on a simple variational mean-field ansatz. This ansatz incorporates both the trapping potential and the RG improved coupling constant, allowing us to accurately describe the two limits of the system: the harmonic oscillator ground state and the universal many-body bound state. As we will discuss, the transition between these two states can be induced by varying two experimentally tunable parameters: the scattering length (e.g., through Feshbach resonances [27]) and the trapping frequency, as illustrated in Fig. 6.1. We further characterize this transition using concepts of the standard description of phase transitions by introducing an observable, the static response of the Bose gas, which is closely related to the isothermal compressibility [214]. This observable shows different behavior for the two states of the system and can be measured by changing the trapping frequency or the scattering length [74, 215]. Furthermore, while finite-range effects are typically small in cold atom systems [18, 23], previous studies have shown that even small finite-range corrections can have a surprisingly large influence in 2D [216]. Therefore, we also explore the influence of finite-range effects on the transition using *ab initio* methods for a few particles.

We also mention a relevant recent study, Ref. [217], which examined bosonic droplets on the surface of a sphere. Due to the curvature of the sphere, another length scale is introduced. Using Monte Carlo simulations, this work showed that for a large number of bosons, an analog of a first-order phase transition occurs between a homogeneously distributed ground state and a localized droplet state. The findings of Ref. [217] help motivate certain aspects of the variational ansatz used in this chapter.

This chapter is structured as follows: In Sec. 6.2, we introduce the system and provide key physical intuition, including a brief explanation of the ansatz from Ref. [39]. We then discuss the methods used in this chapter. We present our main results in Sec. 6.3. We start by discussing the outcome of the variational ansatz, and we compare it to perturbation theory. Then we calculate the static response, demonstrating that it allows one to distinguish between the two states of our system. Finally, we discuss the influence of finite-range effects. In Sec. 6.4, we summarize our findings and outline future research

perspectives. Additional details are provided in App. D.

6.2. Formulation and Methods

6.2.1. System

We study a system of attractively interacting bosons in a two-dimensional harmonic trap. The system's Hamiltonian is given by

$$H = \int d\vec{x} \left[\frac{1}{2} |\nabla\psi(\vec{x})|^2 + \frac{\omega^2 \vec{x}^2}{2} |\psi(\vec{x})|^2 + W \right], \quad (6.1)$$

where $\psi(\vec{x})$ is the bosonic field annihilation operator, with $N = \int d^2x \psi^\dagger(\vec{x})\psi(\vec{x})$ representing the number of bosons. The operator W describes the boson-boson interaction, $W = - \int d\vec{x}' \psi^\dagger(\vec{x})\psi^\dagger(\vec{x}')V(\vec{x} - \vec{x}')\psi(\vec{x}')\psi(\vec{x})$, where the positive function V defines the interaction potential. In the main part of this chapter, we use a contact interaction, $V(\vec{x} - \vec{x}') = g\delta(\vec{x} - \vec{x}')$ with $g > 0$. Zero-range interactions typically provide an accurate description of ultracold gases [18, 23], however, in Sec. 6.3.3, we will also consider an interaction potential with finite range. We show a sketch of the system in Fig. 6.1.

We use a system of units such that $\hbar = m = 1$. We choose to keep the trapping frequency ω to highlight the additional length scale introduced by the trap. To present our results in a dimensionless form, lengths are shown in terms of the harmonic oscillator length $l_{\text{HO}} = \sqrt{\frac{1}{\omega}}$ and energies in terms of ω .

In 2D, the effective range expansion exhibits a logarithmic dependence on the scattering length [218], specifically on $\ln(ka)$, where a is the scattering length and k is the wave number. This implies that the interaction strength g in 2D depends on the considered length/momentum scales. This is used in Ref. [39], where standard RG arguments are employed to introduce a coupling constant for the many-body problem that “runs” with the many-body ground-state energy E , or more specifically, with the characteristic width of the many-body bound state R (connected to E by $E \sim 1/R^2$):

$$g(R) = -\frac{4\pi}{\ln(R^2 B_2)}. \quad (6.2)$$

Here, $B_2 = -E_2$ is the two-body binding energy in free space¹. This equation implies that for a given B_2 , the interaction strength is determined by the size of the many-body

¹The two-body binding energy can be used to define the 2D scattering length as $a = 2e^{-\gamma} \sqrt{1/B_2}$ [218], where γ is the Euler-Mascheroni constant.

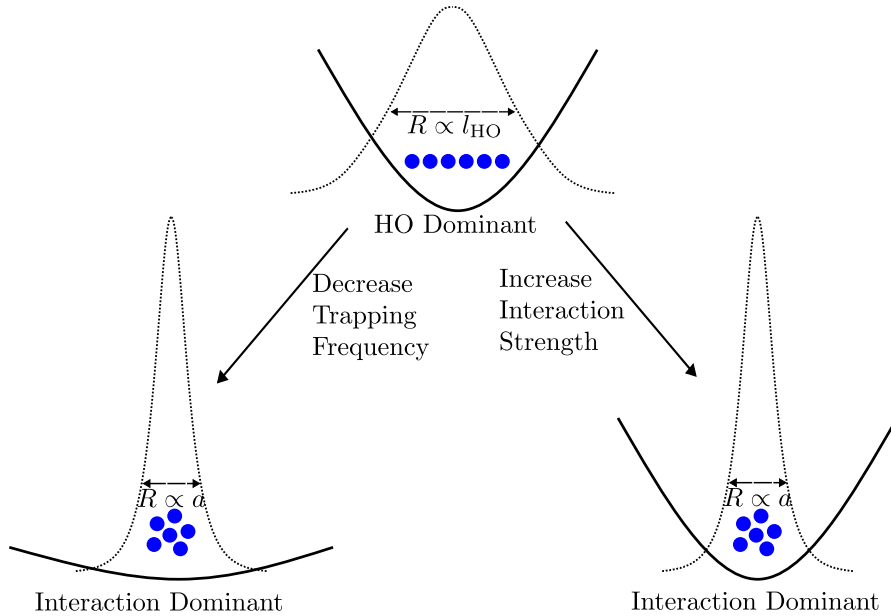


Figure 6.1.: **Sketch of the system.**

Blue balls represent N attractively interacting bosons in 2D. Solid curves display the harmonic confinement. Dashed curves illustrate the density of the bosons. For the trap-dominated regime, the density profile has a Gaussian form while in the interaction-dominated regime, it follows the universal shape found Ref. [39]. In particular, it has an exponentially decaying tail. The characteristic size for the former case is determined by the harmonic oscillator length l_{HO} , while in the latter it is given by the scattering length a . As we show in our sketch, the transition between the two regimes can be induced either by tuning the scattering length, such that the interaction strength is increased, or by decreasing the trapping frequency. Figure taken from Ref. [210].

bound state (equivalently, its energy), such that the size is maximized (and the energy minimized). In the following discussion, we will use the dimensionless quantity B_2/ω as the relevant scale for the interaction.

Basic Physical Considerations

Let us now provide some physical intuition into the properties of the system. First, we summarize the results of Ref. [39] where Eq. (6.1) was studied without an external

trapping potential, i.e., with $\omega = 0$. In this work, the RG improved coupling constant was introduced, effectively replacing the bare coupling constant with the full multiple scattering series. To describe the system, a mean-field ansatz, $\psi(\vec{x}) \sim \Psi(\vec{x})$, where $\Psi(\vec{x})$ is a single particle orbital, was used (for other applications of the mean-field ansatz in the context of one-dimensional systems see Sec. 2.5 and Chaps. 4, 5):

$$\Psi(\vec{x}) = \frac{\sqrt{N}}{R_{\text{free}}\sqrt{2\pi C}} f_{\text{free}}(r/R_{\text{free}}) \quad (6.3)$$

with $r \equiv |\vec{x}|$. The constant C is chosen such that the particle number is conserved, $C = \int d\rho \rho f_{\text{free}}^2(\rho)$.

The characteristic width R_{free} and shape f_{free} are found by minimizing the expectation value of the Hamiltonian, H . The corresponding relation for the ground-state energy reads

$$E(R_{\text{free}}) = \frac{A}{2C} \frac{N}{R_{\text{free}}^2} - \frac{B}{4\pi C^2} \frac{g(R_{\text{free}})N^2}{R_{\text{free}}^2}, \quad (6.4)$$

where $A = \int d\rho \rho [f'_{\text{free}}(\rho)]^2$, $B = \int d\rho \rho f_{\text{free}}^4(\rho)$. Note that the parameter R_{free} depends on N . We indicate this fact with a subscript N when needed. Minimization shows that for a large number of particles, $N \gg 1$, the ground state of the system is described by a universal many-body bound state. This state has a shape f_{free} that is independent of the number of particles, and its energy and width change with the addition of each particle, following the ratios, $E_{N+1}/E_N \approx 8.567$ and $R_{\text{free},N+1}/R_{\text{free},N} \approx 0.3417$.

Now, let us include the harmonic trapping potential to provide an intuitive picture of the relevant physics. This leads to the following ground-state energy

$$E(R) = \frac{A}{2C} \frac{N}{R} - \frac{B}{4\pi C^2} \frac{g(R)N^2}{R^2} + \frac{R^2}{l_{\text{HO}}^4} \frac{ND}{2C} \quad (6.5)$$

with $D = \int d\rho \rho^3 f^2(\rho)$. Note that now the parameters A , B and C are determined by the unknown shape f . If the interactions are strong, the width of the universal many-body bound state in free space is significantly smaller than the harmonic oscillator length, $R_{\text{free}} \ll l_{\text{HO}}$. In this regime, we can approximate $R \approx R_{\text{free}}$ and, hence, the effect of having the trapping potential, $\omega \neq 0$, is negligible. Thus, the system is well-described by Eq. (6.4) and the ground state corresponds to the universal many-body bound state found in Ref. [39]. In the opposite case of weak interactions, the size of the many-body bound state in free space becomes considerably larger than the harmonic oscillator length, $R_{\text{free}} \gg l_{\text{HO}}$. In this regime, the interaction term is small and the ground state is primarily dictated by the trap, i.e. $R \approx l_{\text{HO}}$ and $f \approx f_{\text{HO}}$, the ground state of the 2D harmonic oscillator. We sketch these two limits in Fig. 6.1.

6.2.2. Methods

Variational Ansatz

Following our discussion above, we use the variational ansatz²

$$\Psi(\vec{x}) = \frac{1}{\mathcal{N}} (\alpha_{\text{HO}} f_{\text{HO}}(r) + \alpha_{\text{free}} f_{\text{free}}(r/R)) \quad (6.6)$$

to study the transition between the two limits of the system. f_{HO} is the ground state of a 2D harmonic oscillator

$$f_{\text{HO}}(r) = \sqrt{\frac{1}{l_{\text{HO}}\pi}} e^{-\frac{r^2}{2l_{\text{HO}}^2}}. \quad (6.7)$$

The variables α_{HO} and α_{free} are variational parameters; \mathcal{N} is a normalization coefficient. The characteristic width of the state is given by R . The physical intuition discussed above helps us to determine this width: if R_{free} is smaller than the harmonic oscillator length, we set $R = R_{\text{free}}$; otherwise we use $R = l_{\text{HO}}$. To calculate R_{free} we minimize Eq. (6.4) using the shape f_{free} for the calculation of A, B, C .

The values of α_{HO} and α_{free} determine the properties of the ground state. To find these parameters, we minimize the expectation value of H for a given interaction strength, i.e., for a given two-body binding energy in free space B_2/ω . As we will show below, this approach allows us to characterize the transition between the harmonic oscillator state and the universal many-body bound state. A more detailed explanation of our variational ansatz, including all relevant equations, is provided in App. D.1.

Configuration interaction method

Besides the variational study, we also perform *ab initio* calculations to study the influence of finite range effects on the transition. For this purpose, we use the configuration interaction (CI) method [8, 9], introduced in Sec. 2.2.

For our one-body basis, we use the eigenfunctions of the non-interacting system, i.e., the eigenfunctions of the 2D harmonic oscillator (for simplicity, we set $\omega = 1$ in this equation):

$$\Phi_i(\vec{x}) = \frac{1}{\sqrt{2\pi}} e^{im_i\phi} F_{n_i, m_i}(\rho) = \frac{1}{\sqrt{2\pi}} e^{im_i\phi} (-1)^{n_i} \sqrt{\frac{2\Gamma(n_i + 1)}{\Gamma(|m_i| + n_i + 1)}} e^{-\rho^2/2} \rho^{|m_i|} L_{n_i}^{|m_i|}(\rho^2). \quad (6.8)$$

²Note that we also used another ansatz where both shapes scale with R , $\Psi(\vec{r}) \sim \alpha_{\text{HO}} f_{\text{HO}}(r/R) + \alpha_{\text{free}} f_{\text{free}}(r/R)$ which leads to similar results and the same conclusions. The main difference between the two approaches is that the ansatz used in this chapter leads to a sharp transition, in agreement with Ref. [217], while the other ansatz results in a smooth crossover. For more details, we refer to App. D.2.

The index i is the index of the basis state while n_i and m_i are the corresponding radial and angular quantum numbers. $L_{n_i}^{|m_i|}$ is the generalized Laguerre polynomial. The eigenenergy of this state is

$$E_{m_i, n_i} = (2n_i + |m_i| + 1)\omega. \quad (6.9)$$

To limit the size of our one-body basis, we introduce a cutoff at $n_{2D} = 13\omega$, including all one-body basis states with energy less than or equal to this cutoff. As we are only interested in calculating the ground state properties of our system and because our interactions conserve the angular momentum of the system, we restrict the many-body basis to a total angular momentum of zero. Due to the attractive interaction, the ground state is localized at the trap's center, requiring many basis states to resolve it accurately. To improve convergence, we use a larger trapping frequency for the one-body basis than for the system: $\omega_{\text{basis}} = 4\omega_{\text{system}}$, resulting in a higher “resolution” in the center of the trap. This approach allows us to obtain converged results for stronger interactions than would be possible if we used the same frequency.

As a finite-range interaction we use a Gaussian potential given by

$$V(\vec{x}) = \frac{g}{2\pi\sigma^2} e^{-\vec{x}^2/2\sigma^2}, \quad (6.10)$$

$g > 0$, $\sigma > 0$, in Eq. (6.1). To compare the results obtained with this potential to those using a contact interaction, we calculate B_2 numerically. To this end, we expand the two-body Schrödinger equation in free space using harmonic oscillator eigenfunctions and then diagonalize the Hamiltonian matrix. Here, we can use a much larger number of basis states (up to 500) since we effectively solve a one-body problem in the relative coordinates.

We estimate the size of finite-range effects by calculating the scattering length and the effective range of our Gaussian potential. For the scattering length, we use the semi-analytical expression from Ref. [110]. To obtain the effective range, we use the expression [216]:

$$B_2 = -\frac{1}{r_{\text{eff}}^2} W\left(-2e^{-2\gamma} \frac{r_{\text{eff}}^2}{a^2}\right), \quad (6.11)$$

with r_{eff} the effective range. W is the product logarithm, also known as the Lambert W function, defined as the solution of $z = we^w$ with $W(z) = w$. Then, by inserting the scattering length, a , and the two-body ground-state energy in free space, B_2 , we extract the effective range, r_{eff} .

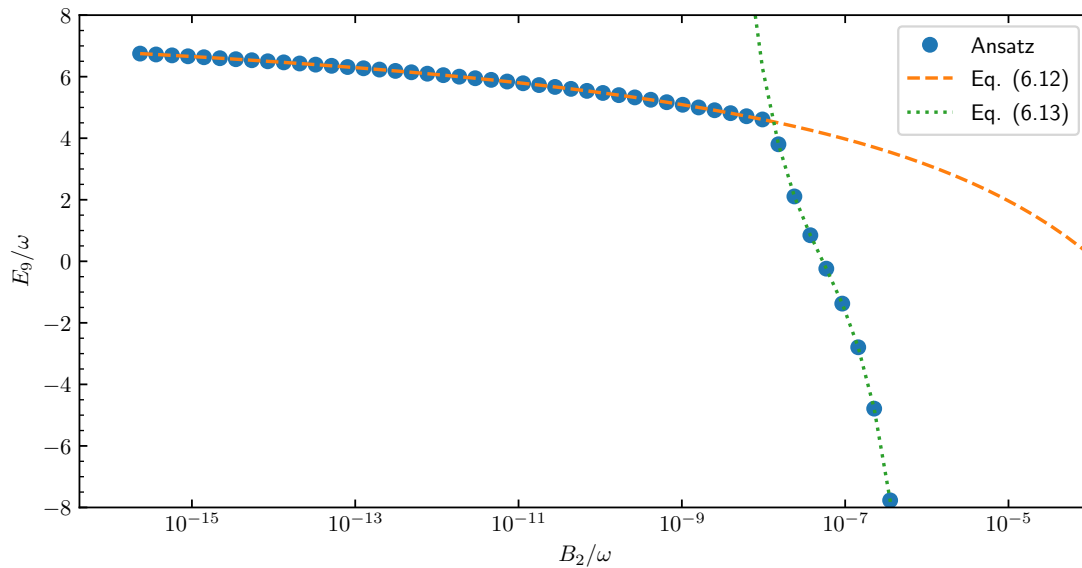


Figure 6.2.: **Energy for $N = 9$ as a function of the binding energy.**

The dots are obtained from the variational ansatz, Eq. (6.6). The results obtained from perturbation theory, see Eqs. (6.12), (6.13), are shown by dashed/dotted lines. Figure modified from Ref. [210].

6.3. Results

6.3.1. Minimization of variational ansatz

Let us begin by discussing the results of the minimization procedure applied to the variational ansatz.

Comparison with perturbation theory

Fig. 6.2 shows typical energies calculated via minimization of our ansatz, Eq. (6.6), as a function of the two-body binding energy B_2/ω . For comparison, we also include energies from perturbation theory, which is constructed for the two limiting cases discussed earlier: $B_2/\omega \rightarrow 0$ (weak boson-boson interactions) and $B_2/\omega \rightarrow \infty$ (strong boson-boson interaction).

For weak interactions we assume that the contact interaction is only a small perturbation

to the Hamiltonian of a 2D harmonic oscillator, and we calculate the energy

$$E(B_2/\omega \rightarrow 0) = N\omega - \frac{g(R=l_{\text{HO}})}{2} N^2 \int d^2x f_{\text{HO}}(\vec{x})^4. \quad (6.12)$$

Note that this integral can be evaluated analytically, yielding $E(B_2/\omega \rightarrow 0) = N\omega - \frac{g(R=l_{\text{HO}})}{4\pi} N^2$. We used that the characteristic width of the ground state, R , is determined by the harmonic oscillator length in this limit, i.e. $R = l_{\text{HO}}$. In the opposite limit of strong interaction, we treat the harmonic trapping potential as a perturbation, resulting in

$$E(B_2/\omega \rightarrow \infty) = E(R_{\text{free}}) + \frac{\omega^2 ND}{2C} R_{\text{free}}^2 \quad (6.13)$$

with $E(R_{\text{free}})$ from Eq. (6.4) and C and D calculated using $f = f_{\text{free}}$.

As shown in Fig. 6.2, perturbation theory is in excellent agreement with our variational ansatz. This allows us to study the ground-state energy in a simple manner. For example, we use perturbation theory to estimate the critical interaction strength at which the state of the system changes, i.e. the crossing of the energies in Fig. 6.2. To find this point, we calculate the value of B_2/ω where the energies given by Eqs. (6.12) and (6.13) are equal. We find that this occurs when $R_{\text{free}} = l_{\text{HO}}$, consistent with the outcome of the minimization calculation. Using Eq. (6.2) and $g(R_{\text{free}}) = \frac{2\pi AC}{NB}$ (as found in Ref. [39] for large N), we calculate the critical interaction strength to be

$$\frac{\ln(B_2/\omega)}{N} = -2.148. \quad (6.14)$$

The fact that $\ln(B_2/\omega)/N$ remains constant at the transition point indicates that this is the appropriate measure of interaction strength in our study. As we will demonstrate, the transition point converges to this value as N increases. This finding is consistent with Ref. [217], where a Monte Carlo calculation showed that, as the particle number increases, the transition between the non-interacting state and the universal many-body bound state converges to $\ln(B_2/\tilde{E})/N = -2.148 + \mathcal{O}(1/N)$, where \tilde{E} is the relevant energy scale in that work.

An examination of the variationally optimized values of α_{HO} and α_{free} reveals that for all particle numbers and interaction strengths, one of these parameters is always zero. This implies that, for any interaction strength, the system's ground state is described either by f_{HO} or f_{free} (see also App. D.1). As a result, we observe a sharp transition between the two states for all particle numbers. This behavior is an intentional feature of our ansatz, inspired by the findings of Ref. [217] for bosons on a sphere. In reality, a sharp transition can only occur for large particle numbers, $N \gg 1$; for smaller particle numbers, the ground-state energy is expected to be a smooth function of the parameters³.

³Here, we assume the absence of any symmetry that could cause a crossing of energy levels.

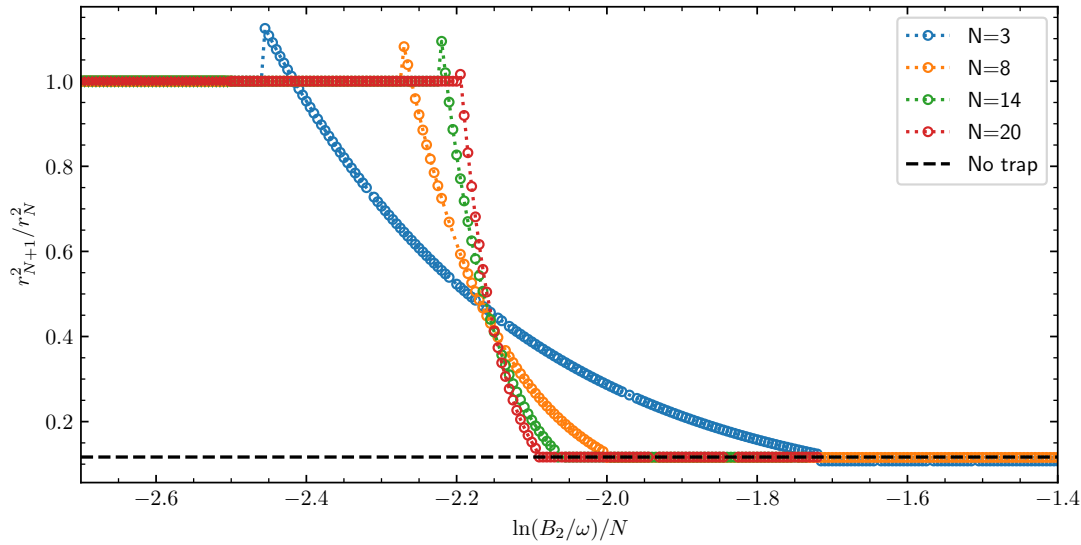


Figure 6.3.: **Ratio of the mean-square radius r_{N+1}^2/r_N^2 as a function of the interaction strength $\ln(B_2/\omega)/N$.** Symbols are the results obtained from the minimization of the energy with our ansatz, Eq. (6.6). The black dashed line is the universal prediction from Ref. [39]. Figure modified from Ref. [210].

Ratio of the radii

Fig. 6.3 also shows the ratio of the mean-square radius r_{N+1}^2/r_N^2 with⁴

$$r_N^2 = \frac{1}{N} \int d^2x \Psi^2(\vec{x}) \vec{x}^2. \quad (6.15)$$

This ratio is a key feature of the universal many-bound state in 2D found in Ref. [39].

For weak interactions, it corresponds to that of non-interacting bosons in a harmonic oscillator, where $r_{N+1}^2/r_N^2 = 1$. For strong interactions, we recover the universal ratio predicted in Ref. [39], with $r_{N+1}^2/r_N^2 \approx 0.116$. Between these two limits, the ratio initially increases slightly above one before decreasing rapidly. This behavior arises because the transition from the trap-dominated to the interaction-dominated state occurs at larger particle numbers for weaker interactions, as shown in the figure. Therefore, as long as the $N + 1$ system is dominated by the interactions, the ratio of the mean-square radii

⁴Note that $\Psi(\vec{x})$ is dependent on N because of the normalization condition.

decreases. The sharp increase from a ratio of one to a value slightly greater than one is due to our ansatz: When the two-body binding energy becomes large enough such that $R_{\text{free}} \leq 1$, the state becomes interaction-dominated, i.e. $\alpha_{\text{HO}} = 0$, $\alpha_{\text{free}} \neq 0$. We can then compute the mean-square radius for $R_{\text{free}} = l_{\text{HO}}$

$$r_N^2 = 2\pi l_{\text{HO}}^2 \int d\rho \rho^3 f_{\text{free}}^2(\rho) \approx 1.2 l_{\text{HO}}^2. \quad (6.16)$$

This represents the maximum value of r_{N+1}^2/r_N^2 , observed in Fig. 6.3.

Most importantly, Fig. 6.3 confirms our estimate for the transition point using perturbation theory, Eq. (6.14). For all considered particle numbers, the transition consistently occurs around $\ln(B_2/\omega)/N \approx -2.2$. While there is a slight dependence on particle number, the transition point converges to the same interaction strength as N increases. This showcases that indeed, as described in the introduction of this chapter, the transition point contains information about universality in 2D and can therefore be used in future *ab initio* studies to test its emergence from few-body physics.

However, given the logarithmic scaling with B_2/ω , detecting the transition requires large and precise values of the scattering length, $a \propto B_2^{-1/2}$. The harmonic trapping confinement can mitigate this challenge: adjusting the trapping frequency offers another way to tune the value of B_2/ω . This added degree of freedom could make it easier to observe the transition experimentally and thus study the emergence of universality in 2D.

6.3.2. Transition indicator: static response

Even with the ability to tune both the trapping frequency and the scattering length, detecting the transition via the ratio of the mean-square radii (or energies) might be very challenging: Due to the exponential scaling, there is only a small experimental window to tune the values of B_2 and ω ; not only for one but for two experimental runs with different particle numbers. However, as we will show below, the mean-square radius on its own contains valuable information about the transition between the two states. In the following, we will use this to calculate another observable, inspired by the standard description of phase transitions, which relies solely on the mean-square radius for a single particle number. Furthermore, this also illustrates the general fact that concepts developed for the description of phases in the thermodynamic limit can be adapted for distinguishing the two states of our system, even though we have a finite number of particles.

Recall that different phases exhibit significantly different properties, such as compressibility [15]. Using linear response theory, it can be shown that the isothermal compressibility of a uniform system is closely related to the so-called static response (or polarizability) χ ,

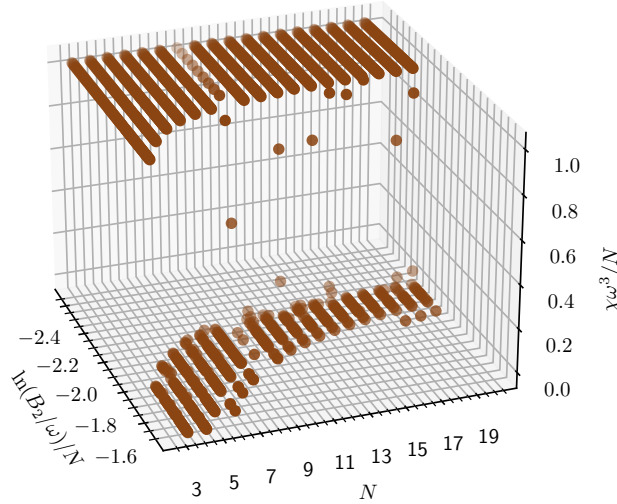


Figure 6.4.: **Static response per particle, Eq. (6.17), as a function of the interaction strength $\ln(B_2/\omega)/N$ and particle number N .**

All points are calculated with our variational ansatz, Eq. (6.6). Note that the calculation of the static response close to the transition point requires a high numerical precision for the evaluation of the derivative, see Eq. (6.17). Figure taken from Ref. [210].

which describes how the density of a system responds to a static force field⁵ [214].

For a harmonically trapped system, χ can be directly calculated from the change in the mean-square radius when the trapping frequency is varied (in this context, χ is also called monopole compressibility) [74, 215]. Consider a small change in the trapping frequency, ϵr^2 . Then, the static response χ is given by $\delta \langle r^2 \rangle = \epsilon \chi$. It can be expressed as⁶

$$\chi = -2N \frac{\partial \langle r^2 \rangle}{\partial (\omega^2)}. \quad (6.17)$$

This observable allows us to distinguish between the two phases without needing to

⁵This is known as the compressibility sum rule.

⁶In our practical calculations, we use a system of units where $\omega = 1$. Thus, we need to convert the derivative with respect to the trapping frequency to a derivative with respect to B_2 , our interaction strength. This leads to the expression $\chi = N \left(B_2 \frac{\partial \langle r^2 \rangle}{\partial B_2} + \langle r^2 \rangle \right)$.

compare different particle numbers at the same two-body binding energies, significantly simplifying the detection of the transition point.

For weak interactions, our system is described by the harmonic oscillator ground state, where the mean-square radius naturally scales with the trapping frequency. Hence, we expect the static response to be $\chi = N/\omega^3$. In the opposite limit of strong interactions, we use the results of Ref. [39] to identify $R^2 \propto \langle r^2 \rangle$ so that $\langle r^2 \rangle \propto \frac{1}{B_2}$. This indicates that the trapping frequency does not influence the state, leading to $\chi = 0$. Thus, the static response should indeed exhibit distinctly different behaviors for the two states of our system.

Fig. 6.4 shows the static response obtained from the minimization procedure as a function of the interaction strength, $\ln(B_2\omega)$ and the particle number N . The plot confirms the expected behavior: for weak interactions, the static response remains constant at $\chi\omega^3/N = 1$ up to the transition point. Beyond this point, the static response drops to zero (within our numerical accuracy). Furthermore, we can see that with increasing particle number, the interaction strength required for this transition converges toward $\ln(B_2/\omega)/N \approx -2.15$, in agreement with our perturbation theory estimate in Eq. (6.14). We conclude, that this observable might not only facilitate the detection of the transition between the two states but also allows for future few-to-many studies on the many-body phenomenon of universality in 2D.

6.3.3. Influence of finite range effects

For the description of cold-atom systems, often zero-range potentials are employed [18, 23]. However, even small effective range corrections can significantly influence the properties of 2D systems, see, e.g., Ref. [216] for a three-boson system in free space. Therefore, it is important to investigate how finite range effects influence the transition⁷. To this end, we employ a Gaussian potential of finite width, as defined in Eq.(6.10), and perform an *ab initio* calculation using the CI method (see Sec. 6.2.2 and 2.2 for an explanation of this method).

We consider Gaussian potentials with widths on the order of the harmonic oscillator length: $\sigma = l_{\text{HO}}/2$ and l_{HO} . These values ensure substantial finite range effects, as we will show below. The width of the potential also acts as a momentum space cutoff, allowing us to perform *ab initio* calculations within the transition region. For strong attractive interactions, such calculations become computationally expensive, preventing us from exploring small effective range corrections⁸ or interactions strong enough for the trapping

⁷Note that for large finite range effects, the many-body bound state is no longer universal; see Ref. [39]

⁸The narrower the Gaussian potential, the smaller the finite range corrections. However, a more narrow Gaussian potential also corresponds to a larger momentum space cutoff.

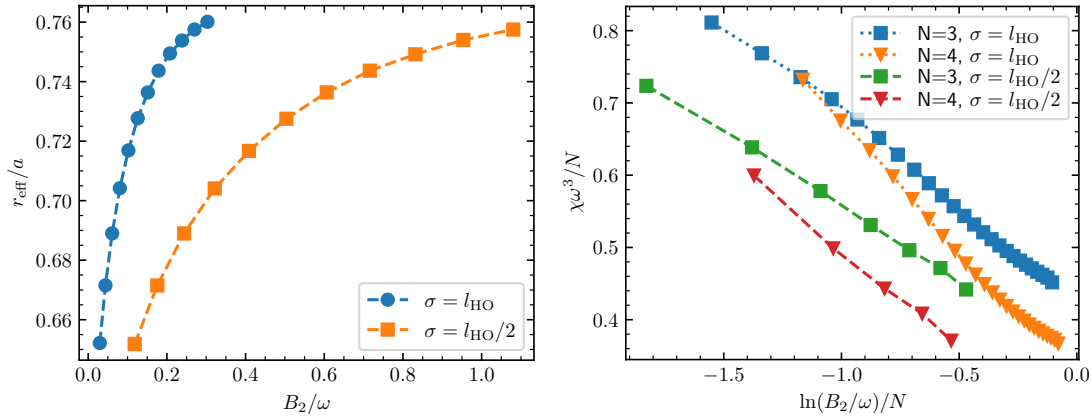


Figure 6.5.: **Finite range effects.**

Left panel: Ratio of the effective range and the scattering length as a function of B_2/ω for a Gaussian potential with $\sigma = l_{\text{HO}}/2$ and $\sigma = l_{\text{HO}}$. Right panel: Static response per particle, Eq. (6.17), calculated with a CI method as a function of the interaction strength given by $\ln(B_2/\omega)/N$. For the interaction we use a Gaussian potential, Eq. (6.10). Squares show results for $\sigma = l_{\text{HO}}$ while triangles are for $\sigma = l_{\text{HO}}/2$. The dashed (dotted) lines are added to guide the eye. Figure modified from Ref. [210].

confinement to become negligible⁹. Despite these limitations, comparing the two widths enables us to assess the impact of finite range effects on the transition.

To estimate the size of finite range effects, we plot the ratio of the effective range to the scattering length as a function¹⁰ of B_2/ω in Fig. 6.5. This figure shows that the influence of the effective range is significant for the chosen parameters; for all considered values of B_2/ω , the effective range cannot be neglected. Note that Eq. (6.11) only accounts for finite range corrections up to the effective range. Given the large values of the effective range, higher-order terms, such as the shape parameter, might also play a role. However, this is not important for us as we are only interested in comparing the size of finite range effects for different σ values. As shown in the figure, the smaller value of σ results in a smaller effective range for the same B_2/ω , indicating that finite range effects are less

⁹Weak attractive interactions also pose challenges, as we calculate the two-body binding energy numerically. For weak interactions, this energy can become exponentially small, making accurate determination difficult.

¹⁰The oscillator units enter the two-body problem via the width of the Gaussian potential which we define with respect to l_{HO} .

significant.

Fig. 6.5 also shows the static response for $N = 3, 4$ particles with the two different Gaussian potential widths as a function of $\ln(B_2/\omega)/N$. We observe that the static response decreases with increasing binding energy. In this *ab initio* calculation, we do not find a sharp transition for small particle numbers as observed in the previous section. Instead, the static response features a steeper decay for larger particle numbers. Note that this is similar to the sharper transition found in Ref. [217] when the particle number was increased for a zero-range potential. Comparing the two σ values reveals the effects of the finite range: the larger σ shifts the decrease in the static response towards higher binding energies. Specifically, compared to the critical interaction strength $\ln(B_2/\omega)/N \approx -2.15$, a significantly stronger attraction is required for the static response to decrease.

Our results highlight the impact of finite range effects on the transition. However, further *ab initio* calculations with larger particle numbers and smaller finite ranges are needed to determine whether the critical interaction strength can be recovered. For future experimental realizations, it will be essential to perform calculations using realistic cold atom potentials to study the emergence of universality in 2D.

6.4. Conclusions

6.4.1. Summary

In this chapter, we studied the transition of attractively interacting bosons in a two-dimensional harmonic oscillator, from the harmonic oscillator ground state at weak interactions to a universal many-body bound state at strong interactions.

Using a physically motivated variational ansatz and perturbation theory, we determined that for sufficiently large particle numbers ($N \gg 1$), this transition occurs at a critical interaction strength, $\ln(B_2/\omega)/N \simeq 2.15$. By calculating the mean-square radius of the system, we confirmed that the ratio $\langle r_N^2 \rangle / \langle r_{N+1}^2 \rangle$ – one of the hallmarks of universality in 2D (see Ref. [39]) – shows an abrupt change in behavior, signaling the transition between the two states when the interaction strength is varied. We observed that the interaction strength at which this change occurs converges toward the critical value as the particle number increases. Since the critical interaction strength depends only on the particle number and the two-body binding energy, it demonstrates that attractively interacting bosons in 2D exhibit universal behavior.

We argued that although very low values of the binding energy B_2/ω are required, the trapping confinement can help in inducing the transition as two experimentally accessible parameters – the scattering length and the trapping frequency – can now be

tuned. However, since detection remains challenging when considering ratios of radii (or energies), we further connected this problem to the classical description of phase transitions, which are typically described in the thermodynamic limit. This connection allows one to study how many-body phenomena, such as the universality of the many-body bound state, emerge from few-body physics. We showed that the static response, which is related to the isothermal compressibility, takes on distinct values for the two states, making it an indicator of the transition. As the particle number increases, the point at which the static response signals the transition converges towards the critical interaction strength.

We further examined the influence of finite range effects through few-body *ab initio* calculations using the configuration interaction method. Our findings revealed that significant finite-range effects shift the transition point to larger values of $\ln(B_2/\omega)/N$ in comparison to the critical interaction strength, Eq. (6.14).

6.4.2. Outlook

Our results pave the way for future experimental few-to-many-body studies on the emergence of universality in 2D. In particular, the ability to tune the interaction strength with two parameters and the possibility of testing universality by measuring the static response make such a study simpler than directly confirming the results of Ref. [39].

Even though we have discussed the effect of finite range interactions on the point of the transition, more *ab initio* calculations are needed to better understand their impact on the emergence of universality in 2D. Especially since Ref. [216] illustrates the strong influence of finite range effects in a three-body system in free space. Such calculations should be performed for realistic cold atom potentials, i.e. for smaller effective range corrections than studied in this thesis. Techniques like renormalized interactions, discussed in Chap. 3, can enhance convergence, potentially allowing for the exploration of stronger interactions and/or narrower Gaussian potentials [53, 112].

Furthermore, we only considered $N = 3, 4$ particles; future few-to-many-body studies need to explore finite range effects with more particles, similar to Refs. [209, 211, 212], which have shown that only if $N > 20$ the universal predictions of Hammer and Son [39] apply. For such large values of N , beyond simple CI methods such as the importance-truncated CI (see, for example, Refs. [64, 65, 79] for applications in ultracold atoms) or Monte Carlo methods, should be utilized.

In this thesis, we used the flow equation approach to study systems with larger particle numbers than possible with the CI method (see Sec. 2.3 for an introduction into this method and Chaps. 4, 5 for applications). We also attempted to apply this method to the problem discussed in this chapter. However, we found that it could not adequately describe

our system. We observed that the flow equation approach worked well only when the interactions were weak enough such that the ground state was dominated by the trapping potential. Once the interactions became stronger, the flow equation approach diverged, signaling that the reference state of our system has too little overlap with the true ground state of the system. We employed various reference states, such as an iterative scheme as explained in Sec. 2.3. For this, we started with the ground state of the 2D harmonic oscillator using varying basis frequencies. We also used the shape found in Ref. [39] as reference state. However, we were unable to include the RG-improved coupling constant in our *ab initio* calculation for the zero-range limit. As shown in Ref. [39], this coupling constant is essential for making a mean-field approximation feasible in the interaction-dominated regime and hence, our reference state, a condensate, cannot be used. A better understanding of the RG-improved coupling constant is needed to incorporate it in *ab initio* calculations, which will hopefully extend the computationally available parameter space. Additionally, further development in the flow equation method, such as the use of a multi-reference state (as applied in nuclear physics to describe open-shell nuclei [70, 219, 220]), may provide a better approximation of the highly correlated ground state and extend the applicability of this method.

Another intriguing aspect of our system is highlighted in Ref. [217]: As briefly mentioned in the main text, the authors of this study observed that the transition between a homogeneously distributed state (i.e. trap dominated) and a localized droplet (i.e. interaction dominated) is smooth for few particles but becomes sharper when the particle number is increased. They concluded that for a large number, a first-order phase transition occurs. It would be worthwhile to conduct few-to-many-body studies to establish a more rigorous criterion for the particle number at which this transition becomes a true phase transition and to determine whether the order of this phase transition is independent of the trapping potential. Furthermore, Ref. [217] and our work have focused exclusively on the ground state of the system. However, excited states might also offer valuable insights into the (phase) transition, similar to the findings in Refs. [42, 52], where excited states in a finite system were interpreted as precursors to a Higgs mode. Such studies could provide additional understanding into the emergence of universality in 2D.

From a methodical point of view, the results of this chapter (along with the divergence of the flow equation approach without the RG-improved coupling constant) further emphasize the importance of using the RG-improved coupling constant from Ref. [39] as a necessary tool for the mean-field description of attractively interacting bosons in 2D. More broadly, it supports the use of modified non-linear equations, such as the Gross-Pitaevskii equation, for describing 2D bosons. Note that this is closely related to earlier studies that demonstrated the need for a density-dependent coupling constant in two-dimensional systems with repulsive interactions (see, e.g., Refs. [221–223]).

7. Summary and Outlook

In this thesis, we contributed to the field of few-to-many-body crossover in systems of low-dimensional ultracold quantum gases by considering three goals.

1. We advanced numerical investigations of this crossover by improving theoretical tools. In particular, we compared different renormalization methods for the one-dimensional contact interaction.
2. Further, we connected many-body concepts with the description of few-to-many systems for a repulsive impurity in a sea of one-dimensional bosons and for a system of two-dimensional attractive bosons trapped by harmonic confinement.
3. Additionally, we explored basic physics of few-body systems that can facilitate new many-body research. We investigated the bound state of an attractive impurity in a one-dimensional Bose gas and we considered finite range interaction for the aforementioned two-dimensional bosons in the few-body sector.

Below, we briefly summarize each chapter and present a short outlook into future research topics. Note that each chapter presenting new research (Chaps. 3, 4, 5, 6), contains a more detailed summary and outlook for the specific system.

In Chap. 2, we introduced the methods used in this thesis. We started with a brief introduction into the description of many-body quantum systems. After that, we explained the *ab initio* methods employed in this thesis: the configuration interaction (CI) method, which we applied in Chap. 3 and Chap. 6, and the flow equation approach for bosons, used in Chap. 4 and Chap. 5. Additionally, we demonstrated how a coordinate transformation to a frame “co-moving” with the impurity simplifies the description of one-dimensional systems with an impurity on a ring. Finally, we briefly reviewed the mean-field approach for bosons, focusing specifically on its application within this thesis.

Further advancement of *ab initio* methods is essential for studies of few-to-many-body physics. As discussed in the introduction, Chap. 1, the challenges faced by *ab initio* studies of this transition are similar to the ones encountered in quantum chemistry and nuclear structure calculations [54, 70, 76, 116]. Adaptation of tools from these fields

could greatly benefit the cold atom community. For example, in nuclear physics, the flow equation approach (also called in-medium similarity renormalization group method), uses the Magnus expansion to accelerate numerical calculations and significantly reduce the computational cost of calculating observables [224]. This approach could potentially be applied to the bosonic formulation of the flow equation method as well. Furthermore, it is worthwhile to extend this technique to fermionic ultracold gases. This could enhance our understanding of the few-to-many experiments on two-dimensional fermions conducted in Heidelberg [42–44]. These systems have been primarily studied using the CI method, which restricts the number of particles to a $3 + 3$ configuration [42]. However, recent experimental progress has enabled the preparation of up to $21 + 21$ fermions [225]. Another option to extend *ab initio* calculations to larger particle numbers, is to employ more sophisticated versions of the CI method such as the importance truncated CI, see Ref. [64] for its introduction in nuclear physics, Refs. [65, 79] for applications in cold atom systems.

In Chap. 3, we discussed another improvement of *ab initio* calculations inspired by nuclear structure studies: the renormalization of interactions to improve the convergence of *ab initio* calculations [116]. Specifically, we compared different renormalization methods for the one-dimensional contact interaction using spin-1/2 fermions in a harmonic trap. We calculated the energy, the density, the expectation value of the one-body Hamiltonian, and transition matrix elements using the CI method. Additionally, we discussed the transformation of observables alongside the renormalization. The results of this chapter can increase the accessible parameter space set by interactions and particle numbers and are valuable for future *ab initio* studies. We found that a simple running coupling constant approach, which uses the two-body ground state energy for renormalization, can serve as a simple ‘go-to’ method to test renormalized interactions. However, the most significant improvement was achieved by using an effective interaction approach based on the full two-body spectrum. Although effective interaction approaches are more complex to implement than a running coupling constant approach, they allow for a transformation of operators alongside renormalization. We found that for some observables, this is crucial to enhance convergence. However, for other observables, it had only a minor impact.

Further research is needed to determine for which classes of operators the transformation alongside the renormalization of interactions is needed. Furthermore, to the best of our knowledge, the application of renormalized interactions has been limited to contact interactions within the cold atom community. Future studies should explore whether this approach is also useful for other types of interactions, such as dipole-dipole interactions. Although our study focused on one dimension, we expect our conclusions to be applicable in higher dimensions as well. We hope that renormalized interactions will eventually become standard in *ab initio* studies in the cold atom community. In particular, incorpo-

rating renormalized interactions with the many-body methods described in Chap. 1 could significantly expand the parameter space available for studies of few-to-many systems.

Next, in Chap. 4, we considered a one-dimensional Bose gas with periodic boundary conditions (i.e., on a ring) and a repulsively interacting impurity coupled to an Aharonov-Bohm flux. We demonstrated that this finite system can be described using concepts from the many-body framework of the Bose polaron, enabling few-to-many studies. This connection allowed for an intuitive and straightforward interpretation of our results for the energy spectrum and currents. We were able to define the effective mass of the polaron in a finite-size system in an experimentally feasible way, which – to the best of our knowledge – was not possible before. We used this to discuss the convergence of the effective mass towards its thermodynamic limit. We found that, due to the high compressibility of the Bose gas, a large number of bosons is required for convergence, with the effective mass converging more slowly than the self-energy. Finally, we discussed the validity of the polaron approximation and studied the impact of defects in the system.

In the future, this setup could be used to study the critical velocity of a one-dimensional impurity. To the best of our knowledge, its value remains unknown for a finite number of particles as well as in the thermodynamic limit. The mean-field approximation predicts a critical velocity higher than the speed of sound, which is clearly unphysical. Therefore, beyond-mean-field effects must account for collective many-body excitations that determine the critical velocity. This makes a few-to-many-body study particularly interesting, as it may help identify these effects, which are crucial to obtain a deeper insight into the dynamical behavior of impurities in one-dimensional systems.

In Chap. 5, we also examined a one-dimensional system with an impurity, however in this case with the focus on an attractively interacting impurity. The attraction between the impurity and bosons leads to a bound state, which complicates many-body studies of the system. We characterized this state, which we called artificial atom of bosons. Using mean-field calculations, we derived an analytical relation for the maximum number of bosons in the bound state as a function of the interaction strengths between the impurity and bosons, as well as among the bosons themselves. We validated these mean-field results using *ab initio* calculations based on the flow equation method for bosons. We found that beyond-mean-field effects are only significant far from the impurity. When the bosons are in the vicinity of the impurity, as for the bound state, the results from the mean-field approach can be applied.

The results of Chap. 5 pave the way for future many-body studies involving attractive impurities. For example, if bosons occupy scattering states, beyond-mean-field effects complicate the description of the system. Our insights into the binding properties may help circumvent this issue by describing the system within an effective theory, using the artificial atom and scattered bosons as the relevant degrees of freedom. This approach

could improve the understanding of attractive impurities in large systems. Additionally, we presented preliminary results on the transition from the homogeneous state of the system to the localized one driven by the interactions. We briefly discussed the excitation energy spectrum, which showed a precursor to a Higgs mode, similar to previous studies on the few-to-many-body crossover [42, 52, 65].

We extended our study to two-dimensional systems in Chap. 6. We investigated a system of attractively interacting bosons, for which Hammer and Son demonstrated that it exhibits universal behavior when the particle number is sufficiently large. For example, the system forms a universal droplet state with a binding energy that increases exponentially with the number of particles [39]. Due to the exponential increase, experimental verification of these results needs to employ few-to-many-body techniques such as increasing the particle number one by one. In this chapter, we studied the influence of harmonic confinement, which is typical for experimental few-to-many-body studies [42–44, 117]. In particular, we discussed the transition from a trap-dominated oscillator state (at weak interactions) to an interaction-dominated droplet state, the universal bound state discussed in Ref. [39]. If scaled appropriately, this transition is independent of the particle number in the many-body regime, showcasing the universal nature of two-dimensional attractive bosons. However, since detecting the transition through ratios of radii or energies – the hallmarks of universality discussed in Ref. [39] – can be challenging, we connected our finite system to the classical description of phase transitions. We introduced the static response of the system which is closely related to the isothermal compressibility and provides an experimentally more accessible indicator of the transition. Lastly, even though cold atom gases are typically well described by zero-range interaction, we tested the influence of finite range corrections on this transition by considering $N = 3, 4$ particles with wide Gaussian potentials and found that the point of transition is washed out.

The results of this chapter provide important groundwork for experimental few-to-many-body tests of universality in two dimensions. In particular, the universal interaction strength which can be tuned with two experimentally available parameters and the static response of the Bose gas might allow for tests of the emergence of universality that are simpler than those of Ref. [39]. Furthermore, our study motivates further theoretical studies employing *ab initio* calculations. In particular, gaining insights of finite range effects for realistic cold atom potentials is needed to better understand the limits of universality in two dimensions. Therefore, other numerical methods should be employed. For example, the techniques described in Chap. 3 might allow to increase the parameter space and go to stronger interactions and/or smaller Gaussian potentials. Another interesting feature is presented in Ref. [217], where a similar transition for a two-dimensional bubble trap was studied. There, it was found that with increasing particle number, the transition becomes more sharp and, for a large number of particles, can be called a “quantum phase

transition”. It would be interesting to establish a more rigorous criterion for the particle number at which this transition qualifies as a phase transition. Finally, our study and Ref. [200], have focused exclusively on the ground state of the system. However, excited states could also offer important insights into the (phase) transition starting from just a few particles, as demonstrated in Refs. [42, 52], where excited states in a finite system were interpreted as precursors of a Higgs mode.

To summarize: In this thesis, we contributed to the understanding of the few-to-many-body crossover in low-dimensional quantum gases. Our study on renormalized interactions expands the available parameter regime for *ab initio* studies which can provide a deeper understanding of the few-to-many regime. Furthermore, we directly connected the polaron concept with a finite system of an impurity coupled to an Aharonov-Bohm flux to enable new few-to-many studies; e.g., we defined the effective mass a in finite system for the first time. Additionally, we investigated an attractive impurity in a repulsive Bose gas, providing a detailed characterization of the impurity-boson bound state to facilitate new many-body research on systems with attractive impurities. Finally, we studied a two-dimensional system of attractive bosons and explored the transition from a trap-dominated state to a universal interaction-dominated one, paving the way for future studies on the emergence of universality in two dimensions. We believe that our contribution to the exciting field of the few-to-many-body crossover will help advance the understanding of many-body quantum systems and inspire future studies.

Bibliography

- [1] P. W. Anderson. “More Is Different”. In: *Science* 177.4047 (1972), pp. 393–396.
- [2] L. Landau and S. Pekar. “Effective mass of a polaron”. In: *Zh. Eksp. Teor. Fiz* 18.5 (1948), pp. 419–423.
- [3] S. Grebenev, J. P. Toennies, and A. F. Vilesov. “Superfluidity within a small helium-4 cluster: The microscopic Andronikashvili experiment”. In: *Science* 279.5359 (1998), pp. 2083–2086.
- [4] A. Migdal. “Superfluidity and the moments of inertia of nuclei”. In: *Nuclear Physics* 13.5 (1959), pp. 655–674.
- [5] M. Goldhaber and E. Teller. “On nuclear dipole vibrations”. In: *Physical Review* 74.9 (1948), p. 1046.
- [6] S. Mistakidis et al. “Few-body Bose gases in low dimensions—A laboratory for quantum dynamics”. In: *Physics Reports* 1042 (2023), pp. 1–108.
- [7] N. T. Zinner. “Exploring the few-to many-body crossover using cold atoms in one dimension”. In: *EPJ Web of Conferences*. Vol. 113. EDP Sciences. 2016, p. 01002.
- [8] J. Cremon. “Quantum Few-Body Physics with the Configuration Interaction Approach: Method Development and Application to Physical Systems”. PhD thesis. Lund University, 2010.
- [9] J. Bjerlin. “Few- to many-body physics in ultracold gases: An exact diagonalization approach”. PhD thesis. Mathematical Physics, 2017.
- [10] A. S. Dehkharghani. “One-Dimensional Quantum Systems - From Few to Many Particles”. In: (2018). arXiv: 1801.04993 [cond-mat.quant-gas].
- [11] M. Holten. “From Pauli Blocking to Cooper Pairs: Emergence in a Mesoscopic 2D Fermi Gas”. PhD thesis. Heidelberg, 2022.
- [12] A. N. Wenz et al. “From few to many: Observing the formation of a Fermi sea one atom at a time”. In: *Science* 342.6157 (2013), pp. 457–460.
- [13] G. Zürn. “Few-fermion systems in one dimension”. PhD thesis. Heidelberg, 2012.

-
-
- [14] L. Bayha. “Emergence of Many-Body Physics in Two-Dimensional Few-Fermion Systems”. PhD thesis. Heidelberg, 2020.
- [15] F. Schwabl. *Statistical Mechanics*. 2nd ed. 2006. Advanced Texts in Physics. Berlin, Heidelberg, 2006.
- [16] K. B. Davis et al. “Bose-Einstein condensation in a gas of sodium atoms”. In: *Physical review letters* 75.22 (1995), p. 3969.
- [17] M. H. Anderson et al. “Observation of Bose-Einstein Condensation in a Dilute Atomic Vapor”. In: *Science* 269.5221 (1995), pp. 198–201.
- [18] I. Bloch, J. Dalibard, and W. Zwerger. “Many-body physics with ultracold gases”. In: *Reviews of modern physics* 80.3 (2008), pp. 885–964.
- [19] E. Zohar, J. I. Cirac, and B. Reznik. “Quantum simulations of lattice gauge theories using ultracold atoms in optical lattices”. In: *Reports on Progress in Physics* 79.1 (2015), p. 014401.
- [20] C. Gross and I. Bloch. “Quantum simulations with ultracold atoms in optical lattices”. In: *Science* 357.6355 (2017), pp. 995–1001.
- [21] S. I. Mistakidis et al. “Many-body quantum dynamics and induced correlations of Bose polarons”. In: *New J. Phys.* 22.4 (2020), p. 043007.
- [22] M. Saffman. “Quantum computing with atomic qubits and Rydberg interactions: progress and challenges”. In: *Journal of Physics B: Atomic, Molecular and Optical Physics* 49.20 (2016), p. 202001.
- [23] E. Braaten and H.-W. Hammer. “Universality in few-body systems with large scattering length”. In: *Physics Reports* 428.5 (2006), pp. 259–390.
- [24] M. A. Baranov et al. “Condensed Matter Theory of Dipolar Quantum Gases”. In: *Chemical Reviews* 112.9 (2012), pp. 5012–5061.
- [25] M. Bara11. “Theoretical progress in many-body physics with ultracold dipolar gases”. In: *Physics Reports* 464.3 (2008), pp. 71–111.
- [26] T. Lahaye et al. “The physics of dipolar bosonic quantum gases”. In: *Reports on Progress in Physics* 72.12 (2009), p. 126401.
- [27] C. Chin et al. “Feshbach resonances in ultracold gases”. In: *Reviews of Modern Physics* 82.2 (2010), pp. 1225–1286.
- [28] S. Giorgini, L. P. Pitaevskii, and S. Stringari. “Theory of ultracold atomic Fermi gases”. In: *Reviews of Modern Physics* 80.4 (2008), pp. 1215–1274.

-
-
- [29] G. C. Strinati et al. “The BCS–BEC crossover: From ultra-cold Fermi gases to nuclear systems”. In: *Physics Reports* 738 (2018), pp. 1–76.
- [30] E. Ising. “Contribution to the Theory of Ferromagnetism”. In: *Z. Phys.* 31 (1925), pp. 253–258.
- [31] L. Onsager. “Crystal statistics. I. A two-dimensional model with an order-disorder transition”. In: *Physical Review* 65.3-4 (1944), p. 117.
- [32] E. H. Lieb and W. Liniger. “Exact Analysis of an Interacting Bose Gas. I. The General Solution and the Ground State”. In: *Phys. Rev.* 130.4 (1963), pp. 1605–1616.
- [33] E. H. Lieb. “Exact Analysis of an Interacting Bose Gas. II. The Excitation Spectrum”. In: *Phys. Rev.* 130.4 (1963), pp. 1616–1624.
- [34] M. Gaudin. “Un système à une dimension de fermions en interaction”. In: *Physics Letters A* 24.1 (1967), pp. 55–56.
- [35] C.-N. Yang. “Some exact results for the many-body problem in one dimension with repulsive delta-function interaction”. In: *Physical Review Letters* 19.23 (1967), p. 1312.
- [36] M. Gaudin. *The bethe wavefunction*. Cambridge University Press, 2014.
- [37] M. Girardeau. “Relationship between Systems of Impenetrable Bosons and Fermions in One Dimension”. In: *Journal of Mathematical Physics* 1.6 (1960), pp. 516–523.
- [38] T. Kinoshita, T. Wenger, and D. S. Weiss. “Observation of a One-Dimensional Tonks-Girardeau Gas”. In: *Science* 305.5687 (2004), pp. 1125–1128.
- [39] H.-W. Hammer and D. Son. “Universal properties of two-dimensional boson droplets”. In: *Physical review letters* 93.25 (2004), p. 250408.
- [40] F. Serwane et al. “Deterministic preparation of a tunable few-fermion system”. In: *Science* 332.6027 (2011), pp. 336–338.
- [41] G. Zürn et al. “Pairing in few-fermion systems with attractive interactions”. In: *Physical review letters* 111.17 (2013), p. 175302.
- [42] L. Bayha et al. “Observing the emergence of a quantum phase transition shell by shell”. In: *Nature* 587.7835 (2020), pp. 583–587.
- [43] M. Holten et al. “Observation of Cooper pairs in a mesoscopic two-dimensional Fermi gas”. In: *Nature* 606.7913 (2022), pp. 287–291.
- [44] S. Brandstetter et al. *Emergent hydrodynamic behaviour of few strongly interacting fermions*. 2023. arXiv: 2308.09699 [cond-mat.quant-gas].

-
-
- [45] N. L. Harshman. “Symmetries of three harmonically trapped particles in one dimension”. In: *Physical Review A* 86.5 (2012), p. 052122.
- [46] S. E. Gharashi and D. Blume. “Correlations of the upper branch of 1D harmonically trapped two-component Fermi gases”. In: *Physical review letters* 111.4 (2013), p. 045302.
- [47] P. D’Amico and M. Rontani. “Three interacting atoms in a one-dimensional trap: a benchmark system for computational approaches”. In: *Journal of Physics B: Atomic, Molecular and Optical Physics* 47.6 (2014), p. 065303.
- [48] D. Pęczak and T. Sowiński. “Few strongly interacting ultracold fermions in one-dimensional traps of different shapes”. In: *Physical Review A* 94.4 (2016), p. 042118.
- [49] D. Włodzyński. “Several fermions strongly interacting with a heavy mobile impurity in a one-dimensional harmonic trap”. In: *Physical Review A* 106.3 (2022), p. 033306.
- [50] L. Rammelmüller, D. Huber, and A. G. Volosniev. “A modular implementation of an effective interaction approach for harmonically trapped fermions in 1D”. In: *SciPost Phys. Codebases* (2023), p. 12.
- [51] M. Rontani et al. “On the renormalization of contact interactions for the configuration-interaction method in two-dimensions”. In: *Journal of Physics B: Atomic, Molecular and Optical Physics* 50.6 (2017), p. 065301.
- [52] J. Bjerlin, S. Reimann, and G. Bruun. “Few-body precursor of the Higgs mode in a Fermi gas”. In: *Physical Review Letters* 116.15 (2016), p. 155302.
- [53] J. Christensson et al. “Effective-interaction approach to the many-boson problem”. In: *Physical Review A* 79.1 (2009), p. 012707.
- [54] B. R. Barrett, P. Navrátil, and J. P. Vary. “Ab initio no core shell model”. In: *Progress in Particle and Nuclear Physics* 69 (2013), pp. 131–181.
- [55] S. Krönke et al. “Non-equilibrium quantum dynamics of ultra-cold atomic mixtures: the multi-layer multi-configuration time-dependent Hartree method for bosons”. In: *New Journal of Physics* 15.6 (2013), p. 063018.
- [56] L. Cao et al. “A unified ab initio approach to the correlated quantum dynamics of ultracold fermionic and bosonic mixtures”. In: *J. Chem. Phys.* 147.4 (2017), p. 044106.
- [57] A. U. Lode et al. “Colloquium: Multiconfigurational time-dependent Hartree approaches for indistinguishable particles”. In: *Reviews of Modern Physics* 92.1 (2020), p. 011001.

-
-
- [58] L. S. Cederbaum, O. E. Alon, and A. I. Streltsov. “Coupled-cluster theory for systems of bosons in external traps”. In: *Physical Review A* 73.4 (2006), p. 043609.
- [59] T. Grining et al. “Many interacting fermions in a one-dimensional harmonic trap: a quantum-chemical treatment”. In: *New Journal of Physics* 17.11 (2015), p. 115001.
- [60] T. Grining et al. “Crossover between few and many fermions in a harmonic trap”. In: *Physical Review A* 92.6 (2015), p. 061601.
- [61] F. Brauneis et al. “Impurities in a one-dimensional Bose gas: The flow equation approach”. In: *SciPost Physics* 11.1 (2021), p. 008.
- [62] F. Brauneis et al. “Artificial atoms from cold bosons in one dimension”. In: *New Journal of Physics* 24.6 (2022), p. 063036.
- [63] F. Brauneis et al. “Emergence of a Bose polaron in a small ring threaded by the Aharonov-Bohm flux”. In: *Communications Physics* 6.1 (2023), p. 224.
- [64] R. Roth. “Importance truncation for large-scale configuration interaction approaches”. In: *Physical Review C* 79.6 (2009), p. 064324.
- [65] L. Chergui et al. “Superfluid-droplet crossover in a binary boson mixture on a ring: Exact diagonalization solutions for few-particle systems in one dimension”. In: *Physical Review A* 108.2 (2023), p. 023313.
- [66] C. Berger et al. “Complex Langevin and other approaches to the sign problem in quantum many-body physics”. In: *Physics Reports* 892 (2021), pp. 1–54.
- [67] L. Pollet. “Recent developments in quantum Monte Carlo simulations with applications for cold gases”. In: *Reports on Progress in Physics* 75.9 (2012), p. 094501.
- [68] S. Kehrein. *The Flow Equation Approach to Many-Particle Systems*. Vol. 217. Berlin: Springer, 2006.
- [69] K. Tsukiyama, S. K. Bogner, and A. Schwenk. “In-Medium Similarity Renormalization Group For Nuclei”. In: *Phys. Rev. Lett.* 106.22 (2011), p. 222502.
- [70] H. Hergert et al. “The In-Medium Similarity Renormalization Group: A novel ab initio method for nuclei”. In: *Physics Reports* 621 (2016), pp. 165–222.
- [71] A. Volosniev and H. Hammer. “Flow equations for cold Bose gases”. In: *New Journal of Physics* 19.11 (2017), p. 113051.
- [72] A. G. Volosniev and H.-W. Hammer. “Analytical approach to the Bose-polaron problem in one dimension”. In: *Phys. Rev. A* 96.3 (2017), p. 031601.
- [73] C. Pethick and H. Smith. *Bose–Einstein Condensation in Dilute Gases*. Cambridge University Press, 2002.

-
- [74] L. Pitaevskii and S. Stringari. *Bose-Einstein condensation and superfluidity*. Vol. 164. Oxford University Press, 2016.
- [75] F. Schwabl. *Advanced Quantum Mechanics*. 4th ed. 2008. Berlin, Heidelberg, 2008.
- [76] C. J. Cramer. *Essentials of computational chemistry: theories and models*. John Wiley & Sons, 2013.
- [77] L. Rammelmüller et al. “Magnetic impurity in a one-dimensional few-fermion system”. In: *SciPost Physics* 14.1 (2023), p. 006.
- [78] A. Rojo-Francàs, A. Polls, and B. Julià-Díaz. “Static and Dynamic Properties of a Few Spin 1/2 Interacting Fermions Trapped in a Harmonic Potential”. In: *Mathematics* 8.7 (2020), p. 1196.
- [79] J. Bengtsson et al. “Interplay between shell structure and trap deformation in dipolar Fermi gases”. In: *Phys. Rev. A* 102.5 (2020), p. 053302.
- [80] G. Golub and C. Van Loan. *Matrix computations*. 1996. ISBN: 0-8018-5414-8.
- [81] S. K. Bogner, R. J. Furnstahl, and R. J. Perry. “Similarity renormalization group for nucleon-nucleon interactions”. In: *Phys. Rev. C* 75.6 (2007), p. 061001.
- [82] F. Wegner. “Flow-equations for Hamiltonians”. In: *Annalen der physik* 506.2 (1994), pp. 77–91.
- [83] S. D. Glazek and K. G. Wilson. “Renormalization of Hamiltonians”. In: *Phys. Rev. D* 48.12 (1993), pp. 5863–5872.
- [84] M. Drescher, M. Salmhofer, and T. Enss. “Theory of a resonantly interacting impurity in a Bose-Einstein condensate”. In: *Phys. Rev. Research* 2.3 (2020), p. 032011.
- [85] O. Hryhorchak, G. Panochko, and V. Pastukhov. “Mean-field study of repulsive 2D and 3D Bose polarons”. In: *Journal of Physics B: Atomic, Molecular and Optical Physics* 53.20 (2020), p. 205302.
- [86] N.-E. Guenther et al. “Mobile impurity in a Bose-Einstein condensate and the orthogonality catastrophe”. In: *Phys. Rev. A* 103.1 (2021), p. 013317.
- [87] P. Massignan, N. Yegovtsev, and V. Gurarie. “Universal Aspects of a Strongly Interacting Impurity in a Dilute Bose Condensate”. In: *Phys. Rev. Lett.* 126.12 (2021), p. 123403.
- [88] M. Maslov, M. Lemeshko, and A. G. Volosniev. “Impurity with a resonance in the vicinity of the Fermi energy”. In: *Phys. Rev. Res.* 4.1 (2022), p. 013160.
- [89] L. Amico et al. “Roadmap on Atomtronics: State of the art and perspective”. In: *AVS Quantum Science* 3.3 (2021), p. 039201.

-
-
- [90] L. Amico et al. “Colloquium: Atomtronic circuits: From many-body physics to quantum technologies”. In: *Reviews of Modern Physics* 94.4 (2022).
- [91] M. Olshanii. “Atomic Scattering in the Presence of an External Confinement and a Gas of Impenetrable Bosons”. In: *Phys. Rev. Lett.* 81.5 (1998), pp. 938–941.
- [92] E. Gross. “Motion of foreign bodies in boson systems”. In: *Annals of Physics* 19.2 (1962), pp. 234–253.
- [93] T. D. Lee, F. E. Low, and D. Pines. “The Motion of Slow Electrons in a Polar Crystal”. In: *Phys. Rev.* 90.2 (1953), pp. 297–302.
- [94] J. Jager et al. “Strong-coupling Bose polarons in one dimension: Condensate deformation and modified Bogoliubov phonons”. In: *Phys. Rev. Research* 2.3 (2020), p. 033142.
- [95] D. H. Smith and A. G. Volosniev. “Engineering momentum profiles of cold-atom beams”. In: *Phys. Rev. A* 100.3 (2019), p. 033604.
- [96] S. I. Mistakidis et al. “Effective approach to impurity dynamics in one-dimensional trapped Bose gases”. In: *Phys. Rev. A* 100.1 (2019), p. 013619.
- [97] G. Panochko and V. Pastukhov. “Mean-field construction for spectrum of one-dimensional Bose polaron”. In: *Annals of Physics* 409 (2019), p. 167933.
- [98] G. M. Koutentakis, S. I. Mistakidis, and P. Schmelcher. “Pattern Formation in One-Dimensional Polaron Systems and Temporal Orthogonality Catastrophe”. In: *Atoms* 10.1 (2022).
- [99] N. D. Mermin and H. Wagner. “Absence of Ferromagnetism or Antiferromagnetism in One- or Two-Dimensional Isotropic Heisenberg Models”. In: *Phys. Rev. Lett.* 17.22 (1966), pp. 1133–1136.
- [100] P. C. Hohenberg. “Existence of Long-Range Order in One and Two Dimensions”. In: *Phys. Rev.* 158.2 (1967), pp. 383–386.
- [101] D. S. Petrov, G. V. Shlyapnikov, and J. T. M. Walraven. “Regimes of Quantum Degeneracy in Trapped 1D Gases”. In: *Phys. Rev. Lett.* 85.18 (2000), pp. 3745–3749.
- [102] M. Abramowitz and I. A. Stegun, eds. *Handbook of mathematical functions : with formulas, graphs, and mathematical tables*. 9. Dover print., (correction reprint). New York, 1972.
- [103] V. N. Popov. *Functional integrals in quantum field theory and statistical physics*. D. Reidel Pub. Co., 1983.

-
-
- [104] D. Hellweg et al. “Phase fluctuations in Bose–Einstein condensates”. In: *Applied Physics B* 73.8 (2001), pp. 781–789.
- [105] J. Rotureau. “Interaction for the trapped Fermi gas from a unitary transformation of the exact two-body spectrum”. In: *The European Physical Journal D* 67 (2013), pp. 1–9.
- [106] E. J. Lindgren et al. “Fermionization of two-component few-fermion systems in a one-dimensional harmonic trap”. In: *New Journal of Physics* 16.6 (2014), p. 063003.
- [107] T. D. Anh-Tai et al. “Quantum chaos in interacting Bose-Bose mixtures”. In: *SciPost Phys.* 15 (2023), p. 048.
- [108] T. Ernst et al. “Simulating strongly correlated multiparticle systems in a truncated Hilbert space”. In: *Phys. Rev. A* 84.2 (2011), p. 023623.
- [109] P. Kościk. “Optimized configuration interaction approach for trapped multiparticle systems interacting via contact forces”. In: *Physics Letters A* 382.36 (2018), pp. 2561–2564.
- [110] P. Jeszenszki et al. “Accelerating the convergence of exact diagonalization with the transcorrelated method: Quantum gas in one dimension with contact interactions”. In: *Phys. Rev. A* 98.5 (2018), p. 053627.
- [111] A. Rojo-Francàs, F. Isaule, and B. Juliá-Díaz. “Direct diagonalization method for a few particles trapped in harmonic potentials”. In: *Phys. Rev. A* 105.6 (2022), p. 063326.
- [112] F. Brauneis et al. “Comparison of renormalized interactions using one-dimensional few-body systems as a testbed”. In: (2024). arXiv: 2408.10052 [cond-mat.quant-gas].
- [113] T. Sowiński and M. Á. García-March. “One-dimensional mixtures of several ultracold atoms: a review”. In: *Reports on Progress in Physics* 82.10 (2019), p. 104401.
- [114] K. Suzuki and S. Y. Lee. “Convergent theory for effective interaction in nuclei”. In: *Progress of Theoretical Physics* 64.6 (1980), pp. 2091–2106.
- [115] S. K. Bogner et al. *Renormalization Group Equation for Low Momentum Effective Nuclear Interactions*. 2001. arXiv: nucl-th/0111042 [nucl-th].
- [116] S. Bogner, R. Furnstahl, and A. Schwenk. “From low-momentum interactions to nuclear structure”. In: *Progress in Particle and Nuclear Physics* 65.1 (2010), pp. 94–147.

-
-
- [117] M. Holten et al. “Observation of Pauli Crystals”. In: *Phys. Rev. Lett.* 126.2 (2021), p. 020401.
- [118] T. Sowiński et al. “Few interacting fermions in a one-dimensional harmonic trap”. In: *Physical Review A—Atomic, Molecular, and Optical Physics* 88.3 (2013), p. 033607.
- [119] G. M. Koutentakis, S. I. Mistakidis, and P. Schmelcher. “Probing ferromagnetic order in few-fermion correlated spin-flip dynamics”. In: *New Journal of Physics* 21.5 (2019), p. 053005.
- [120] M. Avakian et al. “Spectroscopy of a singular linear oscillator”. In: *Physics Letters A* 124.4-5 (1987), pp. 233–236.
- [121] T. Busch et al. “Two Cold Atoms in a Harmonic Trap”. In: *Foundations of Physics* 28.4 (1998), pp. 549–559.
- [122] A. Minguzzi and P. Vignolo. “Strongly interacting trapped one-dimensional quantum gases: Exact solution”. In: *AVS Quantum Science* 4.2 (2022).
- [123] S.-L. Nyeo. “Regularization methods for delta-function potential in two-dimensional quantum mechanics”. In: *American Journal of Physics* 68.6 (2000), pp. 571–575.
- [124] D. J. Griffiths and D. F. Schroeter. *Introduction to quantum mechanics*. Cambridge university press, 2018.
- [125] J. P. Boyd. “Asymptotic coefficients of hermite function series”. In: *Journal of Computational Physics* 54.3 (1984), pp. 382–410.
- [126] M. Barth and W. Zwerger. “Tan relations in one dimension”. In: *Annals of Physics* 326.10 (2011), pp. 2544–2565.
- [127] I. Stetcu et al. “Effective operators within the ab initio no-core shell model”. In: *Phys. Rev. C* 71.4 (2005), p. 044325.
- [128] W. Zwerger. *The BCS-BEC crossover and the unitary Fermi gas*. Vol. 836. Springer Science & Business Media, 2011.
- [129] S. Tan. “Large momentum part of a strongly correlated Fermi gas”. In: *Annals of Physics* 323.12 (2008), pp. 2971–2986.
- [130] B. E. Granger and D. Blume. “Tuning the Interactions of Spin-Polarized Fermions Using Quasi-One-Dimensional Confinement”. In: *Phys. Rev. Lett.* 92.13 (2004), p. 133202.
- [131] K. Günter et al. “ p -Wave Interactions in Low-Dimensional Fermionic Gases”. In: *Phys. Rev. Lett.* 95.23 (2005), p. 230401.

-
-
- [132] Y. Aharonov and D. Bohm. “Significance of Electromagnetic Potentials in the Quantum Theory”. In: *Phys. Rev.* 115.3 (1959), pp. 485–491.
- [133] M. V. Berry. “Quantal phase factors accompanying adiabatic changes”. In: *Proceedings of the Royal Society of London. A. Mathematical and Physical Sciences* 392.1802 (1984), pp. 45–57.
- [134] F. Bloch. “Simple Interpretation of the Josephson Effect”. In: *Phys. Rev. Lett.* 21.17 (1968), pp. 1241–1243.
- [135] M. Büttiker, Y. Imry, and R. Landauer. “Josephson behavior in small normal one-dimensional rings”. In: *Physics Letters A* 96.7 (1983), pp. 365–367.
- [136] A. G. Aronov and Y. V. Sharvin. “Magnetic flux effects in disordered conductors”. In: *Rev. Mod. Phys.* 59.3 (1987), pp. 755–779.
- [137] S. Viefers et al. “Quantum rings for beginners: energy spectra and persistent currents”. In: *Physica E: Low-dimensional Systems and Nanostructures* 21.1 (2004), pp. 1–35.
- [138] A. Lorke et al. “Spectroscopy of Nanoscopic Semiconductor Rings”. In: *Phys. Rev. Lett.* 84.10 (2000), pp. 2223–2226.
- [139] N. Spethmann et al. “Dynamics of Single Neutral Impurity Atoms Immersed in an Ultracold Gas”. In: *Phys. Rev. Lett.* 109.23 (2012), p. 235301.
- [140] J. Catani et al. “Quantum dynamics of impurities in a one-dimensional Bose gas”. In: *Phys. Rev. A* 85.2 (2012), p. 023623.
- [141] M.-G. Hu et al. “Bose Polarons in the Strongly Interacting Regime”. In: *Phys. Rev. Lett.* 117.5 (2016), p. 055301.
- [142] N. B. Jørgensen et al. “Observation of Attractive and Repulsive Polarons in a Bose-Einstein Condensate”. In: *Phys. Rev. Lett.* 117.5 (2016), p. 055302.
- [143] L. A. Peña Ardila et al. “Analyzing a Bose polaron across resonant interactions”. In: *Phys. Rev. A* 99.6 (2019), p. 063607.
- [144] Z. Z. Yan et al. “Bose polarons near quantum criticality”. In: *Science* 368.6487 (2020), pp. 190–194.
- [145] M. G. Skou et al. “Non-equilibrium quantum dynamics and formation of the Bose polaron”. In: *Nature Physics* 17.6 (2021).
- [146] J. Dalibard et al. “Colloquium: Artificial gauge potentials for neutral atoms”. In: *Reviews of Modern Physics* 83.4 (2011), pp. 1523–1543.

-
-
- [147] E. Aladinskaia et al. “Spatial quantization of exciton-polariton condensates in optically induced traps”. In: *Physical Review B* 107.4 (2023), p. 045302.
- [148] V. A. Lukoshkin et al. “Persistent circular currents of exciton-polaritons in cylindrical pillar microcavities”. In: *Physical Review B* 97.19 (2018), p. 195149.
- [149] V. Kalevich et al. “Ring-shaped polariton lasing in pillar microcavities”. In: *Journal of Applied Physics* 115.9 (2014).
- [150] H.-T. Lim et al. “Electrically tunable artificial gauge potential for polaritons”. In: *Nature communications* 8.1 (2017), p. 14540.
- [151] A. Müller-Groeling, H. A. Weidenmüller, and C. H. Lewenkopf. “Interacting Electrons in Mesoscopic Rings”. In: *Europhysics Letters* 22.3 (1993), p. 193.
- [152] M. Manninen, S. Viefers, and S. Reimann. “Quantum rings for beginners II: Bosons versus fermions”. In: *Physica E: Low-dimensional Systems and Nanostructures* 46 (2012), pp. 119–132.
- [153] P. Naldesi et al. “Enhancing sensitivity to rotations with quantum solitonic currents”. In: *SciPost Phys.* 12 (2022), p. 138.
- [154] G. Pecci et al. “Persistent currents in a strongly interacting multicomponent Bose gas on a ring”. In: *Comptes Rendus. Physique* 24.S3 (2023), pp. 87–99.
- [155] R. A. Römer and M. E. Raikh. “Aharonov-Bohm effect for an exciton”. In: *Phys. Rev. B* 62.11 (2000), pp. 7045–7049.
- [156] K. Kyriakou et al. “Arbitrary mixture of two charged interacting particles in a magnetic Aharonov–Bohm ring: persistent currents and Berry’s phases”. In: *Journal of Physics A: Mathematical and Theoretical* 43.35 (2010), p. 354018.
- [157] K. Mouloupoulos and M. Constantinou. “Two interacting charged particles in an Aharonov-Bohm ring: Bound state transitions, symmetry breaking, persistent currents, and Berry’s phase”. In: *Phys. Rev. B* 70.23 (2004), p. 235327.
- [158] A. V. Ghazaryan et al. “Linear dynamic polarizability and the absorption spectrum of an exciton in a quantum ring in a magnetic field”. In: *Physica Scripta* 83.3 (2011), p. 035703.
- [159] W. Casteels, J. Tempere, and J. T. Devreese. “Polaronic properties of an impurity in a Bose-Einstein condensate in reduced dimensions”. In: *Phys. Rev. A* 86.4 (2012), p. 043614.
- [160] A. Petković and Z. Ristivojević. “Dynamics of a mobile impurity in a one-dimensional Bose liquid”. In: *Physical Review Letters* 117.10 (2016), p. 105301.

-
- [161] M. Schechter, D. M. Gangardt, and A. Kamenev. “Quantum impurities: from mobile Josephson junctions to depletions”. In: *New Journal of Physics* 18.6 (2016), p. 065002.
- [162] L. Parisi and S. Giorgini. “Quantum Monte Carlo study of the Bose-polaron problem in a one-dimensional gas with contact interactions”. In: *Phys. Rev. A* 95.2 (2017), p. 023619.
- [163] F. Grusdt, G. E. Astrakharchik, and E. Demler. “Bose polarons in ultracold atoms in one dimension: beyond the Fröhlich paradigm”. In: *New J. Phys.* 19.10 (2017), p. 103035.
- [164] V. Pastukhov. “Impurity states in the one-dimensional Bose gas”. In: *Phys. Rev. A* 96.4 (2017), p. 043625.
- [165] B. Kain and H. Y. Ling. “Analytical study of static beyond-Fröhlich Bose polarons in one dimension”. In: *Phys. Rev. A* 98.3 (2018), p. 033610.
- [166] S. I. Mistakidis et al. “Quench dynamics and orthogonality catastrophe of Bose polarons”. In: *Phys. Rev. Lett.* 122.18 (2019), p. 183001.
- [167] P. Monisha et al. “Persistent current in a correlated quantum ring with electron-phonon interaction in the presence of Rashba interaction and Aharonov-Bohm flux”. In: *Sci Rep* 6 (2016), p. 20056.
- [168] N. Goldman et al. “Light-induced gauge fields for ultracold atoms”. In: *Reports on Progress in Physics* 77.12 (2014), p. 126401.
- [169] J. C. Gunn and J. M. F. Gunn. “An exactly soluble Hartree problem in an external potential”. In: *European Journal of Physics* 9.1 (1988), p. 51.
- [170] E. B. Kolomeisky, J. P. Straley, and R. M. Kalas. “Ground-state properties of artificial bosonic atoms, Bose interaction blockade, and the single-atom pipette”. In: *Phys. Rev. A* 69.6 (2004), p. 063401.
- [171] M. Yang et al. “Polaron-Depletion Transition in the Yrast Excitations of a One-Dimensional Bose Gas with a Mobile Impurity”. In: *Condensed Matter* 7.1 (2022).
- [172] N. Byers and C. N. Yang. “Theoretical Considerations Concerning Quantized Magnetic Flux in Superconducting Cylinders”. In: *Phys. Rev. Lett.* 7.2 (1961), pp. 46–49.
- [173] Y. Imry. “Physics of mesoscopic systems”. In: *Directions in Condensed Matter Physics: Memorial Volume in Honor of Shang-keng Ma*. World Scientific, 1986, pp. 101–163.
- [174] M. A. Cazalilla et al. “One dimensional bosons: From condensed matter systems to ultracold gases”. In: *Rev. Mod. Phys.* 83.4 (2011), pp. 1405–1466.

-
-
- [175] X.-W. Guan, M. T. Batchelor, and C. Lee. “Fermi gases in one dimension: From Bethe ansatz to experiments”. In: *Rev. Mod. Phys.* 85.4 (2013), pp. 1633–1691.
- [176] H. Chen and Y. Chen. “Influence of the Aharonov-Bohm flux on the optical polarons in the molecular-crystal model with the dispersion term in a ring”. In: *Solid state communications* 105.8 (1998), pp. 537–541.
- [177] Y.-C. Zhou, H. Chen, and C.-F. Yu. “Effect of the Aharonov-Bohm potential on the acoustical polaron in one-dimensional rings”. In: *Physics Letters A* 212.3 (1996), pp. 167–170.
- [178] M. Cominotti et al. “Optimal Persistent Currents for Interacting Bosons on a Ring with a Gauge Field”. In: *Phys. Rev. Lett.* 113.2 (2014), p. 025301.
- [179] G. E. Astrakharchik and I. Brouzos. “Trapped one-dimensional ideal Fermi gas with a single impurity”. In: *Phys. Rev. A* 88.2 (2013), p. 021602.
- [180] J. Levinsen et al. “Strong-coupling ansatz for the one-dimensional Fermi gas in a harmonic potential”. In: *Science Advances* 1.6 (2015).
- [181] F. Scazza et al. “Repulsive Fermi Polarons in a Resonant Mixture of Ultracold ^6Li Atoms”. In: *Phys. Rev. Lett.* 118.8 (2017), p. 083602.
- [182] V. Hakim. “Nonlinear Schrödinger flow past an obstacle in one dimension”. In: *Phys. Rev. E* 55.3 (1997), pp. 2835–2845.
- [183] K. C. Wright et al. “Driving Phase Slips in a Superfluid Atom Circuit with a Rotating Weak Link”. In: *Phys. Rev. Lett.* 110.2 (2013), p. 025302.
- [184] G. E. Astrakharchik and L. P. Pitaevskii. “Motion of a heavy impurity through a Bose-Einstein condensate”. In: *Phys. Rev. A* 70.1 (2004), p. 013608.
- [185] D. Boyanovsky et al. “Dynamics of relaxation and dressing of a quenched Bose polaron”. In: *Phys. Rev. A* 100.4 (2019), p. 043617.
- [186] K. K. Nielsen et al. “Critical slowdown of non-equilibrium polaron dynamics”. In: *New Journal of Physics* 21.4 (2019), p. 043014.
- [187] M. Will and M. Fleischhauer. “Dynamics of polaron formation in 1D Bose gases in the strong-coupling regime”. In: *New Journal of Physics* 25.8 (2023), p. 083043.
- [188] T. Karpiuk et al. “Correspondence between dark solitons and the type II excitations of the Lieb-Liniger model”. In: *Physical Review A* 91.1 (2015), p. 013621.
- [189] T. G. Backert. “Attractive Impurity in one-dimensional Bose gas”. Bachelor’s Thesis. Technische Universität Darmstadt, 2021.
- [190] L. Chergui. Private communication. 2024.

-
- [191] L. D. Landau and E. M. Lifshitz. *Quantum Mechanics: Non-relativistic Theory*. Course of theoretical physics. Pergamon Press, 1977.
- [192] B. Simon. In: *Ann. Phys.* 97 (1976), p. 279.
- [193] J. P. Straley and E. B. Kolomeisky. “Interacting bosons in a nearly resonant potential well”. In: *Phys. Rev. A* 75.6 (2007), p. 063421.
- [194] K. Chen, N. V. Prokof’ev, and B. V. Svistunov. “Trapping collapse: Infinite number of repulsive bosons trapped by a generic short-range potential”. In: *Phys. Rev. A* 98.4 (2018), p. 041602.
- [195] J. Levinsen et al. “Quantum Behavior of a Heavy Impurity Strongly Coupled to a Bose Gas”. In: *Phys. Rev. Lett.* 127.3 (2021), p. 033401.
- [196] T. A. Bell et al. “Bose–Einstein condensation in large time-averaged optical ring potentials”. In: *New Journal of Physics* 18.3 (2016), p. 035003.
- [197] B. Mukherjee et al. “Homogeneous Atomic Fermi Gases”. In: *Phys. Rev. Lett.* 118.12 (2017), p. 123401.
- [198] F. Schäfer et al. “Experimental realization of ultracold Yb-⁷Li mixtures in mixed dimensions”. In: *Phys. Rev. A* 98.5 (2018), p. 051602.
- [199] M. Lebrat et al. “Quantized Conductance through a Spin-Selective Atomic Point Contact”. In: *Phys. Rev. Lett.* 123.19 (2019), p. 193605.
- [200] A. Tononi, J. Givois, and D. S. Petrov. “Binding of heavy fermions by a single light atom in one dimension”. In: *Phys. Rev. A* 106.1 (2022), p. L011302.
- [201] E. H. Lieb, J. P. Solovej, and J. Yngvason. “Heavy atoms in the strong magnetic field of a neutron star”. In: *Phys. Rev. Lett.* 69.5 (1992), pp. 749–752.
- [202] J. W. Kane and L. P. Kadanoff. “Long-Range Order in Superfluid Helium”. In: *Phys. Rev.* 155.1 (1967), pp. 80–83.
- [203] V. Popov. “On the theory of the superfluidity of two- and one-dimensional bose systems”. In: *Theor Math Phys* 11 (1972), pp. 565–573.
- [204] N. Spethmann et al. “Dynamics of Single Neutral Impurity Atoms Immersed in an Ultracold Gas”. In: *Phys. Rev. Lett.* 109.23 (2012), p. 235301.
- [205] S. I. Mistakidis et al. “Radiofrequency spectroscopy of one-dimensional trapped Bose polarons: crossover from the adiabatic to the diabatic regime”. In: *New J. Phys.* 23.4 (2021), p. 043051.
- [206] F. Resare and J. Hofmann. *Few-to-many particle crossover of pair excitations in a superfluid*. 2022. arXiv: 2208.03762 [cond-mat.quant-gas].

-
-
- [207] J. Hertkorn et al. “Fate of the Amplitude Mode in a Trapped Dipolar Supersolid”. In: *Phys. Rev. Lett.* 123.19 (2019), p. 193002.
- [208] R. Kanamoto, H. Saito, and M. Ueda. “Quantum phase transition in one-dimensional Bose-Einstein condensates with attractive interactions”. In: *Phys. Rev. A* 67.1 (2003), p. 013608.
- [209] B. Bazak and D. S. Petrov. “Energy of N two-dimensional bosons with zero-range interactions”. In: *New Journal of Physics* 20.2 (2018), p. 023045.
- [210] F. Brauneis, A. G. Volosniev, and H.-W. Hammer. *Two-dimensional bosonic droplets in a harmonic trap*. 2024. arXiv: 2410.00570 [cond-mat.quant-gas].
- [211] D. Blume. “Threshold behavior of bosonic two-dimensional few-body systems”. In: *Phys. Rev. B* 72.9 (2005), p. 094510.
- [212] D. Lee. “Large- N droplets in two dimensions”. In: *Phys. Rev. A* 73.6 (2006), p. 063204.
- [213] Z. Hadzibabic and J. Dalibard. “Two-dimensional Bose fluids: An atomic physics perspective”. In: *La Rivista del Nuovo Cimento* 34.6 (2011), pp. 389–434.
- [214] D. Pines. *The theory of quantum liquids : 1. Normal Fermi liquids*. Repr. of the 1966 ed., 3rd print. Redwood City, Calif.: Avalon Publishing, 1994.
- [215] F. Dalfovo et al. “Theory of Bose-Einstein condensation in trapped gases”. In: *Rev. Mod. Phys.* 71.3 (1999), pp. 463–512.
- [216] K. Helfrich and H.-W. Hammer. “Resonant three-body physics in two spatial dimensions”. In: *Phys. Rev. A* 83.5 (2011), p. 052703.
- [217] A. Tononi, G. E. Astrakharchik, and D. S. Petrov. “Gas-to-soliton transition of attractive bosons on a spherical surface”. In: *AVS Quantum Science* 6.2 (2024), p. 023201.
- [218] B. J. Verhaar et al. “Scattering length and effective range in two dimensions: application to adsorbed hydrogen atoms”. In: *Journal of Physics A: Mathematical and General* 17.3 (1984), p. 595.
- [219] H. Hergert et al. “Ab Initio Calculations of Even Oxygen Isotopes with Chiral Two-Plus-Three-Nucleon Interactions”. In: *Physical Review Letters* 110.24 (2013), p. 242501.
- [220] H. Hergert et al. “Ab initio multireference in-medium similarity renormalization group calculations of even calcium and nickel isotopes”. In: *Phys. Rev. C* 90.4 (2014), p. 041302.

-
- [221] M. Lee et al. “Energy-dependent scattering and the Gross-Pitaevskii equation in two-dimensional Bose-Einstein condensates”. In: *Physical Review A* 65.4 (2002), p. 043617.
- [222] E. H. Lieb, R. Seiringer, and J. Yngvason. “A Rigorous Derivation of the Gross-Pitaevskii Energy Functional for a Two-dimensional Bose Gas”. In: *Communications in Mathematical Physics* 224 (2001), pp. 17–31.
- [223] A. Posazhennikova. “Colloquium: Weakly interacting, dilute Bose gases in 2D”. In: *Rev. Mod. Phys.* 78.4 (2006), pp. 1111–1134.
- [224] T. D. Morris, N. M. Parzuchowski, and S. K. Bogner. “Magnus expansion and in-medium similarity renormalization group”. In: *Phys. Rev. C* 92.3 (2015), p. 034331.
- [225] S. Brandstetter. Private communication. 2024.
- [226] V. Fock. “Bemerkung zur Quantelung des harmonischen Oszillators im Magnetfeld”. In: *Zeitschrift für Physik* 47.5 (1928), pp. 446–448.
- [227] C. G. Darwin. “The diamagnetism of the free electron”. In: *Mathematical Proceedings of the Cambridge Philosophical Society*. Vol. 27. 1. Cambridge University Press. 1931, pp. 86–90.
- [228] M. Olshanii and L. Pricoupenko. “Rigorous Approach to the Problem of Ultraviolet Divergencies in Dilute Bose Gases”. In: *Phys. Rev. Lett.* 88.1 (2001), p. 010402.
- [229] R. Wenying and L. Youyan. “Talmi-Moshinsky Transformation Brackets for Two-Dimensional Systems”. In: *Communications in Theoretical Physics* 28.3 (1997), p. 373.
- [230] M. Moshinsky. *The Harmonic Oscillator in Modern Physics: From Atoms to Quarks*. Documents on Modern Physics: Gordon and Breach. Gordon and Breach, 1969.
- [231] M. Gaudin. “Boundary Energy of a Bose Gas in One Dimension”. In: *Phys. Rev. A* 4.1 (1971), pp. 386–394.
- [232] B. Reichert et al. “Exact results for the boundary energy of one-dimensional bosons”. In: *Physical review letters* 123.25 (2019), p. 250602.
- [233] S. I. Mistakidis et al. “Pump-probe spectroscopy of Bose polarons: Dynamical formation and coherence”. In: *Phys. Rev. Research* 2.3 (2020), p. 033380.
- [234] S. I. Mistakidis, A. G. Volosniev, and P. Schmelcher. “Induced correlations between impurities in a one-dimensional quenched Bose gas”. In: *Phys. Rev. Research* 2.2 (2020), p. 023154.

A. Renormalized interactions in one dimension: Derivations, fitting analysis, larger particle number, technical details and alternative convergence plots

In this Appendix, we provide additional information on Chap. 3. We start by discussing the convergence behavior of the bare contact interaction in a system with harmonic trapping potential. Afterwards, we will provide a detailed discussion of our data using a fitting analysis. Then, we showcase the relevant set of equations and explain our truncation scheme for the two-dimensional harmonic oscillator discussed in the outlook of Chap. 3. In Sec. A.4 we present results for larger particle numbers to show that the claims made in the main part of this chapter also apply for these setups. Next, we explain how the effective interactions used in the main part of the text can be implemented. Afterwards, we show that the renormalization using the effective interaction framework corresponds to a unitary transformation which means that we can also transform operators alongside the renormalization. We also explain how this can be implemented using $V_{\text{eff}}^{\text{rel}}$ and $V_{\text{eff}}^{\text{rel+cm}}$. Then, we derive the running coupling constant in free space, i.e. Eq. (3.10). Afterwards, we connect the momentum space cutoff in the unconfined system with our one-body basis cutoff of the CI-calculation. Lastly, we provide additional convergence plots: All plots shown in the main text are displayed as a function of $1/n$ and for the $1 + 1$ system we show double logarithmic plots.

A.1. Energy convergence for the bare contact interaction

Let us derive the expected convergence before of the energy if the bare contact interaction is used. Therefore, we first expand Eq. (3.10), which defines the running coupling constant

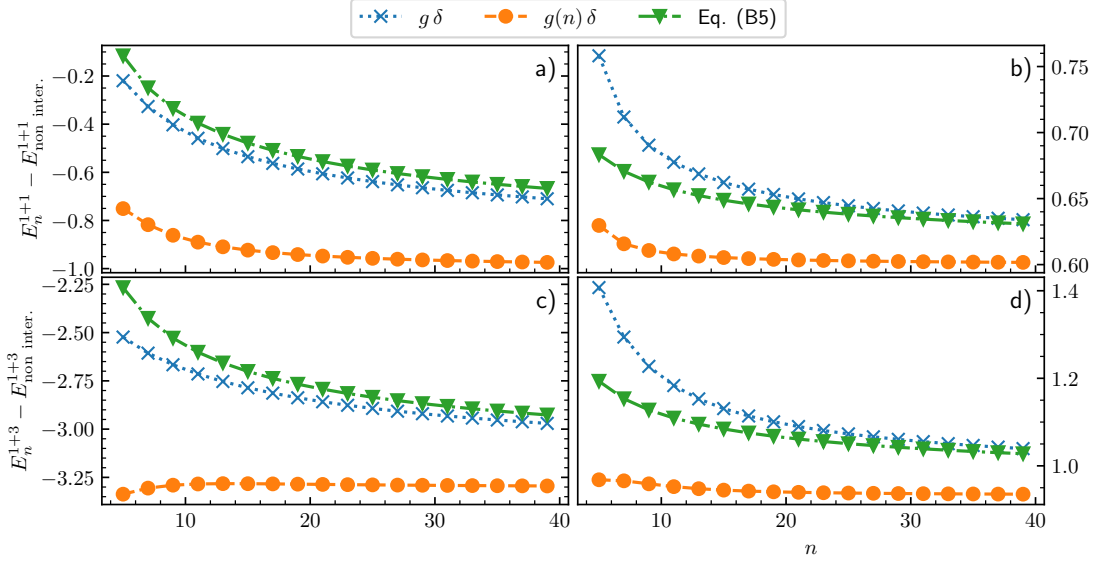


Figure A.1.: **Energies of the 1 + 1 and 1 + 3 systems calculated with the bare contact interaction, running coupling constant and the predicted energy convergence of the bare contact interaction, Eq. (A.5), as a function of the cutoff parameter n .**

Panels a) and b) show the energy of the second excited state of the 1 + 1 system; c) and d) present the ground state energy of 1 + 3. Panels a) and c) are for attractive interactions with $g = -2.5067$ (corresponds to $E_{1+1} = -1$); b) and d) are for repulsive interactions with $g = 3$ (corresponds to $E_{1+1} = 1.6$). Markers are the results of our calculations. Curves in the panels are added to guide the eye. Figure modified from Ref. [112].

in free space for attractive interaction, assuming large cutoffs λ

$$\begin{aligned}
 -\frac{1}{g(\lambda)} &\simeq \frac{1}{2\sqrt{|E_{1+1}^{\text{unconf.}}|}} - \frac{\sqrt{2}}{\pi\lambda} \\
 \Leftrightarrow g &\simeq g(\lambda) + \frac{\sqrt{2}g^2}{\pi\lambda}.
 \end{aligned}
 \tag{A.1}$$

We have used that $E_{1+1}^{\text{unconf.}} = -g^2/4$ and that $\frac{g(\lambda)^2}{\lambda} \simeq \frac{g^2}{\lambda}$ for $\lambda \rightarrow \infty$. Next, we calculate $E_{1+1}^{\text{unconf.}}(\lambda)$. Therefore, we insert our result for g from Eq. (A.1) in the Schrödinger

equation for a finite cutoff λ :

$$\begin{aligned}
E_{1+1}^{\text{unconf.}}(\lambda)\Psi_\lambda(x) &= \left(-\frac{1}{2}\frac{\partial^2}{\partial x^2} + \frac{g}{\sqrt{2}}\delta(x)\right)\Psi_\lambda(x) \\
&= \left(-\frac{1}{2}\frac{\partial^2}{\partial x^2} + \left[g(\lambda) + \frac{\sqrt{2}g^2}{\pi\lambda}\right]\sqrt{2}\delta(x)\right)\Psi_\lambda(x) \quad (\text{A.2}) \\
&= E_{1+1}^{\text{unconf.}(\lambda\rightarrow\infty)}\Psi_\lambda(x) + \frac{\sqrt{2}g^2}{\pi\lambda}\delta(x)\Psi_\lambda(x).
\end{aligned}$$

In the last line, we used that $g(\lambda)$ leads (by construction) to the correct two-body energy. Next, we treat the operator $\sqrt{2}g^2\delta(x)/(\pi\lambda)$ as perturbation, which leads to

$$E_{1+1}^{\text{unconf.}}(\lambda) \simeq E_{1+1}^{\text{unconf.}(\lambda\rightarrow\infty)} + \frac{\sqrt{2}C}{\pi\lambda} \quad (\text{A.3})$$

with the contact parameter $C = g^2 \langle \Psi | \delta(x) | \Psi \rangle$ [126]; Ψ is the wave function in the infinite Hilbert space. Further, we estimated $|\Psi\rangle_\lambda = |\Psi\rangle_{\lambda\rightarrow\infty} + o(1)$ ($o(1)$ meaning that we have only small corrections to the wave function).

Now we adjust this calculation for a many-body system in a trap. To this end, we need to use the connection between λ and n , Eq. (3.14). With this, we write the expectation value of the energy $E_{g\delta}(n) \equiv {}_n\langle \Psi | H | \Psi \rangle_n$ in the following way:

$$\begin{aligned}
E_{g\delta}(n) &= {}_n\langle \Psi | \sum_{i=1}^N -\frac{1}{2}\frac{\partial^2}{\partial x_i^2} + \frac{1}{2}x_i^2 + g \sum_{i<j} \delta(x_i - x_j) | \Psi \rangle_n \\
&= {}_n\langle \Psi | \sum_{i=1}^N -\frac{1}{2}\frac{\partial^2}{\partial x_i^2} + \frac{1}{2}x_i^2 + \left(g(n) + \frac{g^2}{\pi\sqrt{2n}}\right) \sum_{i<j} \delta(x_i - x_j) | \Psi \rangle_n. \quad (\text{A.4})
\end{aligned}$$

If n is sufficiently large, we estimate $|\Psi\rangle_n = |\Psi\rangle_{n\rightarrow\infty} + o(1)$. As shown in the main text, the energy from the running coupling constant approach, $E_{g(n)\delta}$, converges fast, meaning that for sufficiently large cutoffs it is safe to assume that $E_{g(n)\delta}$ is constant. Therefore, we arrive at a $1/\sqrt{n}$ convergence for the many-body energy for large cutoffs n ,

$$E_{g\delta} = E_{g(n)\delta} + \frac{1}{\pi\sqrt{2n}}C \simeq E_{n\rightarrow\infty} + \frac{1}{\pi\sqrt{2n}}C, \quad (\text{A.5})$$

where $C = g^2 \langle \Psi | \sum_{i<j} \delta(x_i - x_j) | \Psi \rangle$ is the contact parameter [126].

In Fig. A.1 we compare Eq. (A.5)¹, and the energy calculated using a bare contact interaction. Furthermore, we also plot the outcome of the running coupling constant approach. Indeed, as described in the main text, the running coupling approach converges fast so that the approximation, $E_{g(n)\delta} \simeq E_{n \rightarrow \infty}$, in Eq. (A.5) is well justified. Furthermore, we see good agreement between the prediction of Eq. (A.5) and the actual data of the bare coupling constant. Interestingly, for repulsive interaction, the convergence in this range of the values of n is somewhat faster than $1/\sqrt{n}$, while for attractive interaction it is slow (see also Tab. A.1 where the fitting analysis shows this quantitatively). This observation is in agreement with the results of Ref. [59].

A.2. Analysis of convergence

In this appendix, we provide a detailed analysis of our data by fitting with the following function

$$f(n) = c + \frac{A}{n^\sigma}, \quad (\text{A.6})$$

where A, c and $\sigma > 0$ are fit parameters. The value of σ can be interpreted as the rate of convergence: the larger σ , the faster the data approaches the result in an infinite Hilbert space. The parameter c corresponds to the extrapolated expectation value of the observable of interest. Note that the values of c can differ from one interaction to another if the maximal value of n used to produce the data is not sufficiently large. However, this difference can be used as an additional estimate of the accuracy of the numerical method.

The fitting function in Eq. (A.6) is partly inspired by the discussion of the above appendix, App. A.1, where Eq. (A.5), shows the convergence behavior of the energy of many fermions in a one-dimensional harmonic trap interacting via bare contact interaction (see also Ref. [59]). Following above discussion, we expect for a bare contact interaction $\sigma \approx 0.5$ for the energy. In Ref. [50] a similar convergence rate was found for the density. Furthermore, the authors of this study compared the convergence for the energy and the density at $x = 0$ between the effective interaction $V_{\text{eff}}^{\text{rel}}$ and the bare contact interaction. We extend their study by also considering the running coupling constant and $V_{\text{eff}}^{\text{rel+cm}}$. We further discuss the convergence rates of the expectation value of the kinetic energy and of the harmonic trapping potential as well as the transition matrix elements for a periodic modulation of the interaction strength.

It is important to note that we do not know the convergence pattern for the data computed using the renormalized interactions. It is possible, that these data do not follow

¹Here, we calculate the contact parameter C using $V_{\text{eff}}^{\text{rel+cm}}$ with a transformed operator and a cutoff of $n = 31$, which is sufficient for an accurate result.

Eq. (A.6). Therefore, in all fitted data shown below, there is a systematic error that we cannot estimate. Nevertheless, our fitting analysis helps us to quantify the convergence, e.g., larger values of σ showcase faster convergence. To test the validity of our fits we performed a χ^2 -test. It showed a test statistic smaller than 10^{-8} and a p-value of one for all fits. This shows that Eq. (A.6) models our data adequately.

A.2.1. Energy

The results of fitting the energies from Fig. 3.3 are presented in Tab. A.1. For the $1 + 1$ system with attractive interactions, the parameter σ is approximately 0.5 for the bare contact interaction, in agreement with our expectation. However, for repulsive interactions, the value of σ is higher, which indicates that the number of one-body basis states is not large enough to effectively suppress higher-order terms, such as $\sim 1/n$, in Eq.(A.5). For $1 + 1$ particles, all renormalized interactions lead to values of σ significantly larger than those for the bare contact interaction. This suggests that the data not only approach the infinite limit more closely, as discussed in Sec. 3.4, but they also converge more rapidly. Additionally, the extrapolated values for c in infinite Hilbert space are somewhat closer to the exact values for renormalized interactions compared to a bare contact potential. There are only minor differences observed between the running coupling constant approach and $V_{\text{eff}}^{\text{rel}}$. Since $V_{\text{eff}}^{\text{rel+cm}}$ is constant by construction, these data points were not included in the fit.

Let us now examine the convergence of the energy for the $1 + 3$ system calculated using the bare contact interaction, $g\delta$. For attractive interactions, we find that $\sigma \approx 0.78$ while for the repulsive $1 + 3$ system, σ is approximately 1, again highlighting the significance of higher-order terms in Eq. (A.5). For the energies of the $1 + 3$ system calculated using the effective interaction in relative coordinates, $V_{\text{eff}}^{\text{rel}}$, and the running coupling constant approach, $g(n)\delta$, we find that σ is less than 0.5 for attractive interactions. It is important to note that the non-monotonic behavior observed in Fig. 3.3 for $V_{\text{eff}}^{\text{rel}}$ cannot be accurately captured by Eq. (A.6). Therefore, we only fit the data for values of n in the range of 21 to 31. For a fair comparison with the other interactions, we also used this restricted fitting range. Nevertheless, the resulting values of c agree well with those obtained for $V_{\text{eff}}^{\text{rel+cm}}$, which produces the largest value of σ and the most stable fit. For repulsive interactions, the data based on the running coupling constant and $V_{\text{eff}}^{\text{rel}}$ show faster convergence compared to the bare contact interaction. For $V_{\text{eff}}^{\text{rel+cm}}$, the value of σ has a high uncertainty because the energy results are nearly converged, leading to minimal variation in the fitted data. This can also be seen by the small values for $A \approx 0$.

	c	A	σ
$E^{1+1}, g = -2.5067$ (corresponds to $E_{1+1} = -1$)			
$g\delta$	$0.9954 \pm 2 \cdot 10^{-4}$	$1.7566 \pm 4 \cdot 10^{-4}$	$0.4877 \pm 3 \cdot 10^{-4}$
$g(n)\delta$	$1.00151 \pm 2 \cdot 10^{-5}$	1.836 ± 0.002	$1.1802 \pm 5 \cdot 10^{-4}$
$V_{\text{eff}}^{\text{rel}}$	$0.9984 \pm 2 \cdot 10^{-4}$	2.14 ± 0.01	1.063 ± 0.003
$V_{\text{eff}}^{\text{rel+cm}}$	Constant by construction. Exact result: $c = 1.00000$		
$E^{1+1}, g = 3$ (corresponds to $E_{1+1} = 1.6$)			
$g\delta$	$2.6124 \pm 5 \cdot 10^{-4}$	0.511 ± 0.008	0.86 ± 0.01
$g(n)\delta$	$2.6004 \pm 3 \cdot 10^{-4}$	0.226 ± 0.005	1.41 ± 0.01
$V_{\text{eff}}^{\text{rel}}$	$2.6006 \pm 4 \cdot 10^{-4}$	$0.2636 \pm 5 \cdot 10^{-4}$	1.319 ± 0.009
$V_{\text{eff}}^{\text{rel+cm}}$	Constant by construction. Exact result: $c = 2.6000$		
$E^{1+3}, g = -2.5067$ (corresponds to $E_{1+1} = -1$)			
$g\delta^*$	2.119 ± 0.003	1.715 ± 0.003	0.390 ± 0.003
$g(n)\delta^*$	2.155 ± 0.009	0.122 ± 0.004	0.25 ± 0.04
$V_{\text{eff}}^{\text{rel}*}$	2.183 ± 0.007	0.74 ± 0.01	0.783 ± 0.009
$V_{\text{eff}}^{\text{rel+cm}*}$	$2.19341 \pm 2 \cdot 10^{-5}$	-17.9 ± 0.1	2.76 ± 0.02
$E^{1+3}, g = 3$ (corresponds to $E_{1+1} = 1.6$)			
$g\delta$	6.481 ± 0.002	2.02 ± 0.05	0.96 ± 0.01
$g(n)\delta$	$6.4331 \pm 1 \cdot 10^{-4}$	1.18 ± 0.05	1.71 ± 0.02
$V_{\text{eff}}^{\text{rel}}$	$6.4338 \pm 1 \cdot 10^{-4}$	0.93 ± 0.02	1.5 ± 0.1
$V_{\text{eff}}^{\text{rel+cm}}$	$6.4313 \pm 5 \cdot 10^{-4}$	0.02 ± 0.02	1.0 ± 0.4

Table A.1.: Fits of the energies from Fig. 3.3 (the second excited state for $1 + 1$ and the ground state for $1 + 3$) with the function $f(n) = c + \frac{A}{n^\sigma}$. The values from $n = 11$ to $n = 31$ were used for all fits except for the ones marked with *, there $n = 21 - 31$ was used. The uncertainties given are the uncertainties from the fitting procedure.

	c	A	σ
$\rho(0)^{1+1}, g = -2.5067$ (corresponds to $E_{1+1} = -1$)			
$g\delta$	$1.4276 \pm 3 \cdot 10^{-4}$	$-0.4137 \pm 7 \cdot 10^{-4}$	0.887 ± 0.001
$g(n)\delta$	$1.4338 \pm 4 \cdot 10^{-4}$	-0.83 ± 0.05	1.31 ± 0.03
$V_{\text{eff}}^{\text{rel}}$	$1.43441 \pm 6 \cdot 10^{-5}$	-0.72 ± 0.05	1.215 ± 0.003
$V_{\text{eff}}^{\text{rel+cm}}$	$1.43607 \pm 2 \cdot 10^{-5}$	-3.1 ± 0.1	2.47 ± 0.02
$\rho(0)^{1+3}, g = -2.5067$ (corresponds to $E_{1+1} = -1$)			
$g\delta$	$1.6001 \pm 3 \cdot 10^{-4}$	-0.297 ± 0.005	0.85 ± 0.01
$g(n)\delta$	$1.6069 \pm 5 \cdot 10^{-4}$	-0.31 ± 0.03	1.10 ± 0.05
$V_{\text{eff}}^{\text{rel}}$	$1.6076 \pm 2 \cdot 10^{-4}$	-0.295 ± 0.006	1.02 ± 0.01
$V_{\text{eff}}^{\text{rel+cm}}$	$1.6071 \pm 4 \cdot 10^{-4}$	-0.04 ± 0.08	2 ± 1

Table A.2.: Fits of the density at the origin from Fig. 3.4 with the function $f(n) = c + \frac{A}{n^\sigma}$. The values from $n = 11$ to $n = 31$ were used. The uncertainties given are the uncertainties from the fitting procedure.

A.2.2. Density

As discussed in the main text, the behavior of the energy as a function of n does not necessarily indicate the convergence properties of other observables. Therefore, in this subsection, we extend our analysis of convergence patterns by examining the density at $z = 0$, as shown in Table A.2, see also Fig. 3.4. The conclusions we can draw are similar to the ones for the energy: Renormalized interactions show larger values of σ , which shows that not only are results obtained using them closer to the $n \rightarrow \infty$ limit but that they also converge more quickly. The outcomes based on $V_{\text{eff}}^{\text{rel}}$ and the running coupling approach, $g(n)\delta$, are similar. The interaction $V_{\text{eff}}^{\text{rel+cm}}$ performs the best, i.e. it has the largest value of σ . Moreover, the data are already nearly constant (i.e. converged), as shown by the fact that $A \approx 0$ within the error margins.

A.2.3. One-body Hamiltonian

Kinetic energy. In Table A.3 we show the results of the fitting procedure for the kinetic energy, see also Fig. 3.5. For the attractive $1 + 1$ system, the bare contact interaction has the slowest convergence rate, characterized by the smallest value of σ . If both, the operator and the interaction, are transformed, the convergence rate is improved: with $V_{\text{eff}}^{\text{rel}}$, the convergence rate nearly doubles, while for $V_{\text{eff}}^{\text{rel+cm}}$, the calculated data remain constant – due to the construction of the interaction matrix and the induced two-body

	c	A	σ
$\langle T \rangle, N_{\uparrow} = 1, N_{\downarrow} = 1, g = -2.5067$ (corresponds to $E_{1+1} = -1$)			
$g\delta$	2.31 ± 0.02	-2.10 ± 0.01	0.245 ± 0.004
$g(n)\delta$	1.966 ± 0.002	-1.945 ± 0.003	0.484 ± 0.002
$V_{\text{eff}}^{\text{rel}}$ obs trans.	$1.9527 \pm 7 \cdot 10^{-4}$	-1.07 ± 0.01	0.879 ± 0.007
$V_{\text{eff}}^{\text{rel+cm}}$ obs trans.	Constant by construction. Exact result: $c = 1.9442$		
$V_{\text{eff}}^{\text{rel}}$ obs non-trans.	1.975 ± 0.003	-1.964 ± 0.004	0.479 ± 0.003
$V_{\text{eff}}^{\text{rel+cm}}$ obs non-trans.	1.884 ± 0.005	-2.16 ± 0.02	0.599 ± 0.007
$\langle T \rangle, N_{\uparrow} = 1, N_{\downarrow} = 1, g = 3$ (corresponds to $E_{1+1} = 1.6$)			
$g\delta$	$0.5919 \pm 2 \cdot 10^{-4}$	-0.261 ± 0.006	1.00 ± 0.01
$g(n)\delta$	$0.5883 \pm 4 \cdot 10^{-4}$	-0.323 ± 0.004	0.726 ± 0.007
$V_{\text{eff}}^{\text{rel}}$ obs trans.	$0.59698 \pm 2 \cdot 10^{-5}$	-0.150 ± 0.006	1.56 ± 0.02
$V_{\text{eff}}^{\text{rel+cm}}$ obs trans.	Constant by construction. Exact result: $c = 0.59731$		
$V_{\text{eff}}^{\text{rel}}$ obs non-trans.	$0.5887 \pm 4 \cdot 10^{-4}$	-0.325 ± 0.003	0.716 ± 0.007
$V_{\text{eff}}^{\text{rel+cm}}$ obs non-trans.	$0.5834 \pm 7 \cdot 10^{-4}$	-0.43 ± 0.01	0.86 ± 0.01
$\langle T \rangle, N_{\uparrow} = 1, N_{\downarrow} = 3, g = -2.5067$ (corresponds to $E_{1+1} = -1$)			
$g\delta$	Data could not be fitted by Eq. (A.6).		
$g(n)\delta$	Data could not be fitted by Eq. (A.6).		
$V_{\text{eff}}^{\text{rel}}$ obs trans.	Data could not be fitted by Eq. (A.6).		
$V_{\text{eff}}^{\text{rel+cm}}$ obs trans.	$4.0187 \pm 4 \cdot 10^{-4}$	56 ± 6	2.71 ± 0.04
$V_{\text{eff}}^{\text{rel}}$ obs non-trans.	Data could not be fitted by Eq. (A.6).		
$V_{\text{eff}}^{\text{rel+cm}}$ obs non-trans.	Data could not be fitted by Eq. (A.6).		
$\langle T \rangle, N_{\uparrow} = 1, N_{\downarrow} = 3, g = 3$ (corresponds to $E_{1+1} = 1.6$)			
$g\delta$ *	2.539 ± 0.001	2.9 ± 0.1	1.22 ± 0.02
$g(n)\delta$ *	2.531 ± 0.001	-1.77 ± 0.05	0.93 ± 0.01
$V_{\text{eff}}^{\text{rel}}$ obs trans. *	$2.5723 \pm 1 \cdot 10^{-4}$	-3.4 ± 0.2	1.92 ± 0.02
$V_{\text{eff}}^{\text{rel+cm}}$ obs trans. *	$2.575092 \pm 9 \cdot 10^{-6}$	-60 ± 20	3.9 ± 0.1
$V_{\text{eff}}^{\text{rel}}$ obs non-trans. *	2.532 ± 0.002	-1.75 ± 0.05	0.90 ± 0.01
$V_{\text{eff}}^{\text{rel+cm}}$ obs non-trans. *	2.525 ± 0.001	-2.12 ± 0.06	0.99 ± 0.01

Table A.3.: Fits of the kinetic energy from Fig. 3.5 with the function $f(n) = c + \frac{A}{n^{\sigma}}$. The values from $n = 11$ to $n = 31$ were used for all fits except the ones marked with *. There values from $n = 17$ to $n = 31$ were fitted. The uncertainties given are the uncertainties from the fitting procedure.

elements, see also Eq.(3.19). In the case of the repulsive $1 + 1$ system, the benefits of transforming the operator are even more visible: Without a transformation of the operator the renormalized interactions perform worse than the bare contact interaction, $g\delta(x)$, i.e. they have notably smaller values of σ .

For the attractive $1 + 3$ system, our fitting procedure has significant systematic uncertainties, which makes it difficult to fit all the data except when using $V_{\text{eff}}^{\text{rel+cm}}$ with a transformed kinetic energy operator. In this case, the large value of σ indicates that the data are nearly converged even for relatively small values of n . For the repulsive $1 + 3$ system, the fitting procedure has similar results as for the $1 + 1$ case discussed earlier: Without transformation of the operator, renormalized interactions do not offer any advantage over the bare contact interaction. However, when both the operator and the potential are transformed, renormalized interactions show a faster convergence than the bare contact interaction.

Harmonic trap.

Next, we discuss the second part of the one-body Hamiltonian: the harmonic trapping confinement². For a comparison plot of the data see Fig. 3.6 in the main text – the results of our fitting analysis are summarized in Table A.4. As mentioned in the main text, the trapping confinement is less sensitive to the transformation of operators compared to the kinetic energy. For the $1 + 1$ system, we observe that the convergence rates for both attractive and repulsive interactions are similar, with the renormalized interactions providing a slight improvement in performance.

Even if the operator of the harmonic trap is not transformed, using the interaction $V_{\text{eff}}^{\text{rel+cm}}$ results in fast convergence. As in the cases considered above, $V_{\text{eff}}^{\text{rel+cm}}$ clearly outperforms other interactions. Interestingly, the running coupling constant shows the weakest performance. Specifically for the $1 + 3$ system with attractive interactions, it fails to produce data that can be fit with Eq. (A.6). Additionally, the convergence of the data calculated with $V_{\text{eff}}^{\text{rel}}$ is slow ($\sigma = 0.24 \pm 0.08$), comparable to the rate of the bare contact interaction, which makes this interaction less ideal to calculate this observable. For the repulsive $1 + 3$ system, all potentials can be used in principle, as their convergence rates are comparable. However, $V_{\text{eff}}^{\text{rel+cm}}$ still provides the most accurate result.

A.2.4. Transition matrix elements

As a last observable, we discuss the transition matrix elements shown in Fig. 3.7. The results from the fitting analysis are shown in Table A.5. Even for the $1 + 1$ system, it is

²Note that in general the confinement is not an observable quantity. However, in the case of a harmonic oscillator, the expectation value of the trapping confinement corresponds to the mean-square radius, which is a standard observable in cold-atom systems.

	c	A	σ
$\langle W \rangle, N_{\uparrow} = 1, N_{\downarrow} = 1, g = -2.5067$ (corresponds to $E_{1+1} = -1$)			
$g\delta$	$0.31782 \pm 9 \cdot 10^{-5}$	0.219 ± 0.002	0.863 ± 0.004
$g(n)\delta$	$0.3153 \pm 2 \cdot 10^{-4}$	0.480 ± 0.003	1.295 ± 0.003
$V_{\text{eff}}^{\text{rel}}$ obs trans.	$0.31474 \pm 2 \cdot 10^{-5}$	0.480 ± 0.001	1.191 ± 0.003
$V_{\text{eff}}^{\text{rel+cm}}$ obs trans.	Constant by construction. Exact result: $c = 0.31472$		
$V_{\text{eff}}^{\text{rel}}$ obs non-trans.	$0.31515 \pm 1 \cdot 10^{-5}$	0.459 ± 0.003	1.233 ± 0.001
$V_{\text{eff}}^{\text{rel+cm}}$ obs non-trans.	$0.31492 \pm 2 \cdot 10^{-5}$	0.377 ± 0.007	1.672 ± 0.009
$\langle W \rangle, N_{\uparrow} = 1, N_{\downarrow} = 1, g = 3$ (corresponds to $E_{1+1} = 1.6$)			
$g\delta$	$0.7399 \pm 3 \cdot 10^{-4}$	0.302 ± 0.006	0.89 ± 0.01
$g(n)\delta$	$0.73265 \pm 1 \cdot 10^{-5}$	0.168 ± 0.005	1.66 ± 0.01
$V_{\text{eff}}^{\text{rel}}$ obs trans.	$0.73277 \pm 2 \cdot 10^{-5}$	0.153 ± 0.004	1.41 ± 0.01
$V_{\text{eff}}^{\text{rel+cm}}$ obs trans.	Constant by construction. Exact result: $c = 0.732404$		
$V_{\text{eff}}^{\text{rel}}$ obs non-trans.	$0.73278 \pm 2 \cdot 10^{-5}$	0.143 ± 0.004	1.42 ± 0.01
$V_{\text{eff}}^{\text{rel+cm}}$ obs non-trans.	$0.732442 \pm 5 \cdot 10^{-6}$	0.088 ± 0.005	1.93 ± 0.03
$\langle W \rangle, N_{\uparrow} = 1, N_{\downarrow} = 3, g = -2.5067$ (corresponds to $E_{1+1} = -1$)			
$g\delta$ *	1.99 ± 0.02	0.26 ± 0.01	0.24 ± 0.04
$g(n)\delta$	Data could not be fitted by Eq. (A.6).		
$V_{\text{eff}}^{\text{rel}}$ obs trans. *	2.01 ± 0.03	0.17 ± 0.01	0.24 ± 0.08
$V_{\text{eff}}^{\text{rel+cm}}$ obs trans. *	$2.070624 \pm 7 \cdot 10^{-6}$	-3000 ± 800	5.13 ± 0.09
$V_{\text{eff}}^{\text{rel}}$ obs non-trans. *	1.9 ± 0.1	0.2 ± 0.1	0.12 ± 0.09
$V_{\text{eff}}^{\text{rel+cm}}$ obs non-trans. *	$2.07192 \pm 3 \cdot 10^{-5}$	$8 \cdot 10^5 \pm 2 \cdot 10^5$	6.9 ± 0.3
$\langle W \rangle, N_{\uparrow} = 1, N_{\downarrow} = 3, g = 3$ (corresponds to $E_{1+1} = 1.6$)			
$g\delta$ *	$3.0307 \pm 8 \cdot 10^{-4}$	2.16 ± 0.09	1.18 ± 0.02
$g(n)\delta$ *	$3.00419 \pm 4 \cdot 10^{-5}$	3.09 ± 0.07	1.918 ± 0.009
$V_{\text{eff}}^{\text{rel}}$ obs trans. *	$3.00227 \pm 1 \cdot 10^{-5}$	2.21 ± 0.08	1.77 ± 0.02
$V_{\text{eff}}^{\text{rel+cm}}$ obs trans. *	$3.00227 \pm 1 \cdot 10^{-5}$	1.6 ± 0.4	2.66 ± 0.09
$V_{\text{eff}}^{\text{rel}}$ obs non-trans. *	$3.00460 \pm 8 \cdot 10^{-5}$	2.21 ± 0.09	1.78 ± 0.02
$V_{\text{eff}}^{\text{rel+cm}}$ obs non-trans. *	$3.00241 \pm 2 \cdot 10^{-5}$	2.7 ± 0.3	2.46 ± 0.04

Table A.4.: Fits of the harmonic trapping potential from Fig. 3.6 with the function $f(n) = c + \frac{A}{n^\sigma}$. The values from $n = 11$ to $n = 31$ were used for all fits except the ones marked with *. Their values from $n = 17$ to $n = 31$ were fitted. The uncertainties given are the uncertainties from the fitting procedure.

	c	A	σ
$M_{0 \rightarrow f}^{1+1}, g = -2.5067$ (corresponds to $E_{1+1} = -1$)			
$g\delta$	$0.4367 \pm 5 \cdot 10^{-4}$	$-0.3490 \pm 1 \cdot 10^{-4}$	0.377 ± 0.002
$g(n)\delta$	$0.4283 \pm 5 \cdot 10^{-4}$	$-0.4348 \pm 6 \cdot 10^{-4}$	0.449 ± 0.002
$V_{\text{eff}}^{\text{rel}}$ obs trans.	$0.4202 \pm 2 \cdot 10^{-4}$	$-0.1642 \pm 8 \cdot 10^{-4}$	0.983 ± 0.003
$V_{\text{eff}}^{\text{rel+cm}}$ obs trans.	Constant by construction. Exact result: $c = 0.4199$		
$g(n)\delta$ obs non-trans.	$0.4181 \pm 5 \cdot 10^{-4}$	-0.279 ± 0.001	0.544 ± 0.005
$V_{\text{eff}}^{\text{rel}}$ obs non-trans.	$0.4271 \pm 4 \cdot 10^{-4}$	$-0.42149 \pm 4 \cdot 10^{-4}$	0.448 ± 0.001
$V_{\text{eff}}^{\text{rel+cm}}$ obs non-trans.	0.411 ± 0.001	-0.485 ± 0.003	0.5421 ± 0.005
$M_{0 \rightarrow f}^{1+1}, g = 3$ (corresponds to $E_{1+1} = 1.6$)			
$g\delta$	$0.0982 \pm 1 \cdot 10^{-4}$	0.137 ± 0.002	0.785 ± 0.007
$g(n)\delta$	0.101 ± 0.002	0.255 ± 0.002	0.744 ± 0.006
$V_{\text{eff}}^{\text{rel}}$ obs trans.	$0.094920 \pm 6 \cdot 10^{-6}$	$0.0209 \pm 4 \cdot 10^{-4}$	1.19 ± 0.01
$V_{\text{eff}}^{\text{rel+cm}}$ obs trans.	Constant by construction. Exact result: 0.094829		
$g(n)\delta$ obs non-trans.	$0.0977 \pm 1 \cdot 10^{-4}$	$0.1034 \pm 9 \cdot 10^{-4}$	0.695 ± 0.006
$V_{\text{eff}}^{\text{rel}}$ obs non-trans.	$0.1014 \pm 3 \cdot 10^{-4}$	0.263 ± 0.003	0.754 ± 0.006
$V_{\text{eff}}^{\text{rel+cm}}$ obs non-trans.	$0.1046 \pm 4 \cdot 10^{-4}$	0.355 ± 0.009	0.89 ± 0.01
$M_{0 \rightarrow f}^{1+3}, g = -2.5067$ (corresponds to $E_{1+1} = -1$)			
$g\delta$	Data could not be fitted by Eq. (A.6).		
$g(n)\delta$	Data could not be fitted by Eq. (A.6).		
$V_{\text{eff}}^{\text{rel}}$ obs trans.	Data could not be fitted by Eq. (A.6).		
$V_{\text{eff}}^{\text{rel+cm}}$ obs trans.	$0.1518 \pm 3 \cdot 10^{-4}$	47 ± 7	2.92 ± 0.07
$g(n)\delta$ obs non-trans.	Data could not be fitted by Eq. (A.6).		
$V_{\text{eff}}^{\text{rel}}$ obs non-trans.	Data could not be fitted by Eq. (A.6).		
$V_{\text{eff}}^{\text{rel+cm}}$ obs non-trans.	Data could not be fitted by Eq. (A.6).		
$M_{0 \rightarrow f}^{1+3}, g = 3$ (corresponds to $E_{1+1} = 1.6$)			
$g\delta$	$0.1256 \pm 2 \cdot 10^{-4}$	1.22 ± 0.03	1.34 ± 0.01
$g(n)\delta$	$0.1265 \pm 6 \cdot 10^{-4}$	0.77 ± 0.03	1.08 ± 0.02
$V_{\text{eff}}^{\text{rel}}$ obs trans.	$0.1124 \pm 3 \cdot 10^{-4}$	0.30 ± 0.07	1.4 ± 0.1
$V_{\text{eff}}^{\text{rel+cm}}$ obs trans.	$0.11239 \pm 7 \cdot 10^{-5}$	0.2 ± 0.2	2.1 ± 0.4
$g(n)\delta$ obs non-trans.	$0.1198 \pm 5 \cdot 10^{-4}$	0.50 ± 0.03	1.16 ± 0.03
$V_{\text{eff}}^{\text{rel}}$ obs non-trans.	$0.2624 \pm 6 \cdot 10^{-4}$	0.77 ± 0.03	1.06 ± 0.02
$V_{\text{eff}}^{\text{rel+cm}}$ obs non-trans.	0.126 ± 0.001	0.95 ± 0.05	1.11 ± 0.03

Table A.5.: Fits of the transition matrix elements from Fig. 3.7 with Eq. (A.6) for $n = 11$ to $n = 31$. Uncertainties are the ones from fitting.

advantageous to transform the operator along with the interaction. For $V_{\text{eff}}^{\text{rel+cm}}$, the result is exact by construction when the operator is transformed with the interaction. For $V_{\text{eff}}^{\text{rel}}$, the data converges significantly faster (indicated by a larger σ) compared to the bare contact interaction. In the case of repulsive interactions, we observe that the value of A is small, suggesting that the expectation value of the operator for $n \rightarrow \infty$ can be reliably estimated using data for relatively small values of n .

For the repulsive $1 + 3$ system, the importance of transforming the operator becomes even more clear. The effective interactions with a transformed operator lead to the best performance: Using $V_{\text{eff}}^{\text{rel+cm}}$ results in the highest convergence rate and a small value of A , indicating that the data are nearly converged for the values of n used. Transforming the operator along the renormalization for $V_{\text{eff}}^{\text{rel}}$ slightly enhances the convergence rate and reduces the value of A . For attractive interactions and $1 + 3$ particles, the fitting procedure could not be used in all cases except when using $V_{\text{eff}}^{\text{rel+cm}}$ with a transformed operator. This is likely because the convergence rate is so slow that the fitting function introduces a significant systematic error in these cases (see also the discussion in the main text). However, with $V_{\text{eff}}^{\text{rel+cm}}$, the convergence rate is fast ($\sigma = 2.92 \pm 0.07$), enabling us to achieve accurate results.

A.3. Two-dimensional harmonic oscillator

In this appendix, we start by introducing the few-fermion problem in a two-dimensional harmonic oscillator. Next, we explain our truncation scheme and the subsequent renormalization employed in our numerical calculations. Finally, we show how the interaction matrix for the effective interaction approach, $V_{\text{eff}}^{\text{rel}}$, is constructed.

The Hamiltonian of the system reads

$$H = \sum_{i=1}^N \left(-\frac{1}{2} \nabla_i^2 + \frac{1}{2} \vec{x}_i^2 \right) + g \sum_{i < j} \delta(\vec{x}_i - \vec{x}_j). \quad (\text{A.7})$$

As in the main text, we consider a system of $N = N_{\uparrow} + N_{\downarrow}$ fermions. The interaction cannot flip the polarization of the spins and due to the Pauli exclusion principle only fermions of different polarization can interact.

For the one-body basis functions, we solve the one-body part of the Hamiltonian, i.e. we use the eigenfunctions of the two-dimensional harmonic oscillator [226, 227]

$$\Phi_i(\vec{x}) = \frac{1}{\sqrt{2\pi}} e^{im_i\phi} F_{n_i, m_i}(\rho) = \frac{1}{\sqrt{2\pi}} e^{im_i\phi} (-1)^{n_i} \sqrt{\frac{2\Gamma(n_i + 1)}{\Gamma(|m_i| + n_i + 1)}} e^{-\rho^2/2} \rho^{|m_i|} L_{n_i}^{|m_i|}(\rho^2), \quad (\text{A.8})$$

where i is the index of the basis state with m_i the angular component of this index and n_i the radial one. We use polar coordinates with ρ and ϕ . L is the generalized Laguerre polynomial. The eigenenergy of this state is

$$E_{m_i, n_i} = 2n_i + |m_i| + 1. \quad (\text{A.9})$$

In the CI calculation we build the Hamiltonian matrix using the eigenfunctions as one-body basis states up to a cutoff n_{2D} in the one-body energy. For details on the CI-method we refer to Sec. 2.2.

In two dimensions, the contact interaction diverges (see Ref. [51] and references therein). We address this divergence by regularizing the contact interaction using a finite cutoff in the one-body basis. For renormalization we use the two-body ground state energy, i.e. this energy is our measure of interaction strength. In practice, this means that we calculate the two-body energy for each cutoff for different values of g , together with our desired quantities, such as the ground-state energy of systems with more particles or the energies of higher excited states in the $1 + 1$ system. This renormalization approach is consistent with the method outlined in Ref. [51]. Note that this approach is similar to the running coupling constant approach employed for one-dimensional systems.

For the effective interaction approach, we need to know the exact two-body spectrum. It can be obtained from the analytical solution [120, 121] where a regularized pseudopotential is used [228]

$$V_{\text{Pseudo}} = -\frac{2\pi\delta(\vec{x})}{\ln(\mathcal{A}a\Lambda)} \left[1 - \ln(\mathcal{A}\Lambda\rho)\rho\frac{\partial}{\partial\rho} \right]_{\rho \rightarrow 0^+} \quad (\text{A.10})$$

with Λ an arbitrary constant, $\mathcal{A} = e^\gamma/2$ where γ is the Euler-Mascheroni constant, and a is the scattering length in two dimensions.

As for the one-dimensional system, the Schrödinger equation factorizes in a center-of-mass $\vec{X} = \frac{1}{\sqrt{2}}(\vec{x}_1 + \vec{x}_2)$ and a relative part $\vec{x} = \frac{1}{\sqrt{2}}(\vec{x}_1 - \vec{x}_2)$. As the interaction only affects the latter, the eigenstates of the former are the solutions of the non-interacting harmonic oscillator. Because we have s-wave interaction, only relative states with angular momentum equal to zero are influenced by the interaction. All other states are also the eigenstates of the non-interacting harmonic oscillator. For the states with vanishing angular momentum, we solve the Schrödinger equation in relative coordinates

$$\left(-\frac{\nabla_\rho^2}{2} + \frac{\rho^2}{2} + V_{\text{Pseudo}} \right) \Psi_i(\rho) = \epsilon_i \Psi(\rho). \quad (\text{A.11})$$

The solution depends only on the radial coordinate

$$\Psi_i(\rho) = \frac{1}{\sqrt{2\pi}} \mathcal{N}_{\nu_i} \Gamma(-\nu_i) e^{-\rho^2/2} U(-\nu_i, 1, \rho^2), \quad (\text{A.12})$$

where U is the Tricomi function [102] and Γ is the gamma function. The values ν_i are determined from the equation

$$\psi(-\nu) = \ln(2/a^2) - 2\gamma, \quad (\text{A.13})$$

where ψ is the digamma function. The normalization constant \mathcal{N}_ν is

$$\mathcal{N}_\nu = \frac{\sqrt{2}}{\sqrt{\psi'(-\nu)}}. \quad (\text{A.14})$$

Here, ψ' is the trigamma function. The energy of these states is given by $\epsilon_i = 2\nu_i + 1$.

To build the effective interaction matrix, we can use that the Talmi-Moshinsky-Smirnov brackets,

$$\alpha_{ij,ab} = \int d\vec{x}_1 \int d\vec{x}_2 \Phi_i(\vec{x}_1) \Phi_j(\vec{x}_2) \Phi_a(\vec{x}) \Phi_b(\vec{X}), \quad (\text{A.15})$$

are known analytically in two dimensions [8, 229] and that the overlap integral,

$$U_{ij} = \int d\vec{x} \Phi_i(\vec{x}) \Psi_j(\vec{x}), \quad (\text{A.16})$$

can be calculated analytically. To show this we use that $\Psi_i(\vec{x})$ solves the Schrödinger equation with the pseudopotential. This allows us to rewrite the integral as

$$U_{ij} = \frac{\int d\vec{x} V_{\text{pseudo}} \Phi_i(\vec{x}) \Psi_j(\vec{x})}{\epsilon_{\nu_j} - T_i} \quad (\text{A.17})$$

with $T_i = 2i + 1$ the energy of the non-interacting system. Next, we apply $U(-\nu, 1, \rho^2) \rightarrow -(2\ln(\rho) + 2\gamma + \psi(-\nu))/\Gamma(-\nu)$ in the limit $\rho \rightarrow 0$, and we arrive at

$$U_{ij} = \sqrt{2\pi} \frac{\Phi_i(0) \mathcal{N}_{\nu_j}}{\epsilon_{\nu_j} - T_i}. \quad (\text{A.18})$$

We calculate V_{ijkl} (using orthogonality of the harmonic oscillator eigenfunctions and that we have s-wave interaction together with momentum conservation) via

$$\begin{aligned} V_{ijkl} &= \sum_{a,b,a_1,b_1} \alpha_{ij,ab}^\dagger \alpha_{kl,a_1b_1} \int d\vec{x} \int d\vec{X} \Phi_a^\dagger(\vec{x}) \Phi_b^\dagger(\vec{X}) V(\vec{x}) \Phi_{a_1}(\vec{x}) \Phi_{b_1}(\vec{X}) \\ &= \sum_{a,b,a_1} \alpha_{ij,ab}^\dagger \alpha_{kl,a_1b} \delta_{m_a,0} \delta_{m_{a_1},0} v_{aa_1}, \end{aligned} \quad (\text{A.19})$$

where $V(\vec{x})$ is the potential we want to implement. Because we have no explicit expression for the effective interaction in coordinate space, we rewrite it in terms of v_{aa_1} which we build using the effective interaction approach. Therefore, we determine v_{aa_1} from our effective interaction calculation

$$v^{\text{eff}} = Q^\dagger E Q - T, \quad \text{with } Q = \frac{U}{\sqrt{U^\dagger U}} \quad (\text{A.20})$$

with $T_{ij} = \delta_{ij}(2n_i + |m_i| + 1)$ a diagonal matrix representing the energies of the non-interacting system and E a diagonal matrix containing the energies of the interacting system on its diagonal. Because only matrix elements with vanishing angular momentum contribute to the interaction, we only need to consider them, i.e. $m_i = 0$. Therefore, all matrices are restricted by a cutoff in the n -quantum number. Since center-of-mass excitations can be distributed between two quantum numbers, there is an inherent ambiguity between the cutoffs for the laboratory and center-of-mass reference frame. Empirically, we found that choosing $n_{\text{rel}} = n_{2D}/2 + 1^3$ works well in our calculations. However, this ambiguity prevents us from identifying a useful relation for the cutoffs for the $V_{\text{eff}}^{\text{rel+cm}}$ interaction. As a result, we leave the construction of this interaction in 2D to future studies.

A.4. Convergence of energy for larger particle number

Let us now show that the conclusions drawn in the main text also hold for larger particle numbers, which is particularly important if one wants to study the few-to-many-body crossover using renormalized interactions. Therefore, we present additional data for the ground state energy of the $1 + N$ system, with N up to six particles, and the $2 + N$ system, with N up to four particles. As described in the main text of Chap. 3, the size of the Hilbert space grows exponentially with the number of particles and therefore we have to restrict the maximum one-body cutoff to $n = 21$ instead of $n = 31$. For the largest particle number shown in this Appendix, this corresponds to more than one million many-body basis states, making an even larger cutoff impossible on a standard computer. This cutoff is insufficient in producing converged results for large particle numbers and the interaction strengths used in the main text. However, as we show below, the main characteristics of the convergence behavior remains the same as in the main part.

³Recall that n_{2D} defines the maximal one-body energy, while n_{rel} is the highest radial quantum number used to construct the effective interaction in relative coordinates.

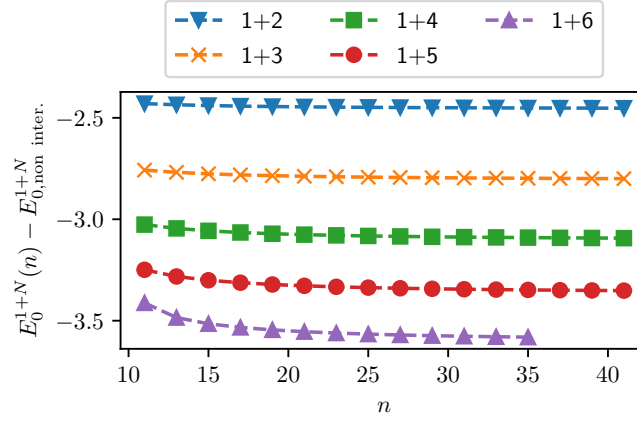


Figure A.2.: **Interaction energy of the $1 + N$ system for different particle numbers as a function of the one-body cutoff n calculated by diagonalizing Eq. (A.22).** We show data for an attractive interaction of $g = -2.5067$ (which corresponds to $E_{1+1} = -1$). Numerical data are shown with markers of different shape for different particle numbers; lines are added to guide the eye. Figure taken from Ref. [112].

A.4.1. Calculation in relative coordinates

Because our renormalized interactions do not lead to converged results, we employ an additional calculation to judge the performance of the $1 + N$ calculations. Therefore, we use the symmetries of our Hamiltonian, Eq. (3.1), and transform to the frame of reference centered at the impurity (similar to the Lee-Low-Pines transformation in real space, see Sec. 2.4). As described in Sec. 2.4, such a transformation effectively reduces the particle number by one and allows us to implement the contact interaction as a boundary condition of the one-body basis. The resulting Hamiltonian in center-of-mass and relative coordinates reads:

$$H^{\text{cm}} = -\frac{\hbar}{2N} \frac{\partial^2}{\partial y^2} + \frac{N}{2} y^2, \quad (\text{A.21})$$

$$H^{\text{rel}} = -\sum_{i=1}^N \frac{\partial^2}{\partial x_i^2} + \frac{1}{2} \frac{N-1}{N} \sum_{i=1}^N x_i^2 + \sum_{i=1}^N g \delta(x_i) + \sum_{i,j} V(x_i, x_j), \quad (\text{A.22})$$

where $V(x_i, x_j) = -\frac{1}{2} \partial_{x_i} \partial_{x_j} - \frac{1}{N+1} x_i x_j$. The center-of-mass part is simply solved by the eigenstates of the harmonic oscillator. For the Hamiltonian in relative coordinates, H^{rel} ,

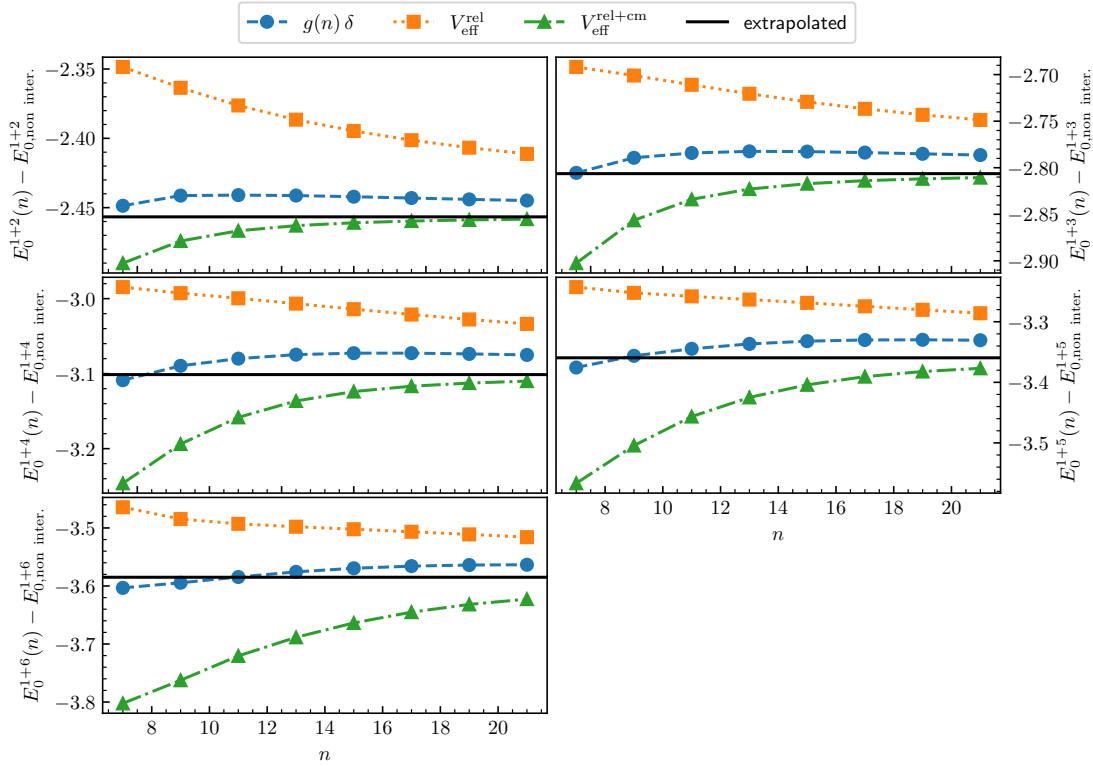


Figure A.3.: **Interaction energy for $1 + N$ particles as a function of the one-body cutoff n calculated with renormalized interactions.**

In all panels we use attractive interactions with $g = -2.5067$ (which corresponds to $E_{1+1} = -1$). Numerical data are shown with markers of different shape for the different particle numbers; dashed lines are added to guide the eye. The black solid line corresponds to an extrapolation of the data shown in Fig. A.2 using the fitting function from Eq. (A.6). Different panels correspond to different particle numbers. Figure modified from Ref. [112].

we employ a CI-calculation where we use the exact solution of the one-body part of the Hamiltonian, Eq. (3.6), as one-body basis states. For more details on this approach we refer the interested reader to Ref. [49]. For similar applications for a one-dimensional ring we refer to Sec. 2.4 and Chaps. 5, 4.

Because we now only have to solve a N -body problem instead of a $1 + N$ system, we

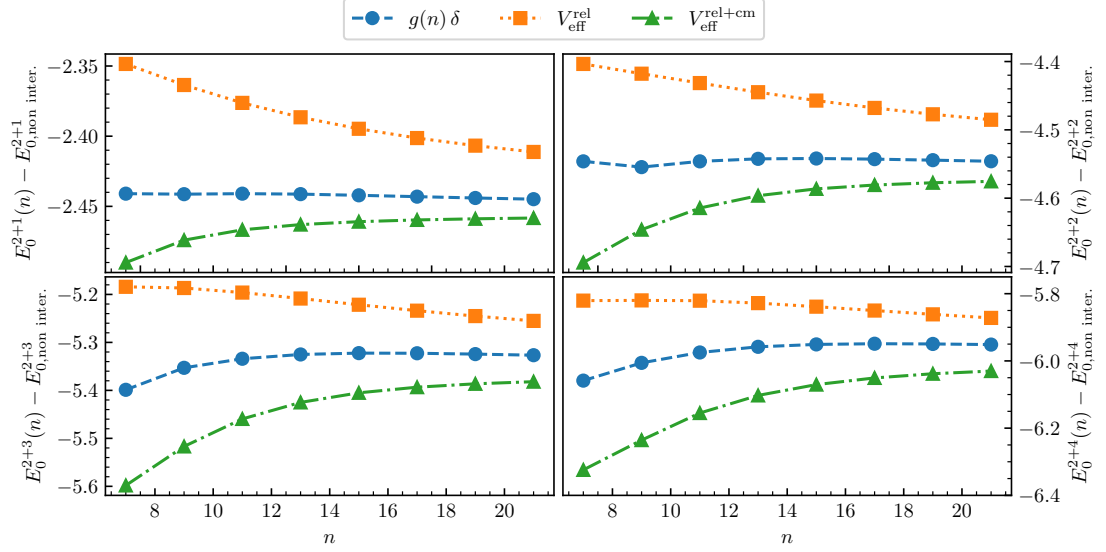


Figure A.4.: **Interaction energy for $2 + N$ particles as a function of the one-body cutoff n calculated with renormalized interactions.**

We consider attractive interactions with $g = -2.5067$ (which corresponds to $E_{1+1} = -1$) in all panels. Numerical data are shown with markers of different shape for the different particle numbers; dashed lines are added to guide the eye. Different panels correspond to different particle numbers. Figure modified from Ref. [112].

can use a larger one-body basis cutoff, i.e. $n = 37$ for the $1 + 6$ system and $n = 41$ for lower particle numbers. Furthermore, because the one-body basis states already include information about the delta-interaction, we can reach nearly converged results as we show in Fig. A.2. We further extrapolate these data to $n \rightarrow \infty$ using the fitting function described above, Eq. (A.6). Below, we use these results as benchmark for our calculations with effective interactions.

A.4.2. Energy convergence $1 + N$ system

We show in Fig. A.3 the interaction energy, $E(g) - E(g = 0)$, as a function of the one-body cutoff, n , for $1 + N$ systems. Because the bare contact interaction converges considerably slower than the renormalized ones, we display only the latter. Furthermore, we plot the extrapolated data of Fig. A.2 which we use as benchmark.

Indeed, we see that the conclusions drawn in the main part of our work also hold for larger particle numbers. For the 1 + 2, 1 + 3, 1 + 4 and 1 + 5 systems the $V_{\text{eff}}^{\text{rel+cm}}$ interaction leads to results that are closest to the benchmark values. For the 1 + 6 system, at a first glance it looks as if the running coupling constant approach, $g(n)\delta$, outperforms the other potentials. However, as discussed in the main part of Chap. 3 this interaction leads to non-monotonic results, and for the cutoffs considered here, the energy is still an increasing function of n . This means that increasing the cutoff leads to an energy farther from the benchmark result. Only for larger cutoffs will it converge to the correct value.

A.4.3. Energy convergence 2 + N system

Furthermore, we want to show that our results also hold for configurations, for which a transformation to the relative frame does not bring any advantage, i.e. we show results for the ground-state energy of the 2 + N system in Fig. A.4. This figure features similar convergence patterns and therefore shows that our conclusions also hold for systems that cannot be represented as an impurity in a Fermi gas.

A.5. Implementation of effective interactions

A.5.1. Implementation of $V_{\text{eff}}^{\text{rel}}$

To make this thesis self-contained, we explain in this Appendix the necessary steps to construct the interaction matrix for the $V_{\text{eff}}^{\text{rel}}$ interaction. The discussion follows Ref. [50].

To start, we define the interaction matrix needed for the CI calculation (see Sec. 2.2)

$$V_{ijkl} = \int dx_1 \int dx_2 \Phi_i(x_1) \Phi_j(x_2) V(x_1 - x_2) \Phi_k(x_1) \Phi_l(x_2). \quad (\text{A.23})$$

Since we employ a contact interaction, $V(x_1 - x_2)$ depends only on the relative distance between two particles. Because we have a harmonic trapping confinement, we can factorize the two-body wavefunction in relative $x = \frac{1}{\sqrt{2}}(x_1 - x_2)$ and center-of-mass $X = \frac{1}{\sqrt{2}}(x_1 + x_2)$ coordinates:

$$\Phi_i(x_1) \Phi_j(x_2) = \sum_{a,b} \alpha_{ij,ab} \Phi_a(x) \Phi_b(X), \quad (\text{A.24})$$

where the expansion coefficients (Talmi-Moshinsky-Smirnov brackets),

$$\alpha_{ij,ab} = \int dx_1 \int dx_2 \Phi_i(x_1) \Phi_j(x_2) \Phi_a(x) \Phi_b(X), \quad (\text{A.25})$$

can be calculated analytically [50, 230]. With these coefficients, we can calculate the interaction matrix as follows:

$$V_{ijkl} = \sum_{a,a',b} \alpha_{ij,ab} \alpha_{kl,a'b} v_{aa'} \quad \text{with} \quad v_{aa'} = \int dx \Phi_a(x) V(\sqrt{2}x) \Phi_{a'}. \quad (\text{A.26})$$

Next, we want to use the framework of the effective interaction (see Sec. 3.3.2) to construct the matrix $v_{aa'}$. Therefore, we solve the Schrödinger equation in relative coordinates (see Eqs. (3.7), (3.5))

$$\left(-\frac{1}{2} \frac{\partial^2}{\partial x^2} + \frac{x^2}{2} + \frac{g}{\sqrt{2}} \delta(x) \right) \Psi_i(x) = \epsilon_i \Psi_i(x). \quad (\text{A.27})$$

Now, we use the eigenenergies to build the diagonal matrix $E_{ij} = \delta_{ij} \epsilon_i$ and the eigenstates to calculate the overlap matrix $U_{ij} = \int dx \Psi_i(x) \Phi_j(x)$:

$$U_{ij} = \begin{cases} -g \frac{\Psi_i(0) \Phi_j(0)}{j+1/2-\epsilon_i} & \text{for } i \text{ and } j \text{ even,} \\ \delta_{ij} & \text{for } i \text{ and } j \text{ odd,} \\ 0 & \text{otherwise.} \end{cases} \quad (\text{A.28})$$

Putting everything together we can construct the effective interaction matrix in relative coordinates

$$v^{\text{eff}} = Q^\dagger E Q - T, \quad \text{with} \quad Q = \frac{U}{\sqrt{U^\dagger U}}, \quad (\text{A.29})$$

where we omitted the indices of the matrices for better readability. The matrix T is the diagonal non-interacting matrix $T_{ij} = \delta_{ij} (i + 1/2)$. The dimensions of the matrices U , E and T are $n_{\text{rel}} \times n_{\text{rel}}$ with $n_{\text{rel}} = 2n$. Remember: n is the one-body cutoff of our CI calculation in the laboratory frame. To relate n and n_{rel} we used energy conservation between the maximal two-body energy in the laboratory frame ($2n + 1$) with the maximal two-body energy in relative and center-of-mass coordinates. As a last step, we use matrix Eq. (A.26) to transform v^{eff} to V_{ijkl} .

In App. A.6.3 we explain the transformation of operators alongside this interaction.

A.5.2. Implementation of $V_{\text{eff}}^{\text{rel+cm}}$

Now, we explain how to build an effective interaction matrix by including not only the relative exact solution but also the center-of-mass excitations:

$$\begin{aligned}
V_{ijkl} &= \left[QEQ^\dagger \right]_{p(i,j),t(k,l)} - (i+l+1)\delta_{i,k}\delta_{j,l} \\
&= \sum_{r,m} Q_{p(i,j),r} E_{r,m} Q_{m,t(k,l)}^\dagger - (i+l+1)\delta_{i,k}\delta_{j,l} \\
&= \sum_r Q_{p(i,j),r} E_{r,r} Q_{r,t(k,l)}^\dagger - (i+l+1)\delta_{i,k}\delta_{j,l}
\end{aligned} \tag{A.30}$$

with $E_{r,m} = \delta_{rm}(\epsilon_{a(r)} + b(r) + 1/2)$ the diagonal interacting eigenenergy matrix, with $\epsilon_{a(r)}$ the eigenenergy of the Hamiltonian in relative coordinates and $b(r) + 1/2$ the eigenenergy of the corresponding center-of-mass part. The two-body indices p, t, r, m are functions of the one-body indices i, j, k, l, a, b , e.g. $p = in + j$ with n the single-body cutoff introduced in the main text. Note that i, j, k, l, p, t are defined in the laboratory frame while a, b, m, r operate in the space defined by relative and center-of-mass coordinates.

To efficiently construct the effective interaction matrix, we need to calculate the unitary overlap matrix

$$Q_{pr} = \sum_d \frac{U_{pd}}{\sqrt{\sum_b U_{db}^\dagger U_{br}}} \quad \text{where} \quad U_{r(a,b),t(k,l)} = \int dx_1 \int dx_2 \Psi_{r(a,b)}(x_1, x_2) \Phi_k(x_1) \Phi_l(x_2), \tag{A.31}$$

where $\Psi_{r(a,b)}(x_1, x_2) = \psi_{a(r)}(x) \Phi_{b(r)}(X)$; $\psi_{a(r)}(x)$ is the solution of the Schrödinger equation in relative coordinates (Eq. (3.6)) and $\Phi_{b(r)}(X)$ is the harmonic oscillator wave function. If $a(r)$ is odd, the relative wave function is just a solution of the non-interacting harmonic oscillator, $\psi_{a(r)}(x) = \Phi_{a(r)}(x)$, and the overlap matrix element is given by

$$U_{r(a,b),t(k,l)} = \alpha_{ab,kl}. \tag{A.32}$$

In case that $a(r)$ is even, we can utilize that $\Psi_r(x_1, x_2)$ solves the two-body Schrödinger equation,

$$U_{r(a,b),t(k,l)} = g \frac{\int dx \Psi_{r(a,b)}(x, x) \Phi_k(x) \Phi_l(x)}{E_{r(a,b),r(a,b)} - (k+l+1)}. \tag{A.33}$$

Now, we use

$$\Psi_{r(a,b)}(x, x) = \psi_{a(r)}(0) \Phi_{b(r)}(\sqrt{2}x) \tag{A.34}$$

and

$$\Phi_k(x) \Phi_l(x) = \sum_{a_1, b_1} \alpha_{kl, a_1 b_1} \Phi_{a_1}(0) \Phi_{b_1}(\sqrt{2}x) \tag{A.35}$$

to arrive at

$$U_{r(a,b),t(k,l)} = g\psi_{a(r)}(0) \sum_{b_1} \alpha_{kl,(k+l-b_1)b_1} \Phi_{k+l-b_1}(0) \frac{\int dx \Phi_{b(r)}(\sqrt{2}x) \Phi_{b_1}(\sqrt{2}x)}{E_{r(a,b),r(a,b)} - (k+l+1)}, \quad (\text{A.36})$$

where we used energy conservation in the transformation from the laboratory to center-of-mass frames, $2a_1 + 2b_1 + 1 = 2k + 2l + 1$. We can further simplify this expression using the orthogonality of the harmonic oscillator eigenfunctions

$$U_{r(a,b),t(k,l)} = \frac{g\psi_{a(r)}(0)}{\sqrt{2}} \alpha_{kl,(k+l-b(r))b(r)} \frac{\Phi_{k+l-b(r)}(0)}{E_{r(a,b),r(a,b)} - (k+l+1)}. \quad (\text{A.37})$$

Putting everything together, we construct the interaction matrix V_{ijkl} . Note that all one-body indices i, j, k, l, a, b are restricted by the cutoff n from our one-body basis and the two-body indices by n^2 . Therefore the matrices E, U, Q are of dimension $n^2 \times n^2$.

We discuss the transformation of operators that correspond to this interaction in App. A.6.4.

A.6. Transformation of operators

Let us now derive the transformation of one-, Eq. (A.47) and two-body operators, Eq. (A.48), alongside the renormalization with the effective interaction discussed in the main text.

A.6.1. Two-body system

We start by showing that the effective interaction framework is indeed a unitary transformation for the two-body system described by the Hamiltonian $H^{(2)}$ ⁴. Therefore, we extend the effective two-body Hamiltonian to an infinite Hilbert space

$$H^{\text{eff},(2)} = \left(\begin{array}{c|c} Q_{\mathcal{M}\mathcal{M}}^T & 0 \\ \hline 0 & \mathbb{I} \end{array} \right) \left(\begin{array}{c|c} E_{\mathcal{M}\mathcal{M}}^{(2)} & 0 \\ \hline 0 & E_{\text{high}}^{(2)} \end{array} \right) \left(\begin{array}{c|c} Q_{\mathcal{M}\mathcal{M}} & 0 \\ \hline 0 & \mathbb{I} \end{array} \right). \quad (\text{A.38})$$

Here, $E_{\mathcal{M}\mathcal{M}}^{(2)}$ describes the low-energy spectrum that we use in our calculations. Adding the high-energy spectrum $E_{\text{high}}^{(2)}$ allows us to introduce a unitary matrix in an infinite Hilbert space, $Q = \left(\begin{array}{c|c} Q_{\mathcal{M}\mathcal{M}} & 0 \\ \hline 0 & \mathbb{I} \end{array} \right)$.

⁴In the following, the subscript (2) denotes that we work with a two-particle system.

As a next step, we can define the diagonal matrix that contains eigenvalues of the Hamiltonian $H^{(2)}$

$$E^{(2)} \equiv UH^{(2)}U^T = \tilde{H}^{(2)}, \quad (\text{A.39})$$

where as before $U_{ij} = \langle \Phi_i | \Psi_j \rangle$, here $\Phi_i^{(2)}$ is a two-body basis state, and Ψ_i describes the exact interacting two-body solution. Remember that the tilde shows that the matrix is expanded in the eigenbasis of the interacting system.

With these equations we can now connect $H^{\text{eff},(2)}$ with $H^{(2)}$ via a unitary transformation $\mathcal{W} = QU^T$:

$$H^{\text{eff},(2)} = Q^T E^{(2)} Q = Q^T UH^{(2)}U^T Q = \mathcal{W}^T H^{(2)} \mathcal{W}. \quad (\text{A.40})$$

With this, we have shown that the effective interaction framework does indeed correspond to a unitary transformation for the two-particle system. This means that the matrix \mathcal{W} can be used to transform also other operators than the Hamiltonian.

A.6.2. Many-body system

Now, we can extend our discussion to the many-body case. Therefore, we rewrite the interaction

$$V_{ij}^{\text{eff}} = \left(\mathcal{W}^T H^{(2)} \mathcal{W} \right)_{ij} - T_i - T_j. \quad (\text{A.41})$$

Here, we have assumed that the operator only acts on the particles i and j . Using this interaction, we can write the effective many-body Hamiltonian as

$$H^{\text{eff}} = \sum_i T_i + \sum_{i>j} V_{ij}^{\text{eff}}. \quad (\text{A.42})$$

Since increasing the cutoff means that Q converges to U , we introduce the following approximation

$$\mathcal{W} \approx \mathbb{I} + \Delta, \quad (\text{A.43})$$

where Δ describes a small perturbation if the Hilbert space is sufficiently large. Using that $\mathcal{W}\mathcal{W}^T = \mathbb{I}$, it follows that $\Delta^T = -\Delta$. Next, we insert our approximation into the effective

many-body Hamiltonian:

$$\begin{aligned}
H^{\text{eff}} &\approx \sum_i T_i + \sum_{i>j} \left\{ \left((\mathbb{I} + \Delta)^T H^{(2)} (\mathbb{I} + \Delta) \right)_{ij} - T_i - T_j \right\} \\
&\approx \sum_i T_i + \sum_{i>j} \left\{ T_i + T_j + V_{ij} - \left(\Delta H^{(2)} \mathbb{I} \right)_{ij} + \left(\mathbb{I} H^{(2)} \Delta \right)_{ij} - T_i - T_j \right\} \\
&\approx \sum_i T_i + \sum_{i>j} V_{ij} - \sum_{i>j} \left(\Delta H^{(2)} \mathbb{I} \right)_{ij} + \sum_{i>j} \left(\mathbb{I} H^{(2)} \Delta \right)_{ij} \\
&\approx H - \sum_{i>j} \left(\Delta H^{(2)} \mathbb{I} \right)_{ij} + \sum_{i>j} \left(\mathbb{I} H^{(2)} \Delta \right)_{ij}.
\end{aligned} \tag{A.44}$$

In this calculation we have used that: $H = \sum_i T_i + \sum_{i>j} V_{ij}$. As a next step, we extend Δ such that $\Delta H = \Delta H^{(2)}$, i.e. $\Delta_{ij} T_k = 0$ if $k \neq i, j$ and $\Delta_{ij} V_{ik} = 0$ if $k \neq j$:

$$H^{\text{eff}} \approx \left(\mathbb{I} - \sum_{i>j} \Delta \right) H \left(\mathbb{I} + \sum_{i>j} \Delta \right) = \mathcal{W}^T H \mathcal{W}, \tag{A.45}$$

With this, we have shown that for sufficiently large cutoffs the transformation for the effective Hamiltonian of the many-body system is approximately unitary.

This means, that we can apply the same transformation also to operators other than the Hamiltonian:

$$O^{\text{eff}} = \mathcal{W}^T O \mathcal{W}. \tag{A.46}$$

For a one-body operator $O^{(1)} = \sum_i O_i$, this results in:

$$\begin{aligned}
O^{\text{eff},(1,2)} &= \left(\mathbb{I} - \sum_{i>j} \Delta \right) O^{(1)} \left(\mathbb{I} + \sum_{i>j} \Delta \right) \\
&= \sum_i O_i - \sum_{ij} \left(\Delta O^{(2)} \right)_{ij} + \sum_{ij} \left(O^{(2)} \Delta \right)_{ij} \\
&= \sum_i O_i + \sum_{ij} \left((\mathbb{I} + \Delta)^T O^{(2)} (\mathbb{I} + \Delta) \right)_{ij} - O^{(2)} \\
&= \sum_i O_i + \sum_{ij} \left(Q^T \tilde{O}^{(2)} Q \right)_{ij} - O^{(2)}.
\end{aligned} \tag{A.47}$$

For a two-body operator $O^{(2)} = \sum_{i>j} O_{ij}$ we derive:

$$\begin{aligned}
O^{\text{eff},(2)} &= \left(\mathbb{I} - \sum_{i>j} \Delta \right) O^{(2)} \left(\mathbb{I} + \sum_{i>j} \Delta \right) \\
&= \sum_{i>j} O_{ij} - \sum_{ij} \left(\Delta O^{(2)} \right)_{ij} + \sum_{ij} \left(O^{(2)} \Delta \right)_{ij} \\
&= \sum_{i>j} O_{ij} + \sum_{ij} \left((\mathbb{I} + \Delta)^T O^{(2)} (\mathbb{I} + \Delta) \right)_{ij} - O^{(2)} \\
&= \sum_{ij} \left(Q^T \tilde{O}^{(2)} Q \right)_{ij}.
\end{aligned} \tag{A.48}$$

Since we only have a finite Hilbert space in our CI-calculations, we have to restrict the Hilbert space again by using the projection operator $P_{\mathcal{M}}$.

A.6.3. Implementation for $V_{\text{eff}}^{\text{rel}}$

If we use the $V_{\text{eff}}^{\text{rel}}$, we have to transform the (induced) two-body operator into relative and center-of-mass coordinates, $O(x_1, x_2) \rightarrow O(x, X)$ with $x = (x_1 - x_2)/\sqrt{2}$ and $X = (x_1 + x_2)/\sqrt{2}$, to transform the operators alongside the renormalization. In case that the two-body operator factorizes, $O(x, X) = O(x)O(X)$, the calculation is straightforward: One can simply evaluate the relative part of the operator, $O(x)$, using the exact solution in relative coordinates and then build a matrix equivalent to E in Eq. (A.29). The next step is then to apply the same overlap matrices Q and (in case we transform a one-body operator) subtract the matrix build from using the non-interacting solution (T in Eq. (A.29)). However, if the operator does not factorize, the computation can become more involved as we have to transform $O(x_1, x_2)$ to relative coordinates first.

A.6.4. Implementation for $V_{\text{eff}}^{\text{rel+cm}}$

If we use the $V_{\text{eff}}^{\text{rel+cm}}$ interaction, we start by building a matrix equivalent to E in Eq. (A.30) using the exact two-body solution. Then, we use the same overlap matrices Q as for the effective interaction to transform the (induced) two-body operator. If this operator is induced, we need to subtract the matrix which is constructed using the non-interacting two-body basis states. This calculation is easiest if the two-body operator $O(x_1, x_2)$ factorizes in relative and center-of-mass coordinates, $O(x, X) = O(x)O(X)$. In this case, only one-dimensional integrals need to be evaluated. If the operator does not factorize,

two-dimensional integrals have to be calculated which can result in long run times if there is no analytical expression. Still, this approach might be easier to implement than the transformation needed for $V_{\text{eff}}^{\text{rel}}$, see Sec. A.6.3.

A.7. Derivation of the running coupling constant $g_{\text{unconf.}}(\lambda)$ in free space

In this Appendix, we provide a detailed derivation of Eq. (3.10):

$$-\frac{1}{g_{\text{unconf.}}(\lambda)} = \frac{1}{\pi\sqrt{|E_{1+1}^{\text{unconf.}}|}} \arctan \left[\frac{\lambda}{\sqrt{|2E_{1+1}^{\text{unconf.}}|}} \right]. \quad (\text{A.49})$$

This discussion adapts the approach for 2D systems presented in Ref. [123].

We start with the Schrödinger equation for two particles in relative coordinates interacting via an attractive contact interaction, $g < 0$, in free space

$$\left(-\frac{1}{2} \frac{\partial^2}{\partial x^2} + \frac{g}{\sqrt{2}} \delta(x) \right) \Psi(x) = E_{1+1}^{\text{unconf.}} \Psi(x), \quad (\text{A.50})$$

where $x = \frac{1}{\sqrt{2}}(x_1 - x_2)$ describes the relative coordinate. Because we have a one-dimensional system with attractive interactions, there exists a bound state, $E_{1+1}^{\text{unconf.}} < 0$ [124], whose energy we use for renormalization. Next, we transform this equation to momentum space by performing a Fourier transformation

$$\Psi(x) = \int \frac{dk}{2\pi} e^{ikx} \phi(k) \quad (\text{A.51})$$

$$\frac{1}{2} k^2 \phi(k) + \frac{g}{\sqrt{2}} \Psi(0) = E_{1+1}^{\text{unconf.}} \phi(k). \quad (\text{A.52})$$

We write its solution as

$$\phi(k) = -\frac{\sqrt{2}g\Psi(0)}{k^2 - 2E_{1+1}^{\text{unconf.}}}. \quad (\text{A.53})$$

Using that $\Psi(0) = \int \frac{dk}{2\pi} \phi(k)$, we arrive at:

$$\int \phi(k) dk = - \int \frac{\sqrt{2}g}{k^2 - 2E_{1+1}^{\text{unconf.}}} dk \int \phi(k') \frac{dk'}{2\pi}. \quad (\text{A.54})$$

To further simplify this, we can divide by the norm of the wavefunction in momentum space, $\int \phi(k)dk$:

$$1 = -\frac{\sqrt{2}g}{2\pi} \int \frac{1}{k^2 - 2E_{1+1}^{\text{unconf.}}} dk. \quad (\text{A.55})$$

As a last step, we introduce a momentum space cutoff λ and change g to $g_{\text{unconf.}}(\lambda)$:

$$\frac{1}{g_{\text{unconf.}}(\lambda)} = -\frac{\sqrt{2}}{2\pi} \int_{-\lambda}^{\lambda} \frac{dk}{k^2 - 2E_{1+1}^{\text{unconf.}}} = -\frac{\text{Arctan}(\lambda/\sqrt{|2E_{1+1}^{\text{unconf.}}|})}{\pi\sqrt{|E_{1+1}^{\text{unconf.}}|}} \quad (\text{A.56})$$

A.8. Connecting quantum numbers to momenta

In the main text, we used the connection between the momentum space cutoff λ in the relative coordinates with the one-body basis cutoff n to compare the running coupling constant used for the CI calculation and $g_{\text{unconf.}}(\lambda)$ from Eq. (3.10). Here, we provide a derivation for this connection for a general polynomial potential x^k . Therefore, we use the Wilson–Sommerfeld rule to connect the quantum number n with the energy

$$\oint_{H(p,x)=E} p dx = 2\pi n, \quad (\text{A.57})$$

with $H = \frac{1}{2}p^2 + \frac{1}{2^{k-1}}x^k$. Evaluating this integral leads to:

$$2\pi n = 2 \int_{x=-2^{1-1/k}E^{1/k}}^{x=2^{1-1/k}E^{1/k}} \sqrt{2E - \frac{1}{2^{k-2}}x^k} dx \quad (\text{A.58})$$

$$= 2\sqrt{2E}x {}_2F_1(-1/2, 1/k, 1 + 1/k, 2^{1-k}x^k/E) \Big|_{x=-2^{1-1/k}E^{1/k}}^{x=2^{1-1/k}E^{1/k}} \quad (\text{A.59})$$

$$= 2^{7/2-1/k}E^{1/2+1/k} \frac{\sqrt{\pi}\Gamma(1/k)}{(2+k)\Gamma(1/2+1/k)}, \quad (\text{A.60})$$

where ${}_2F_1$ is the hypergeometric function [102].

As a next step, we connect the energy cutoff E in the single particle Hilbert space with λ , the momentum space cutoff in relative coordinates. Therefore, we use that the maximal two-body energy given by E should be equal to the maximum energy obtainable by λ

$$2E = \frac{1}{2}\lambda^2. \quad (\text{A.61})$$

Note that this expression can in principle only be used in either a harmonic oscillator or in a system on a ring where the center of mass and relative motion factorize. However, if

one uses other potentials and large cutoffs, this relation holds approximately. Using this connection, we derive

$$2\pi n = 2^{5/2-3/k} \lambda^{1+2/k} \frac{\sqrt{\pi} \Gamma(1/k)}{(2+k) \Gamma(1/2+1/k)}. \quad (\text{A.62})$$

Restricting $k = 2$, which corresponds to the harmonic oscillator discussed in the main text, this expression can be simplified to

$$2\pi n = \frac{\pi}{2} \lambda^2 \Leftrightarrow \lambda = 2\sqrt{n}. \quad (\text{A.63})$$

Note that for hard wall boundary conditions, which can be approximated with $k \rightarrow \infty$, we can derive

$$2\pi n = 2^{5/2} \lambda \Leftrightarrow \lambda = \frac{\pi n}{\sqrt{8}}. \quad (\text{A.64})$$

A.9. Additional convergence plots

For the interested reader we provide a different depiction of the convergence plots.

A.9.1. Convergence plots as a function of $1/n$

Here, we show the convergence plots as a function of $1/n$ with n the one-body basis cutoff. Fig. A.5 shows the convergence of the energy, Fig. A.6 of the density at the trap center, Fig A.7 of the kinetic energy, Fig A.8 of the trapping confinement and Fig. A.9 of the transition matrix elements.

A.9.2. Double logarithmic plots

We also provide double logarithmic plots for the $1 + 1$ utilizing that, in this case, we know the exact result: The energy is shown in Fig. A.10, the density at the middle of the trap in Fig. A.11, the kinetic energy in Fig. A.12, the expectation value of the harmonic trapping confinement in Fig. A.13 and the transition matrix elements are shown in Fig. A.14. Note that the results for $V_{\text{eff}}^{\text{rel+cm}}$ and transformed operators are not shown as they are exact by construction. The double logarithmic plots showcase (by the steeper slope) that the renormalized interactions lead to faster convergence in comparison with the bare contact interaction.

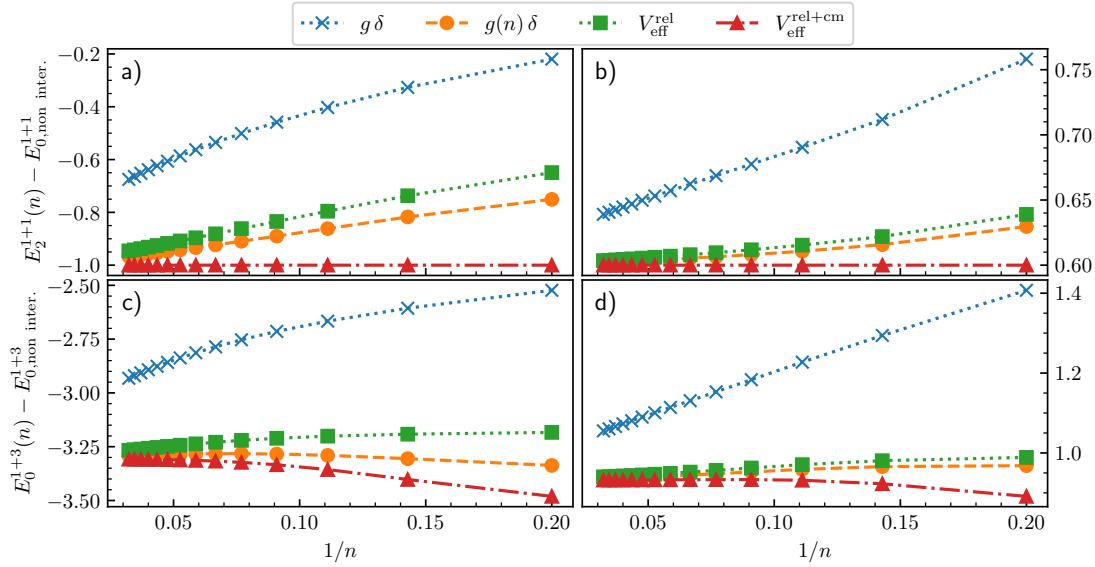


Figure A.5.: **Energy of the system for different particle numbers and interactions calculated with the bare contact interaction, running coupling constant, $V_{\text{eff}}^{\text{rel}}$ and $V_{\text{eff}}^{\text{rel+cm}}$ as a function of $1/n$.**

Panels a) and b) show the result for the second excited state of the $1 + 1$ system; c) and d) present the ground state energy of $1 + 3$. Panels a) and c) are for attractive interaction with $g = -2.5067$ (corresponds to $E_{1+1} = -1$); panels b) and d) are for repulsive interactions with $g = 3$ (corresponds to $E_{1+1} = 1.6$). Our numerical results are presented with markers; lines are added to guide the eye. Figure modified from Ref. [112].

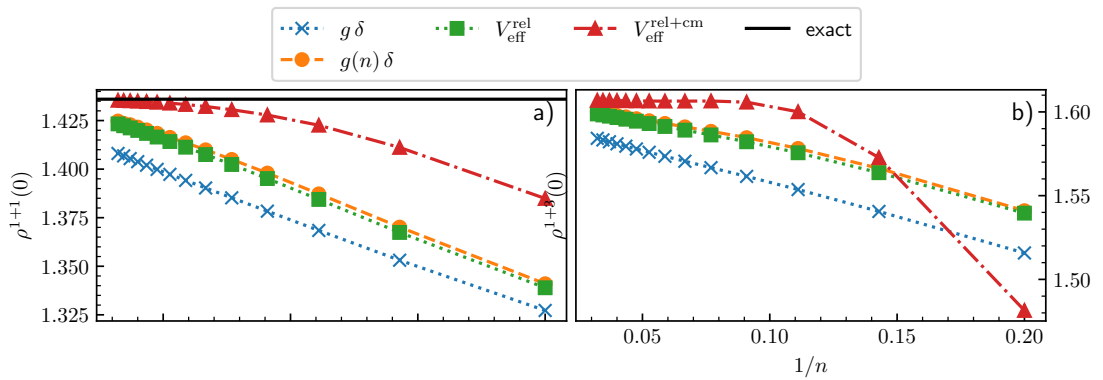


Figure A.6.: **Ground state density at the center of the trap calculated with bare contact interaction, running coupling constant, $V_{\text{eff}}^{\text{rel}}$ and $V_{\text{eff}}^{\text{rel+cm}}$ as a function of $1/n$.**

Panel a) shows results for the $1 + 1$ system; panel b) is for $1 + 3$. All panels are for attractive interactions with $g = -2.5067$ (corresponds to $E_{1+1} = -1$). Our numerical results are presented with markers; lines are added to guide the eye. The exact value of the density for the $1 + 1$ system is shown as a horizontal solid line. Figure modified from Ref. [112].

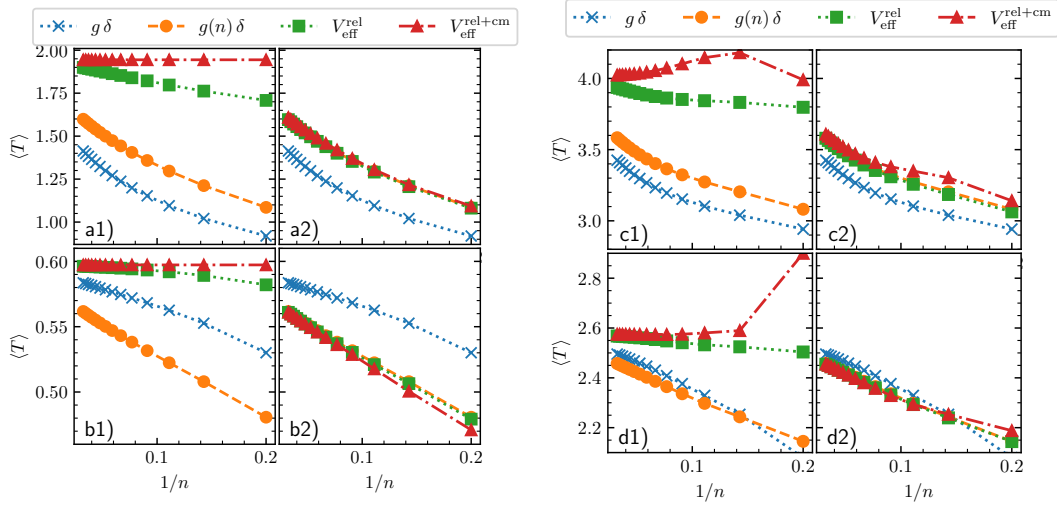


Figure A.7.: Kinetic energy for different particle numbers and interactions as a function of $1/n$.

Panels *1) show results where the operator T that has been transformed together with $V_{\text{eff}}^{\text{rel}}$ and $V_{\text{eff}}^{\text{rel+cm}}$, while panels *2) show results when only the potential is renormalized but the operator T is not transformed. Panels a) and b) are for the $1 + 1$ system, while panels c) and d) are for $1 + 3$. Panels a) and c) are for $g = -2.5067$ (corresponds to $E_{1+1} = -1$); panels b) and d) are for $g = 3$ (corresponds to $E_{1+1} = 1.6$). Data is shown with markers; lines are added to guide the eye. Figure modified from Ref. [112].

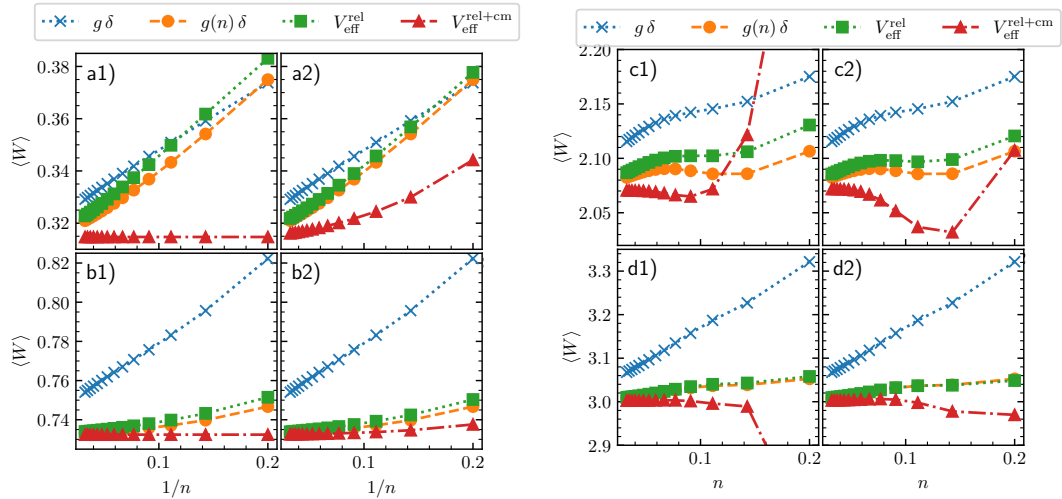


Figure A.8.: **Expectation value of the trapping potential for different particle numbers and interactions as a function of $1/n$.**

Panels *1) show results for $\langle W \rangle$ when the operator W has been transformed together with $V_{\text{eff}}^{\text{rel}}$ and $V_{\text{eff}}^{\text{rel+cm}}$, while panels *2) correspond to only renormalizing the interaction while keeping W unchanged. Panels a) and b) are for the $1 + 1$ system, while panels c) and d) are for $1 + 3$. Panels a) and c) are for $g = -2.5067$ (corresponds to $E_{1+1} = -1$); panels b) and d) are for $g = 3$ (corresponds to $E_{1+1} = 1.6$). Data is shown with markers; lines are added to guide the eye. Figure modified from Ref. [112].

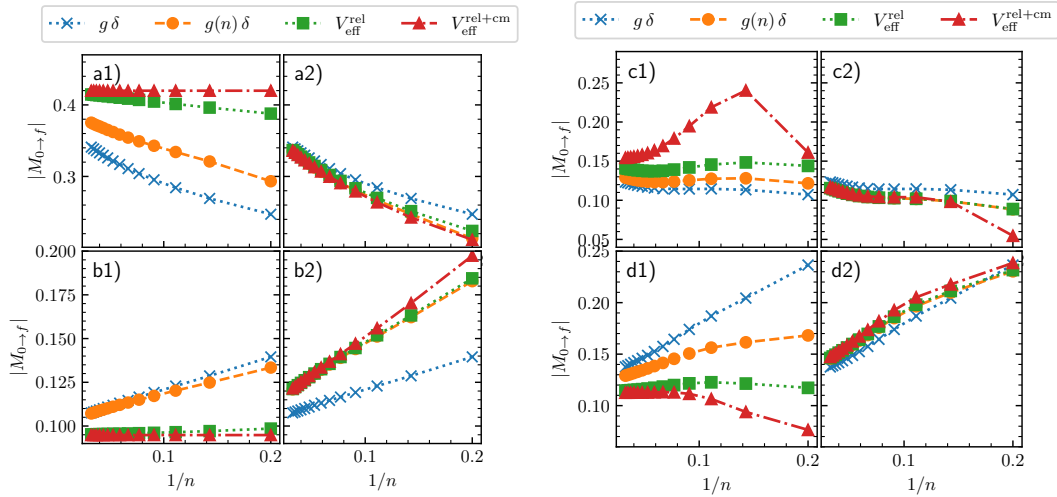


Figure A.9.: **Transition matrix elements from the ground state to the lowest-energy state that can be excited by a periodic modulation of the interaction as a function of $1/n$.**

Panels *1) show $M_{0 \rightarrow f}$ for the operator that has been transformed together with the potential while panels *2) show results when only the potential has been renormalized but the operator has not been modified. Panels a) and b) are for the 1 + 1 system while panels c) and d) are for the 1 + 3 system. Panels a) and c) are for $g = -2.5067$ (corresponds to $E_{1+1} = -1$); panels b) and d) are for $g = 3$ (corresponds to $E_{1+1} = 1.6$). Our data are shown with markers; lines are added to guide the eye. Figure modified from Ref. [112].

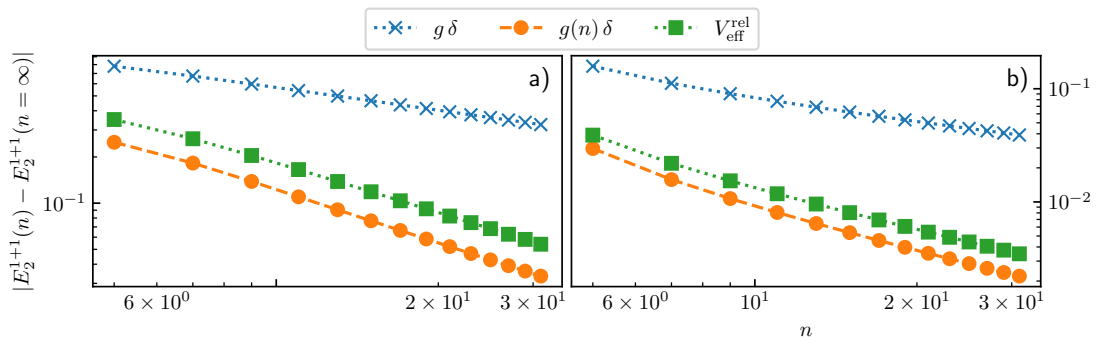


Figure A.10.: **Double logarithmic plot of the energy of the second excited state of the $1 + 1$ system calculated with the bare contact interaction, running coupling constant and $V_{\text{eff}}^{\text{rel}}$.**

We subtract the exact result given by the solution of Refs. [120, 121] and plot the data on a double logarithmic graph. Panel a) is for attractive interactions with $g = -2.5067$ (corresponds to $E_{1+1} = -1$); panel b) is for repulsive interaction with $g = 3$ (corresponds to $E_{1+1} = 1.6$). Our numerical results are presented with markers; lines are added to guide the eye. Figure modified from Ref. [112].

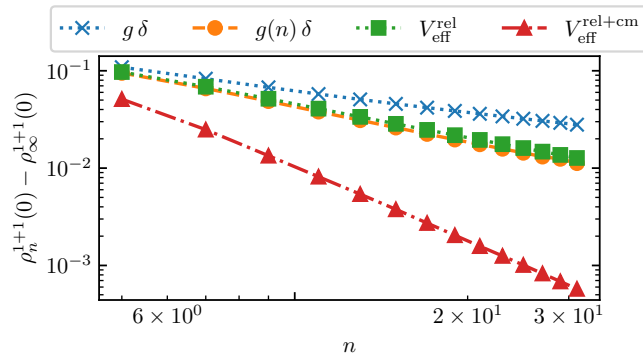


Figure A.11.: **Double logarithmic plot of the density of the ground state in the middle of the trap as a function of the cutoff parameter for the four potentials considered in this study for the $1 + 1$ system.**

We subtract the exact result given by the solution of Refs. [120, 121] and plot the data as a double logarithmic graph. We use attractive interaction $g = -2.5067$, which corresponds to $E_{1+1} = -1$. Our numerical results are presented with markers; lines are added to guide the eye. Figure modified from Ref. [112].

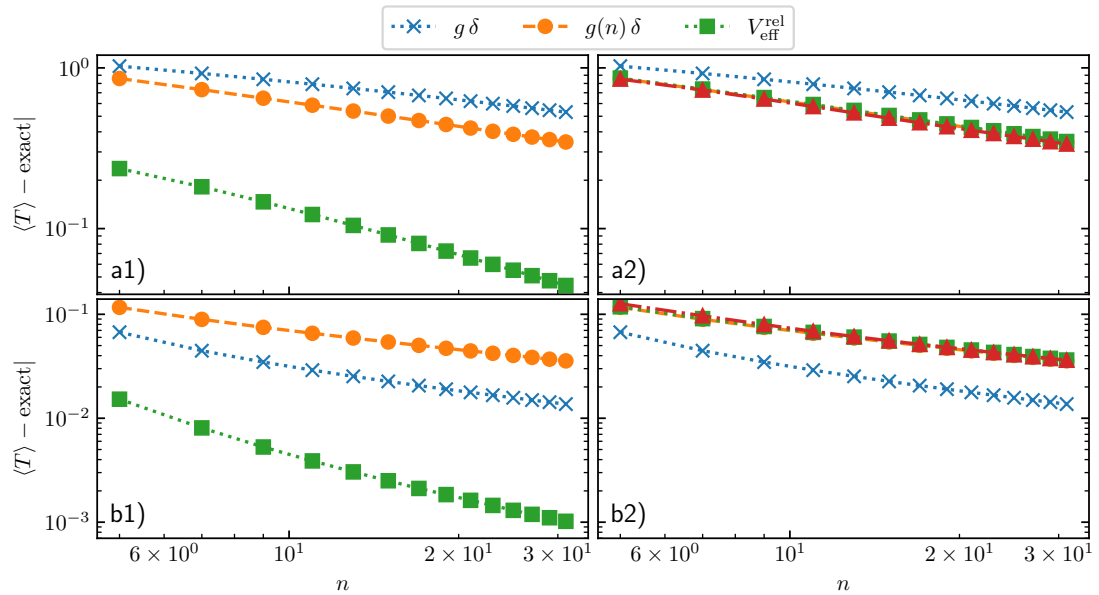


Figure A.12.: **Double logarithmic plot of the kinetic energy for the 1 + 1 system.**

Left panels [*1]) show the results where the operator has been transformed together with the interaction potential for $V_{\text{eff}}^{\text{rel}}$ and $V_{\text{eff}}^{\text{rel+cm}}$ while the right ones [*2]) show results where only the potential but not the operator has been transformed. Panel a) is for $g = -2.5067$ (corresponds to $E_{1+1} = -1$); panel b) shows results for $g = 3$ (corresponds to $E_{1+1} = 1.6$). Note that we have subtracted the exact result calculated as in Refs. [120, 121]. Our numerical results are presented with markers; lines are added to guide the eye. Figure modified from Ref. [112].

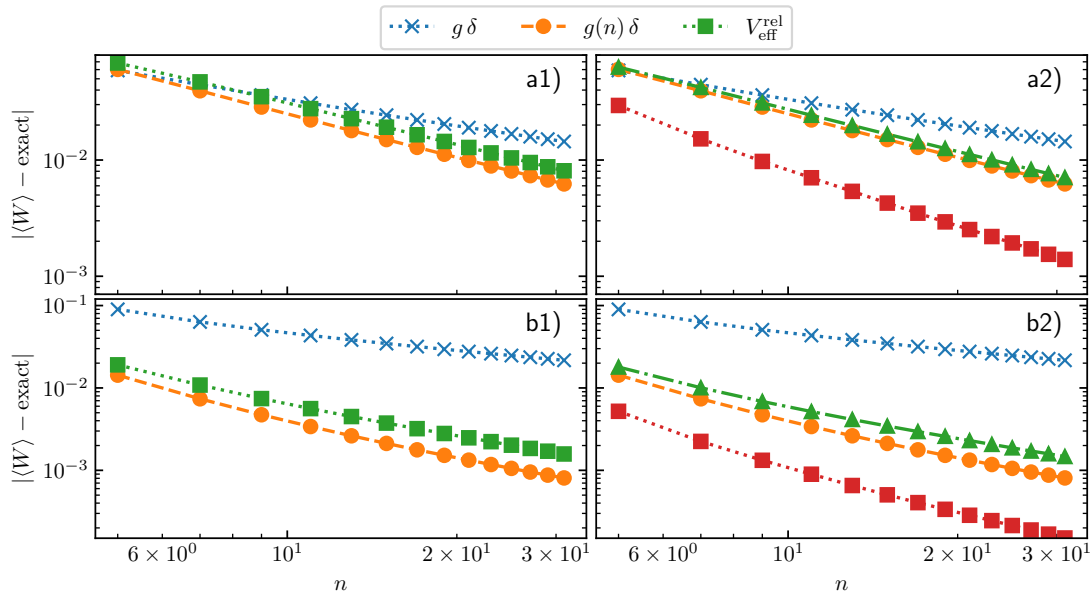


Figure A.13.: **Double logarithmic plot of the expectation value of the trapping potential for the $1 + 1$ system.**

Left panels [*1]) show the results where the operator has been transformed together with the interaction potential for $V_{\text{eff}}^{\text{rel}}$ and $V_{\text{eff}}^{\text{rel+cm}}$ while the right ones [*2]) show results where only the potential but not the operator has been transformed. Panel a) is for $g = -2.5067$ (corresponds to $E_{1+1} = -1$); panel b) shows results for $g = 3$ (corresponds to $E_{1+1} = 1.6$). Note that we have subtracted the exact result calculated as in Refs. [120, 121]. Our numerical results are presented with markers; lines are added to guide the eye. Figure modified from Ref. [112].

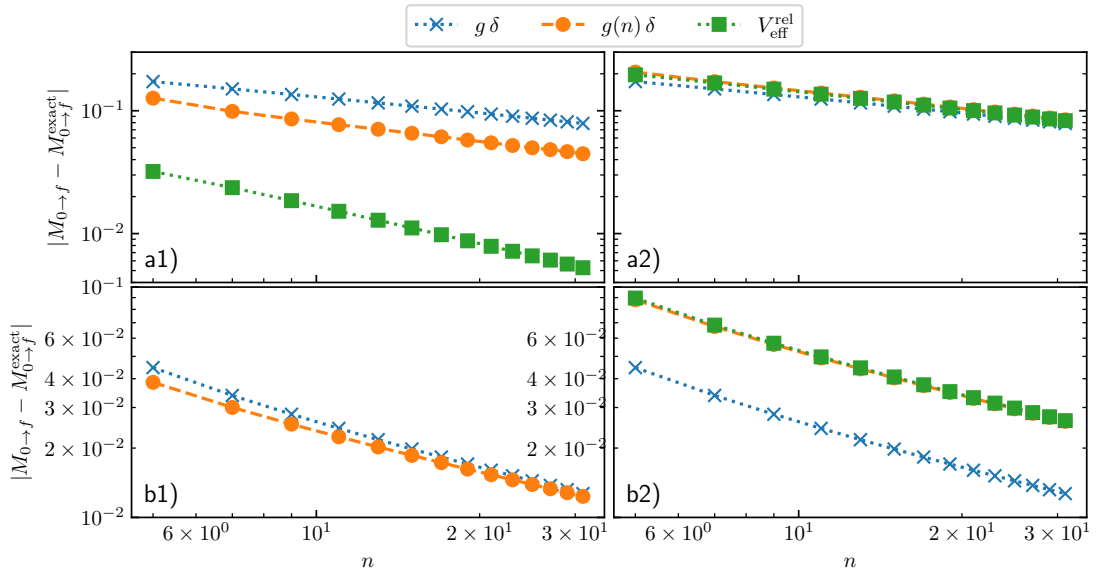


Figure A.14.: **Double logarithmic plot of the transition matrix elements from the ground to the fourth excited states for the 1 + 1 system.**

Left panels [*1]) show the results where the operator has been transformed together with the interaction potential for $g(n)\delta$, $V_{\text{eff}}^{\text{rel}}$ and $V_{\text{eff}}^{\text{rel+cm}}$ while the right ones [*2]) show results where only the potential but not the operator has been transformed. Panel a) is for $g = -2.5067$ (corresponds to $E_{1+1} = -1$); panel b) shows results for $g = 3$ (corresponds to $E_{1+1} = 1.6$). Note that we have subtracted the exact result calculated as in Refs. [120, 121]. Our numerical results are presented with markers; lines are added to guide the eye. Figure modified from Ref. [112].

B. Aharonov-Bohm Bose polaron: Generalization, definitions and analysis convergence towards thermodynamic limit

In this appendix, we provide additional details to Chap. 4. In the main part of this chapter, we have considered the Aharonov-Bohm flux coupled only to the impurity. First, we will showcase that the more general case, where the flux is coupled also to the bosonic medium, can also be easily incorporated into our model. After that, we will discuss the influence of the impurity mass on our results (in the main part, we only presented results for the equal mass case). Then, we will shortly showcase different definitions of the effective mass of a polaron. At the end, we will discuss and contrast the convergence of the self-energy and effective mass to the thermodynamic limit.

B.1. Coupling flux to bosons and impurity

In Chap. 4, we discussed the case where flux is coupled only to the impurity. However, as we will show now, the more general case where flux is coupled to the bosons can also be included in our model. The Hamiltonian now reads

$$\mathcal{H} = \frac{1}{2L^2} \left(-i \frac{\partial}{\partial y} + \Phi_I \right)^2 + \frac{1}{2L^2} \sum_i \left(-i \frac{\partial}{\partial x_i} + \Phi_B \right)^2 + V_{ib} + V_{bb}. \quad (\text{B.1})$$

Again, we first perform a transformation of the Schrödinger equation to the frame co-moving with the impurity

$$\left[-\frac{1}{2} \left(\sum_i \frac{\partial}{\partial z_i} \right)^2 - \frac{1}{2} \sum_i \frac{\partial^2}{\partial z_i^2} + \frac{(P + \Phi_I)^2}{2} + \frac{N}{2} \Phi_B^2 \right. \\ \left. + L^2 V_{ib} + L^2 V_{bb} + i(P + \Phi_I - \Phi_B) \sum_i \frac{\partial}{\partial z_i} \right] \tilde{\Psi} = E \tilde{\Psi}. \quad (\text{B.2})$$

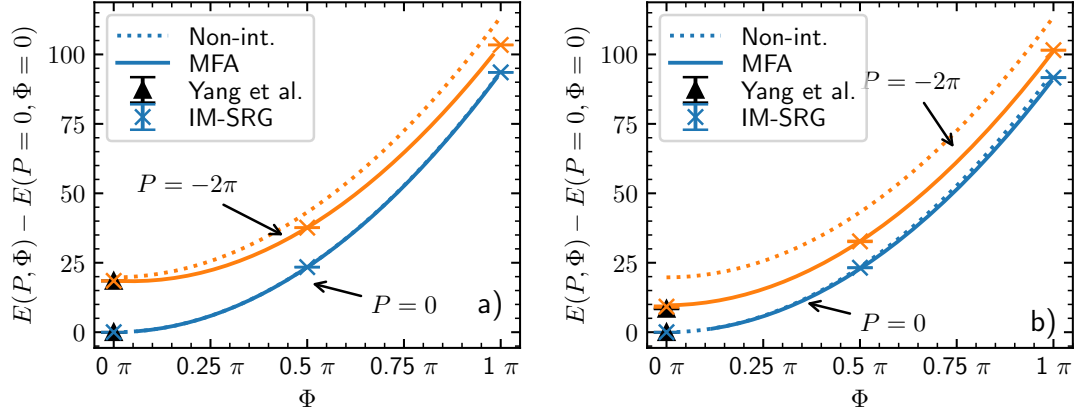


Figure B.1.: **Energy spectrum as a function of the AB flux coupled to the bosons:** $\Phi_I = 0$, $\Phi_B = \Phi$ **for different total momenta.**

Blue color shows results for the Yrast line with $P = 0$ while orange color corresponds to $P = -2\pi$. The parameters of the system are $N = 19$ and $\gamma = 0.2$. Panel a) shows results for $c/g = 1$ while in panel b) the impurity-boson interaction is $c/g = 5$. Data are obtained with the mean-field ansatz (solid curves) and the IM-SRG method (crosses with error bars), black triangles are the results of Ref. [171] for $\Phi = 0$. The dotted curves show the energy of the non-interacting system. Figure modified from Ref. [63].

Different from the Schrödinger equation in the main text, one can no longer introduce a single effective total momentum (cf. \mathcal{P}) that parameterizes the energy of the system. However, we can still rewrite Eq. (B.2) into a form similar to the one discussed in the main part

$$\left[-\frac{1}{2} \left(\sum_i \frac{\partial}{\partial z_i} \right)^2 + \frac{1}{2} \sum_i \frac{\partial^2}{\partial z_i^2} + \frac{k^2}{2} + L^2 V_{ib} + L^2 V_{bb} + ik \sum_i \frac{\partial}{\partial z_i} \right] \tilde{\Psi} = E_k \tilde{\Psi}, \quad (\text{B.3})$$

where $k = P + \Phi_I - \Phi_B$ and $E_k = E - (P + \Phi_I)\Phi_B - (N - 1)\Phi_B^2/2$. With this, we can study the more general case with the methods and results of the main part.

To illustrate this, we show in Fig. B.1 the energy of the system for the same parameters as in Fig. 4.4 but with $\Phi_I = 0$, $\Phi_B > 0$. Although the energies for $\Phi_B = 0$ remain

unchanged, the spectrum looks considerably different for $\Phi_B > 0$. Now, the term $N\Phi_B^2/2$ leads to a faster increase of the energy as a function of the flux. Furthermore, there is no longer an energy level crossing of the Yrast states with $P = 0$ and $|P| = 2\pi$. This can be understood from the fact that there is no longer an effective total momentum \mathcal{P} : Although the spectrum must still be periodic in $\Phi_B/2\pi$, states with $0 < \Phi_B < \pi$ cannot be related to states with $P = -2\pi$ and $\Phi_B > \pi$.

Lastly, we want to mention the special scenario of equal fluxes $\Phi_I = \Phi_B$. In this case, the energy depends on the AB flux only via a constant energy shift, i.e., the flux couples only to the center-of-mass motion of the system leaving the relative part unchanged. This is in agreement with previous studies, see, e.g., Ref. [137]. A simple interpretation of this scenario is that all particles ‘rotate’ around the ring with the same ‘velocity’.

B.2. Mass imbalance

Now, we briefly discuss the influence of a mass imbalance, in the main part of Chap. 4 we only considered the equal mass case. We write the Schrödinger equation again in the co-moving frame:

$$\left[-\frac{1}{2m} \left(\sum_i \frac{\partial}{\partial z_i} \right)^2 - \frac{1}{2} \sum_i \frac{\partial^2}{\partial z_i^2} + \frac{(P + \Phi)^2}{2m} + L^2 V_{ib} + L^2 V_{bb} + i \frac{(P + \Phi)}{m} \sum_i \frac{\partial}{\partial z_i} \right] \tilde{\Psi} = E \tilde{\Psi}. \quad (\text{B.4})$$

The corresponding Gross-Pitaevskii equation is:

$$-\frac{1}{2\kappa} \frac{\partial^2 f}{\partial z^2} + i \frac{\mathcal{P}}{m} \frac{\partial f}{\partial z} - i(N-1) \frac{P_{\text{bos}}}{m} \frac{\partial f}{\partial z} + g(N-1)|f|^2 f = \mu f \quad (\text{B.5})$$

with $\kappa = m/(m+1)$ the reduced mass¹. It is important to note that only one parameter is different from the equal mass case: the reduced mass κ . Therefore, the mean-field solution can be found with the same approach as in the main part (see Sec. 2.5 and Sec. 4.3.1). Therefore, the qualitative conclusions from the main part persist also for the mass-imbalanced case.

In Fig. B.2, we showcase the quantitative changes by presenting the energies as well as the currents for a heavy ($m = 5$) and a light ($m = 0.5$) impurity². As mentioned before,

¹Recall that we use a system of units in which $\hbar = M = 1$.

²The definition of the impurity current has to be modified to contain an additional factor $1/m$ in Eq. (4.23).

In practice, we only calculate the bosonic current, and use the momentum conservation such that $j_I = \mathcal{P} - N j_B$.

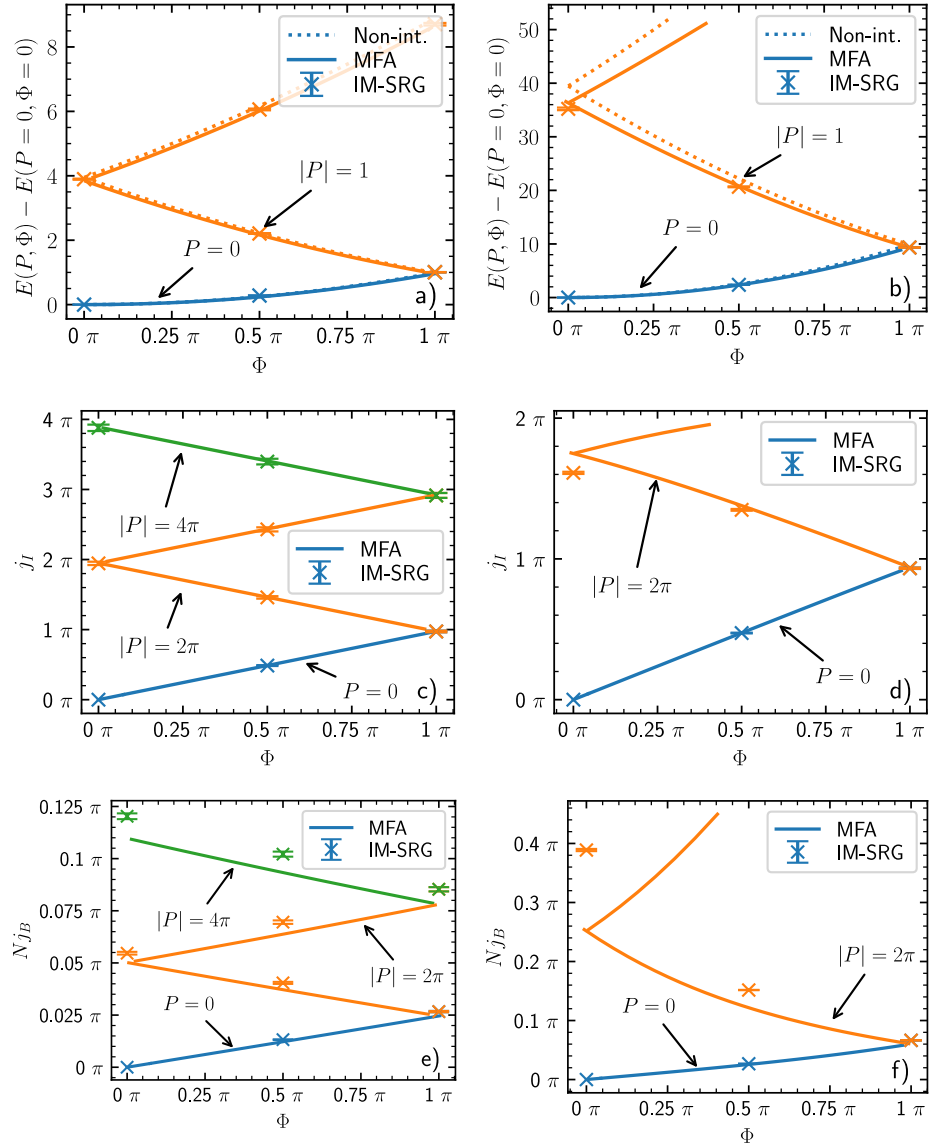


Figure B.2.: **Energy, impurity and bosonic current for mass imbalance.**

We show Energy [a), b)], impurity current [c), d)] and bosonic current [e), f)]. Panels a), c), e) showcase results for a heavy impurity ($m = 5$) while b), d), f) are for a light impurity ($m = 0.5$). The other parameters are $N = 19$, $\gamma = 0.2$ and $c/g = 1$. The results are obtained with the MFA (solid lines) and IM-SRG calculations (symbols). Dotted curves in the upper panels showcase the energies for a non-interacting impurity. Figure taken from Ref. [63].

there is no qualitative change in the behavior of the observables. However, we can clearly see that a light (heavy) impurity generates stronger (weaker) bosonic currents. This can be understood from the fact that the kinetic energy of the impurity scales with the inverse mass and is therefore large (small) for a light (heavy) impurity.

Lastly, we want to shortly remark that the heavy impurity case shows better agreement between mean-field and IM-SRG. There are two reasons for this: First, as discussed above, a heavy impurity carries larger impurity current and leads therefore to weaker bosonic currents, which in turn makes the excitation of the Bose gas less important (see Sec. 4.5.2). Second, the mean-field approximation neglects the mixed derivative terms which scale as $1/m$. Therefore, the higher the impurity mass, the better the approximation of the Schrödinger equation by the Gross-Pitaevskii equation.

B.3. Definition of effective mass

For convenience of the reader, we shortly review and explain different equations that define the effective mass in the thermodynamic limit with $\Phi = 0$, cf. Refs. [94, 163].

In the polaron approximation, the ground state energy of the system grows quadratically with the total momentum P

$$E = E_0 + \frac{P^2}{2m_{\text{eff}}}, \quad (\text{B.6})$$

where m_{eff} is the so-called effective mass which parameterizes the quadratic increase and depends on the interactions in the system. The velocity of the impurity (which is closely related to the probability current) can be written as

$$v_{\text{imp}} = P/m_{\text{eff}}. \quad (\text{B.7})$$

This velocity has to be equal to the velocity of the polaron and therefore $v_{\text{pol}} = v_{\text{imp}}$.

We can use this, to rewrite the energy of the system in terms of the impurity velocity and define the effective mass via this equation

$$E = E_0 + \frac{m_{\text{eff}} v_{\text{imp}}^2}{2}. \quad (\text{B.8})$$

Lastly, we want to connect the effective mass to the momentum of the bosonic medium. Therefore, we use that the total momentum is conserved, i.e. it is distributed between the impurity and the bosons $P = P_{\text{imp}} + P_{\text{bos}}$ and that the impurity momentum is defined via $P_{\text{imp}} = m v_{\text{imp}}$. Putting everything together, we can define the effective mass via

$$m/m_{\text{eff}} = 1 - P_{\text{bos}}/P. \quad (\text{B.9})$$

All three equations, Eqs. (B.6)-(B.9), are equivalent and can be used to define and calculate the effective mass. We noticed in our IM-SRG calculations that the last equation is numerically the most stable one and therefore we used it in this thesis.

B.4. Convergence towards thermodynamic limit

One of the main conclusions of Chap. 4 was that the AB ring can be used to study the convergence of the effective mass to the thermodynamic limit ($N, L \rightarrow \infty, N/L = \rho = \text{const}$). Here, we want to discuss the few-to-many-body crossover for the effective mass in more detail and contrast it with the self-energy of the impurity. Note that the latter has already been discussed in Ref. [72]. There, it was shown that the energy decays as $E - E(c = 0) = \rho^2 \pi^2 / (2N\kappa)$ if the bosons are non-interacting.

First, we will use the analytic expressions of the mean-field solution of Ref. [72] to provide further analytical insight into the convergence of the energy. After that, we analyze the self-energy and the effective mass obtained from our semi-analytic mean-field calculation by a fitting procedure.

B.4.1. Self-energy of the impurity

In Ref. [72] it was shown that the energy of an impenetrable impurity ($c \rightarrow \infty$) can be calculated via

$$\frac{E - E(c = 0)}{\rho^2} = \frac{8K^4(p)p + 2K^2(p)\kappa\gamma N(N-1)(p+1)}{3\kappa^2\gamma N^2(N-1)} - \frac{\gamma(N-1)}{2}, \quad (\text{B.10})$$

where K is the complete elliptic integral of first kind and p is a parameter determined from the equation:

$$\frac{4K(p)(K(p) - E(p))}{\kappa\gamma N(N-1)} = 1, \quad (\text{B.11})$$

with the complete elliptic integral of second kind, E , [102]. We can use this expression to derive analytically the behavior of the polaron energy for large N . Therefore, we use that in the limit of $N \rightarrow \infty, p \rightarrow 1$ and therefore $E(p) \rightarrow 1$. Hence, we can write

$$\frac{E - E(c = 0)}{\rho^2} = \frac{2}{\kappa N} + \frac{4}{3\kappa} \sqrt{\kappa\gamma + \frac{1}{N^2}} + \mathcal{O}\left(\frac{1}{N^{3/2}}\right). \quad (\text{B.12})$$

With this we have shown that for $N \rightarrow \infty$ the energy decays as $2/\kappa N$ to the value $\sqrt{16\gamma/9\kappa}$. This corresponds to the boundary energy of the Bose gas (cf. Refs. [231, 232] for an infinitely heavy impurity with $\kappa = 1$).

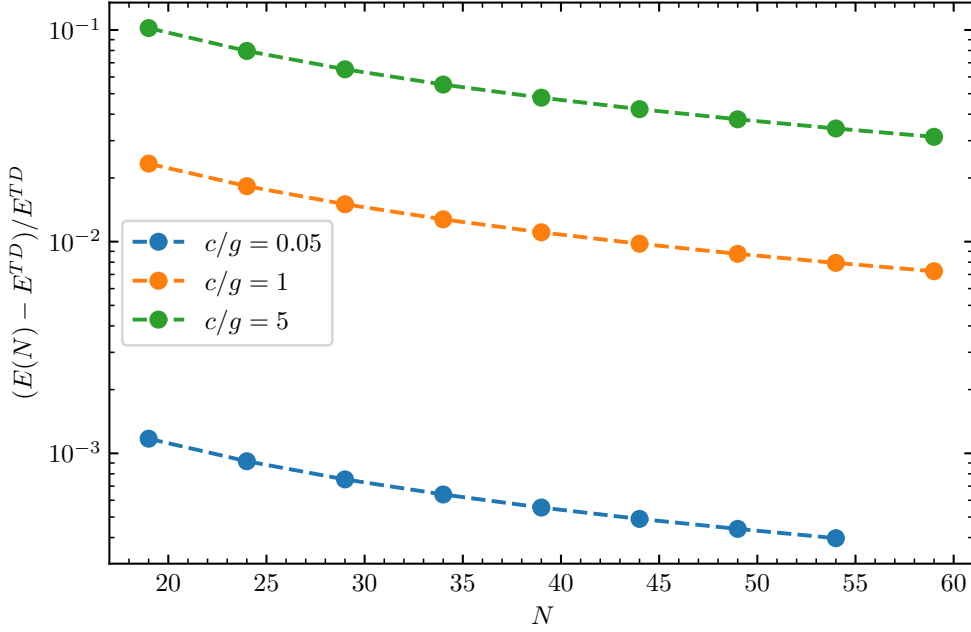


Figure B.3.: **Energy for increasing particle numbers.**

We show the energy as a function of N with respect to its thermodynamic value for $m = M = 1, \gamma = 0.2$. The values of c/g are given in the figures label. Figure taken from Ref. [63].

For finite impurity-boson interaction, we fit the mean-field results of the energy with

$$f(N) = f_{\infty} + \frac{A}{N^{\sigma}}. \quad (\text{B.13})$$

We show in Fig. B.3 the energy for $\gamma = 0.2$ and $c/g = 0.05, 1, 5$ as a function of the particle number. Fitting of these data shows that the parameter σ is in the range of $\sigma = 1.065 - 1.08$. This suggests that also for finite impurity-boson interactions the energy decays like $1/N$. We attribute deviations to the $1/N$ behavior to higher than leading order terms. We checked this statement by adjusting the number of particles.

B.4.2. Effective mass

For the effective mass, we were not able to gain analytic insight into the few-to-many-body crossover. Instead, we directly fit the results of Fig. 4.5. Different from the energy of the

impurity, the convergence pattern now seems to depend strongly on the impurity-boson interaction. For the weakest considered interaction ($c/g = 0.05$), we find the fastest convergence with $\sigma = 1.07 \pm 0.15$. For $c/g = 1$, the effective mass converges with $\sigma = 0.99 \pm 0.01$. For strong interactions ($c/g = 5$), the convergence is significantly slower $\sigma = 0.67 \pm 0.03$. Note that in the limit of an impenetrable impurity ($c \rightarrow \infty$), the impurity acts effectively as a wall that moves through the bosons. In this case, the effective mass should be the mass of the whole system, i.e., the effective mass should actually increase linearly with N in this case.

Our results demonstrate that the effective mass is highly sensitive to the value of c/g , unlike the self-energy. In particular for strong impurity-boson interactions, one needs more bosons to observe convergence of the effective mass.

C. Bosonic artificial atom in one dimension: Benchmarks, mean-field derivations and additional data for few-body limit

We provide additional details to our findings in Chap. 5. First, we benchmark the IM-SRG method against the well-established multi-layer multi-configuration time-dependent Hartree method for atomic mixtures. The multi-layer multi-configuration time-dependent Hartree method for atomic mixtures simulations, shown in App. C.1, were performed by Simeon Mistakidis. Then, we showcase the mean-field solution in a box trap. After that, we present details on our extension of the mean-field solutions in the low-density limit. In the end, we consider the smallest artificial atom systems.

C.1. Comparison between the ML-MCTDHX and IM-SRG

We benchmark the relatively novel method of the flow equation approach for cold gases, see Refs. [61–63, 71, 72] against the well established multi-layer multi-configuration time-dependent Hartree method for atomic mixtures (ML-MCTDHX) [56] (for a relevant review of this method see Ref. [57]). The latter method is a variational approach that has been used extensively for studying systems with impurities [21, 96, 166, 205, 233, 234]. The data from the ML-MCTDHX calculation were provided by Simeon Mistakidis.

Let us start by comparing the density, Eq. (5.19) and phase fluctuations, Eq. (2.48) for the largest value of N considered in the main text (cf. Fig. 5.4). We show the results in Fig. C.1. We can clearly see that both methods are in good agreement. We also compared the energy per particle and found for IM-SRG $EM/Nc^2 = -0.100722 \pm 0.000089$ and with the ML-MCDTHX $EM/Nc^2 = -0.097$.

We further use a box potential instead of the periodic boundary conditions to explore the formation of the artificial atom from bosons in the presence of hard-wall boundary conditions. This gives us another benchmark in a different setup for the IM-SRG method. We show the results for energy, density and phase fluctuations for different particle numbers N in Fig. C.2. We use values of N which correspond to bound, critical and

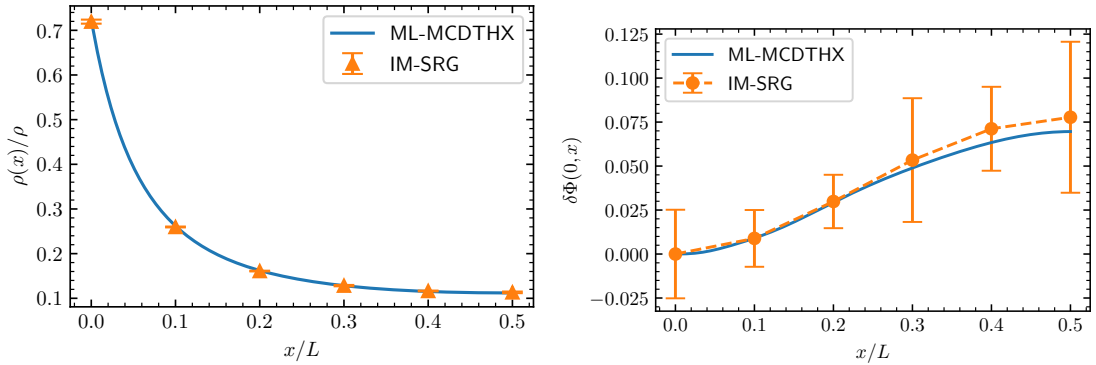


Figure C.1.: **Comparison between IM-SRG and ML-MCDTHX for density and phase fluctuations.**

We show the Bose-gas density (left) and phase fluctuations (right) for a system consisting of a single impurity potential and $N = 15$ particles. The other parameters of the system are $\alpha = -5$, $LM|c| = 0.5N$. Circles show results obtained with the IM-SRG method while the solid curve corresponds to the ML-MCDTHX result. The numerical error bars are calculated according to the prescription given in 2.3. Figure taken from Ref. [62].

scattering state according to our discussion in the main text. Note that because we use different boundary conditions now (hard wall instead of periodic) the properties of the system are strongly modified if L is in the order of $1/M|c|$. As an example: We need to use stronger impurity-boson interaction than in the main text to observe significant beyond-mean-field effects.

We can see that while the results for energy and density are in good agreement, phase fluctuations show deviations. We noticed that although energy and density might be well converged with a simple ML-MCDTHX calculation, the calculation of phase fluctuations requires more involved calculations (e.g. more orbitals, see Ref. [56]). We checked this by increasing the number of orbitals used in the ML-MCDTHX, see panel d). We can clearly see a systematic improvement in the agreement between IM-SRG and ML-MCDTHX. The main disagreement between the two methods is close to the boundaries of the box trap. In this case, the calculation of the phase fluctuations becomes difficult because very precise data of the density is needed as it approaches zero, see Eq. (2.48). We attribute the small decrease in phase fluctuations visible from the ML-MCDTHX data to numerical artifacts. Therefore, we also only showcase results for $x < 0.35L$.

Our conclusion from this comparison is that both methods are in good agreement

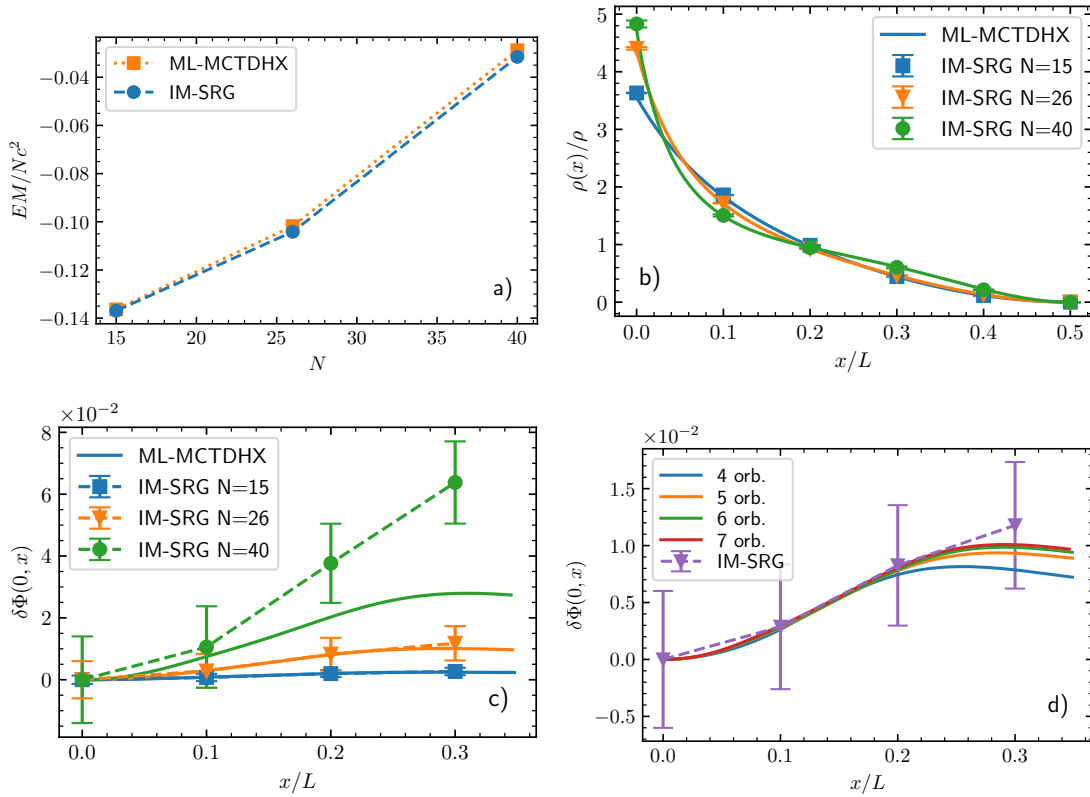


Figure C.2.: **Comparison between IM-SRG and ML-MCDTHX for energy, density and phase fluctuations for a system with hard wall boundary conditions.** Energy [panel a)], density [panel b)] and phase fluctuations [panel c)] for a Bose gas with an impurity in the middle of the trap supplemented by hard wall boundary conditions. The parameters of the system are: $\alpha = -12.5$, $LM|c| = 0.25N$, and $N = 15, 26, 40$. [Note that the critical particle number for these parameters in a ring is $N_{cr} = 26$]. We show results obtained with IM-SRG (symbols) and ML-MCDTHX (solid lines). Dashed lines are added to guide the eye. In panel d) we showcase phase fluctuations for different numbers of orbitals in the ML-MCDTHX. Note that already for three orbitals, the values of the energy and density are in agreement with IM-SRG. Figure taken from Ref. [62].

although they employ different approximation schemes to be able to go to large particle numbers. While the ML-MCTDHX contains in general more information about the Hilbert space of the system compared to the IM-SRG, the calculation of higher-order observables such as phase fluctuations might be advantageous using the IM-SRG framework.

C.2. Mean-field solution for hard-wall boundary conditions

For the sake of completeness, we present shortly the mean-field solution of a Bose gas confined by hard wall boundary conditions with an attractive impurity potential in the middle of the trap. We found that the function given from the Jacobi-cs function [102]:

$$f(x) = \sqrt{\frac{4K(p)^2}{MgL^2\delta^2(N-1)}} \operatorname{cs} \left(\frac{2K(p)}{\delta} \left[\frac{|x|}{L} + \frac{\delta-1}{2} \right], p \right), \quad (\text{C.1})$$

with

$$\mu = 2K(p)^2 \frac{p-2}{M\delta^2L^2}, \quad (\text{C.2})$$

reproduces the correct many-body bound state in the limit $L \rightarrow \infty$. The parameters p and δ are again determined from the normalization and impurity boundary condition:

$$\int |f|^2(x) dx = 1, \quad \left. \frac{\partial f}{\partial x} \right|_{x=0^+} = -cMf(0). \quad (\text{C.3})$$

Note that also other Jacobi-elliptic functions exist that solve the GPE with our boundary conditions such as:

$$f(x) = \sqrt{\frac{4K(p)^2(1-p)}{MgL^2\delta^2(N-1)}} \operatorname{sc} \left(2K(p) \left[-\frac{|x|}{\delta L} + \frac{1}{2\delta} \right], p \right), \quad (\text{C.4})$$

with

$$\mu = 2K(p)^2 \frac{p-2}{\delta^2L^2}. \quad (\text{C.5})$$

However, this function leads to nonsensical results in the limit $L \rightarrow \infty$. Additional solutions that correspond to the scattering solution are harder to find. We leave them to future studies.

C.3. Zero-Density Limit within Mean-field Approximation

Let us provide some technical details on the results presented in Sec. 5.4.

C.3.1. Many-body bound state

We start by considering the many-body bound state solution, Eq. (5.4), for a finite ring. In the limit $L \rightarrow \infty$, we have $p \rightarrow 1$ ¹:

$$f(x) = \sqrt{\frac{1}{Mg(N-1)}} \frac{\ln(a)}{\delta L} \sinh \left(\ln(a) \left[\frac{|x|}{\delta L} + b \right] \right)^{-1}, \quad (\text{C.6})$$

with $a := \frac{16}{1-p}$ and $b := \frac{\delta-1}{2\delta}$. We used that $K(p) \rightarrow 1/2 \ln(a)$ [102].

The boundary condition due to the impurity-boson interaction can be written as

$$-f'(0^+) = Mcf(0) \quad (\text{C.7})$$

$$\Rightarrow \frac{x+1}{x-1} = \coth(\ln(a)b) = \frac{-cM\delta L}{\ln(a)}, \quad \text{for } x := a^{2b} \quad (\text{C.8})$$

while we get

$$1 = \lim_{L \rightarrow \infty} \int_{-L/2}^{L/2} f(x)^2 dx \quad (\text{C.9})$$

$$\Rightarrow 1 = \frac{4}{Mg(N-1)} \frac{\ln(a)}{\delta L} \left[\frac{1}{1-a} - \frac{1}{1-x} \right] \stackrel{a \gg 1}{\approx} \frac{4}{\kappa g(N-1)} \frac{\ln(a)}{\delta L} \frac{1}{x-1} \quad (\text{C.10})$$

from the normalization. We can combine both conditions to

$$\frac{\ln(a)}{\delta L} = \frac{Mg(N-1)}{2} \zeta, \quad (\text{C.11})$$

with

$$\zeta = -\frac{2c}{g(N-1)-1} = \frac{N_{\text{cr}} - N}{N-1}. \quad (\text{C.12})$$

Because $x > 1$ by definition, we derive the condition for the existence of the solution:

$$N \leq 2 \frac{|c|}{g} + 1, \quad (\text{C.13})$$

which is in agreement with the PoT condition Eq. (5.10) from the main text.

¹Note that the mean-field solution with hard wall boundary conditions, Eq. (C.1), leads to an identical expression.

We can also derive analytic expressions for the chemical potential:

$$\mu = -\frac{\ln(a)^2}{2M\delta^2L^2} = -\frac{Mg^2(N-1)^2}{8}\zeta^2 = -\frac{1}{2Mx_{\text{mbb}}^2}, \quad (\text{C.14})$$

with $x_{\text{mbb}} = \frac{1}{M|c|} \frac{\zeta+1}{\zeta}$, the characteristic width defined in the main text, and the energy per particle

$$\begin{aligned} E/N &= \lim_{L \rightarrow \infty} \mu - \frac{g(N-1)}{2} \int_{-L/2}^{L/2} dx f(x)^4 \stackrel{a \gg 1}{\approx} -Mg^2(N-1)^2 \left(\frac{\zeta(\zeta+1)}{8} + \frac{1}{24} \right) \\ &= -\frac{1}{Mx_{\text{mbb}}^2\zeta^2} \left(\frac{\zeta(\zeta+1)}{2} + \frac{1}{6} \right). \end{aligned} \quad (\text{C.15})$$

We can also further simplify our mean-field solution by using Eq. (C.11)

$$\begin{aligned} f(x) &= \sqrt{\frac{Mg(N-1)}{4}} \zeta \sinh \left(\frac{Mg(N-1)}{2} \zeta x + \ln(\sqrt{2\zeta+1}) \right)^{-1} \\ &= \sqrt{\frac{2\zeta(2\zeta+1)}{x_{\text{mbb}}}} \frac{1}{(2\zeta+1)e^{x/x_{\text{mbb}}} - e^{-x/x_{\text{mbb}}}}, \end{aligned} \quad (\text{C.16})$$

Note that for $N = N_{\text{cr}}$ we have $\zeta \rightarrow 0$. An expansion of this function around $x\zeta \rightarrow 0$ leads to

$$f(x) = \sqrt{\frac{|c|M}{2}} \frac{1}{|c|Mx+1}. \quad (\text{C.17})$$

C.3.2. Point of transition

Let us now consider the case of $N = N_{\text{cr}}$. In this case, the mean-field solution reads

$$f(x) = \sqrt{\frac{\pi^2}{MgL^2\delta^2(N-1)}} \frac{1}{\cos\left(\frac{\pi(x-L/2)}{\delta L}\right)}. \quad (\text{C.18})$$

We found empirically that in the limit $L \rightarrow \infty$, we have $\delta \rightarrow 1$ and therefore $\frac{\pi x}{\delta L} \rightarrow 0$. Inserting these expressions leads us to:

$$f(x) \approx \sqrt{\frac{|c|M}{2}} \frac{1}{|x| + \frac{L\delta(\delta-1)}{2}}. \quad (\text{C.19})$$

With this, we get the following normalization condition,

$$\frac{Mg\delta L(N-1)}{2\pi} = \tan\left(\frac{\pi}{2\delta}\right), \quad (\text{C.20})$$

which we use to derive

$$\tan\left(\frac{\pi}{2\delta}\right) \stackrel{\delta \rightarrow 1}{\approx} \frac{2}{\delta-1}, \quad (\text{C.21})$$

which leads to

$$f(x) = \sqrt{\frac{|c|M}{2}} \frac{1}{|c|Mx+1}. \quad (\text{C.22})$$

Note, that this expression is equivalent to the one we got in the previous subsection by expanding the solution of the many-body bound state limit to the critical case. We find for the chemical potential that it vanishes:

$$\mu = \lim_{L \rightarrow \infty} \frac{\pi^2}{2M\delta^2 L^2} = 0. \quad (\text{C.23})$$

C.4. Smallest artificial atom

Let us shortly discuss the smallest non-trivial artificial atom with $N = 2$ where we use a relative interaction strength such that $N_{\text{cr}} = 2$ or $N_{\text{cr}} = 3$. For these small systems, it is *a priori* unclear if the mean-field approximation is applicable.

If we consider only two particles, the IM-SRG method is essentially exact except for the errors due to the finite Hilbert space, see Sec. 2.3. Therefore, we can benchmark the mean-field approximation even for very large ring sizes. We show results for density and phase fluctuations in Fig. C.3. A comparison of the density shows that the mean-field approximation is in excellent agreement with the IM-SRG method. Also, the calculation of phase fluctuations reveals that beyond-mean-field effects are small. Note that for the largest ring size considered, $LM|c| = 2.5N$, the density becomes too low which renders the definition of phase fluctuations, eq. (2.48), meaningless.

This discussion further showcases that the physical picture given in Sec. 5.2.2 is accurate even for the smallest setups.

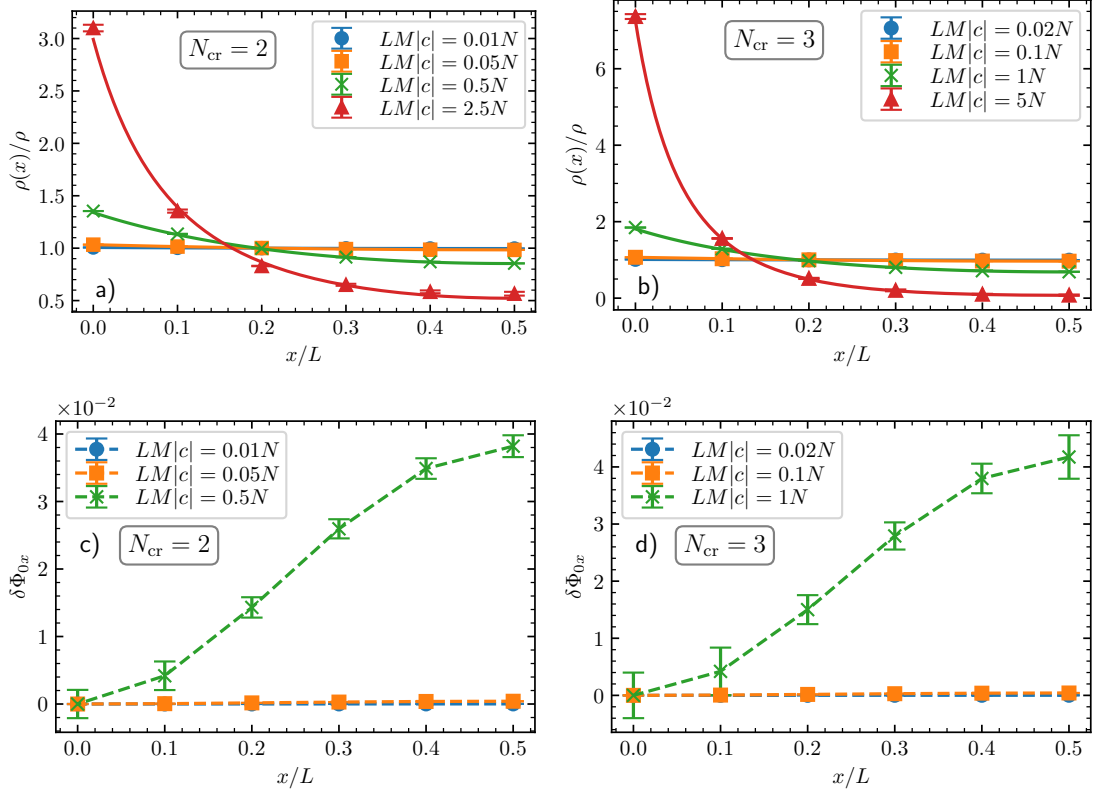


Figure C.3.: **Density and phase fluctuations for the smallest artificial atom.**

We show in panels a) and b) show the density of the Bose gas while panels c) and d) demonstrate phase fluctuations. All data are for $N = 2$ bosons. Panels a) and c) are for systems with $\alpha = -0.5$ ($N_{\text{cr}} = 2$), and panels b) and d) for $\alpha = -1$ ($N_{\text{cr}} = 3$). Circles, boxes, crosses and triangles are calculated with IM-SRG, and the solid curves are the corresponding mean-field results (Eqs. (5.4), (5.8)). The dashed curves are provided to guide the eye. Figure taken from Ref. [62].

D. Two-dimensional bosonic droplets: Variational ansatz

In this appendix, we want to provide additional details on the variational ansatz employed in Chap. 6. We present all relevant equations for the one used in the main part of this chapter. Furthermore, we present results obtained with a different variational ansatz in which both shapes, the universal from Ref. [39] and the harmonic oscillator scale with the characteristic width of the ground state.

D.1. Details on variational ansatz

Let us start with all relevant equations for the variational approach used in Chap. 6, Eq. (6.6). For better readability, we use here a system of units such that $\hbar = m = \omega = 1$. For the mean-field orbital we use:

$$\Psi(\vec{r}) = \frac{1}{\sqrt{\alpha_{\text{HO}}^2 + \alpha_{\text{free}}^2 + 2\alpha_{\text{HO}}\alpha_{\text{free}}\frac{\bar{C}}{\sqrt{C}C_2R}}} \left(\alpha_{\text{HO}} \frac{\sqrt{N}}{\sqrt{2\pi C_2}} f_{\text{HO}}(r) + \alpha_{\text{free}} \frac{\sqrt{N}}{\sqrt{2\pi CR}} f_{\text{free}}(r/R) \right) \quad (\text{D.1})$$

with

$$C_2 = \int dr r f_{\text{HO}}^2(r), \quad \bar{C} = \int dr r f_{\text{HO}}(r) f_{\text{free}}(r/R).$$

Inserting this ansatz into the Hamiltonian leads to an energy of:

$$\begin{aligned}
E = & \frac{\alpha_{\text{HO}}^2}{\alpha_{\text{HO}}^2 + \alpha_{\text{free}}^2 + 2\alpha_{\text{HO}}\alpha_{\text{free}}\frac{\bar{C}}{\sqrt{CC_2R}}} \left(\frac{N}{2C_2} A_2 - \frac{\alpha_{\text{HO}}^2}{\alpha_{\text{HO}}^2 + \alpha_{\text{free}}^2 + 2\alpha_{\text{HO}}\alpha_{\text{free}}\frac{\bar{C}}{\sqrt{CC_2R}}} \frac{gN^2 B_2}{4\pi C_2} \right. \\
& \left. + \frac{1}{2} \frac{\omega^2 N D_2}{C_2} \right) + \frac{\alpha_{\text{free}}^2}{\alpha_{\text{HO}}^2 + \alpha_{\text{free}}^2 + 2\alpha_{\text{HO}}\alpha_{\text{free}}\frac{\bar{C}}{\sqrt{CC_2R}}} \left(\frac{N}{2C_2 R^2} A \right. \\
& \left. - \frac{\alpha_{\text{free}}^2}{\alpha_{\text{HO}}^2 + \alpha_{\text{free}}^2 + 2\alpha_{\text{HO}}\alpha_{\text{free}}\frac{\bar{C}}{\sqrt{CC_2R}}} \frac{gN^2 B}{4\pi C R^2} + \frac{1}{2} \frac{\omega^2 N D R^2}{C} \right) \\
& + 2 \frac{\alpha_{\text{HO}}\alpha_{\text{free}}}{\alpha_{\text{HO}}^2 + \alpha_{\text{free}}^2 + 2\alpha_{\text{HO}}\alpha_{\text{free}}\frac{\bar{C}}{\sqrt{CC_2R}}} \left(\frac{N}{2\sqrt{CC_2}} \tilde{A} + \frac{1}{2} \frac{\omega^2 N}{\sqrt{CC_2}} \tilde{D} \right) \\
& + \frac{\alpha_{\text{HO}}\alpha_{\text{free}}}{\left(\alpha_{\text{HO}}^2 + \alpha_{\text{free}}^2 + 2\alpha_{\text{HO}}\alpha_{\text{free}}\frac{\bar{C}}{\sqrt{CC_2R}} \right)^2} \frac{gN^2}{4\pi} \left(4 \frac{\alpha_{\text{HO}}^2}{\sqrt{C_2^3 C}} \tilde{B} + 4 \frac{\alpha_{\text{free}}^2}{\sqrt{C_2 C^3}} \bar{B} + 6 \frac{\alpha_{\text{free}}\alpha_{\text{HO}}}{\sqrt{C_2^2 C^2}} \hat{B} \right)
\end{aligned} \tag{D.2}$$

with

$$\begin{aligned}
A &= \int dr r [f'_{\text{HO}}(r)]^2, \quad B_2 = \int dr r f_{\text{HO}}^4(r), \quad D_2 = \int dr r^3 f_{\text{HO}}^2(r) \\
\tilde{A} &= \int dr r f'_{\text{HO}}(r) f'_{\text{free}}(r/R), \quad \tilde{D} = \int dr r^3 f_{\text{HO}}(r) f_{\text{free}}(r/R) \\
\tilde{B} &= \int dr r f_{\text{HO}}^3(r) f_{\text{free}}(r/R), \quad \bar{B} = \int dr r f_{\text{HO}}(r) f_{\text{free}}^3(r/R), \quad \hat{B} = \int dr r f_{\text{HO}}^2(r) f_{\text{free}}^2(r/R).
\end{aligned}$$

Because it is numerically very expensive to calculate all R -dependent integrals in each step of the minimization calculation, we assume that $R = R_{\text{free}}$ if $R_{\text{free}} < 1$ and in all other cases that $R = 1$ (see main text of Chap. 6). Next, we minimize the energy, Eq. (D.2), with respect to α_{HO} and α_{free} for each interaction strength. We show a plot of the energy as a function of these parameters in Fig. D.1 for two different interaction strengths: Once $R_{\text{free}} < 1$ (right panel) and once $R_{\text{free}} > 1$ (left panel). We can clearly see that the energy is minimized when one of the parameters is zero, i.e., at the boundaries of the plot. For the left panel with $R_{\text{free}} > 1$ we can see that it is energetically favorable to have $\alpha_{\text{free}} = 0$ while in the right one $\alpha_{\text{HO}} = 0$ is preferred. This explains the sharp transition discussed in the main text: there is no particle number or interaction strength for which both α -values are non-zero after the minimization of the energy.

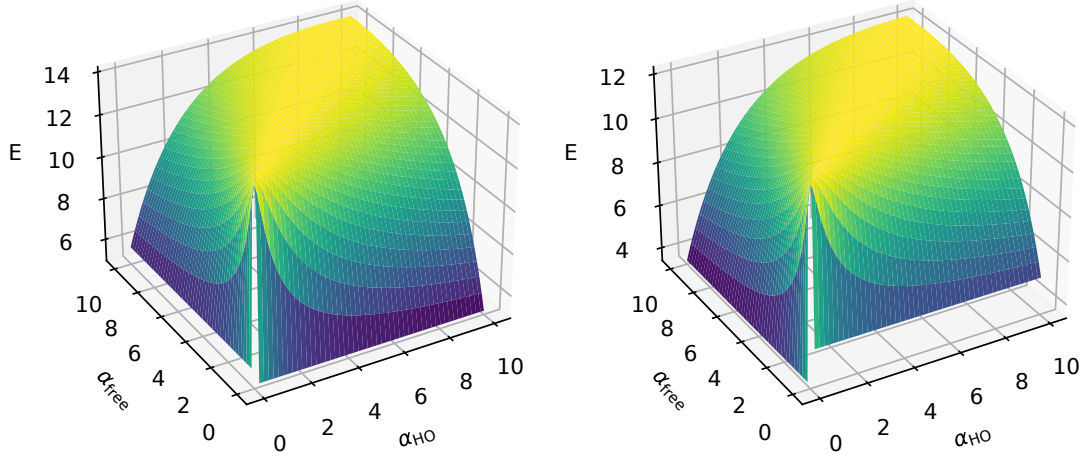


Figure D.1.: **Energy calculated with our ansatz, Eq. (D.2) as a function of the parameters α_{HO} and α_{free} for $N = 9$ bosons.** In the left panel, we have a two-body interaction of $\ln(B_2)/N = -2.05$ while in the right panel, we have $\ln(B_2)/N = -2$. Note that the α -parameters are defined to be positive. Figure taken from Ref. [210].

D.2. Alternative variational ansatz

As briefly mentioned in the main text, we also employed a different variational ansatz to study the system. In this approach, both shapes are scaled with the characteristic width R :

$$\Psi(\vec{x}) = \mathcal{N} (\alpha_{\text{HO}} f_{\text{HO}}(r/R) + \alpha_{\text{free}} f_{\text{free}}(r/R)) , \quad (\text{D.3})$$

where \mathcal{N} is the normalization coefficient. The advantage of this ansatz, compared to the one used in the main text, is that the energy can be minimized with respect to α_{HO} , α_{free} and R with similar numerical effort as for the previous ansatz. This eliminates the need to rely on physical intuition to determine R . The disadvantage is that it is difficult to justify why both shapes should scale with R ; the physically more relevant scenario is presented in the main text.

Furthermore, this ansatz does not capture the sharp transition between the two states, which we inferred from the results of Ref. [217]. Instead, minimization of this ansatz leads to a smooth transition between the trap dominated state and the interaction dominated one. We show this in Fig. D.2, where we display the ratio of the mean-square radius. As

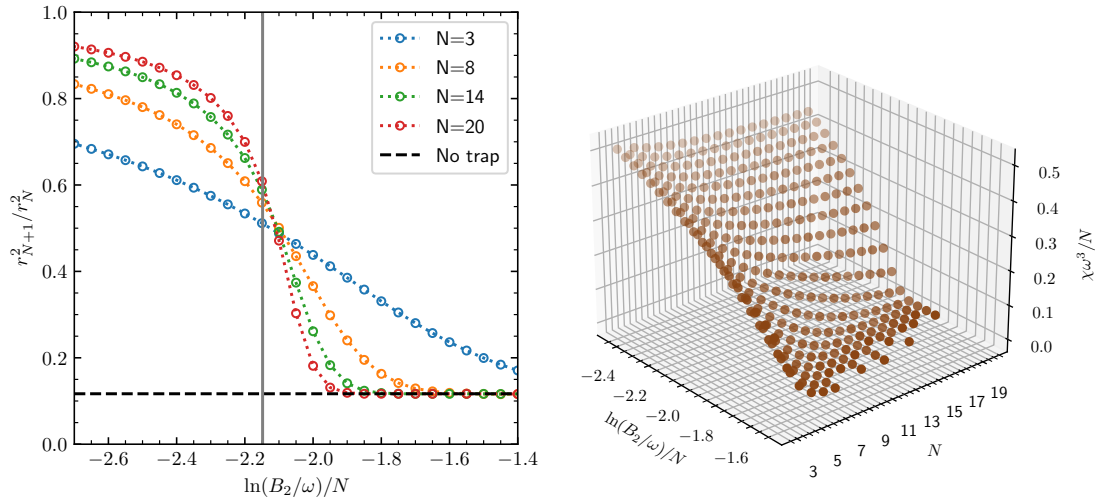


Figure D.2.: **Ratio of radii (left), r_{N+1}^2/r_N^2 , and static response per particle (right), χ/N , calculated using the ansatz where both shapes are scaled with R , Eq. (D.3).** Left panel: Symbols are the results obtained from the minimization of the energy with. The black dashed line in the left panel is the universal prediction from Ref. [39] and the vertical solid grey line shows the critical interaction strength $\ln(B_2/\omega)/N = -2.148$, Eq. (6.14). Dashed lines are added to guide the eye.

one can see, in contrast to Fig. 6.3, we now observe a smooth crossover between the two states of the system for all particle numbers, with the transition becoming sharper as the particle number increases. We can also see that the critical interaction strength predicted using perturbation theory in the main text, $\ln(B_2/\omega)/N \approx -2.15$, roughly matches the point where the system transitions between the two states using Eq. (D.3).

Additionally, we present the static response in this figure. The difference between this ansatz and the one used in the main text becomes even more clear: instead of a sharp transition from a static response of one to zero, we observe a smooth decrease in compressibility. From this observable, we cannot infer an increase in sharpness with increasing particle number. Nevertheless, this figure demonstrates that the static response can still be used to distinguish between the trap-dominated and interaction-dominated states.

In summary, the conclusions drawn in Chap. 6 remain valid if the ansatz discussed in this appendix, Eq. (D.3), is employed. The primary difference is that, unlike the ansatz used

in the main text, this one results in a smooth crossover between the two states, contrary to the sharp transition suggested by Ref. [217]. As discussed in the outlook of Chap. 6, more *ab initio* calculations are necessary to confirm the sharp transition between the two states in our system. Additionally, incorporating density-dependent coupling constants into the Gross-Pitaevskii equation might help determine which of the two variational approaches is physically more accurate. Based on our current understanding, we believe that the approach used in the main text better captures the physics of attractively interacting bosons in a 2D harmonic trap.

Curriculum vitae

Personal information

Name: Fabian Brauneis

Academic and professional experience

January 2021 - December 2024	Ph.D. Candidate and Research Assistant Technische Universität Darmstadt
October 2019 - December 2024	Tutor and Teaching Assistant Technische Universität Darmstadt
April 2023 - May 2023 & September 2023 - October 2023	Visiting Researcher Lunds universitet, Lund, Sweden
February 2020 - March 2020 & July 2020 - September 2020	Scientific Intern Institute of Science and Technology Austria, Klosterneuburg, Austria

Education

January 2021 - December 2024	Ph.D. in Physics Technische Universität Darmstadt
October 2018 - December 2020	M.Sc. in Physics Technische Universität Darmstadt
October 2015 - September 2018	B.Sc. in Physics Technische Universität Darmstadt
August 2007 - June 2015	Abitur Einhardtschule Seligenstadt

Acknowledgements

Now that my time as a Ph.D. student comes to an end, I would like to thank all the people who helped me along this way and made this time very enjoyable.

First of all, I would like to thank Hans-Werner for supervising this thesis. I already joined his group for my Master's thesis, and I have always enjoyed our discussions about physics; I learned a lot from him over the years. I would like to thank him for the freedom he gave me during my PhD, for enabling me to attend various conferences, and for supporting my research visit to Sweden.

Furthermore, I want to thank Artem Volosniev. I am really grateful for the opportunity to work with him. He was a great mentor and guided me through the last five years. Even though we only worked in the same place for a few months in 2020, a quick Zoom call made it possible that this distance was never really there. I also want to thank him for agreeing to be the second referee for this work. I wish him all the best for his future career.

Next, I want to thank all the people with whom I collaborated over the years: Timothy Backert, Areg Ghazaryan, Mikhail Lemeshko, Simeon Mistakidis, and Stephanie Reimann. I thoroughly enjoyed our discussions and learned a lot from them.

I would also like to thank Matthias Heinz for discussions about the IM-SRG method, which sharpened my understanding, and for sharing his code with me, which helped me bring my version up to speed.

In addition, I want to thank Stephanie Reimann for giving me access to the CI-library of her group and for hosting me as a visiting researcher. I will never forget my time in Lund, and I want to thank everyone in the Mathematical Physics division for creating a very pleasant atmosphere, whether during work, lunch, or in our free time. I still miss Friday's Fika! I would also like to thank the DAAD for financially supporting this research visit.

My thanks also go to Stephanie Reimann for connecting me with some really great scientists: Lila Chergui, Georg Bruun and of course the experimentalists from Heidelberg: Sandra Brandstetter, Maciej Gałka, Carl Heintze and Selim Jochim. I thoroughly enjoyed our discussions; it really was a pleasure to work with people doing physics in the "real world", i.e., a laboratory.

Let's not forget my working group. Thanks a lot to all current and former members for

creating a very pleasant working environment but also for many funny discussions during lunch, coffee, our yearly hike and of course the board game evenings. I hope that I will still be invited to those.

If you find any error in this thesis, you have to complain to my proofreaders: Timothy Backert, Lila Chergui, Wael Elkamhawy, David Huber, Tanja Kirchner, Daniel Kromm and Niklas Schild. (I am kidding, of course; thanks a lot for reading parts of my thesis and for your helpful comments.)

Schlussendlich möchte ich mich bei den wahrscheinlich wichtigsten Menschen bedanken: Meinen Freunden und meiner Familie. Danke für eure unentwegte Unterstützung, auch bereits während meines Studiums. Ein besonderer Dank gebührt meinen Eltern, Andrea und Roger Brauneis, ohne deren Unterstützung ich mit Sicherheit niemals so weit gekommen wäre. Vielen Dank für alles! Und natürlich tausend Dank an Annka, dafür, dass du mich immer unterstützt und mich vor allem während der letzten Wochen ausgehalten hast.

Danke!